Premise

Among the human cancers, the number of breast and uterine cancer cases are alarming. In fact, they represent the almost death cause in 26% and 7% of women, respectively [1]. For these reasons, research is essential for discovering new life-saving drugs. In the past decade, numerous molecules have been designed, synthesized and successfully studied for their promising anticancer activity. In particular, considerable development in oncology has been reached with the use of numerous effective drugs, Ellipticine (**XIII**), Vinblastine (**XIV**), *Cis*platin (**II**), Thalidomide (**XV**) and Quercetin (**XVI**). Nevertheless, the main limitation in therapy is often due to numerous side effects or their poor bioavailability.

In addition, another important limit is the frequent onset of resistance, sometimes the low solubility and high instability in physiological systems.

Most of the new anticancer agents demonstrate a single cellular target activity. Considering that cancer is a multifactorial disease and its development involves more signaling pathways, a single targeted therapy might not be efficient to block tumor progression. Additionally, single target agents do not produce always the desired effect, primarily because of the ability of the organism to activate compensatory ways. This single target therapy could lead to the onset of resistance and dramatic side effects. In this context, the multi-target drug design concept represents the current trend for future drug research and development.

Thus, new and effective pharmaceutical strategies with a synergistic mechanism, able to overcome these limitations, are urgently needed.

Considering this scenario, my PhD was focused on the design and biological evaluation of various synthetic analogues of some known anticancer drugs, in order to obtain molecules with improved pharmaceutical profiles.

Considering that the development of new drugs is expensive is taking a long time, the improvement of the safety and efficacy of old active molecules has become a very attractive and smart alternative in oncology, showing a significantly higher benefit/risk ratio when compared to the development of a new drug. Thus, the attention was also focused on the realization and the study of appropriate vehicles for the development of new formulations for anticancer compounds, using innovative pharmaceutical matrices, in order to obtain molecules with enhanced physical-chemical and pharmacokinetic/pharmacodynamics properties.

Chapter 1: Breast and uterine cancers

The term cancer or tumor refers to a disease characterized by uncontrolled cell growth, no longer regulated by the organism's control processes. Most of the time, our body is able to manage this through reparative processes involving the immune system. When this control fails, normal cells can turn into cancer cells. While cancer cells have common characteristics, there are about 200 different types of tumors. In Italy, cancers affecting the reproductive organs and the breasts are alarming for their number of cases incidences. More than 40,000 women die from breast cancer every year, while over 13,000 are diagnosed with uterine cancer. Mammograms and other preventions can save lives. Even today, too many women have no access to lifesaving breast and uterine cancer screenings, and there is a need to increase efforts for breast and uterine cancer research that could lead to new life-saving drugs.

1.1 BREAST CANCER

1.1.1 Breast anatomy

The breast is an equal and symmetrical organ, positioned inside the chest between the third and sixth intercostal space (Figure 1). The breast tissue is formed by:

- A glandular component that consists of 15-20 lobes, that lead to the nipple through a lactiferous duct;
- A component of adipose tissue, in which these glandular structures are dipped;
- A fibrous supporting component that divides the glandular parenchyma into lobes and lobules.

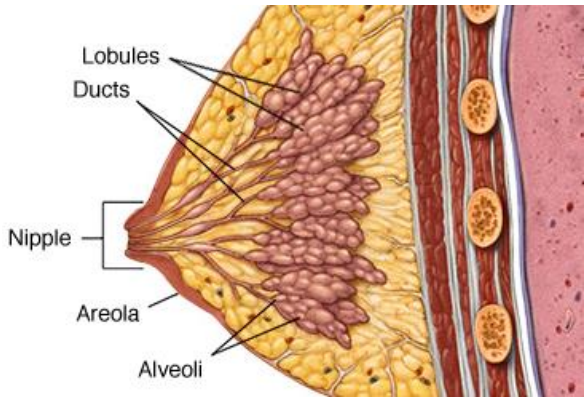

https://www.mayoclinic.org/healthy-lifestyle/womens-health/multimedia/breast-cancer-early-stage/sls-20076628?s=2

Figure 1. *Female breast anatomy.*

In the top of the breast there is the nipple, an external cone-shaped protrusion, in whose apical region it has about 15-20 milk pores that constitute the outlet of the lactiferous ducts. The nipple is in turn surrounded by the areola, a pigmented circular region having an average diameter ranging from 3 to 8 cm. Small protrusions, called Montgomery's tubercles, due to the underlying presence of sebaceous and areolar glands, characterize the areola. The fibrous bundles of the breast, sometimes called retinacula, extend in depth and divide the glandular parenchyma into lobes and lobules. Each lobule includes the alveoli that act as secreting units. The alveoli are covered by a simple epithelium that rests on a basement membrane in which myoepithelial cells are interleaved which favor the progression of the secretion through ducts of progressively increasing caliber. Each lobule presents a lactiferous duct, which opens laterally to the nipple in an ampoule, dedicated to the accumulation of the secretion. The simple cubic epithelium, in the alveolar ducts, becomes non-keratinized multilayered in the lactiferous ducts. The mammary gland represents the target of different hormones, which allow the normal physiology of the organ, such as female sex hormones. Some hormones are responsible, both directly and through the mediation of hormones produced by other organs, of different alterations to take place in the various forms of benign breast pathologies and can assume the role of precancerous lesions. For example, the pituitary gland is able to interact with the mammary gland directly by prolactin (PRL) and by growth hormone (GH) secretion, and indirectly by other hormones:

- The folliculo-stimulating (FSH) and luteinized (LH) hormones stimulate the ovary, that acts on the breast through estrogens and progesterone and also through some androgens;
- The thyroid stimulating hormone (TSH) affects thyroid function, releasing its two hormones triiodothyronine (T3) and thyroxine (T4), able to interfere with the breast;
- The adrenocorticotropic hormone (ACTH) exerts its action on the adrenal glands, which then determine their action on the breast not only through androgens, but also with cortisol and aldosterone.
- During the pregnancy, the placenta, through the release of chorionic mammotropin, estrogen and progesterone, promotes structural changes of the mammary gland;
- A not still clear role seems to be played by the pancreas using insulin.

All of these hormones are able to interact with the mammary gland thanks to specific receptors, that are basically divided into two types:

- Cytoplasmic receptors for steroid hormones (estrogens, progesterone, androgens);
- Membrane receptors for other hormones (PRL, GH, T3, T4, insulin).

Female puberty is characterized by a growth of the mammary gland due to a hormonal stimulation. Simultaneously, the quantity of adipose tissue of the subcutaneous tissue and of the connective tissue increases with a proliferation of ductal elements. The gland undergoes changes even after the pubertal development phase, for example, during the menstrual cycle, pregnancy, lactation and menopause [2].

1.1.2 Pathophysiology of breast cancer

1.1.2.1 Epidemiology

Breast cancers represent, overall, the most frequently diagnosed type of cancer among women of all ages: 0-49 years (41%), 50-69 years (35%), ≥70 years (21%) (Table 1) [3]. The pathology has great geographical variability and is more widespread in economically most advanced countries.

0-49	**50-69**	**70+**
Breast (40%)	Breast (35%)	Breast (22%)
Thyroid (16%)	Colorectal (11%)	Colorectal (16%)
Skin (melanome) (7%)	Uterus body (7%)	Lung (7%)
Colorectal (4%)	Lung (7%)	Pancreas (6%)
Uterine cervix (4%)	Thyroid (5%)	Stomach (5%)

Table 1. *Cancer incidence related to the women age [3].*

Breast cancer is the most diagnosed women malignancy in Italy (29% of all diagnosed cancers) and it represents the first cause of oncological death. In fact, it ranks first in all age groups considering oncological deaths: it represents 28% of deaths among young people, 21% among adults and finally 14% among women over 70 years. In 2016, approximately 12,616 deaths were recorded (according to ISTAT data). However, since the beginning of the 20th century a moderate but continuous decrease in breast cancer mortality

has been detected (-1.6% per year) due to increased awareness, prevention, and to therapeutic progress [3].

1.1.2.2 Risk factor

Age is a recognized risk factor. The risk of contracting breast cancer increases with age, with a chance to develop breast cancer of 2.3% up to 49 years (1 woman in 43), 5.4% between 50 and 69 years (1 woman in 18) and 4.5% between 70 and 84 (1 woman in 22). This correlation with age could be related to the continuous and progressive endocrine proliferative stimulus that the mammary epithelium undergoes over the years, combined with the progressive damage to DNA and the accumulation of epigenetic alterations and with alteration of the balance between oncogenes and suppressor genes expression. The incidence rate increases exponentially up to the menopausal age (around 50-55 years), then slows down with a plateau after menopause and, at the end, starts to rise again after the age of 60. This specific trend is linked both to the woman's endocrinological history and to the presence and coverage of mammography screening programs.

New risk factors have been identified:

- **Reproductive factors**: a long exposure of the glandular epithelium to proliferative stimuli of ovarian estrogens due to a long duration of the fertile period and a late menopause; a first pregnancy after the age of 30 and no breastfeeding.
- **Hormonal factors**: increased risk in women who use hormone replacement therapy during menopause, especially if based on synthetic estrogen-progestin with androgenic activity and in women taking oral contraceptives. Estrogens have an important role in breast cancer development: estrogen metabolites can cause mutations or generate free radicals that damage DNA [4]. However, other mechanisms also play a fundamental role, and some breast cancer are estrogen-negative or occur in women without increased exposure to these hormones.
- **Dietary and metabolic factors**: a low vegetable fibers intake seems to be associated with an increased risk of breast cancer. Diet and behaviors leading to the onset of obesity and metabolic syndrome are also becoming important. This is probably related to the excess of adipose tissue that in post-menopause represents the main source of estrogen synthesis, thus stimulating the mammary gland. The metabolic syndrome has certainly a genetic component, but lifestyles with low physical activity

and high-calorie, fat-rich, simple carbohydrate diets, clearly contribute to development.

- **Previous radiotherapy or breast dysplasia and cancers**.
- **Familiarity and inheritance**: although most breast cancer are sporadic, 5-7% are related to hereditary factors, 1/4 of which are determined by the mutation of two genes, BRCA-1 and BRCA-2. Women carrying mutation of the BRCA-1 and BRCA-2 genes, exhibit a 65% and 40% risk of getting breast cancer over the course of life, respectively [5]. These two dominant autosomal genes act as oncosuppressors and have several key functions, including transcription regulation, cell cycle control, ubiquitin-mediated protein degradation and DNA damage prevention. The loss of these functions leads to the risk of developing a malignant tumor, mainly breast, but also ovarian cancer [6].

1.1.3 Breast cancer classification

Breast cancer develops from the epithelial cells of the breast glandular tree and can give rise to various "isotypes", among which the most frequent are represented by "ductal carcinoma" and "lobular carcinoma". The first form derives from the main ducts and the second from the lobules. However, most of the breast cancer arise at the level of the terminal ductal lobular unit (TDLU) and subsequently, as a result of several mechanisms not known yet, give rise to several kinds of tumors, differing in morphological and biological behavior. For both types, two forms are recognized: in situ and invasive form. The in situ form refers to the proliferation of epithelial cells without infiltrating capacity; its proliferation is limited to ducts and lobules of the basement membrane, causing the carcinoma ductal in situ (CDIS) and carcinoma lobular in situ (CLIS), respectively. Instead, invasive or infiltrating carcinoma passes the basement membrane, invading the stroma and the blood vessels. This ability is due to a reduced production of E-cadherin, a protein responsible of the intercellular junction. A decrease in E-cadherin expression leads to the disintegration of the neoplastic mass, making its cells able, individually or in small clusters, to infiltrate the surrounding tissues. Other, but less common, forms are the tubular, papillary, mucinous and cribriform carcinoma, generally associated with a favorable prognosis [7].

Figure 2 outlines the main development stages of ductal breast cancer: first, it is possible to recognize the reversible phases that evolve from the presence of normal ducts to hyperplasia

and atypical hyperplasia; then there are the irreversible phases characterized by ductal carcinoma in situ and invasive ductal carcinoma.

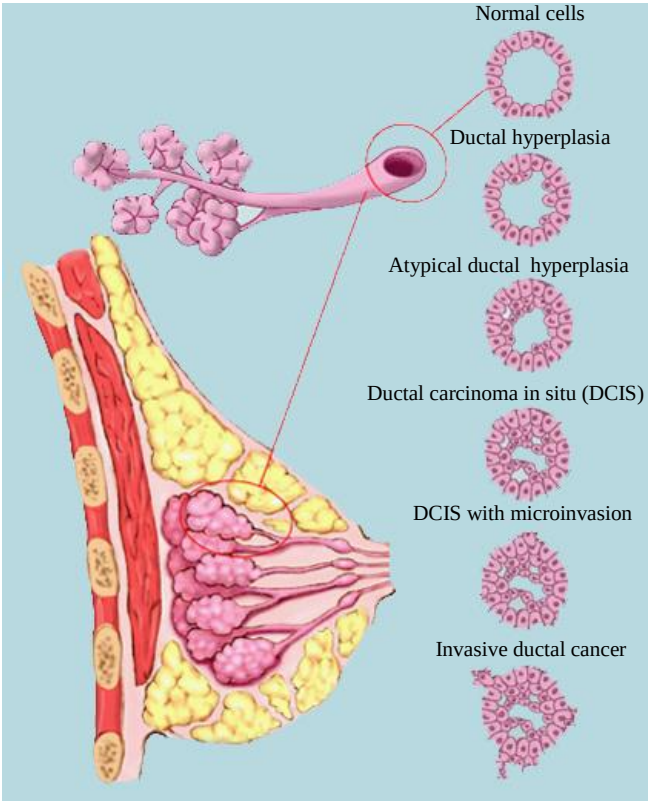

https://www.breastcancer.org/symptoms/types/dcis/diagnosis

Figure 2. *Development stages of ductal breast cancer.*

A further classification has been found thanks to the application of molecular biology methods. This classification divides breast cancers into five different cellular subtypes based on the specific receptors expression:

- **Luminal carcinoma A**: neoplasia characterized by the expression of estrogen (ER) and progesterone (PR) receptors, absence of HER2/neu receptor over-expression and low proliferative index (reduced expression of the Ki67 antigen).
- **Luminal carcinomas B** (HER2 negative): neoplasia characterized by the expression of hormone receptors, absence of HER2/neu receptor over-expression and intense proliferative activity (high expression of the Ki67 antigen).
- **Luminal carcinomas B** (HER2 positive): neoplasia characterized by the expression of hormone receptors and the HER2/neu receptor over-expression
- **HER2 positive (non-luminal) carcinomas**: neoplasia characterized by the HER2/neu receptor over-expression that do not express hormone receptors.

- **Basal-like carcinomas**: neoplasia characterized by lack of hormone receptor expression and absence of HER2 / neu receptors over-expression.

Estrogen (ER) and progestin (PR) receptors belong to the nuclear receptor family and are able to regulate gene expression by interacting with specific DNA sequences located on target genes. The activation of these intracellular receptors occurs through different mechanisms:

- **Ligand-dependent path**: In the absence of the ligand, the receptor is sequestered in the target cell's nucleus where it is complexed with the heat shock proteins (Hsp) which keeps it in an inactive conformation. Following the binding to the specific ligand, the receptor undergoes a conformational change that determines the detachment of Hsp and facilitates the dimerization and the binding of the receptor to DNA responsive elements located on target genes.
- **Ligand-independent path**: Receptor activation can occur in the absence of a ligand, following receptor phosphorylation by kinases involved in different signal transduction pathways, whose activity is in turn stimulated by substrates of various nature [8].

1.1.4 Breast cancer therapy

Considering the different forms of breast cancer, the personalized therapy represents the most important and demanding challenge. In fact, the choice of treatment must consider several factors that greatly influence the therapy response, such as histological features, molecular characteristics and tumor staging. However, the main therapeutic strategies consist in loco-regional treatments, such as surgery and radiotherapy, and in systemic pharmacological treatments, such as chemotherapy, hormone therapy and monoclonal antibody therapy (immunotherapy). In the surgical field, demolytic surgery (radical mastectomy, simple and subcutaneous mastectomy) and conservative surgery (tumorectomy, quadrantectomy) can be distinguished [9]. Radiation therapy is a therapeutic strategy that consists of using high-energy radiation to destroy neoplastic cells and prevent their growth. The main purpose of preoperative radiotherapy is to reduce the volume of the tumor and to prevent it from infiltrating the surrounding structures. In this way, radiotherapy can make operable lesions otherwise unresectable or can allow the surgeon to perform less

destructive interventions. The pharmacological treatments consist of different chemotherapy drugs used alone or in combination. Among these are (see Figure 3):

- **Nitrogen mustards**, such as cyclophosphamide (**I**) whose activity depends on the alkylating capacity of its active metabolite against the nitrogenous bases of DNA, and in particular guanine;
- **Platinum coordination complexes**, such as *Cis*platin (**II**) which is able to bind to the nitrogenous bases of DNA forming cross-link bonds;
- **Taxanes** how among these Paclitaxel (**III**) and Docetaxel (**IV**);
- **Anthracycline**: such as Doxorubicin (**V**) and Epirubicin (**VI**);
- **Folic acid analogues**: such as Methotrexate (**VII**) which reversibly and competitively inhibits the dihydrofolate reductase (DHFR);
- **Pyrimidine analogues** how among these 5 –fluorouracile (**VIII**) [10].

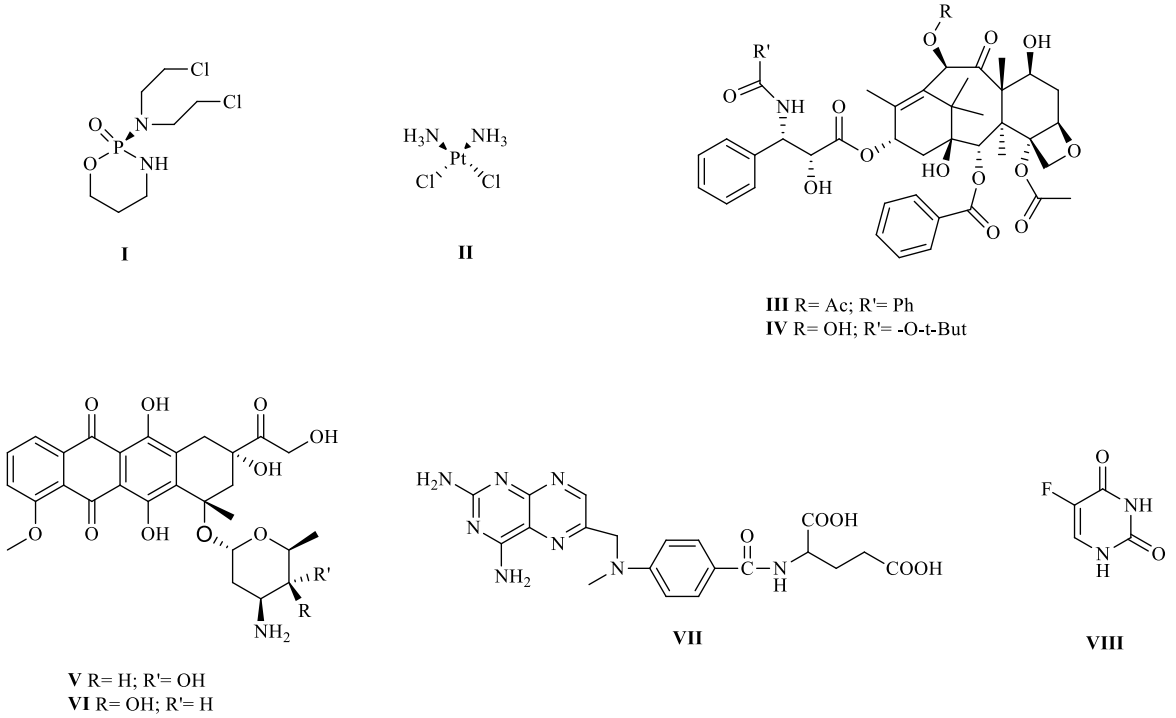

Figure 3. *Chemical structures of the principal drugs used in pharmacological treatment of breast cancer (**I-VIII**).*

1.2 UTERINE CANCER

Uterine cancers (cervix and endometrium) take the second place, after breast cancer, among the tumors that affect women.

1.2.1 Uterus anatomy

The uterus is a hollow organ placed in the pelvis, in the lower part of the abdomen, between the bladder, with which it makes contact anteriorly, and rectum, located posteriorly. It has the shape of a truncated cone with its apex pointing downwards. It measures about 8-10 cm in length [11]. The uterus is formed by two main parts: the body that represents the upper part; the cervix, which is the lower extremity and extends into the vagina (Figure 4).

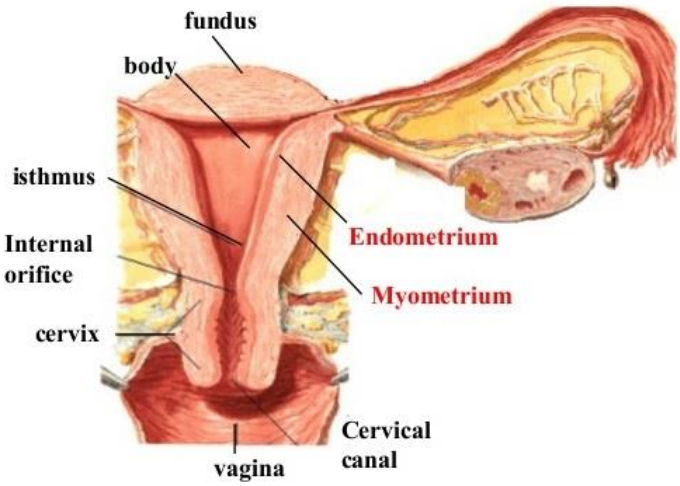

https://www.slideshare.net/doctorbobm/uterus-video

Figure 4. *Uterus anatomy*

The body of the uterus is in turn composed of two structures: an internal lining called endometrium (tissue directly involved in the various phases of the menstrual cycle following the activity of female hormones) and an external one, known as myometrium (fundamental muscle during the childbirth). The cervix can be divided into two parts: the endocervix (the one closest to the body of the uterus) and the exocervix (the one closest to the vagina). At the microscopic level the endocervix is covered by glandular cells, while the exocervix is lined with squamous cells. These two cell types make contact in the so-called transition zone, the area where most of the cervical tumors originate. The lining tissue outside the uterus is called serous.

1.2.2 Cervix cancer

The presence of two cellular subtypes in the uterine cervix lead to development of two types of carcinoma: squamous cell carcinoma (or epidermoid) which represents about 80% of tumors and adenocarcinoma (formed by cells in the glandular structure) which constitutes about 15%. There are 3-5% of tumors called adenosquamosis which are formed by both cellular components. As in other cancers, even in cervical cancer the risk factors can

be genetic but also linked to life styles (nutrition, cigarette smoking, hygiene and use of oral contraceptives). In the 1980s it has been demonstrated that this type of cancer has also an infectious viral origin and can derive from a persistent human papillomavirus (HPV) infection [12].

1.2.2.1 Human papillomavirus (HPV)

Papillomaviruses (PVs) belong to the Papillomaviridae family [13]. They are small, icosahedral symmetry-naked viruses with double-stranded circular DNA of about 8 kilobases. They contain an icosahedral capsid of 55 nm in diameter without a shell and possess a specific tropism for cutaneous and mucous epithelia (Figure 5). Their replication is restricted to this type of cell and is conditioned by the cell differentiation stage. About 200 types of HPV have been identified. Today the genomes of 100 viral types have been sequenced and characterized.

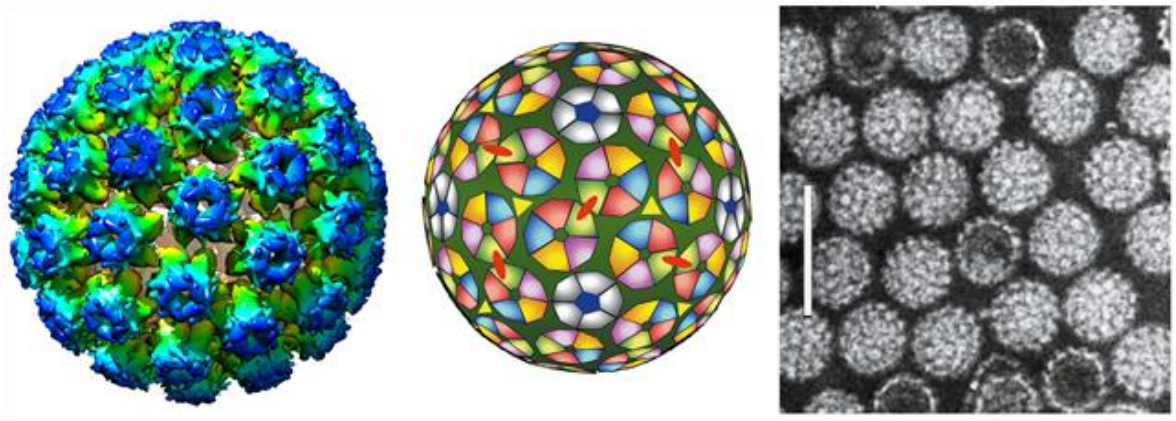

https://talk.ictvonline.org/ictv-reports/ictv_online_report/dsdna-viruses/w/papillomaviridae

Figure 5. *Rendering of a papillomavirus capsid.*

The genome of these viruses is divided into three regions:

- A non-coding region called “Long Control Region” (LCR), whose dimensions are significantly different between the genomes of the different types of HPV. The LCR has a molecular weight ranging from 400 to 1000 base pairs and contain sequences that regulate viral replication and transcription.
- An Early (E) region encoding early viral proteins, that contains six genes expressed in the initial phase of the replicative cycle, which encode non-structural proteins, named from E1 to E8, involved in viral replication and oncogenesis.

- A Late (L) region encoding late viral proteins, coding for capsidic structural proteins, named L1 and L2 [14].

1.2.2.1.1 HPV viral cycle and infection

The infection begins when the viral particles enter inside the basal layer cells (see Figure 6). The virus adheres to the host cell, thanks to the presence of specific receptors. There are strong controversies about the nature of cell surface receptors that allow the initial adhesion of the virus to the host cell. Several studies have shown some dependence on the presence of heparin sulfate [15]. Other studies, carried out with the use of VLP (Virus like particles), report that integrin α6 is responsible for the entry of the virus into the infected cell [16]. VLPs bind to integrin and the antibodies directed against α6 block the binding of the virus to the cell. However, the expression of these integrin is not necessary: in fact, some HPV are able to enter in the cells without these receptors.

The infection of basal cells leads to the activation of the viral gene expression cascade, which allows the production of 20-100 copies per cell of viral DNA in episomal form together with the cellular DNA. At the basal level, the expression of viral genes is limited to specific early genes. Some of these, such as E5, E6, E7 stimulate the infected cell to proliferate and expand laterally. In particular, E5 stimulates EGF receptor activation and therefore cell proliferation, E6 is able to induce p53 protein degradation and E7 promotes DNA replication interacting with pRb. A group of daughter cells leaves the basement membrane to stratify and differentiate, making it possible for the virus to enter in the upper layers of the epidermis. Thus, the late phase of the HPV replication cycle begins - in absence of viral DNA replication - with the expression of late viral genes and the translation of structural proteins. Subsequently, the control of the number of genomic copies is completely lost in the differentiated cells, and DNA is amplified and there will be thousands of copies per cell. Finally, assembly and release of mature viral particles into the extracellular environment occurs in the upper layers of the epithelium [17]. Obviously, the proliferative phase is accompanied by structural modifications of the infected cells. These changes affect the keratin filaments and the lipid secretion process that allows the creation of a physical barrier against the surrounding environment in the surface epithelium [18]. The consequence of this infection is the loss of cell cycle control, DNA repair and the slowdown of the cell differentiation process at the epithelial level. Therefore, HPV infection is strongly conditioned by the balance between host and infecting agent. In most cases, the virus is eliminated by the host's immune response before developing a pathogenic effect. In other

cases, it can remain latent or undergo replication causing a lesion at the genital level that can manifest different clinical forms, if it does not regress spontaneously. About 80% of infections are transient, asymptomatic and heal spontaneously due to the cell-mediated immune response. The persistence of the infection represent the necessary condition for the development of the carcinoma [19].

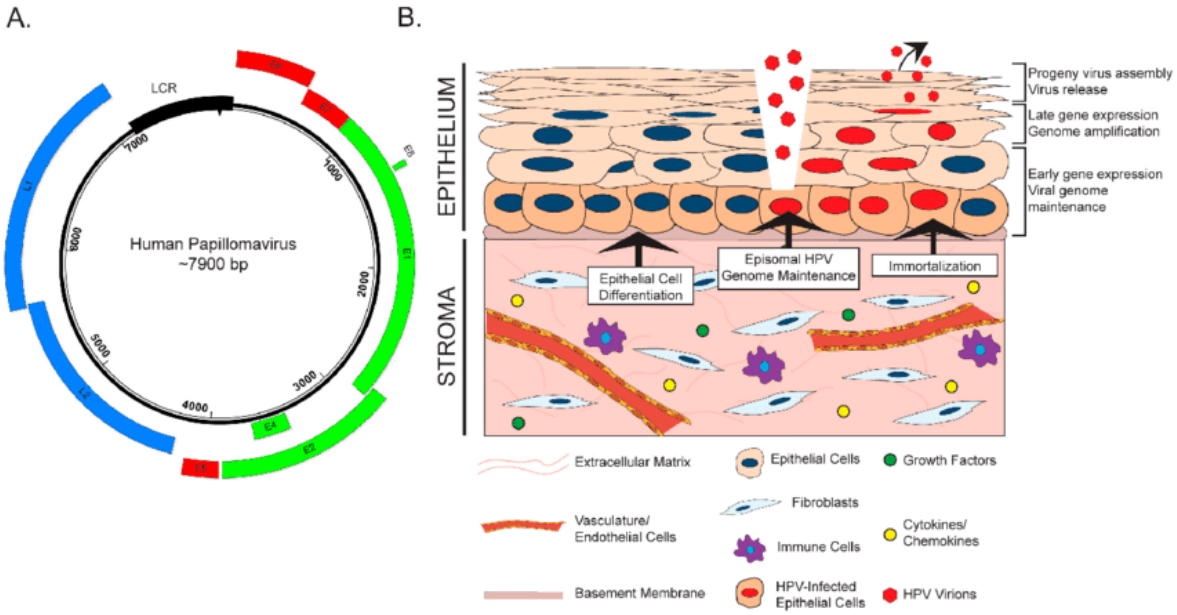

https://www.mdpi.com/1999-4915/9/8/219

Figure 6. *Viral and infectious cycle of Human papilloma virus*

1.2.2.2 Cervix cancer treatment

The treatment depends on several factors, including age and health conditions, but primarily on the types of the neoplasm. The therapeutic approaches are surgery, radiotherapy and chemotherapy. The most important surgical interventions consist in:

- Conization, in which a "cone" of tissue is taken in order to analyze it under a microscope;
- Hysterectomy, the total removal of the uterus;
- Radical trachelectomy, the removal of the cervix, surrounding tissue, a part of the vagina but not of the uterus to allow a possible pregnancy [20].

The main therapeutic regime consists in the use of Platin and Taxane-based drugs (see Figure 7). Among them, Carboplatin (**IX**) and Paclitaxel (**III**) are usually employed. Recent studies have shown that the addition of Bevacizumab to the chemotherapy with Carboplatin-Paclitaxel (**III**) increases progression-free survival by about 3 months and overall survival by about 4 months compared to chemotherapy alone. Antiangiogenic drugs, such as PARP-

1 inhibitors (Olaparib (**X**), Rucaparib (**XI**) and Niraparib (**XII**)), in combination with first-line chemotherapy are often used. While this strategy leads to an increased efficacy and costs, the use of antiangiogenic drugs is accompanied by an increased risk of arterial hypertension (25%), fistulas (6%) and thromboembolic events (8%). For this reason, the above mentioned combined therapy has been validated only for the treatment of advanced and recurrent diseases [21].

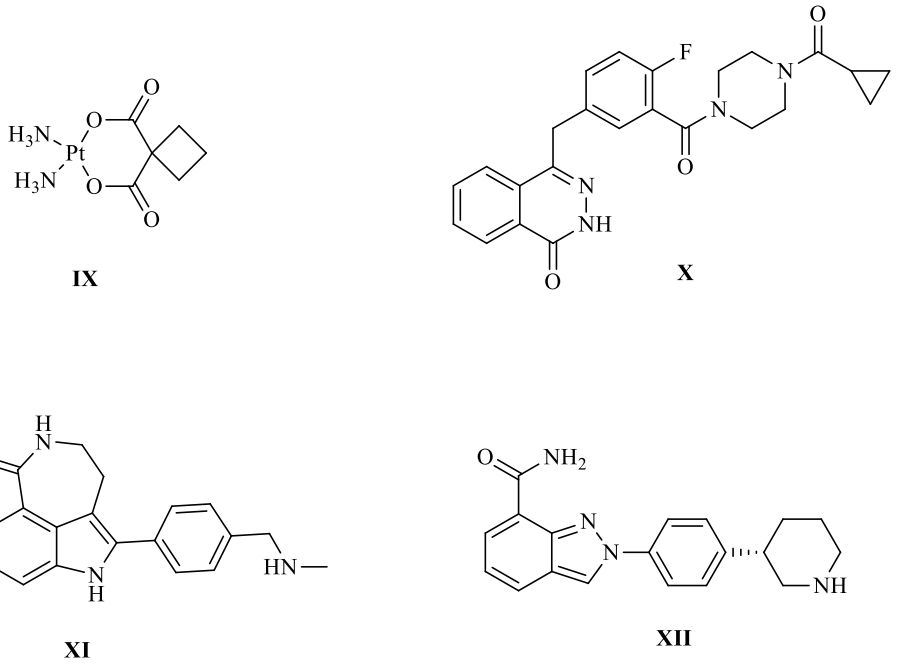

Figure 7. *Chemical structures of the principal drugs used in pharmacological treatment of cervix cancer (**IX-XII**).*

1.2.3 Endometrial cancer

Endometrial carcinoma (EC) is one of the most frequent tumors occurring in women. In about 80% of these lesions, an overexpression of estrogen plays a fundamental role and characterizes endometrioid neoplasms, which tend to be well or moderately differentiated. They arise at the end of a carcinogenic pathway comprising a series of precancerous lesions (complex hyperplasia, possibly with atypia) [3].

Although it is the fourth most common cancer in women, EC has been little investigated and remains a not well-funded research area.

Endometrial cancer is a tumor that originates from "cancerous" cells that belong to the inner lining of the uterus, the endometrium. Most of these cells are glandular and the resulting tumor is called adenocarcinoma. It represents the most common type of endometrial cancer.

In over 80% of endometrial tumors, the glandular cells look very similar to those of normal uterine lining (endometrium). This kind of tumors are defined as typical or endometrioid adenocarcinomas. Other less frequent histotypes are:

- Squamous cell carcinoma (<1%);
- Serum-capillary adenocarcinoma (<10%);
- Clear cell adenocarcinoma (2-4%);
- Mucinous adenocarcinoma (<1%);
- Undifferentiated adenocarcinoma (<1%) [22].

1.2.3.1 Staging of endometrial cancer

The FIGO (International Federation of Gynecology and Obstetrics) classifies the endometrial cancer in 4 stages:

- **Stage I**: the tumor is limited to the body of the uterus. It is divided into stages IA and IB according to the depth of infiltration of the muscular part (Figure 8). Stage IA: cancer is in the endometrium only or less than halfway through the myometrium (muscle layer of the uterus). Stage IB: Cancer has spread halfway or more into the myometrium;

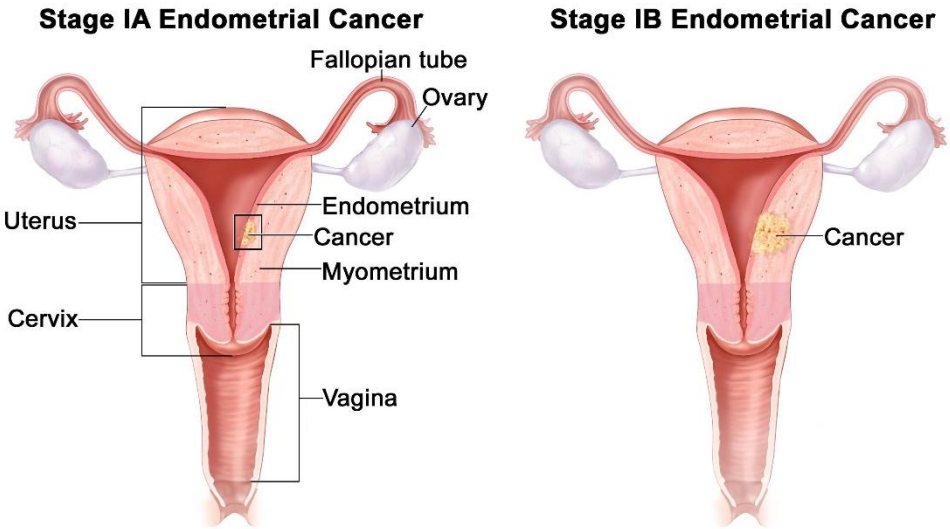

https://www.oncolink.org/healthcare-professionals/nci/pqid-CDR00000629642

Figure 8. *Stages IA and IB of endometrial cancer by International Federation of Gynecology and Obstetrics (FIGO)*

- **Stage II** : cancer has spread into connective tissue of the cervix, but has not spread outside the uterus (Figure 9);

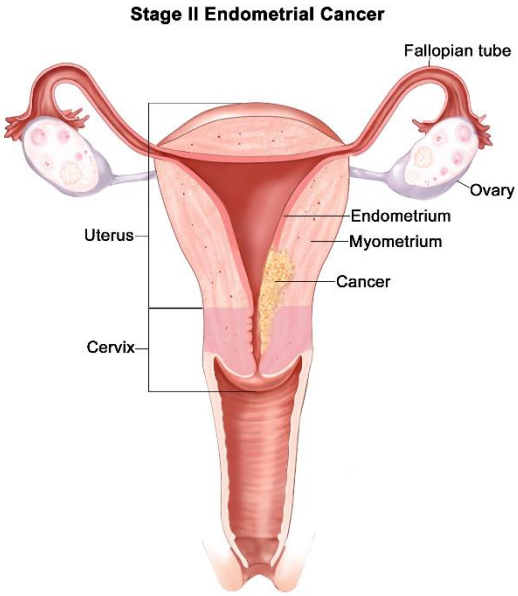

https://www.oncolink.org/healthcare-professionals/nci/pqid-CDR00000629642

Figure 9. *Stage II of endometrial cancer by International Federation of Gynecology and Obstetrics (FIGO)*

- **Stage III**: cancer has spread beyond the uterus and cervix, but has remained within the pelvis. It is divided into stages IIIA, IIIB, and IIIC, based on where the cancer has spread (ovaries, vagina or lymphonodes) (Figure 10);

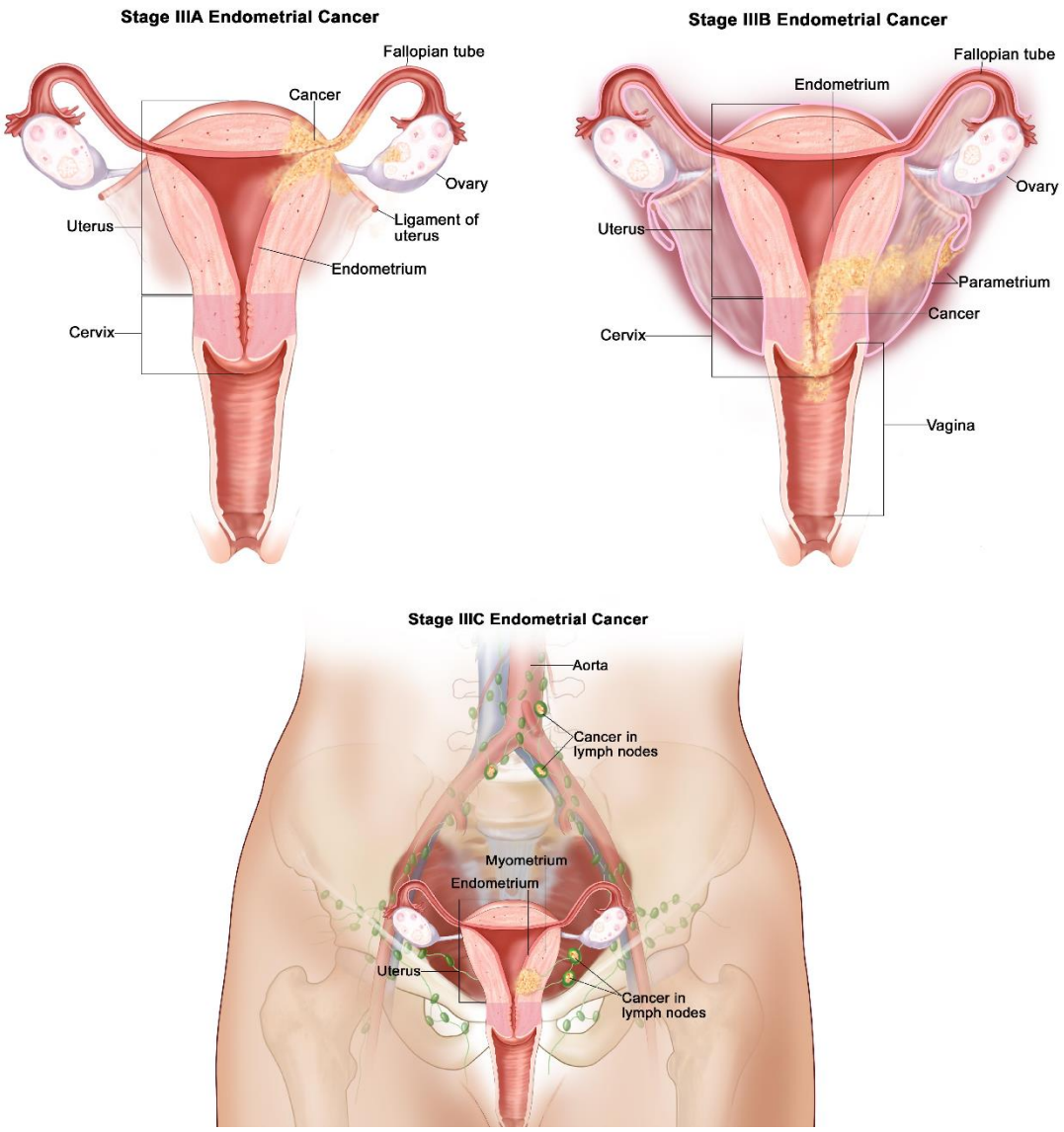

https://www.oncolink.org/healthcare-professionals/nci/pqid-CDR00000629642

Figure 10. *Stages IIIA, IIIB and IIIC of endometrial cancer by International Federation of Gynecology and Obstetrics (FIGO)*

- **Stage IV**: cancer has spread beyond the pelvis. It is divided into stages IVA and IVB, based on where the cancer has spread (bladder or abdomen) (Figure 11).

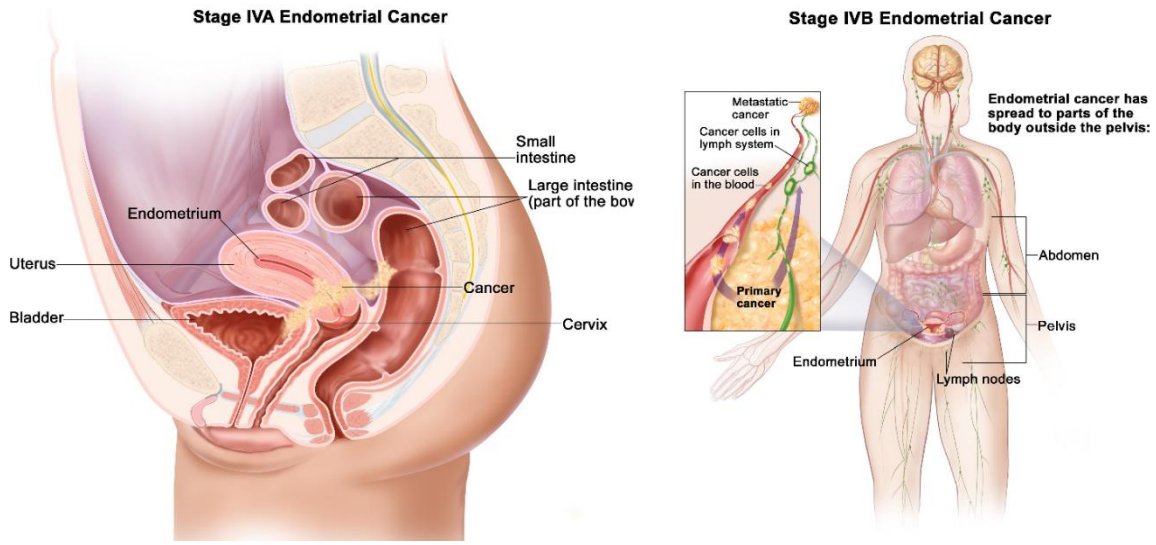

https://www.oncolink.org/healthcare-professionals/nci/pqid-CDR00000629642

Figure 11. *Stages IVA and IVB of endometrial cancer by International Federation of Gynecology and Obstetrics (FIGO)*

1.2.3.2 Risk factors of EC

EC risk factors are similar to those found in breast cancer. Hormonal (which play a crucial role in tumor development) and heredofamilial factors are particularly important. Furthermore, a recent study indicates exposure to endogenous and exogenous estrogens as an important risk factor for the development of EC. Rising rates of obesity worldwide have altered the endogenous hormonal environment of perimenopause and postmenopausal women. As a result, the rise in global obesity is one of the causes of the increasing EC cases [23].

Phosphoinositide 3 kinase (PI3K) plays an important role in the development of obesity. This protein is often not well regulated in the EC [24]. Recently, improved survival has been also associated with loss of PTEN (Phosphatase and Tensin homologue) in obese women compared to non-obese women with EC [25]. Also an increase in the expression of STMN1 and KRAS in women who have atypical hyperplasia with a body mass index > 30 kg/m^2 compared to non-obese women has been found. Obesity can limit surgical options, increase the toxicity of radiotherapy because of the need for higher doses of chemotherapy.

1.2.3.3 Screening for EC

Cervical cancer screening in Italy, according to the National Screening Observatory, involves the execution of a Pap test every three years in women aged between 25 and 64 years. Pap testing is well-established and has been used since the 1950th. It provides

important information about the tumor. However, this type of test in not useful before the age of 25 because infections with the Papilloma virus, while more frequent in the younger age groups, regress in almost all cases spontaneously. Due to the slow development of EC, women aged 64 and tested negative the Pap test, are excluded from further tests. The Pap test is carried out in a normal gynecological examination, during which the speculum, a special instrument that slightly dilates the vagina, is applied in order to facilitate the access. The operator then gently inserts a special spatula and a cotton bud to collect small amounts of mucus from the cervix and cervical canal. In the laboratory, the exfoliated cells have been studied thorough computerized examination and using special coloring methods.

Association of cervical cancer with Papilloma virus infection, and improvements in diagnostic techniques (in particular the development of genetic tests e.g. the HPV-DNA test), have provided new strategies to prevent this disease. The HPV-DNA test is able to detect the genome of the Papilloma virus present on the cervix, and allows the detection of viral strains that possess a greater carcinogenic activity. HPV test should be performed at longer intervals (at least five years) and should not be used before the age of 30-35 [12].

1.2.3.4 EC treatment

EC therapy is based primarily on a surgical treatment followed, in cases of intermediate and high risk, by a complementary or adjuvant treatment. The intervention of choice is represented by the total extra-fascial hysterectomy (uterus export) performed by laparoscopy in the initial stage. In the advanced stage, the hysterectomy is performed by abdominal way together with bilateral antrectomy (export of ovaries) and colpectomy of the upper third of the vagina (removal of a part of the vaginal collar). It is important to understand the right staging when to perform lymphadenectomy in EC and its therapeutic role is controversial. Recent evidence suggests a therapeutic role in high-risk stages but not in the low-intermediate [26].

*Cis*platin (**II**), Doxorubicin (**V**) and Paclitaxel (**III**) represent the most successful drugs in the treatment of EC (Figure 3), with percentages of responses to treatment higher than 20%. *Cis*platin (**II**) is a platinum-based drug able to crosslink with the purine bases on the DNA, interfering with DNA repair mechanisms, causing DNA damage, and subsequently inducing apoptosis in cancer cells [27]. Doxorubicin (**V**) is an antibiotic of natural origin belonging to the anthracycline class. It forms a complex with topoisomerase II and DNA, inhibiting the re-joining of DNA fragments during the replication process and inducing apoptosis [28].

Paclitaxel (**III**) is a chemotherapeutic agent belonging to the group of taxanes and can be administered by injection into a vein or drop-infusion [29].

The main limitation in the use of these drugs in EC is represented b the presence of same severe side effects due to their ability to damage normal cells together with tumoral cells. These toxic effects vary in intensity and type, depending on the drugs used during chemotherapy, their dose and duration of treatment. The most common side effects are:

- **Myelotoxicity**: This term indicates the toxicity of chemotherapy on bone marrow cells, resulting in the abnormal production of white and red blood cells. The reduction of corpuscular elements in the blood has a significant impact on the patient, with a major risk to develop infections and anemia.
- **Gastrointestinal toxicity** includes loss of appetite, taste alteration (dysgeusia), nausea, vomiting and diarrhea and depends on the drugs and doses used. Administration of anti-emetics helps to reduce the same of the side effects.
- **Mucositis** (inflammation of the oral mucosa) usually manifests itself with the appearance of aphthae (small ulcers).
- **Transient alopecia** is not associated with all chemotherapy schemes but typical for treatments with Paclitaxel (**III**). Usually, this event occurs during the first cycle of the treatment and the duration is parallel to that of chemotherapy, independently from the intensity.
- **Asthenia** is the tiredness often described in the patients during chemotherapy.

Most of the drugs used on chemotherapeutics are also nephrotoxic, ototoxic. They can cause a peripheral neuropathy that manifests itself with extremities numbness and sometimes tingling. Side effects vary from person to person both in the intensity and in the type of the disorders themselves, and supportive therapy should be adjusted to the individuals.

Another limitation of the known anticancer drugs are development of resistance and their sometimes low solubility and high instability in physiological systems.

Chapter 2: Biological evaluation of new synthetic analogues of known anticancer agents

Recently, considerable development in anticancer therapies has been achieved with the use of numerous effective drugs (Figure 12), such as Ellipticine (**XIII**), Vinblastine (**XIV**), *Cis*platin (**II**), Thalidomide (**XV**) and Quercetin (**XVI**). However, the main limitation in their use in therapy is often represented by the presence of numerous side effects and/or their poor bioavailability.

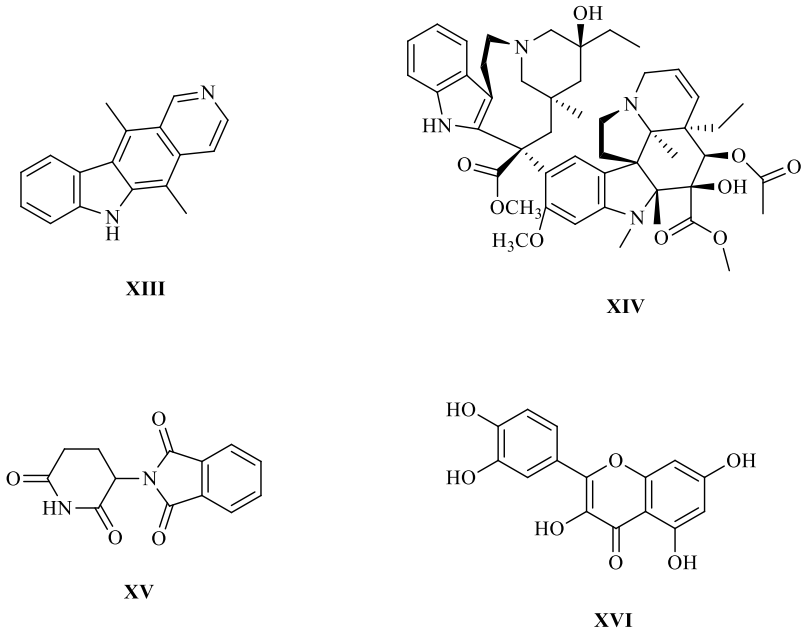

Figure 12. *Chemical structures of several anticancer agents;* ***XIII****) Ellipticine;* ***XIV****) Vinblastine;* ***II****) Cisplatin;* ***XV****) Thalidomide;* ***XVI****) Quercetin.*

The focus during my PhD was on the study of various synthetic analogues of these known anticancer drugs in order to obtain molecules with improved pharmaceutical profiles.

2.1 CARBAZOLIC TOOLS: ELLIPTICINE (XIII) AND VINBLASTINE (XIV) DERIVATIVES

Carbazoles are an important class of indole-containing heterocycles with antitumor as well as antibacterial [30], anti-inflammatory, psychotropic, and anti-histamine properties [31]. Ellipticine (**XIII**) is a representative compound of this class and was used in the treatment of metastatic breast cancer [31-34], but got dismissed because of its poor solubility in water and dramatic side effects [28,35]. Carbazolic compounds can also be structurally considered as molecular simplifications of Vinblastine (**XIV**), a Vinca alkaloid used for the treatment of different tumors, but with several toxic effects (leukopenia, neurotoxicity and gastrolesivity) [36].

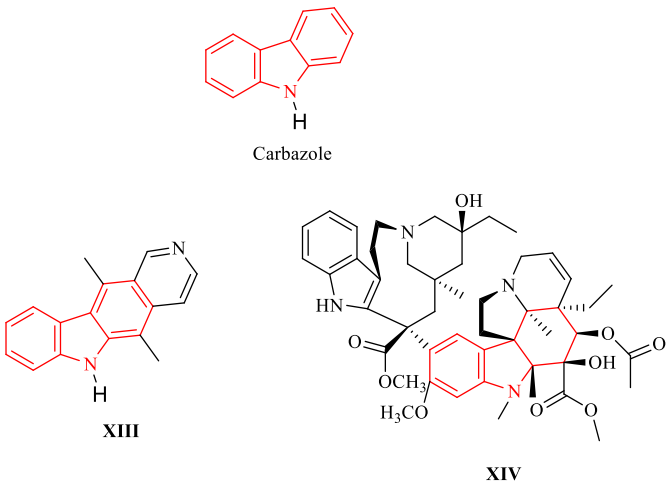

Figure 13. *Carbazole as Ellipticine (**XIII**) derivative and as Vinblastine (**XIV**) molecular simplifications analogue.*

Some carbazolic derivatives showed interesting pharmaceutical properties interacting both with DNA-dependent enzymes, as topoisomerases I/II and telomerase, and other targets such as cyclin-dependent kinases and estrogen receptors. These properties made them important tools in preclinical and clinical trials [37-48].

Nowadays one of the principal targets of the pharmaceutical research is the design of new antitumor drugs with higher selectivity on neoplastic cells, fewer side effects, reduced risk of resistance development. In this contest, carbazole derivatives have received particular attention.

Thus, we studied different series of new carbazole derivatives. In particular:

- *N*-alkylcarbazole derivatives and their quaternary ammonium iodide salts;

- *N*-thioalkylcarbazoles differently substituted at the 1,4,6 and 9 positions of the carbazole core;
- 3-(alkyl(dialkyl)amino)benzothieno[2,3-f]quinazolin-1(2*H*)-ones.

2.1.1 *N*-alkylcarbazole derivatives and their quaternary ammonium iodide salts

The design, the synthesis and the biological evaluation of a new serie of *N*-alkylcarbazole derivatives and their quaternary ammonium iodide salts (Figure 14) have been published including all experimental details [49].

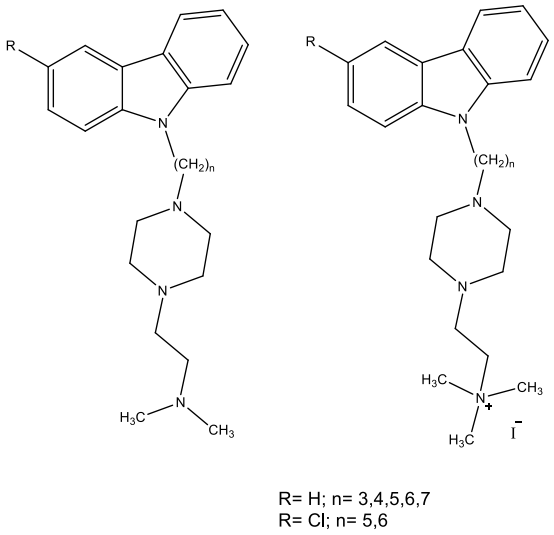

Figure 14. *General structure of N-alkylcarbazole derivatives and their quaternary ammonium iodide salts.*

These compounds hav exhibit an appreciable cytotoxic activity against two breast cancer cells (MCF-7 and MDA-MB-231) by inhibiting human Topoisomerase II and triggering the programmed cell death. Therefore, they may be considered as promising tools for the evaluation of the signaling pathways involved in breast cancer growth and progression.

2.1.1.1 Chemistry

The *N*-alkylcarbazole derivatives (**3a-g** and **4a-g, Scheme 1**) were obtained from the carbazole (**1a**) for **3a-e** and **4a-e**. 3-Chloro-9H-carbazole (**1b**), commercially available, was the starting material for **3f-g** and **4f-g**. Compounds **3a-g** and **4a-g** were obtained in two or three steps, respectively (Scheme 1).

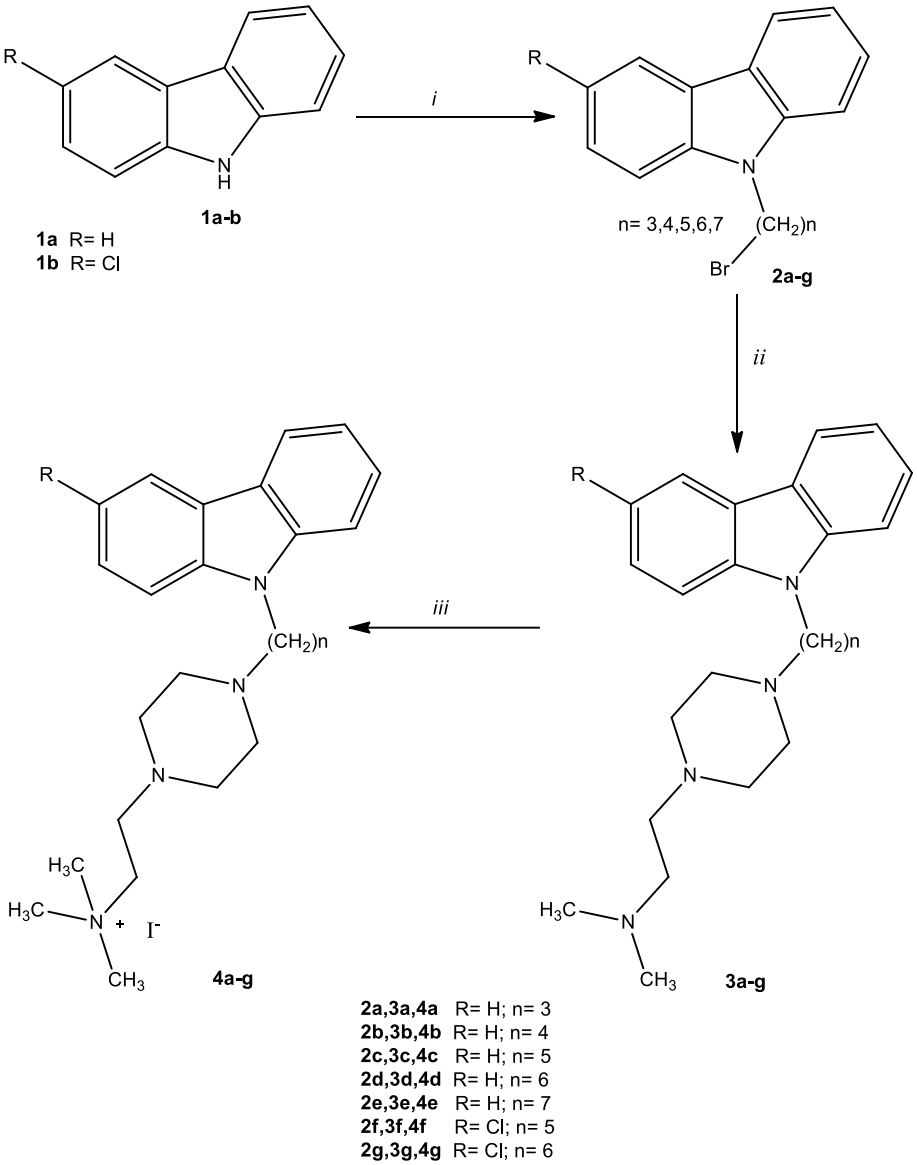

Compounds	Yields (%)	Compounds	Yields (%)
3a	68	**4a**	70
3b	20	**4b**	75
3c	33	**4c**	55
3d	60	**4d**	78
3e	24	**4e**	68
3f	66	**4f**	56
3g	33	**4g**	78

Scheme 1. *Synthetic route for the preparation of compounds **3a-g** and **4a-g**. i) Dibromoalkane, NaOH/TBEA; ii) 1-[2-(Dimethylamino)ethyl]piperazine, Na_2CO_3/DMF; iii) Methyl iodide, Acetone. Yields of all compounds are also shown in the table.*

First the carbazole **1a** or **1b** was *N*-alkylated with 1,3-dibromopropane or 1,4-dibromobutane or 1,5-dibromopentane or 1,6-dibromohexane or 1,7-dibromoheptane to obtain the

intermediates **2a-g,** respectively. In the second step, these *N*-alkylated derivatives were reacted with 1-[2-(dimethylamino) ethyl]piperazine to give the (9H-carbazol-9-yl)piperazin-1-yl)-*N*,*N*-dimethylethanamine derivatives (**3a-g**). Compounds **3a-g** were reacted with an excess of methyl iodide in acetone to give the quaternary ammonium iodide derivatives **4a-g** (mass spectrometry and NMR analysis were used to characterize all the synthesized compounds as reported by Saturnino *et al*. [49]).

2.1.1.2 Docking studies

Several studies report that many carbazole derivatives are good inhibitors of human Topoisomerase II (hTopo II) [27,33,50]. Thus, we studied the binding modes and affinities between our compounds, as ligands, and hTopo IIα by molecular docking simulations (Figure 15). All compounds bind the ATPase domain, near the ATP binding site. Particularly, compounds bind the residues Ile 125, Val 132, Leu 140, Ile 141, Thr 147 in a hydrophobic pocket and form a π-stacking with the aromatic ring of Tyr 151. Moreover, they establish some hydrogen bonds with Ser 149, Asp 152, Asp 154 and Glu 155. Through "*in silico*" screening, we demonstrate that compounds **3c**, **4c**, **3d**, **4d**, **3f**, **4f**, **3g** and **4g** present good binding energies. *In vitro* studies highlighted a lack of inhibitory activity for compounds **3c**, **4c**, **3d** and **4d**, probably related to the absence of the chlorine atom, useful in stabilizing the interaction between the compounds and the protein. Interestingly, the chlorinated carbazole moiety of **3f** and **4f** is positioned within the hydrophobic cleft (see described above), in different orientations with the two rings rotated of about 180 degrees (Figure 15, Panels H and I). In this way, the chlorine atom in **4f** points towards the ATP binding cleft in hydrophobic contact with protein residues Ile 125, His 130, Val 137, Leu 140 and Ile 141, maintaining the polar bonds with Ser 149, Asp 152 and Glu 155. For **3f**, the chlorine is pointing outside the protein, towards the solvent, where the carbazole is in stacking with Tyr 151 and forms hydrophobic contacts with Val 132, Leu 140 and Thr 147. Compound **4f**, therefore, is supposed to have a better inhibitory activity than **3f** on hTopo IIα *in vitro* due to its minor exposition to the solvent molecules (Figure 15, Panels H and I).

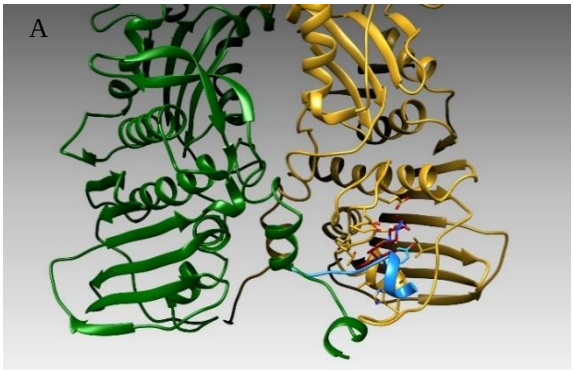
A

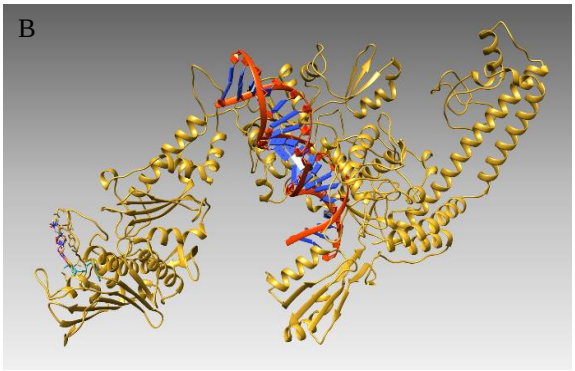
B

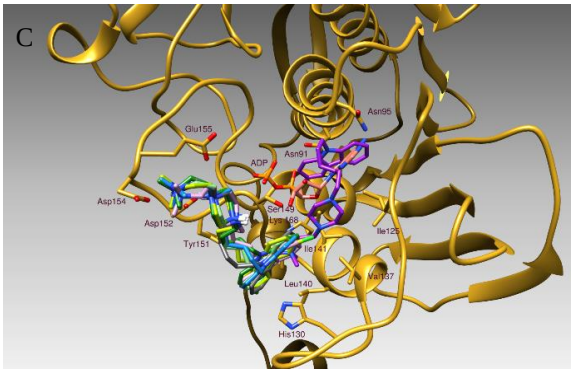
C
Asn95
Glu155
Asn91
ADP
Asp154
Ser149
Asp152
Lys 168
Ile125
Tyr151
Ile141
Val137
Leu140
His130

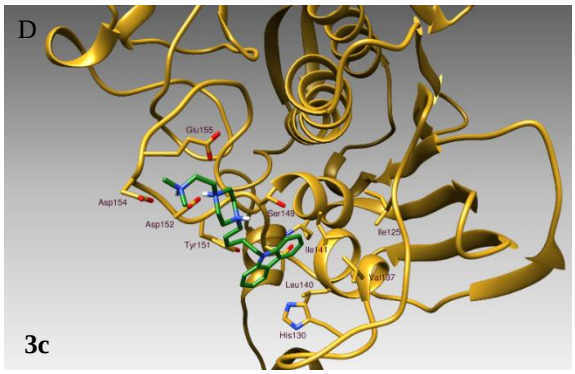
D
Glu155
Asp154
Asp152
Ser149
Tyr151
Ile141
Ile125
Val137
Leu140
His130
3c

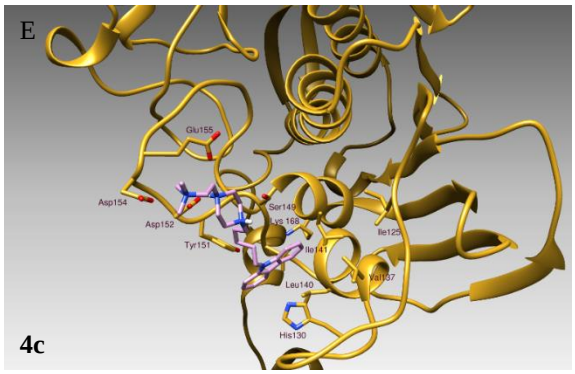
E
Glu155
Asp154
Asp152
Ser149
Lys 168
Tyr151
Ile141
Ile125
Val137
Leu140
His130
4c

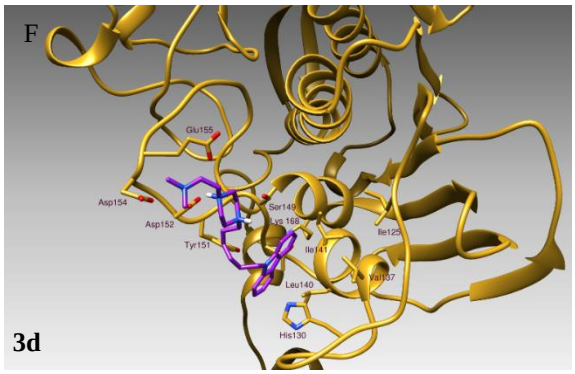
F
Glu155
Asp154
Asp152
Ser149
Lys 168
Tyr151
Ile141
Ile125
Val137
Leu140
His130
3d

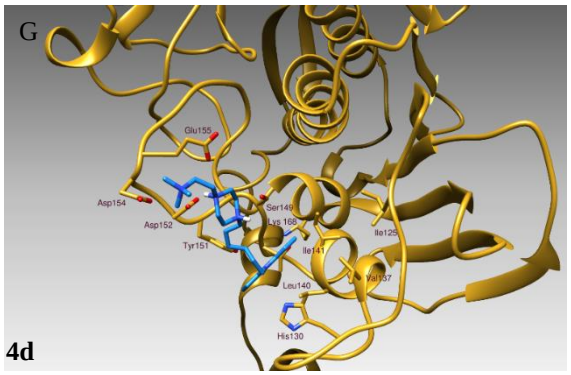
G
Glu155
Asp154
Asp152
Ser149
Lys 168
Tyr151
Ile141
Ile125
Val137
Leu140
His130
4d

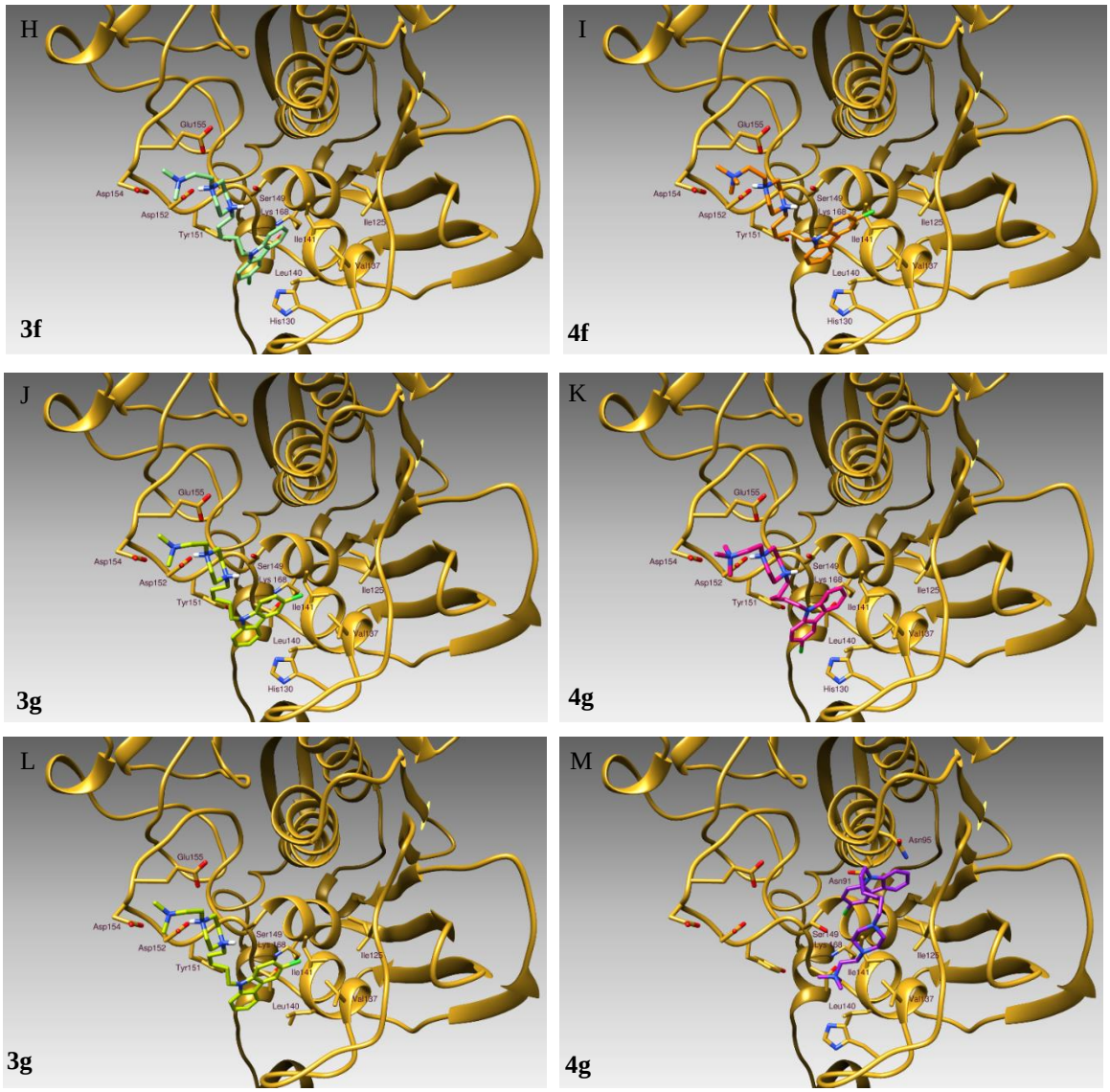

Figure 15. *Panel A) The three dimensional structure of the dimeric human Topoisomerase IIa is reported. Subunit A, drawn in green, adopt a different C-terminal conformation according to the presence (or absence) of the ligand in its binding site. When in the dimeric conformation, the C-terminal alpha-helix (light blue) is positioned inside a cleft of the b subunit, close to the ATP binding site, interacting with different residues, thus conferring stability to the dimeric structure. When the ligand is bound, the C-term helix is pointing out (green helix) and the formation of the oligomer is prevented. Panel B) represents a model of the human Topoisomerase IIa, bound to a DNA fragment. On the left of the figure, the ATP binding domain. Panel C) different molecules of this series in their binding mode as forecasted by docking simulations. The crystallographic position of an ADP molecule is reported as reference. Panel D-K binding modes of the N-alkylcarbazole derivatives as determined by docking simulations. Panel D) molecule **3c**, Panel E) **4c**, Panel F) **3d**, Panel G) **4d**, Panel H) **3f**, Panel I) **4f**, Panel J) **3g**, Panel K) **4g**, Panel L) **3g**, Panel M) **4g** (with the carbazole occupying the Adenine binding site).*

2.1.1.3 Biology

The new series of *N*-alkyl carbazoles was tested to evaluate the antitumor properties towards two models of breast cancer, the human ERα positive MCF-7 and the triple negative MDA-MB-231 cell lines. Table 2 reports the IC_{50} values calculated for all compounds. Among them, compounds **3a**, **4a**, **3b**, **4b**, **3e** and **4e** did not exert any inhibitory effects, while compounds **3c**, **4c**, **3d** and **4d** exhibited a very poor antitumor activity on the two breast cancer cell lines. A marked improvement has been reached using the chlorinated derivatives **3f**, **4f**, **3g** and **4g**. Particularly, the ammonium salts **4f** and **4g** displayed the best antitumor activity, also the highly aggressive and metastatic MDA-MB-231 cells resulted more sensitive to treatment. In particular, **4f** having an alkylic chain with 5 atoms showed a better activity than its analogues **4g** (with an alkyl chain with 6 atoms). Because of their higher duplication rate, MDA-MB-231 cells need a faster DNA synthesis to proceed through mitosis. Thus, they must possess an operative duplication apparatus, including high levels of topoisomerases. Therefore **4f** being the best hTopo II inhibitor (see Figure 16 discussed below), it is not surprising that it exerts the best antitumor activity against these cells. At the end, it should be pointed out that the active compounds did not elicit the viability of the normal breast cells (MCF-10A), while Ellipticine (**XIII**), used as reference compound, exhibited high toxicity towards the healthy breast cells.

	IC_{50} (μM)		
	MCF-7	**MDA-MB-231**	**MCF-10A**
Ellipticine (XIII)	1.35 ± 0.30	1.75 ± 0.15	1.50 ± 0.15
3a	>500	>500	>500
4a	>500	>500	>500
3b	>500	>500	>500
4b	>500	>500	>500
3c	357.0 ± 1.20	296.5 ± 1.10	> 500
4c	314.2 ± 0.90	270.3 ± 1.25	> 500
3d	381.0 ± 1.12	257.2 ± 1.35	> 500
4d	388.8 ± 1.27	221.9 ± 0.95	> 500
3e	>500	>500	>500
4e	>500	>500	>500
3f	35.9 ± 0.55	12. 4± 0.75	> 500
4f	10.2 ± 0.45	4.4 ± 0.20	> 500
3g	77.4 ± 0.35	17.2 ± 0.25	>500
4g	20.4 ± 0.22	5.8 ± 0.28	> 500

Table 2. *IC_{50} values of carbazole derivatives (**3a-g**, **4a-g**) and Ellipticine (**XIII**), expressed in micromolar (μM) against breast cell lines used.*

Considering that the *in silico* studies results indicated potential important interactions with the carbazole derivatives and hTopoII, we performed, in parallel, a direct enzymatic assay using all the derivatives. Human TopoII is a nuclear enzyme indispensable to remofor the removal of topological complications that occur during DNA replication, transcription and chromosome segregation through a DNA breaking/reunion mechanism [52]. Thus, this enzyme has become one of the most promising target in the anticancer drugs discovery field. The obtained data from the enzyme assays (Figure 16, panels A and B), indicated that compounds **3a**, **4a**, **3b**, **4b**, **3c**, **4c**, **3d**, **4d**, **3e** and **4e** at a dose of 10μM, did not block hTopo II enzymatic activity. The enzyme bound its substrate (kDNA) and released the decatenation products appreciable as two bands at the bottom of gel, representing the nicked open circular minicircles and fully closed circular rings. The same reaction happened in the control experiment where only the vehicle (DMSO) was added (Figure 16, panel A, lane C). On the contrary, the halogenated compounds **3g, 4g** and **3f** (10μM, Figure 16, panel B) were able to partially inhibit hTopo II activity. In addition to the two DNA bands visible at the bottom

of the gel, one band appeared at the top of agarose gel, corresponding to the not-cleaved kDNA, unable to migrate on agarose gel. Finally, a total blockade of hTopo II activity was reached with the chlorinated ammonium salt **4f** (10µM, Figure 16, panel B). This was evidenced by the presence of a marked kDNA band at the top of the gel and by the absence of the bottom DNA bands. Ellipticine (**XIII**), used as reference molecule, was able to completely block hTopoII activity (Figure 16, panel C, lane E), at a concentration five-fold higher with respect to the most active compound **4f**, as already evidenced by several literature works for Ellipticine (**XIII**) [45,51-54].

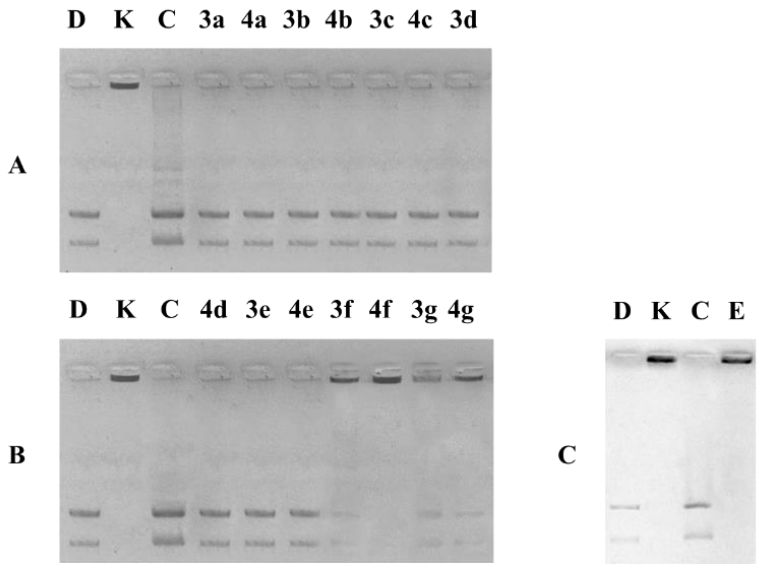

Figure 16. *Human topoisomerase II decatenation assay. hTopo II has been incubated in absence (control) or presence of the compounds to test at 10µM for 1 h at 37 °C. The image is representative of three separated experiments. Panels A, B and C= D: decatenated DNA marker; K: Kinetoplast DNA; C: Control (DMSO);* ***3a-g*** *and* ***4a-g****: assayed compounds, E: Ellipticine (****XIII****) at 50µM.*

The biological functions of human topoisomerases are fundamental to ensure genomic integrity, thus a blockage of their activity causes DNA damage and, consequently, cell death by apoptosis [55].

Thus, in order to demonstrate if the observed hTopo II inhibition induced by **4f** could trigger apoptosis in MDA-MB-231 cells, we performed a TUNEL assay (as described in the experimental section). Figure 17 highlighted that the treatment of cancer cells for 24 h with **4f** at a dose of 10 µM caused genomic DNA fragmentation, as evidenced by the presence of a green fluorescence (Figure 17, panel B, **4f**) that perfectly overlaps with the blue

fluorescence corresponding to cell nuclei DAPI-stained (Figure 17, panel C, **4f**). In the control, performed in the same conditions with the vehicle alone (DMSO), no green fluorescence was visible (Figure 17, panel B, CTRL), confirming that no DNA damage has occurred.

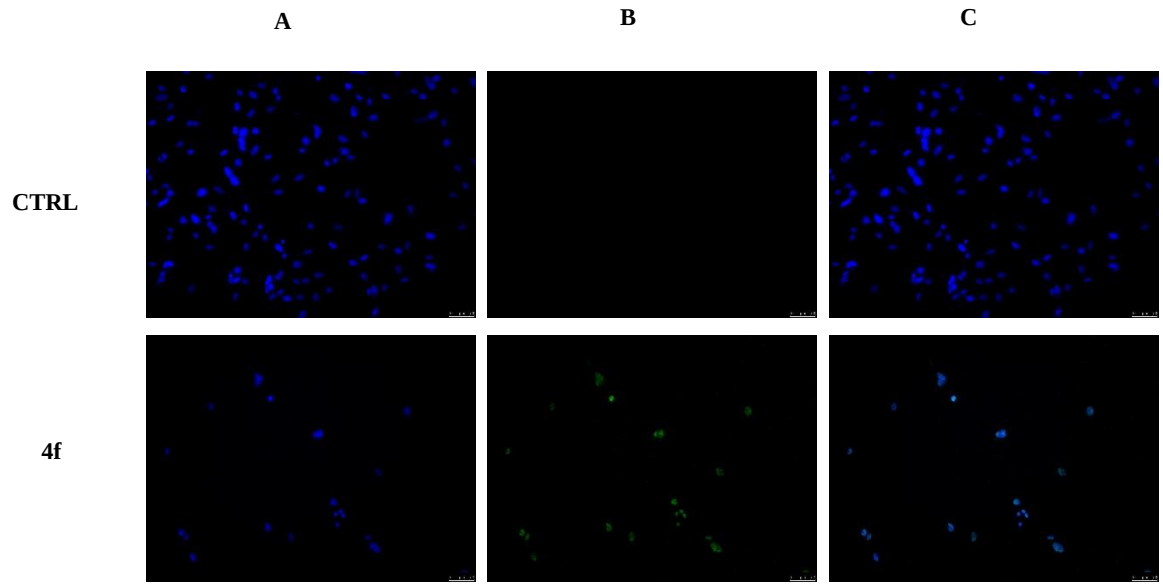

Figure 17. *TUNEL assay. Apoptotic effect of **4f** used at 10 μM or vehicle (CTRL) on MDA-MB-231 cells determined after 24 hours of treatment. Panels A: DAPI (excitation/emission wavelength 350 nm/460 nm), used to locate the nuclei of the cells; Panels B: CF™488A (excitation/emission wavelength 490 nm/515 nm), the green fluorescence indicates nuclei of cells undergoing apoptosis; Panels C: Shows the overlay channel.*

Subsequently, we carried out a luminescent assay in order to establish the involvement of caspases activity in apoptotic pathways. In particular, we treated MDA-MB-231 cells for 24 hours with **4f** (or vehicle) at a concentration of 10 μM and measured the variation of caspases levels. We evaluated the activity levels of the initiator caspases 8 and 9, involved in the extrinsic and intrinsic pathway respectively, and of the effectors caspases 3 and 7. Effectively, we noticed an increase of caspases 9 and 3/7 activity under **4f** treatment (Figure 18) with respect to the control reaction, where cancer cells were exposed to the vehicle only (DMSO).

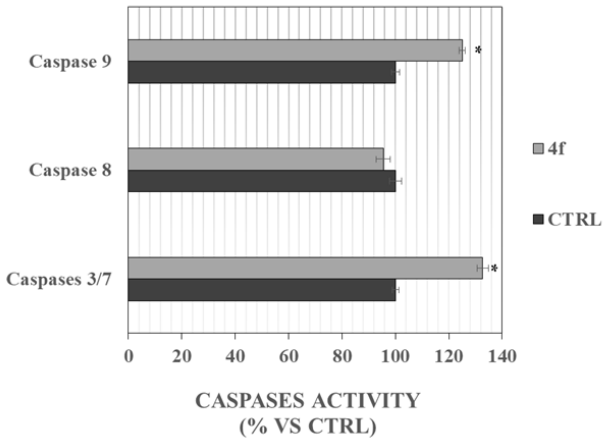

Figure 18. *Caspases activity assay. The treatment of MDA-MB-231 cells with **4f** at the concentration of 10 μM for 24h caused the activation of caspases 3/7 and 9 (% over the CTRL, vehicle-treated cells). Columns mean, bars SD, *p<0.001.*

2.1.2 Differently substituted *N*-thioalkylcarbazoles

In a second paper, we have published a new library of *N*-thioalkylcarbazoles, as Ellipticine (**XIII**) analogues or as molecular simplifications of Vinblastine (**XIV**). They bear several substituents at the 1, 4, 6 and 9 positions of the carbazolic moiety and the carbazole nitrogen is substituted with alkyl chains with seven, eight and nine methylene groups, linked to a terminal thiol group (all experimental details are described by Sinicropi *et al.*) [45]. Two of these molecules have exerted an interesting anti-proliferative activity, mostly against cervical HeLa cells, triggering the apoptotic intrinsic pathway and inhibiting the hTopo II activity. These results make the most active brominated compound **9c** valid lead compound for the development of new agents for cancer treatment.

2.1.2.1 Chemistry

The *N*-thioalkylcarbazole derivatives (**9**-**11a**-**c**) were synthesized as reported in Sinicropi *et al.* [45]. The intermediates 9-(bromoalkyl)-9*H*-carbazoles (**6**-**8a**-**c**) were prepared following general synthetic methods [56]. In particular, carbazole derivatives (**5a**-**c**) and dry DMF were stirred at room temperature until became clear. Then, NaH 60% oil dispersion and, successively, the appropriate dibromoalkane at 0°C were added. After 5 hours, water was added and the resulting mixture was extracted with EtOAc. The obtained residue was purified by silica gel column chromatography (Et_2O/hexane, 2/3 as eluent) to give the pure compounds. After alkylation, the 9-(bromoalkyl)-9*H*-carbazoles (**6**-**8a**-**c**) were reacted with thiourea in *i*-PrOH. The crude products were purified by PTLC (Preparative Thin Layer Chromatography) to give the pure compounds (**9**-**11a**-**c**) (Scheme 2).

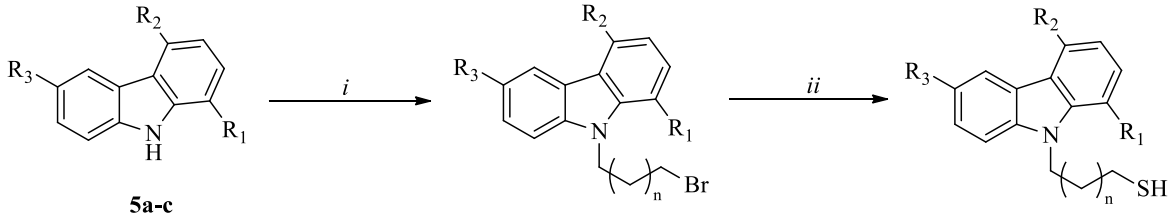

5a-c

a R_1, R_2, R_3= H
b R_1, R_2, R_3= CH_3
c R_1, R_2= CH_3 R_3= Br

6a-c n=5
7a-c n=6
8a-c n=7

9a-c n=5
10a-c n=6
11a-c n=7

Compounds	Yields (%)	Compounds	Yields (%)	Compounds	Yields (%)
9a	25	**10a**	23	**11a**	40
9b	52	**10b**	31	**11b**	51
9c	48	**10c**	31	**11c**	29

Scheme 2. *Synthesis of N-9H-alkyltiocarbazoles **9–11a–c**. i) 1, N-dibromoalkane, NaH 60%, DMF, rt; ii) 1. Thiourea, i-PrOH, reflux, 12h; 2. NaOH 6N, reflux, 5h; 3. HCl 3N, rt, 10 min. Yields of all compounds are also shown in the table.*

2.1.2.2 Biology

The anti-proliferative activity of the synthesized carbazolic compounds (**9a**–**c**, **10a**–**c**, **11a**–**c**) was evaluated towards two human breast cancer cell lines, the estrogen receptor α positive (ERα+) MCF-7 cells and the triple negative (ER-, PR- and HER-2/Neu not overexpressed) MDA-MB-231 cells. In addition, we tested their anti-proliferative activity against two uterine cancer cell lines, Hela cells, from uterine cervix epithelium (ERα-), and endometrial ISHIKAWA cells (ERα+). A natural molecule containing the carbazolic core, Ellipticine (**XIII**), was used as reference molecule. The obtained data (Table 3) shows that only the derivatives **9a** and **9c,** carrying a seven methylene chain terminated by a thiol, exhibited antitumor activity. The best antitumor activity was exerted against HeLa and ISHIKAWA cells, where compound **9a** showed IC_{50} values of 12.8 ± 0.62 μM and 19.2 ± 1.13 μM, respectively. Compound **9c** showed IC_{50} values of 11.3 ± 0.63 μM (HeLa) and 15.7 ± 0.95 μM (ISHIKAWA).

These compounds possessed also a minor antitumor activity in both breast cancer cells, with IC_{50} values for compound **9a** and **9c** in MCF-7 cells amounting of 50.4 ± 0.96 μM and 54.9 ± 1.00 μM, respectively. In MDA-MB-231 cells, the IC_{50} values were lower than those calculated for the MCF-7 cells (39.9 ± 0.52 μM and 27.2 ± 0.75 μM, respectively for **9a** and **9c**).

Finally, Ellipticine (**XIII**) showed a higher antitumor activity in all cell lines used in these assays compared to both our compounds, but with a serious cytotoxicity on non-tumoral cells MCF-10A and 3T3-L1 (Table 3). In contrast, our compounds did not elicit the proliferation of these normal cell lines, up to a concentration of 100 μM. These results demonstrated that compound **9c** possessed a high selectivity for uterine cancer cells, and that both the bromine in position 6 and length of the alkyl chain is of importance. The replacement of bromine at position 6 with a methyl group (**9b**) [32,56,57] and the elongation of the chain caused a loss of the antitumor activity (**10c** and **11c**).

	IC_{50} (μM)					
	MCF-7	**MDA-MB-231**	**ISHIKAWA**	**HeLa**	**MCF-10A**	**3T3-L1**
Ellipticine (XIII)	1.25±0.30	1.85±0.15	1.70±0.80	1.05±0.50	1.20±0.20	0.98±0.7
9a	50.4±0.96	39.9±0.52	19.2±1.13	12.8±0.62	>100	>100
9b	>100	>100	>100	>100	>100	>100
9c	54.9±1.00	27.2±0.75	15.70±0.95	11.3±0.63	>100	>100
10a	>100	>100	>100	>100	>100	>100
10b	>100	>100	>100	>100	>100	>100
10c	>100	>100	>100	>100	>100	>100
11a	>100	>100	>100	>100	>100	>100
11b	>100	>100	>100	>100	>100	>100
11c	>100	>100	>100	>100	>100	>100

Table 3. *IC_{50} values of carbazole derivatives (**9a-c**, **10a-c** and **11a-c**) and Ellipticine (**XIII**), expressed in micromolar (μM).*

Literature data highlights that carbazolic compounds are inhibitors of human Topoisomerases I and II [51]. With this in mind, the most active compound **9c** was assessed for its capability to inhibit both isoforms of these metabolizing enzymes, using an *in vitro* assays. Under the experimental conditions, compound **9c** did not interfere with the hTopoI activity (data not shown). Instead, in hTopo II decatenation assays, our compound was able to inhibit activity of this enzyme at 10 μM concentration (Figure 19, lane **9c**), as shown by

the absence of two DNA bands at the bottom of gel, corresponding to the decatenation products of the kDNA. Contrarily, these two DNA bands are visible in the experimental control (Figure 19, lane C). Ellipticine (**XIII**), used as reference molecule (Figure 19, lane E), was also able to totally inhibit the activity oh hTopoII, but at the concentration of 50 μM [52].

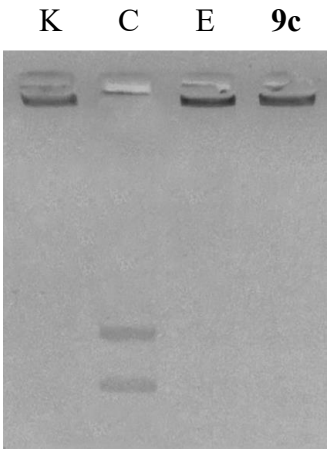

Figure 19. *hTopoII inhibition assay. kDNA was incubated with human Topoisomerase II in the absence (lane C, vehicle DMSO) or presence of compound **9c** (lane **9c**) or Ellipticine (**XIII**) (lane E) at 10 and 50 μM, respectively. Lane K, kinetoplast DNA (kDNA).*

The inhibition of hTopoII causes genotoxic and mutagenic effects because of the involvement of this enzyme in DNA replication, transcription, recombination, triggering the programmed cell death. In response to DNA damage, cells may utilize the poly-(ADP) ribose polymerase (PARP-1), a protein playing a crucial role in many processes, including DNA repair and cell death [58,59].

The cleavage of this protein PARP-1 induces apoptosis by avoiding DNA repair-promoted survival [60]. With this in mind, HeLa cells were exposed to compound **9c** at concentration of 10 μM at three different times (24, 48 and 72 h). Then, the protein content was extracted and used for western blot analyses. The data (Figure 20) showed that in HeLa cells treated with compound **9c** it was possible to observe the cleaved form of PARP-1 (about 89 KDa), in appreciable quantities after 24 h and increased quantities after 48 h, together with a decrease of the native protein. After 72 h, a complete conversion to the cleaved PARP-1 was achieved, while the control cells treated with DMSO stayed intact.

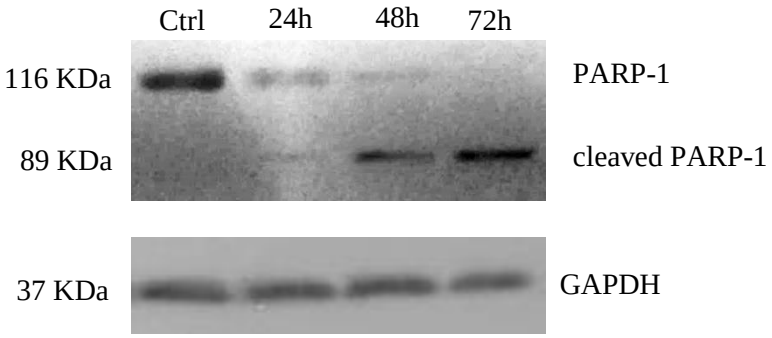

Figure 20. *PARP-1 cleavage: Time course of PARP-1 cleavage in uterine cancer Hela cells treated with **9c**, used at a concentration equal to its IC_{50} value. The control shown is referred to 72 hours of vehicle exposure, but same results was obtained for 24 and 48 hours (data not shown). GAPDH was used as loading normalization.*

We performed a TUNEL assay in order to verify the triggering of the apoptosis, exposing Hela cells to compound **9c** at its IC_{50} value for 24 h. Figure 21 demonstrates a green nuclear fluorescence in the cells treated with our compound (**9c**, panel B), indicating the presence of DNA damage. On the contrary, in the control cells no fluorescence was observed (Figure 21, CTRL, panel B). These results confirm that the carbazole **9c** was able to cause DNA damage and led to cell death by apoptosis.

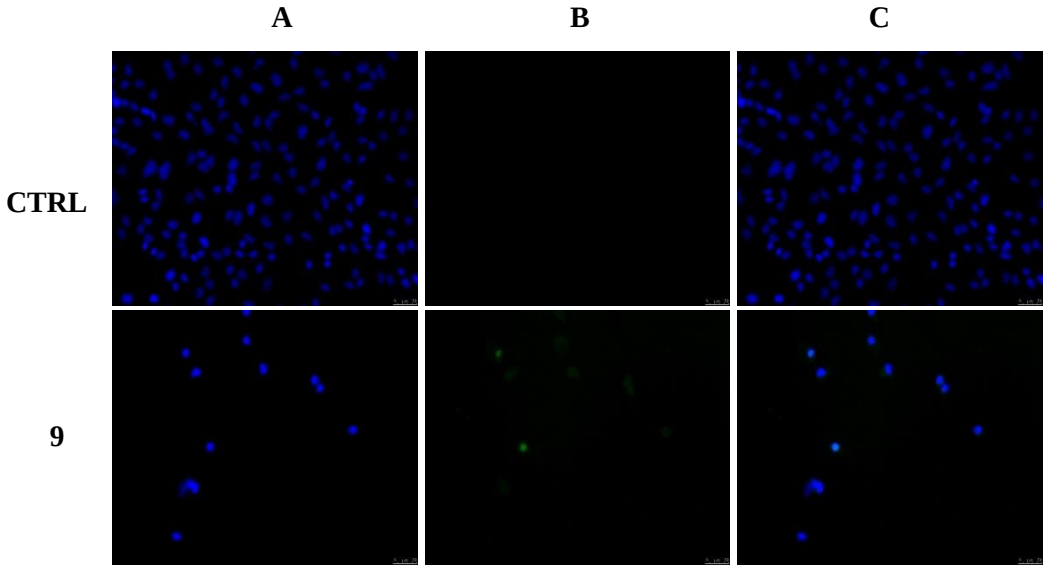

Figure 21. *TUNEL assay of HeLa cells. Cells were treated for 24 h with compound **9c** (at the concentration equal to its IC_{50}) or with vehicle (CTRL). Then they were fixed, subjected to TdT reaction, washed, dyed with DAPI and imaged under a fluorescence microscope (20X magnification, excitation/emission wavelength 490 nm/515 nm for CF™488A, panels B, and 350 nm/460nm for DAPI, panels A). Panels C show the merge.*

The apoptotic pathway is a complex process involving many biochemical events [61], including the activation of caspases, proteolytic protein, that initiate the proteolytic cascade [62], in which one caspase may activate other caspases or cleave cell proteins, included PARP-1, amplifying the apoptotic cell death [61]. Thus, we have established, using a cell-based luminescent assay, if our compound **9c** was able to interfere with the activity of the initiator's caspases (caspases 8 and 9), involved, respectively, in the extrinsic and intrinsic pathway, and with the effectors caspases (caspases 3 and 7). The obtained results (Figure 22) demonstrated a slight increase of caspase-9 activity in HeLa cells treated with compound **9c** for 24 h, but no change in caspase-8 activity was detectable. In addition, we noticed a clear increase of caspase 3 and 7 activity (Figure 22). These are cleaved by the initiator caspase-9, and this in turn, may activate other pro-apoptotic proteins and cleave PARP-1, as we already demonstrated (Figure 21). Summarizing, compound **9c** was able to activate the intrinsic apoptotic pathway, increasing the activity of caspases 9, 3 and 7.

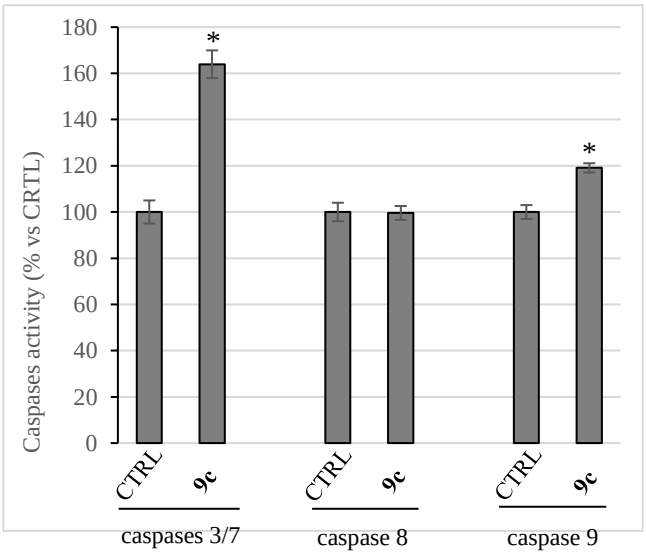

Figure 22. *Caspases activity. Activation of caspases 3/7 and 9 following to the treatment of HeLa cells with the compound* ***9c*** *at a concentration equal to its* IC_{50} *value for 24 hours. Columns mean, bars SD, *p<0.001*

In the intrinsic apoptotic pathway it is possible to notice a decreased mitochondrial permeability, with a subsequent release of Cytochrome c from mitochondria to the cytosol [63]. Thus, in order to study the localization of Cytochrome c, we performed immunofluorescence assays using HeLa cells exposed to **9c** at a concentration corresponding to its IC_{50} value.

In cells treated with **9c,** the red fluorescence corresponding to Cytocrome c, was diffused and delocalized throughout the cell cytoplasm (Figure 23, **9c**). In the control cells (exposed only to the vehicle), the red fluorescence was strictly localized in well-defined areas of the cell, corresponding to the mitochondrial compartment (Figure 23, CTRL). In Figure 23 the different stages of mitochondria disruption during apoptosis are highlighted [64]. The white arrow 1 indicates the early stages of apoptosis, in which a punctiform fluorescence in the cytosol demonstrates mitochondria disruption and partial release of Cytochrome c into the cytosol. In the late stage, the release of Cytochrome c was complete and the red fluorescence was greatly increased and diffused throughout the cytosol, as indicated by the white arrow 2.

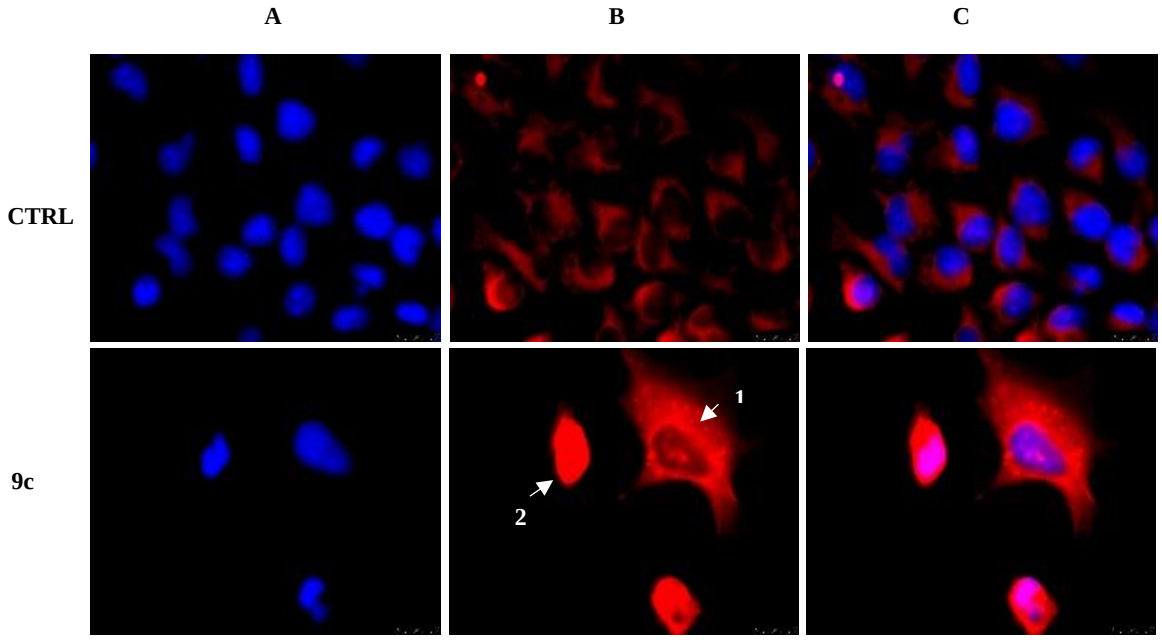

Figure 23. *Cytochrome c release during apoptosis in Hela cells. In vehicle-treated cells Cytochrome c is localized within the mitochondria (panel B, CTRL). During the early stages of apoptosis, induced by compound* ***9c*** *treatment at the concentration equal to its* IC_{50} *for 24h, mitochondria fragmentation occurs (as shown by the red dots indicated by arrow 1 in panel B,* ***9c****) and Cytochrome c is partially released. In the last apoptotic cell stage, a full release of Cytochrome c is observed (diffused red fluorescence, indicated by the white arrow 2). Panel A, DAPI (excitation/emission wavelength 350 nm/460 nm), panel B, Alexa Fluor® 568 (excitation/emission wavelength 578nm/603 nm), panel C, overlay. Images were acquired at 63x magnification and are representative of three separated experiments.*

2.1.2.3 Docking studies

Docking studies highlighted that compound **9c** located at one of the AMP-PNPs (a non-hydrolysable ATP analogue) of the the hTopoII ATP-binding site (Figure 24, panel A). AMP-PNP forms some hydrogen bonds that contribute to binding stability (Figure 24, Panel B):

- Between the adenine moiety and the residues Asn 67, Asn 92 and Thr 187;
- Between the ribose ring and the residues Ser 120 and Ser 121;
- Between the phosphates tail and the peptidic nitrogen of Gly 138 and the side chains of Asn 63 Ser 120, Asn 122, Lys 140, Gln 348 and Lys 350.

Our simulation demonstrated that **9c** forms halogen bonds through the interaction of bromine with Asn 92 and Thr 187, and the SH group creates a weak hydrogen bond to Asn 122. Finally, we found some hydrophobic interactions with residues Asp 66, Ile 97, Ile 113, Phe 114, and Ala 139 that stabilize the **9c** binding mode to hTopoII (Figure 24, Panel C).

A

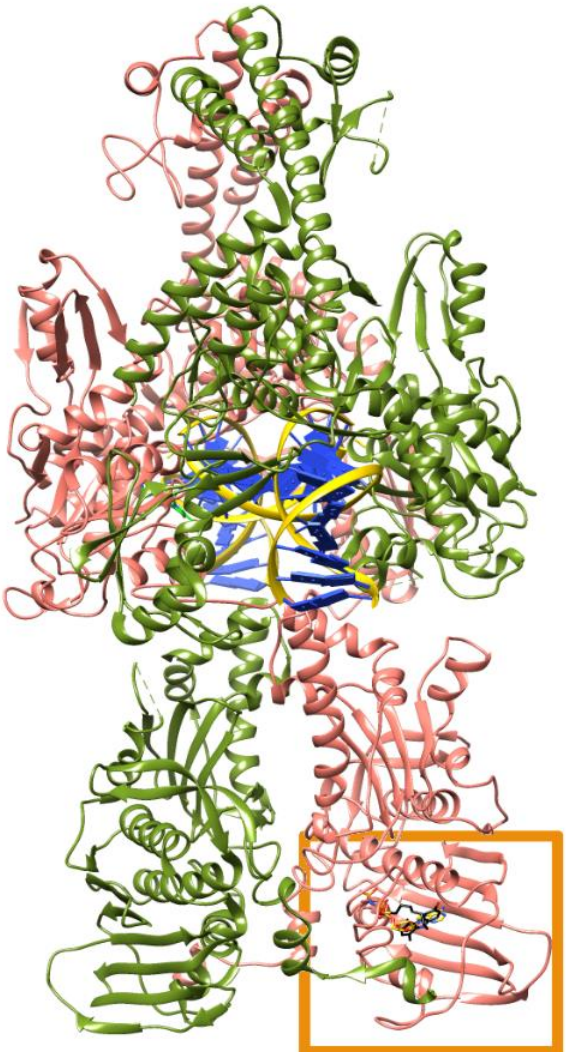

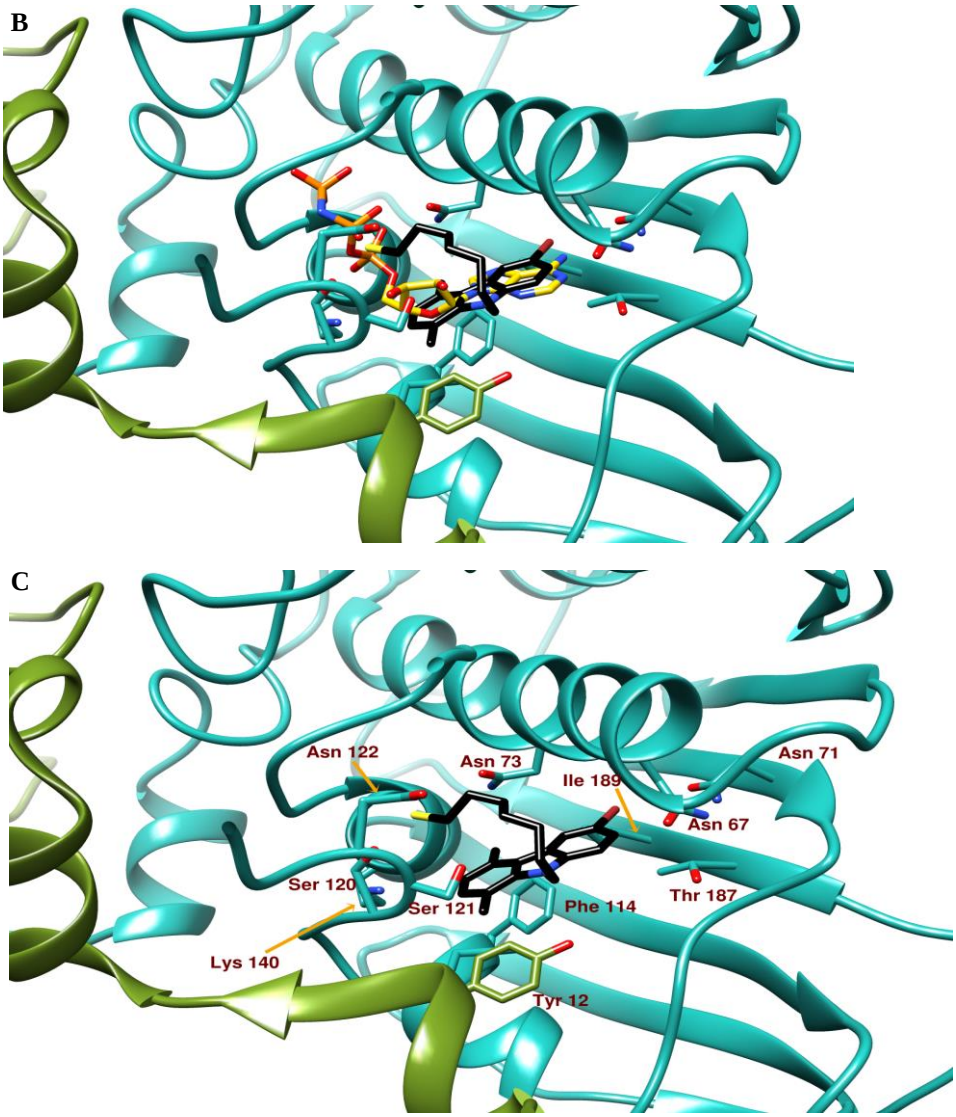

Figure 24. *Panel A) Ribbon representation of a dimeric hTopoII (chains A and B coloured in pink and olive green respectively) in complex with DNA (yellow ribbon and blue lego). The area within the orange rectangle highlights ATP binding site. Panel B) A close up of the ATP binding site showing the different binding modes of AMP-PNP, a non-hydrolizable ATP analogue, (orange) and* ***9c*** *(black sticks) as suggested by docking simulations. Panel C) shows the protein residues involved in* ***9c*** *binding.*

2.1.3 Benzothienoquinazolinones

Considering that benzofuran was a promising scaffold for the synthesis of anticancer agents [65], in a previous paper an efficient and simple synthesis of a series of 3-(alkyl(dialkyl)amino)benzofuro[2,3-f]quinazolin-1(2H)-ones was described and also their biological activities on two models of breast cancer was evaluated [52].

The encouraging results obtained, together with other data previously reported [66,67], prompted us to extend the synthetic methodology to the synthesis of their thiophenic isosteres. For this reason, the synthesis of a series of planar fused tetracyclic heterocyclic compounds (3-(alkyl(dialkyl)amino) benzothieno[2,3-f]quinazolin-1(2H)-ones, **15a-f**), as new Ellipticine (**XIII**) analogues and structurally correlated to 3-(alkyl(dialkyl)amino)benzofuro [2,3-f]quinazolin-1(2H)-ones [52], has been published including all experimental details [68].

The compounds have been tested for their antitumor activity against two human breast cancer cell lines: ERα-positive MCF-7 and triple negative MDA-MB-231. The most active compound could be considered a promising tool for the development of new multi-target agent due to its capability to inhibit human Topoisomerases I and Tubulin. It could also overcome some of the issue, as undesired side effects and drug-resistance, associated with anticancer agents currently used in oncology.

2.1.3.1 Chemistry

The new series of new 3-(alkyl(dialkyl)amino)benzothieno[2,3-*f*]quinazolin-1(2*H*)-ones **15a-f** was obtained using a one-pot three-component reaction with 3-aminodibenzothiophene **12** as starting material (Scheme 3, Table 4) [52,57,69,70]. Compound **12** was obtained following a previously described synthetic route [71]. The thiourea intermediate **13** was formed by reacting the amino derivative **12** with ethoxycarbonylisothiocyanate. Intermediate **13** was in situ converted into the ethoxycarbonylguanidine intermediates **14a-f** by reaction with the appropriate alkyl- or dialkylamine in presence of $HgCl_2$. Cyclization at 160 °C in the same reaction vessel gave the 3-(alkyl(dialkyl)amino)benzothieno[2,3-f]quinazolin-1(2*H*)-ones **15a-f** after removal of the by-product HgS by filtration.

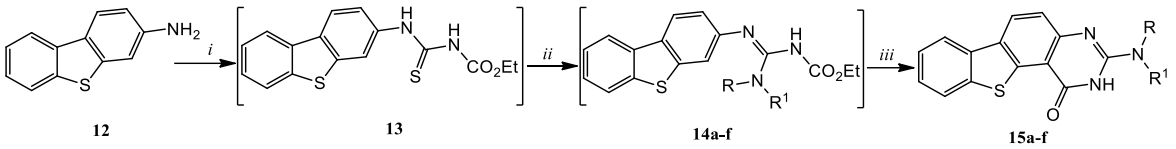

Compounds	Yields (%)	Compounds	Yields (%)
15a	41	**15d**	40
15b	35	**15e**	44
15c	40	**15f**	50

Scheme 3. *Synthetic route for the preparation of benzothienoquinazolinones **15a-f**. (i) EtOCONCS (1 eq.), DMF, 4h, rt; (ii) alkylamines or dialkylamines (3 eq.), $HgCl_2$ (1 eq.), 10 min, 0 °C, then 18 h, rt; (iii) 2h, 160 °C. R and R' see Table 4.*

Compounds	R	R^1
15a	H	n-propyl
15b	H	n-butyl
15c	H	cyclopentyl
15d	n-propyl	n-propyl
15e	n-pentyl	n-pentyl
15f	morpholin-1-yl	_

Table 4. *3-(Alkyl(dialkyl)amino)benzothieno[2,3-f]quinazolin-1(2H)-ones **15a-f**.*

2.1.3.2 Biology

The ability of the synthetized compounds to inhibit the cells growth was evaluated towards two breast cancer cell lines, the ER-α positive MCF-7 and triple negative MDA-MB-231 cells. As shown in Table 5, the most active compounds were the *N*-propylamine derivative **15a** and the N-butylamine derivative **15d**, mostly toward the highly aggressive MDA-MB-231 cell line (IC_{50}= 3.88 ± 0.81 µM and 4.69 ± 1.00 µM, respectively). Extention of the alkyl chain, e.g. the *N*-butyl derivatives **15b** and **15e**, decreased the activity substantially (IC_{50}= 38.90 ± 1.22 µM and 42.35 ± 1.63 µM, respectively). Introducing a cyclic amine (cyclopentyl amine) was well accepted. Cyclopentylamine **15c** exerted a good antitumor activity towards MDA-MB-231 with an IC_{50} value of 5.59 ± 0.90 µM. The presence of a morpholinic group at C-3 in **15f** gave a slightly lower activity (IC_{50}= 9.43 ± 1.44 µM). MCF-7 cell line was a less sensitive towards all compounds tested. All the tested derivatives did not show any cytotoxicity on normal mammary epithelial MCF-10A cells. The reference molecules used in this assay, Ellipticine (**XIII**) and Vinblastine (**XIV**), exerted

a scarce selectivity between the tumoral and non-tumoral cells, thus, causing a strong cytotoxicity.

	IC_{50} (µM)		
Compound	**MDA-MB-231**	**MCF-7**	**MCF-10A**
15a	3.88 ± 0.81	40.70 ± 0.23	>100
15b	38.90 ± 1.22	74.46 ± 1.52	>100
15c	5.59 ± 0.90	45.61 ± 0.23	>100
15d	4.69 ± 1.00	41.99 ± 0.51	>100
15e	42.35 ± 1.63	75.23 ± 0.93	>100
15f	9.43 ± 1.44	21.17 ± 1.18	>100
Ellipticine (XIII)	1.85 ± 0.28	1.25 ± 0.35	1.20 ± 0.26
Vinblastine (XIV)	31.64 ± 0.86	15.00 ± 1.41	25.86 ± 1.33

Table 5. *IC_{50} values of carbazole derivatives (**15a-f**), Ellipticine (**XIII**) and Vinblastine (**XIV**), expressed in micromolar (µM).*

Bibliographic data report that Ellipticine (**XIII**) and Vinblastine (**XIV**) represent promising lead compounds for the development of new agents against cancer. Ellipticine (**XIII**) is promising due to its capacity to interfere with different proteins involved in DNA replication and cellular growth such as Telomerases, Topoisomerases I and II, Tubulin and Kinases [51,72], while Vinblastine (**XIV**) is able to interact with microtubules' dynamics [73,74].

Considering the importance of cytoskeleton dynamics in the main cell functions, such as mitosis, maintaining of cell shape, cell division, intracellular transport and chromosome segregation [75-77] and in apoptosis induction [78], we performed an *in vitro* tubulin-polymerization inhibition assay to assess if the most active compounds, **15a** and **15d**, could be inhibitors of the tubulin polymerization. In this assay, we measured the tubulin polymerization through turbidity variation at 350 nm, using a vehicle (DMSO) control, compounds **15a** and **15d** and Paclitaxel (**III**) and Vinblastine (**XIV**), as controls, at 10 µM concentration.

Figure 25 shows, that in the control experiment (DMSO) tubulin heterodimers self-assemble, as indicated by the turbidity increase in a time-dependent manner, reaching the steady state after about 15 minutes and with a final optical density value at 350 nm (OD_{350}) of about 0.47. The microtubule-stabilizing agent Paclitaxel (**III**) provoked a similar pattern but with a higher rate and amount of tubulin heterodimers assembly (OD_{350} of about 0.52), reaching

the plateau after about 10 minutes. The microtubule-destabilizing agent Vinblastine (**XIV**) was able to block strongly the tubulin polymerization, as indicated by the lower final turbidity value less than the half of the control reaction (OD_{350} of about 0.2) and by the reaching of the steady state only after about 40 minutes. Compounds **15a** and **15d** influenced tubulin polymerization reaction but less compared to Vinblastine (**XIV**). Compound **15a** and **15d** presented a similar behaviour as Vinblastine (**XIV**). The steady state was reached at 15 minutes for **15a** and 30 minutes for **15d**. Even though Vinblastine (**XIV**) is a faster inhibitor with respect to compounds **15a** and **15d**, it should be noticed that the final OD_{350} values for compounds **15a** and **15d** (OD_{350} of about 0.24 and 0.26, respectively) are similar to that of Vinblastine (**XIV**). Thus, our outcomes demonstrate that compounds **15a** and **15d** are valid tubulin polymerization inhibitors, with the important advantage lacking cytotoxicity on non-tumoral cell line (**Table 5**, comparing IC_{50} values of compounds **15a**, **15d** and Vinblastine (**XIV**) for MCF-10A cells).

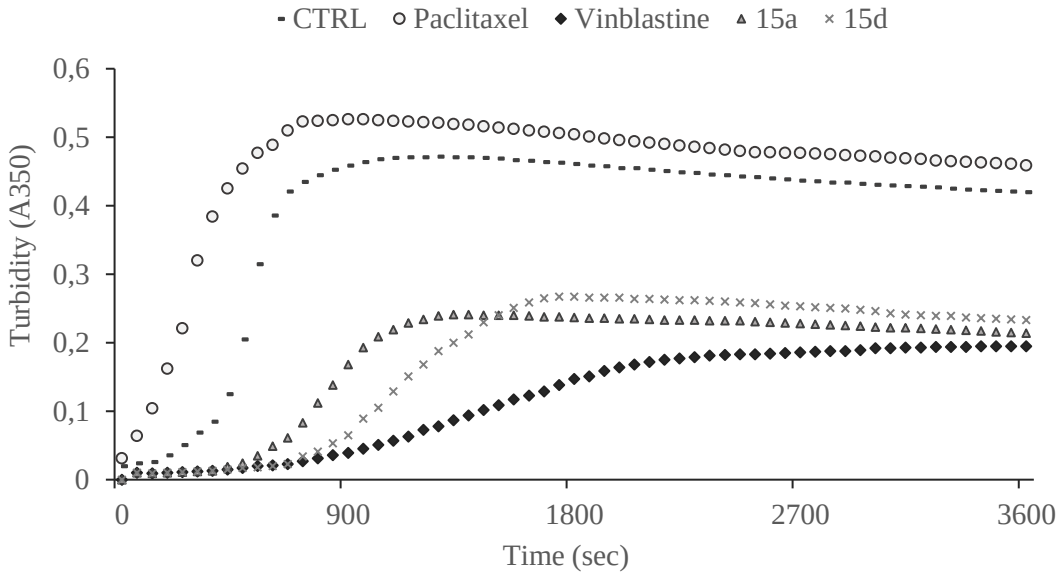

Figure 25. *Tubulin polymerization assay. Tubulin heterodimers polymerization into microtubules was determined by measuring the turbidity at 350 nm for 3600 seconds at 37 °C. The effect of compounds **15a** and **15d** (10 μM) on tubulin polymerization in vitro was examined. DMSO was used as a negative control. Tubulin-targeting agent Paclitaxel (**III**, 10 μM) and Vinblastine (**XIV**, 10 μM) were used as tubulin-stabilizing and tubulin-destabilizing reference agents, respectively.*

Since topoisomerases are often over-expressed in cancer cells, allowing an uncontrolled proliferation, we evaluated if our compounds would be able to inhibit the human topoisomerases I (hTopo I) and II (hTopo II).

Compound **15a** (Figure 26) was able to inhibit hTopo I, as evidenced by the presence of a single band at the bottom of the gel (lane 4) corresponding to the not-cleaved plasmid pHOT1. In contrast, compound **15d** did not exert any inhibitory activity, under the conditions and concentration used in this assay, and multiple bands due to pHOT1 DNA cleavage were visible (lane 5), as in the control (lane 2), where the enzyme was exposed only to the vehicle (DMSO). The reference Ellipticine (**XIII**) was, as expected, able to inhibit hTopo I enzyme and capable to shift the super coiled plasmid DNA electrophoretic migration [33,52] (Figure 26, lane 3).

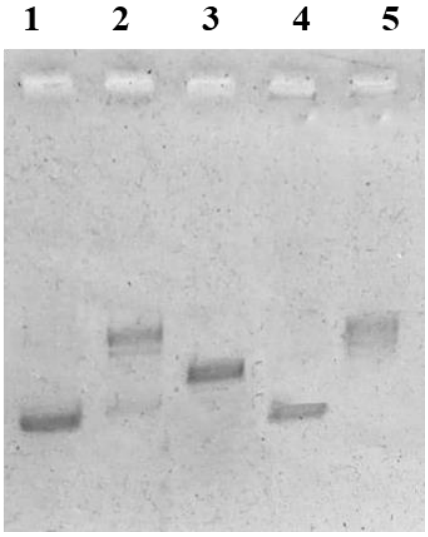

Figure 26. *hTopoI assay***.** *Supercoiled DNA was incubated without or with human topo I in the absence or presence of the test compounds at 50 μM : lane 1, super coiled DNA, lane 2, vehicle (DMSO), lane 3, Ellipticine (**XIII**), lane 4, compound **15a**, lane 5, compound **15d**.*

Neither, compound **15a** and **15d** was not able to inhibit hTopo II, at concentration up to 100 μM (data not shown).

These data demonstrate that compounds **15a** represent a good lead for the development of multi-targeting agents toward different cellular proteins/enzymes.

2.1.3.3 Molecular docking

In order to predict the molecular mechanism that could be responsible for the antitumor activity, molecular docking of compounds **15a** and **15d** was performed on the

crystallographic structures of Tubulin, Topoisomerase I and Topoisomerase II, obtained from the Protein Data Bank (PDB).

As shown in Figure 27 the two benzothienoquinazolinone derivatives **15a** and **15d** interact with the catalytic residue in the Tubulin active site, particularly:

- **15a** forms a hydrogen bond having the N atoms of the appended aliphatic chain as a donor and the backbone of Asn349 as acceptor (binding energy = -7.3 kcal/mol).
- **15d** binds with its pentacyclic moiety to the side chain of the protein residue Leu248 through a π-hydrogen interaction (binding energy = -8.1 kcal/mol);

In the case of Topoisomerase I (Figure 28), derivatives **15a** and **15d** bind the same binding site of the crystallographic ligand Topotecan, forming:

- several aromatic π-π interactions with two bases (G11 and A113);
- a relatively weak hydrogen bond with one of the terminal N atoms in the side chain of Arg364 acting as donor, and the N at position 4 of the quinazolinone moiety of the ligands as acceptor.

The binding energies of the two ligands are highly favourable: 10.3 kcal/mol for **15a** and -10.2 kcal/mol for **15d**.

In Figure 29, we report docking experiments of both benzothienoquinazolinone derivatives **15a** and **15d** on the Topoisomerase II active site, forming:

- several aromatic π-π interactions with the DNA;
- hydrogen-π interaction between the S atom of pentacyclic moiety of the ligand and the 5-membered ring of an adenine base (A12).

The binding energy obtained for **15a** and **15d** are, respectively, -7.9 and -7.3 kcal/mol.

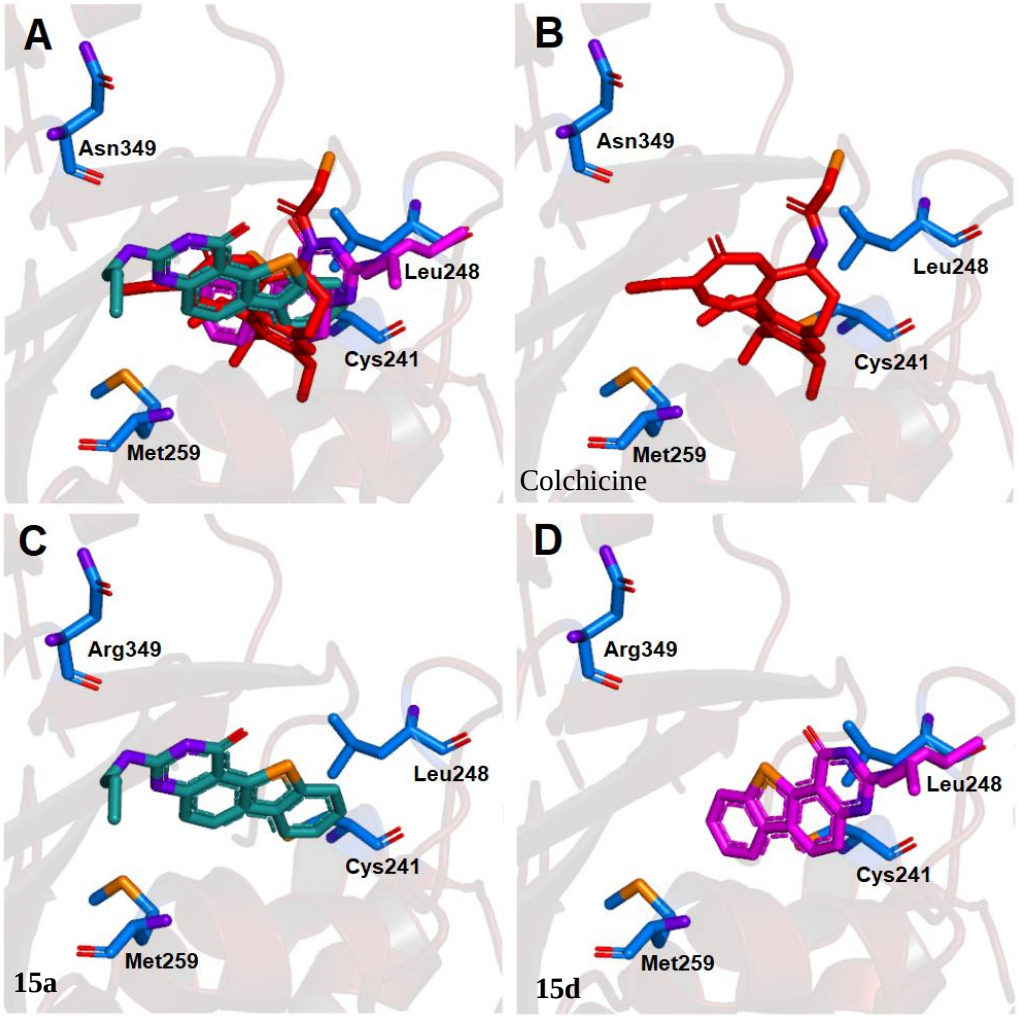

Figure 27. *Ligand-binding pocket of the active site of Tubulin. Protein backbone is represented in background as ribbons, and key protein residues are in blue. (A) Superimposed binding modes of the Colchine (red),* ***15a*** *(cyan) and* ***15d*** *(magenta). The ligands are also shown separately: (B) Colchicine, (C) compound* ***15a****, and (D) compound* ***15d****.*

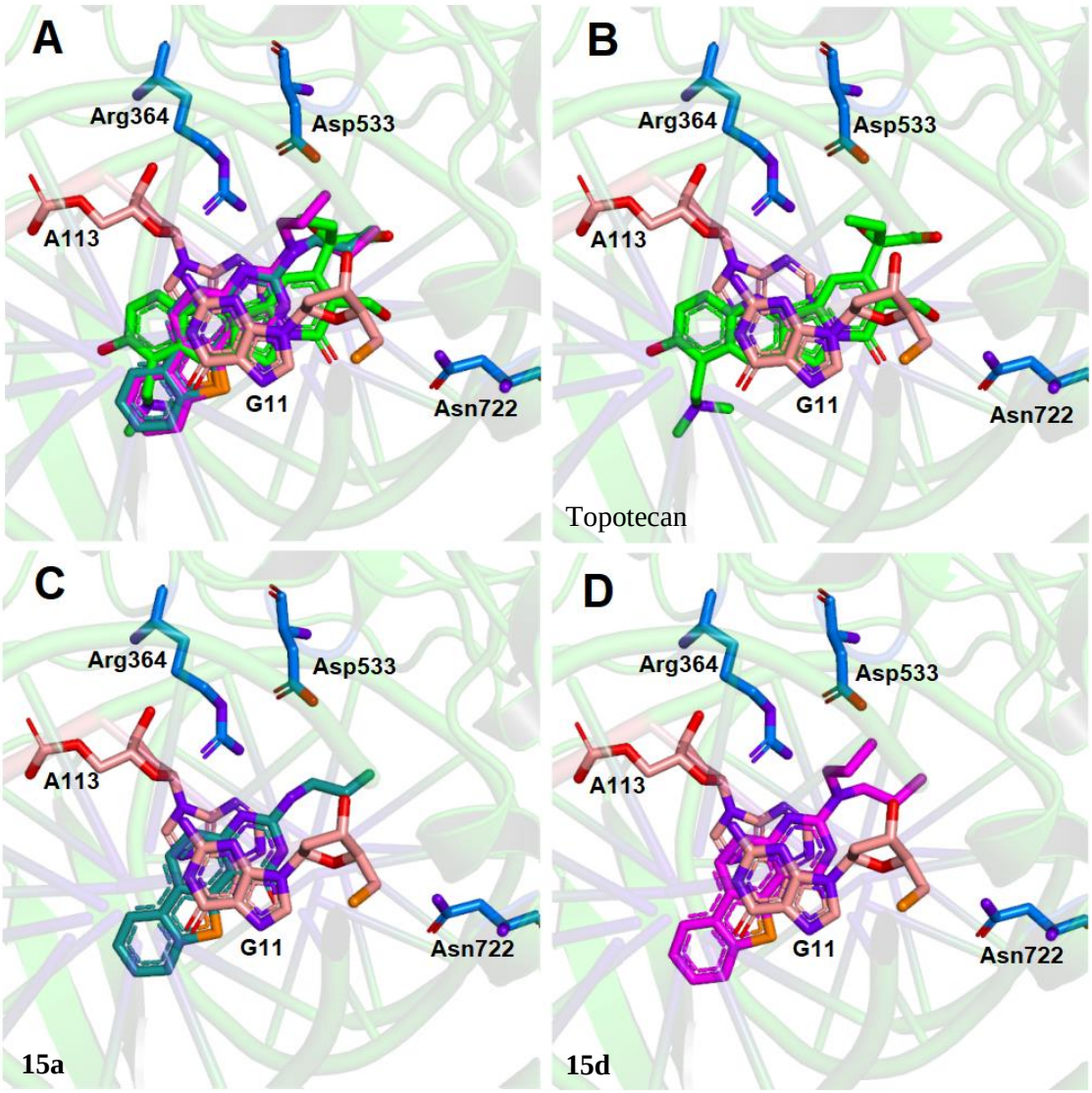

Figure 28. *Ligand-binding pocket of the active site of Topoisomerase I–DNA complex. Protein backbone is represented in background as ribbons, and key protein residues are in blue. (A) Superimposed binding modes of the Topotecan (green),* ***15a*** *(cyan) and* ***15d*** *(magenta). The ligands are also shown separately: (B) Topotecan, (C) compound* ***15a****, and (D) compound* ***15d****.*

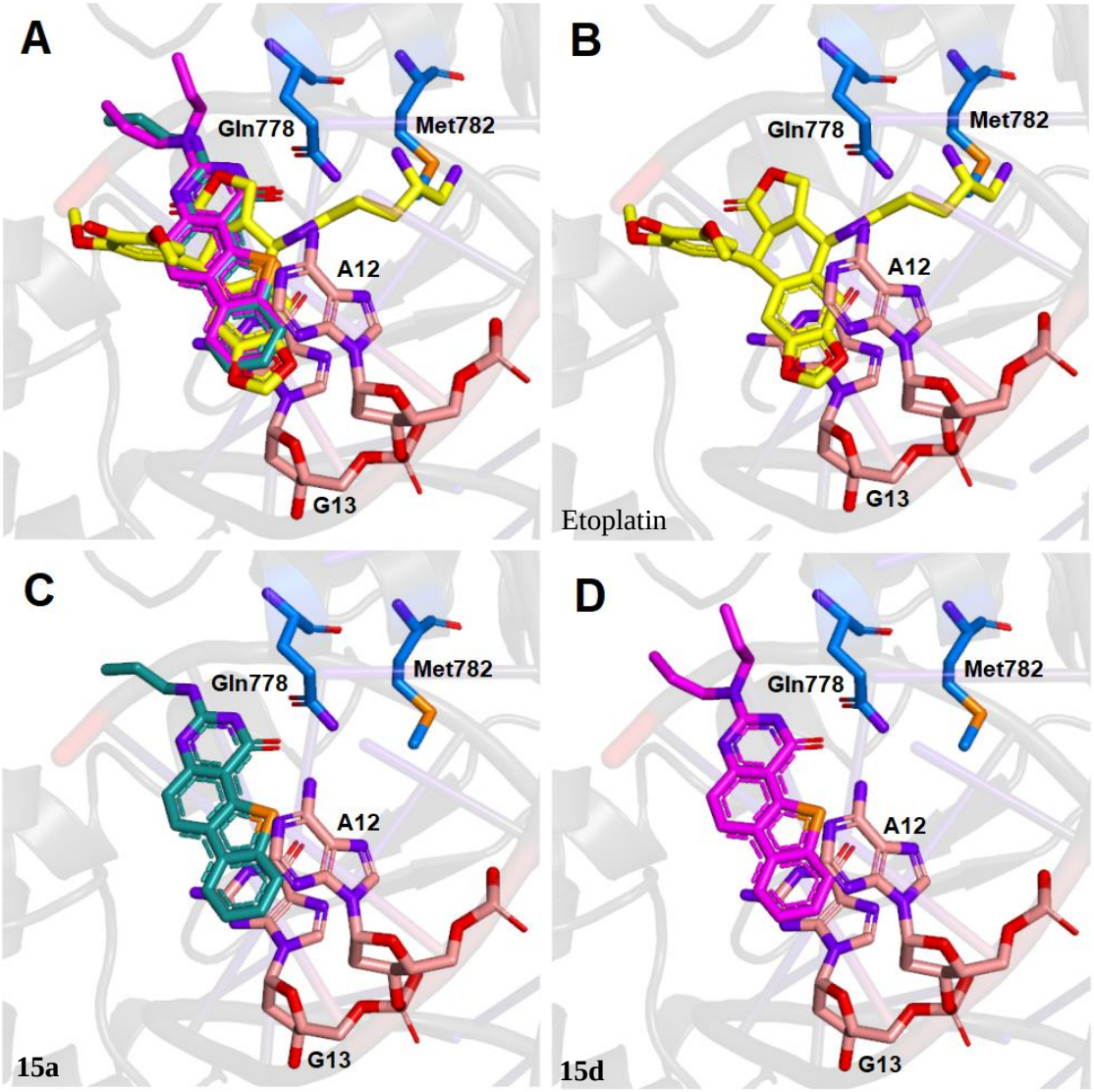

Figure 29. *Ligand-binding pocket of the active site of Topoisomerase II–DNA complex. Protein backbone is represented in background as ribbons, and key protein residues are in blue. (A) Superimposed binding modes of Etoplatin N2β (yellow),* ***15a*** *(cyan) and* ***15d*** *(magenta). The ligands are also shown separately: (B) Etoplatin N2β (yellow), (C) compound* ***15a****, and (D) compound* ***15d****.*

Among the human cancers, Breast and uterine cancers caused the death of almost the 26% and 7% of women, respectively [1]. The availability of new and improved chemotherapies with few side effects and less risk of development of resistance is still a major challenge. The carbazolic compounds **4f**, **9c**, **15a** and **15d**, structurally correlated to the most known Ellipticine (**XIII**) and Vinblastine (**XIV**) (see Figure 12), could represent new potential anticancer molecules. These compounds were able to exert good antiproliferative effects on *in vitro* models of the most common cancer types in women.

Considering the biological features of these new carbazolic compounds, they could be new lead compounds and new tools for the treatment of women's cancers. Particularly, compound **15a** may represent a good tool for the development of new multi-target agents, a current trend in drug research in oncology.

2.2 NEW GOLD AND SILVER CARBENE METAL COMPLEXES: *CIS*PLATIN (II) ANALOGUES

*Cis*platin (**II**) and other platinum-based drugs (carboplatin, oxaliplatin, nedaplatin and lobaplatin) are still in use for their antitumor properties. Their clinical use is often limited because of severe toxicity and the onset of frequent resistance phenomena [79-83]. In order to overcome these limitations, many research groups have developed new metal complexes [84-93].

Among the numerous synthesized complexes, significant anti-proliferative effects have been obtained using silver or gold based compounds [94,95]. Silver salts are known since ancient time for their antimicrobial properties [96,97]. Nowadays, in addition to their antibacterial activity, these complexes have shown promising antitumor activities *in vitro* and *in vivo* [98-101].The Ag cation is the responsible for the activity and it is able to interact with the cell membrane or the thiol groups of bacterial enzymes and interfere with the mitochondrial electron-transport system [102].

Gold complexes been used for a long time. They are employed in arthritis and cancer treatment [103-105], exerting multiple mechanisms of action. They induce cellular apoptosis that could result from mitochondrial or DNA damage, can act as enzyme inhibitor (thioredoxin reductase) and modulate some kinases and phosphatases [52,95,106-108].

N-heterocyclic carbenes (NHCs) represent promising ligands for both silver and gold complexes because of their σ-donor properties, π backbonding and transition-metal-binding abilities [109,110]. They are also easily accessible in a few steps and they can bind large and various classes of substituents [111-113]. This make them suitable ligands for fast and efficient drug design and for the stabilization of biologically active metal complexes [114].

Recently, promising results have been obtained by Saturnino *et al.* in 2016 [115], concerning the anticancer properties of some silver and gold NHC complexes (Figure 30).

The antitumor activity of these metal complexes, containing the ligands **L1**, **L2** and **L3**, was evaluated toward the breast carcinoma cell line MCF-7. The obtained results showed that **AgL3** and **AuL3** possessed a good cytotoxic activity on this line (IC_{50} = 4.0 ± 0.2 μM and 1.0 ± 0.2 μM, respectively), while the gold and silver complexes containing the ligands **L1** and **L2** did not produce any anti-proliferative activity [115].

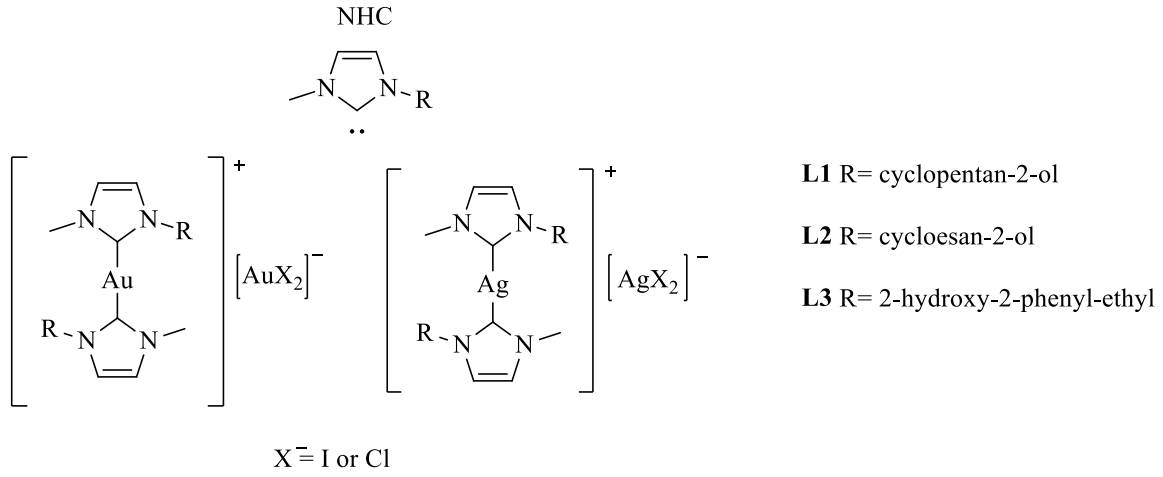

Figure 30. *Silver and gold complexes (**L1**-**L3**) [115].*

These interesting data pushed us to design and study two new series of metal complexes, showed in Figure 31 (**L4**-**L8**).

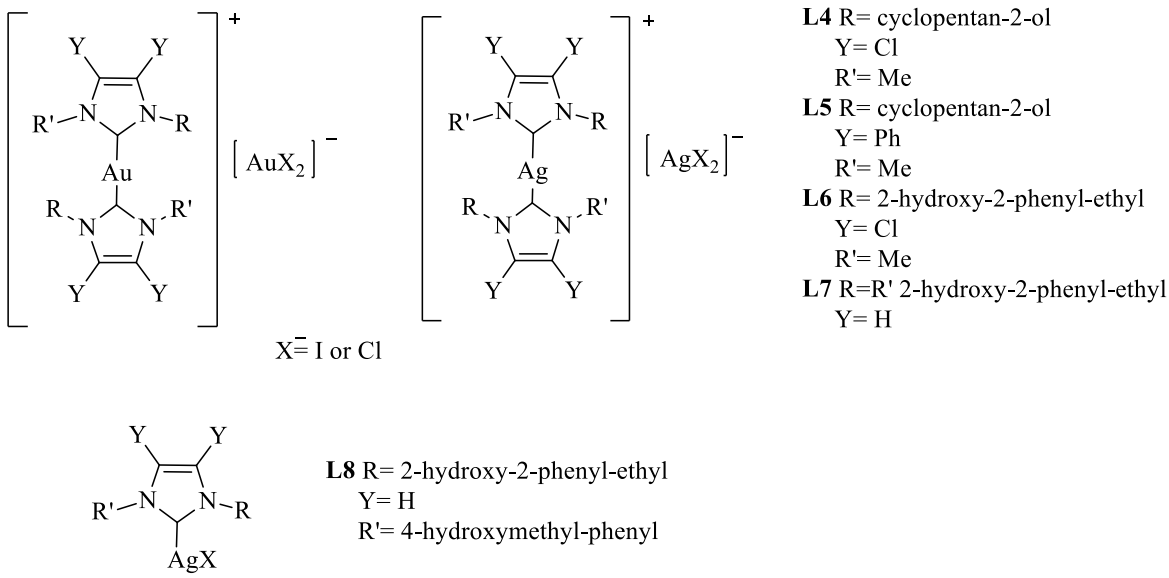

Figure 31. *New silver and gold complexes (**L4**-**L8**).*

2.2.1 Novel Au and Ag carbene complexes

In order to deepen the results obtained by Saturnino *et al.* [115], in a first work [116] we made some structural modifications on the **L1** complexes, introducing two chlorine atoms or two phenyl groups on the NHC fragment, obtaining four new metal complexes (**AgL4**, **AuL4**, **AgL5** and **AuL5**) (Figure 32).

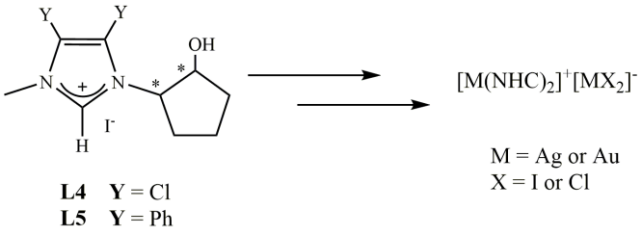

Figure 32. *New synthesized silver and gold complexes (***AgL4**, **AuL4**, **AgL5** and **AuL5)**

The new synthesized complexes exerted a promising antitumor effect on two breast cancer cell lines (MCF-7 and MDA-MB-231), and mostly toward two uterine cancer cell lines (HeLa and ISHIKAWA). In particular, the most active gold complex **AuL4** was able to induce the intrinsic (or mitochondrial) apoptotic pathway increasing ROS production in HeLa cells. *Cis*platin (**II**), used as a reference molecule, exhibited a lower cytotoxicity than our compounds.

2.2.1.1 Chemistry

The ligand 4,5-dichloro-imidazolium-*N*-methyl-*N*'-cyclopentan-2-ol iodide (**L4**) was obtained over two steps previously reported [117]. First, 4,5-dichloroimidazole was transformed into the monoalkylated product (Scheme 4), via epoxide opening of cyclopentene oxide. The second nitrogen atom was methylated using CH_3I (Scheme 4). The salt **L4** was obtained as a racemic mixture (74% yield) [116].

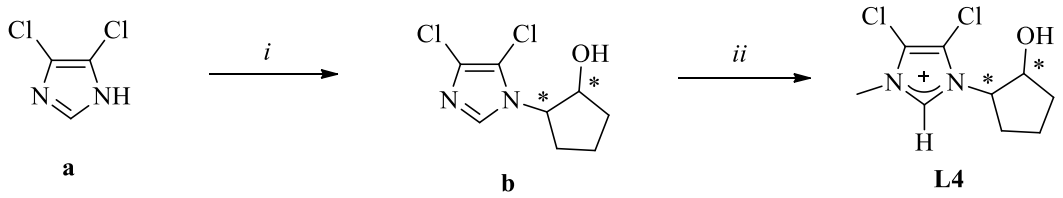

Scheme 4. *Synthesis of 4,5-dichloroimidazolium N-methyl-N'-cyclopentan-2-ol iodide (**L4**). i) cyclopentene oxide, 60 °C 12h; ii) methyliodide, acetonitrile, reflux, 12 h, 74% yield.*

4,5-Diphenylimidazolium-*N*-methyl-*N*'-cyclopentan-2-ol iodide (**L5**) was obtained as previously reported [118], with some modifications. First small pieces of potassium were added to a solution of 4,5-diphenylimidazole in dimethylformamide. Then, after dissolution of the alkaline metal, cyclopentene oxide was added to a warm (100 °C) solution (Scheme 5), obtaining 4,5-diphenylimidazolium-*N*-cyclopentan-2-ol as a white solid (60% yield).

This product was dissolved in acetonitrile and after the addition of methyl iodide we obtained salt **L5** in 52% yield (Scheme 5, second step) [116].

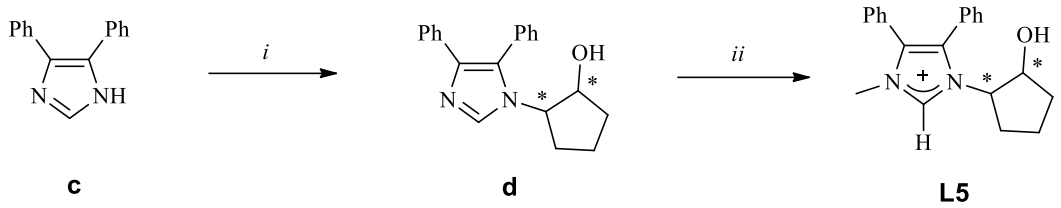

Scheme 5. *Synthesis of 4,5-diphenylimidazolium-N-methyl-N'-cyclopentan-2-ol iodide (**L5**). i) cyclopentene oxide, DMF, potassium 100 °C, 17 h, 60 % yield; ii), methyl iodide, acetonitrile, 80°C, 2h, 52% yield.*

Reactions of the salts with silver oxide (Ag_2O), under an inert nitrogen atmosphere, as reported earlier [97,119], produced corresponding Ag–NHC complexes **AgL4** and **AgL5** (see Scheme 6). They were characterized by ^{1}HNMR and ^{13}CNMR spectroscopy, mass spectrometry and elemental analysis [116].

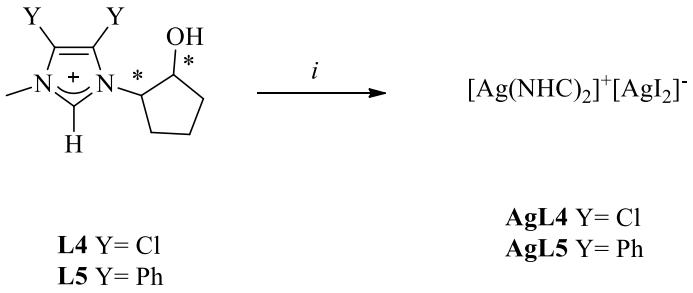

Scheme 6. *Scheme for the preparation of Ag–NHC complexes **AgL4** and **AgL5**. i) Ag_2O, CH_2Cl_2, reflux, 4h, 25 % yield.*

AuL4 and **AuL5** were synthesized by transmetalation in dichloromethane between the corresponding Ag–NHC complexes and the chloro(dimethylsulfide)gold(I) [$(Me_2S)AuCl$] complex, according to the procedure already reported [120] (see Scheme 7). $(Me_2S)AuCl$ was added to a solution of the silver complex in CH_2Cl_2 (molar ratio of 1:1), and after purification, a yellow powder in good yield (77%) was obtained for both gold complexes. The products were analyzed by NMR spectroscopy, mass spectrometry and elemental analysis [116].

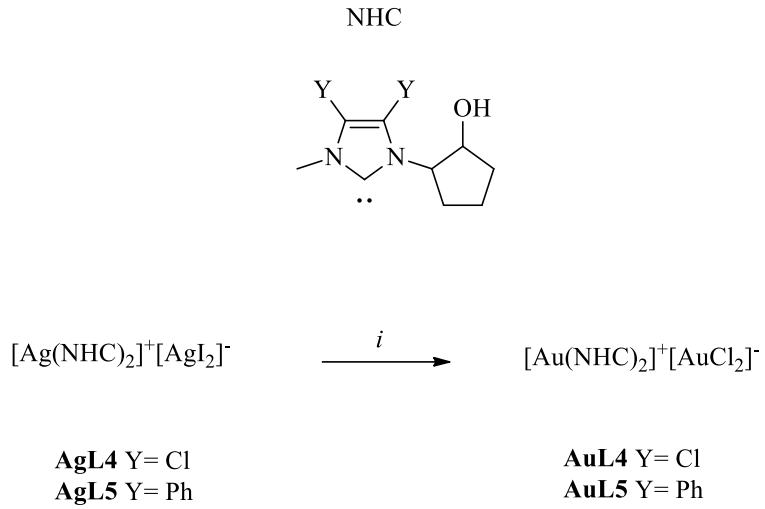

Scheme 7. *Scheme for the preparation of Au–NHC complexes **AuL4** and **AuL5**. i) (Me_2S)AuCl, dichloromethane, rt, 4h, 77% yield.*

2.2.1.2 Biology

The antitumor properties of the new series of Au and Ag complexes were evaluated towards two breast cancer cells (MCF-7 and MDA-MB-231) and two ovarian cancer cells (HeLa and ISHIKAWA). Gold complex **AuL4** resulted the most active complex and all the other metal complexes exerted good inhibitory effects on the proliferation of the cells used in these assay (Table 6). **AuL4** drastically reduced the growth of HeLa cells (IC_{50} value amounting to 1.63±0.5 μM. It also exhibited good antiproliferative activity on breast cancer cells, MCF-7 and MDA-MB-231 with IC_{50} values of 3.98±0.4 and 6.02±0.7 μM, respectively. **AgL4** possessed a lower activity than **AuL4** towards all cancer cells used, but it exhibited a better inhibitory activity than *Cis*platin (**II**) on breast cancer cells proliferation. In contrast, both silver and gold **L5** complexes exerted a lower, although still good, antitumor activity than the corresponding **L4** complexes. This characteristic could due to the different lipophilicities and in the steric and electronic properties of the two ligands. We evaluated if the ligands **L4** and **L5** by themselves could possess any cytotoxic activity. Data showed in Table 6 demonstrate that both ligands did not exert any antitumor effect up to a concentration of 200 μM. The cytotoxicity of all complexes towards two non-tumoral cell lines, human nonmalignant breast epithelial MCF-10A cells and human embryonic kidney HEK-293 cells was also evaluated. They did not show any cytotoxic up to 200 μM. These outcomes highlight that these complexes are more effective towards uterine tumor cells and still maintain good antiproliferative effects towards breast cancer cells. The lack of cytotoxicity

against normal cells pushed us to study the mechanism of action of the lead compound **AuL4**.

	IC_{50} (μM)					
	MCF-7	**MDA-MB-231**	**HeLa**	**ISHIKAWA**	**MCF-10A**	**HEK-293**
AuL4	3.98±0.4	6.02±0.7	1.63±0.5	4.81±0.9	>200	>200
AgL4	16.5±0.8	20.8±1.2	15.6±0.6	15.0±0.9	>200	>200
AuL5	21.2±0.6	20.2±0.9	15.2±0.8	16.7±1.2	>200	>200
AgL5	51.7±1.1	35.8±0.7	24.4±0.9	24.7±0.8	>200	>200
L4	>200	>200	>200	>200	>200	>200
L5	>200	>200	>200	>200	>200	>200
***Cis*platin (II)**	35.8±1.3	28.7±1.0	15.7±1.1	15.1±0.8	81.3±1.2	16.8±0.7

Table 6. *IC_{50} values of Au- and Ag-NHC complexes and Cisplatin (**II**), expressed in micromolar (μM).*

In order to study the molecular mechanism underlying the antitumor properties of most active complex **AuL4**, we exposed HeLa to it. **AuL4** was able to cause dramatic morphological changes (Figure 33): at 24 h cells possessed a dissimilar form compared to the control cells, with elongated and threadlike cytoplasm. At 48 h cells appeared to be round and small (cell shrinkage).

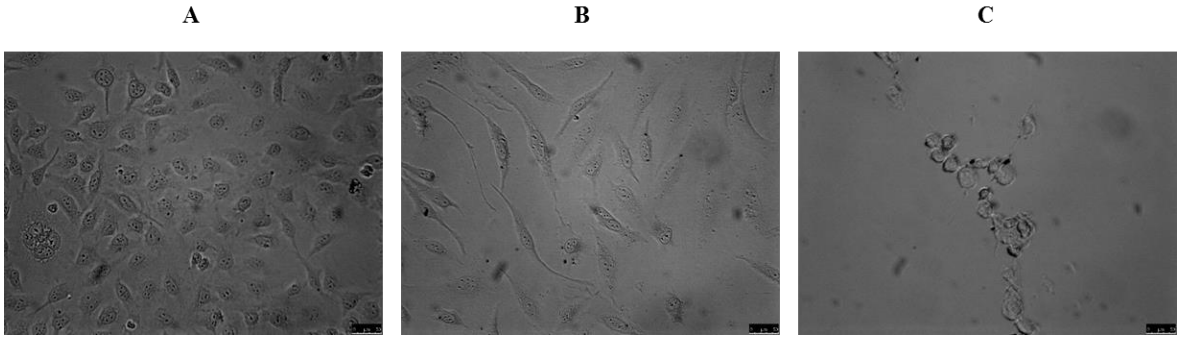

Figure 33. *Morphological changes after the exposure of HeLa cells to **AuL4**. a) Vehicle-treated cells with normal morphology; b, c) Cell morphology changes after 24 and 72 h, respectively; cells appeared filiform and then round and small (20x magnification).*

TUNEL assay was used for the evaluation of **AuL4**-inducted apoptosis in HeLa cells. The presence of a green fluorescence in cells treated with **AuL4** (Figure 34, panel B, **AuL4**), absent in the CTRL cells (Figure 34, panel B, CTRL), indicated that nuclear DNA is damaged and fragmented, leading to cell death by apoptosis.

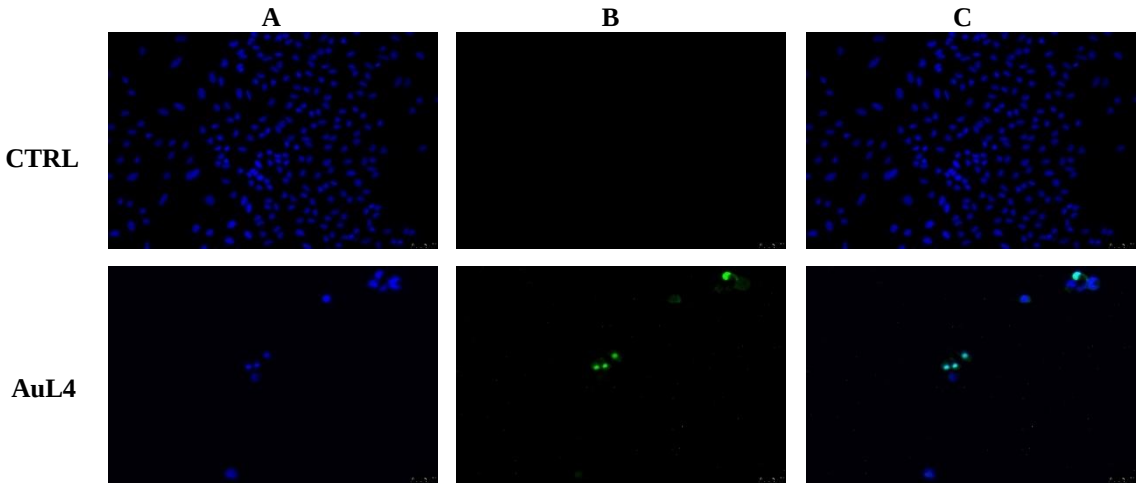

Figure 34. *Apoptosis detection by TUNEL assay on HeLa cells. Cells were treated for 24 h with* ***AuL4*** *and then cold-methanol fixed and subjected to the TUNEL procedure and to DAPI counterstain, as reported in Material and methods section. Fixed cells were observed and imaged under an inverted fluorescence microscope at 20X magnification. A) DAPI (excitation/emission wavelength 350 nm/460 nm), B) CF™488A (excitation/emission wavelength 490 nm/515 nm), C) overlay channel; representative fields are shown.*

Generally, cells develop several strategies in order to identify and repair DNA damage. Amongst them, poly-(ADP-ribose) polymerase-1 (PARP-1) play a major role in repairing DNA lesions, thanks to its poly(ADP-ribosyl)ation that induces chromatin decondensation around the damage site, allowing the recruitment of DNA-repair apparatuses. If PARP-1 cannot exert this action, DNA damage cannot be repaired and the cell dies. Thus, we performed Western blot analyses in order to study the status of PARP-1 in HeLa cells treated with **AuL4**. Figure 35 demonstrates that this complex induced PARP-1 cleavage in a time-dependent manner, preventing genomic DNA reparation.

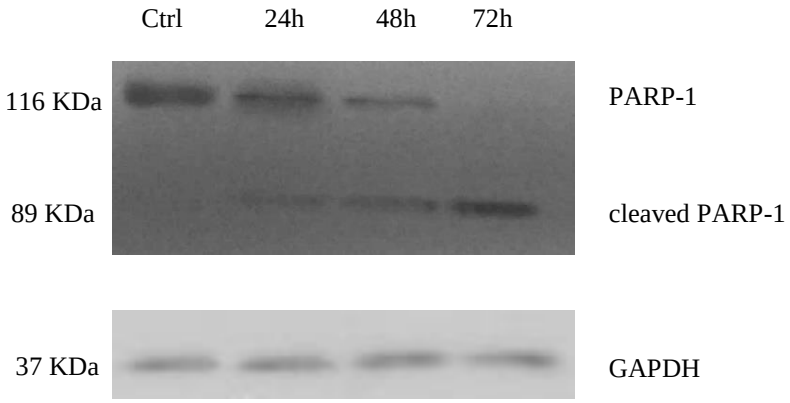

Figure 35. *Time course of PARP-1 cleavage. Uterine cancer Hela cells were treated with **AuL4** at 1 μM concentration, then the total protein content was extracted and processed as reported in Material and methods. Ctrl: protein extract from vehicle-treated cells (only at 72h is visible); 24h, 48h and 72h: protein extract of **AuL4**-treated cells at the indicated time point. GAPDH: loading normalization.*

PARP-1 appears to be a substrate of 3/7 effector caspases in the cascade of biochemical events that occur during the sophisticated and well-regulated apoptotic process [121]. We measured the activity of the activating caspases 8 and 9 and of the executing caspases 3/7: the fluorescence assay underlined a significant increase in caspases 3/7 and 9 in the HeLa cells exposed to **AuL4**, while the levels of activity of caspase 8 remained unchanged compared to the control cells (vehicle-treated) (Figure 36). These data demonstrate that **AuL4** treatment promoted the activation of caspase 9 that in turn activated caspases 3/7, which leads to the above-mentioned PARP-1 cleavage.

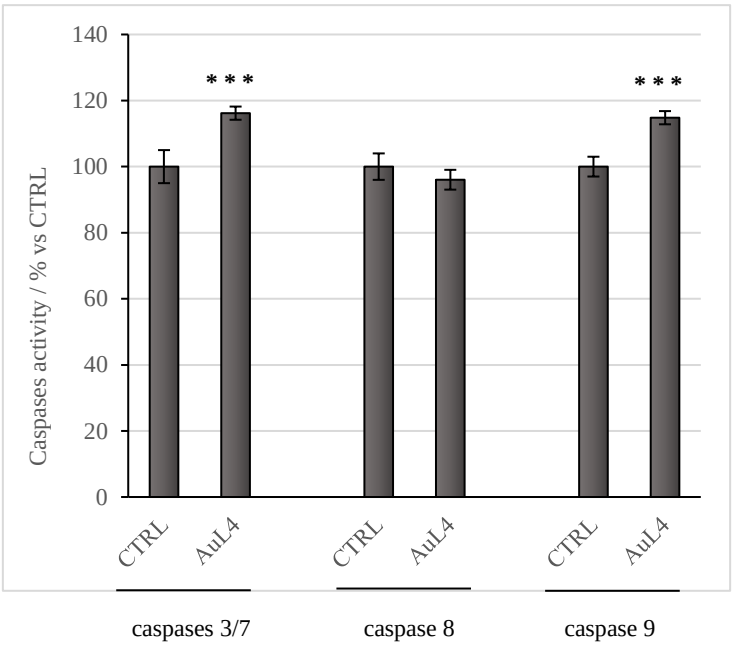

Figure 36. *Caspases activity. Activation of caspases 3/7 and 9 (percentage over the vehicle-treated cells used as control) following to the treatment of HeLa cells with the **AuL4** at 1 µM for 24 hours. Columns mean, bars SD, *p<0.001.*

Considering that the exposure of HeLa cells to the **AuL4** complex appears to trigger the intrinsic apoptotic process and that many metal complexes accumulate in the mitochondrial network [115,122], we carried out a fluorescence assay. We used a specific mitochondrial probe, the MitoTracker Deep Red FM, together with an anti-cytochrome c antibody to follow the eventual release of this protein from mitochondria to the cell cytoplasm (Figure 37). In the control cells, mitochondria are integral and cytochrome c is located within them (panel D, merge). The green fluorescence corresponding to the cytochrome c (panel B, CTRL) is well defined and localized in the perinuclear area and is perfectly co-localize with red fluorescence (panel C, CTRL), associated with the mitochondrial probe (MitoTracker Deep Red FM). In **AuL4**-treated HeLa cells, cytochrome c is released into the cell cytoplasm because of mitochondria fragmentation. Indeed, green fluorescence (panel F) is higher and clearly diffused into the cell cytoplasm, and red fluorescence (panel G) is punctiform and diffused in the cytoplasm, due to the mitochondria fragmentation. The perfect overlay between the green and red fluorescence is not noticeable after **AuL4** treatment (panel H).

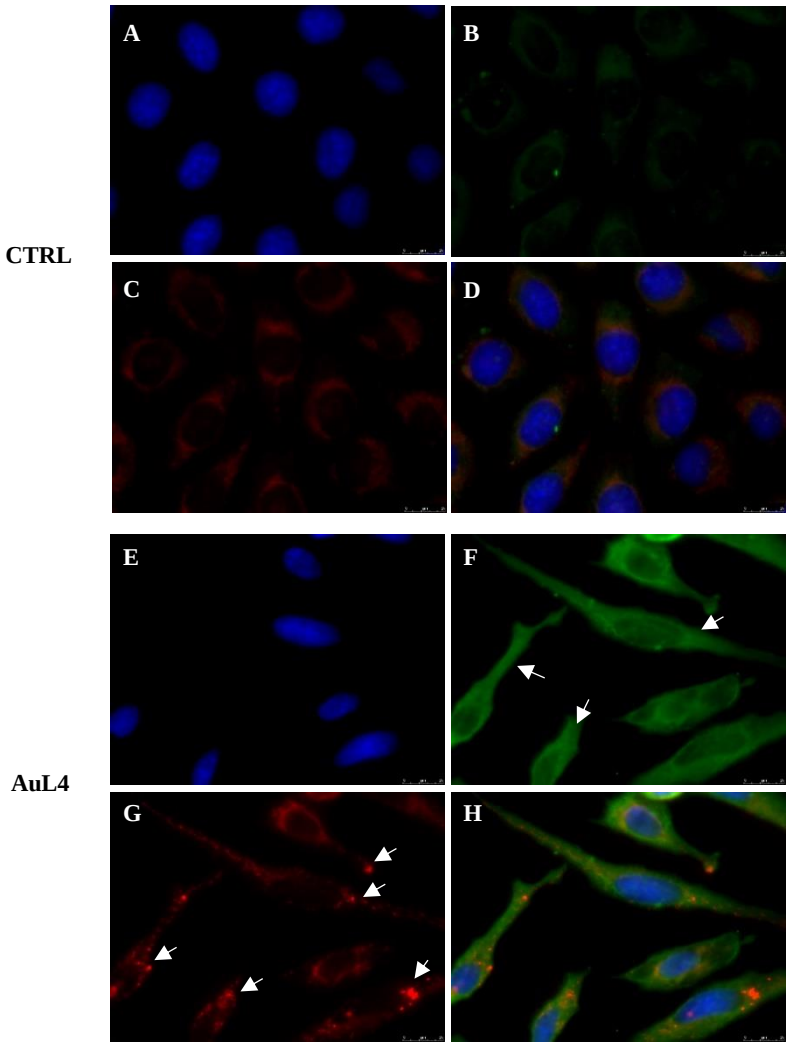

Figure 37. *Mitochondria disruption and cytochrome c release in Hela cells. In vehicle-treated cells cytochrome c (panel B) is localized within intact mitochondria (panel C), as noticeable in panel D where the merge is shown. The treatment of Hela cells with* ***AuL4*** *1 µM for 24h induce cytochrome c release in the cytosol (panel F, white arrows) and mitochondria fragmentation (panel G, white arrows). Panels A and E, nuclear stain with DAPI (excitation/emission wavelength 350 nm/460 nm); Panels B and F, Alexa Fluor® CF™488 (excitation/emission wavelength 490 nm/515 nm); Panels C and G, MitoTracker® Deep Red FM probe (Fluorescence excitation= 644 nm, Fluorescence emission= 665 nm); Panels D and H, merge. Images were acquired at 63x magnification and representative fields were shown.*

Mitochondrial dysfunction usually induces intracellular oxidative stress and both phenomena are involved in the induction of cell death by apoptosis [123-126]. With this in mind, we studied also the ability of **AuL4** to produce cellular ROS in HeLa cells, using as positive control Menadione (Men) because of its known ability to cause ROS production and cell death due to oxidative stress [127]. After treatment of HeLa cells with **AuL4,** 1 µM for

24 h with or with Men 10 μM for 1 h, cells were incubated with 2'-7'-dichlorofluorescein diacetate (DCF-DA), a non-fluorescent compound that in the presence of intracellular ROS is oxidized to DCF, which produces green fluorescence. Figure 38a underlines the presence of a similar green fluorescence in the cytoplasm of cells treated with **AuL4** and Men (panel B, Men and **AuL4**, white arrows), which is indicative of increased ROS production. In the control cells (treated with the only vehicle) this green fluorescence was absent. Cell nuclei were dyed with DAPI (panel A), and the overlay is shown in panel C. The fluorescence quantification, performed using ImageJ (Figure 38b) confirmed the capacity of **AuL4** to induce ROS production in HeLa cancer cells similarly to that of Menadione.

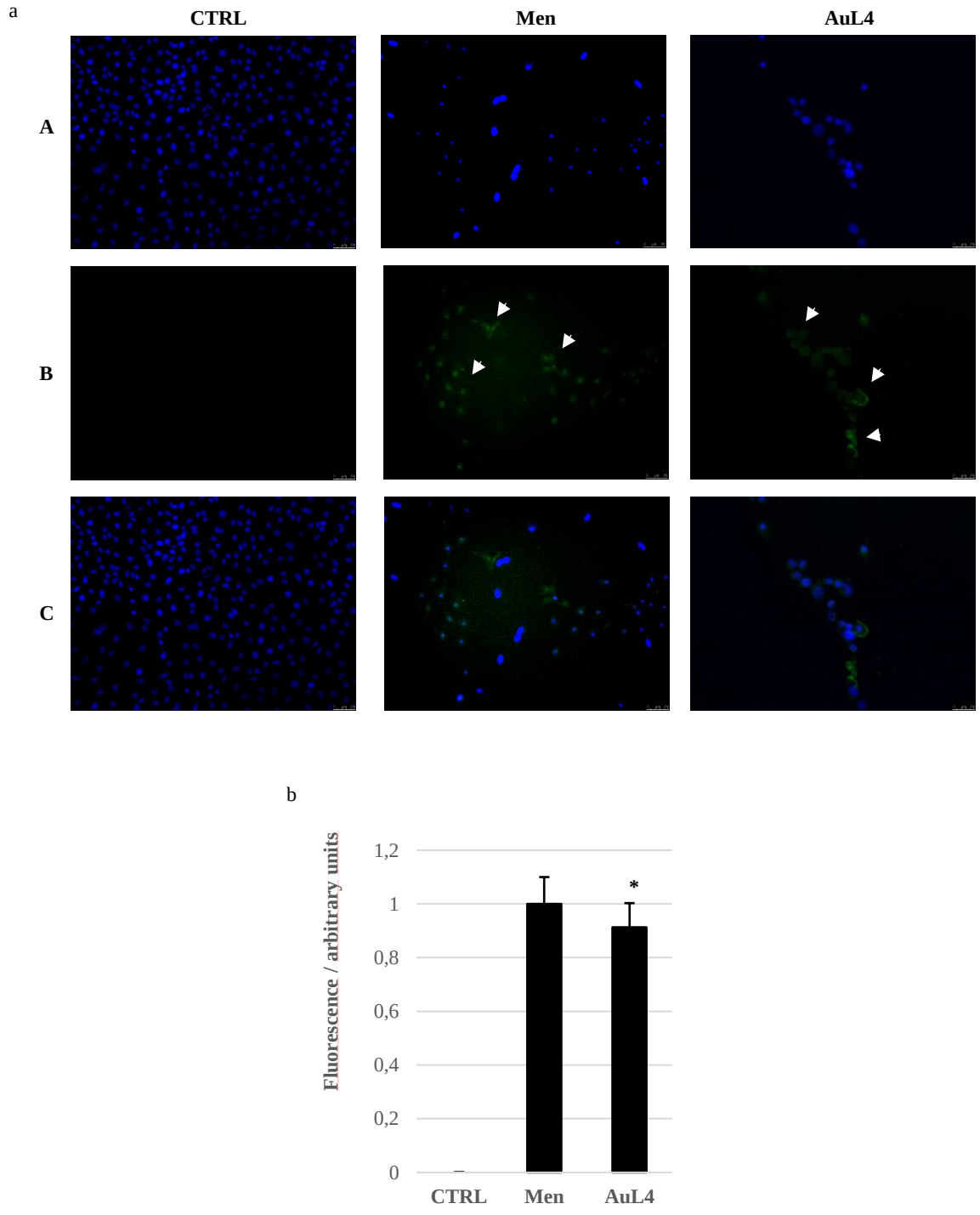

Figure 38. *ROS induction by **AuL4** treatment in Hela cells. (A) ROS production was evaluated using DCF-DA in HeLa cells treated with Menadione (Men, used as positive control), **AuL4** or vehicle. Images were acquired at 20x magnification. Panels A, nuclear stain with DAPI (excitation/emission wavelength 350 nm/460 nm) in treated (Men or **AuL4**) and untreated cells (vehicle, CTRL). Panels B, DCF (490 nm/515 nm for CF™488A) in treated (Men or **AuL4**) and untreated cells (vehicle, CTRL). Panels C show the merge channel. (B) Fluorescence quantification. *p<0.001, **AuL4** vs Men.*

2.2.2 New multi-target Au an Ag metal complexes

With the aim to improve these results, our research also concerned the structural modification of the complexes containing the **L3** ligand (Figure 30), in order to improve its antitumoral properties. In particular, the new synthesized **L3** analogues (Figure 39) contain two chlorine atoms on the carbene unit (**L6**). This substitution would further increase their lipophilicity and therefore could increase their biological activity. Considering that the 2-hydroxy-2-phenylethyl substituent on the nitrogen could represent an important portion for biological activity, the other methyl group of the imidazole ring was also replaced with a 2-hydroxy-2-phenylethyl group (**L7**) or with a 4-(hydroxymethyl)phenyl (**L8**). These substituents could represent a good compromise between solubility and lipophilicity. Another alcoholic function would make the complexes more soluble in a physiological environment and the aryl substituent could increase their lipophilicity.

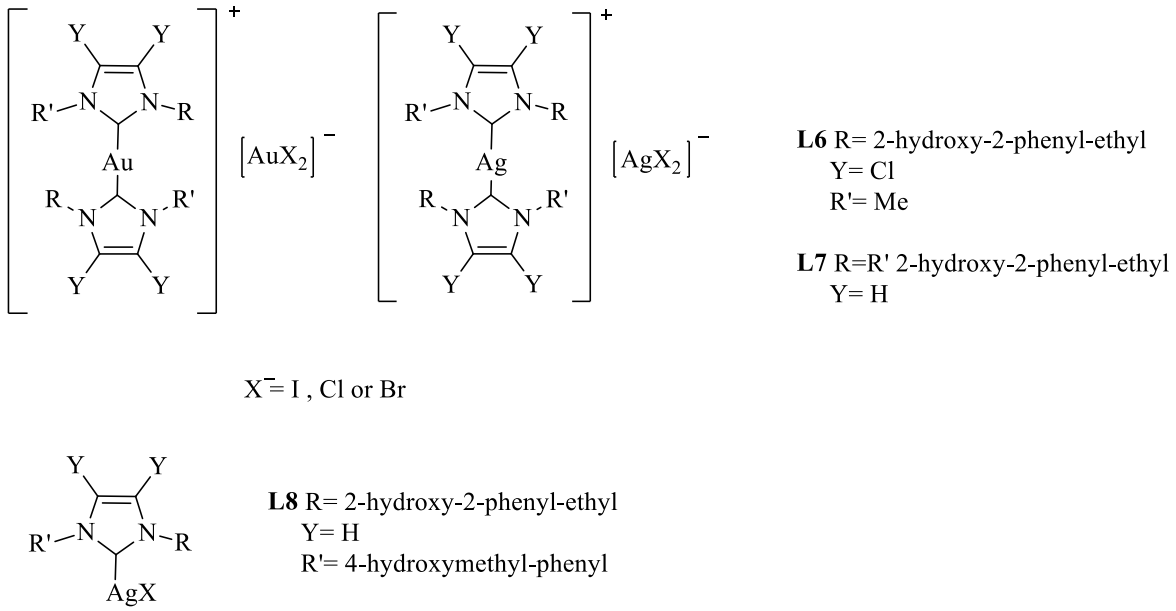

Figure 39: *New synthetized Ag and Au complexes.*

The anti-tumor activity of these new complexes was evaluated on two breast and on two uterine carcinoma lines. The obtained results showed, in particular on the highly aggressive and metastatic MDA-MB-231 cell lines, an interesting anti-tumor activity of the compound **AuL6** that was also able to interfere with two important targets involved in carcinogenesis. It acts as valid tubulin polymerization inhibitor and it was a potent hTopo I

and II inhibitor. **AuL6** can be considered a promising lead complex for the development of multi-targets agents in cancer therapy.

2.2.2.1 Chemistry

All compounds were synthetized according to literature procedures with small modification [128-132].

The synthesis of the carbene complexes 4,5-dichloroimidazole *N*-methyl-*N'*-[(2-hydroxy-2-phenyl)ethyl]-2-ylidene silver (I) iodide (**AgL6**) and 4,5-dichloroimidazole *N*-methyl-*N'*-[(2-hydroxy-2-phenyl)ethyl]-2-ylidene gold (I) chloride (**AuL6**) (see Figure 39), has been recently reported [133].

For the synthesis of the pro-ligand salt **L7**, having on both nitrogen of the heterocycle nucleus the same substituent (2-hydroxy-2-phenyl-ethyl) (Scheme 8), imidazole was reacted with styrene oxide. In this reaction the opening of the epoxy ring occured with formation of the dialkylated product. To unify the counter ion, the crude salt was heated with HI. The salt **L7** was characterized by ^{1}H- and ^{13}C-NMR spectroscopy, mass spectrometry and elemental analysis.

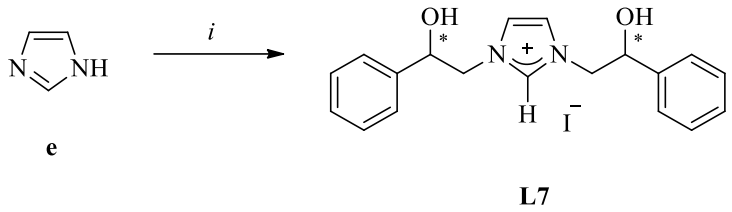

e **L7**

Scheme 8: *Synthesis of N,N'-bis-[(2-hydroxy-2-phenyl)ethyl]-imidazolium iodide (**L7**). i) 1. styrene oxide, THF, 60°C, 24h, 2. HI, DMC, 43% yield.*

The salt **L7** was reacted in CH_3CN with silver oxide (Ag_2O) in nitrogen atmosphere and in the presence of molecular sieves. In these conditions, as earlier reported [115], the silver oxide deprotonates at carbon-2 giving the corresponding Ag–NHC complex (**AgL7**) (Scheme 9). The molecular sieves are used to capture the water, which is a byproduct of the reaction, and to shift the equilibrium. The complex was characterized by NMR, elemental analysis and mass spectroscopy.

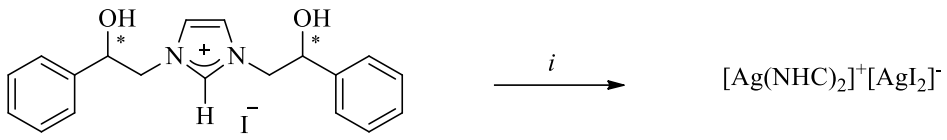

L7 **AgL7**

Scheme 9: *Synthesis of bis-N,N'-[(2-hydroxy-2-phenyl)ethyl]-imidazole-[2-ylidine] [silver(I)]$^{+}$[diiodide-silver(I)]$^{-}$ (**AgL7**). i) Ag_2O, CH_3CN, 50% yield.*

The salt **L7** was reacted in DMF (dimethylformamide) with the base KHMDS (potassium-bis-(trimethylsilyl)-amide) and with chloro-(dimethylsulfide)-gold(I) [$(CH_3)_2SAuCl$] (see Scheme 10). The obtained complex **AuL7** was characterized by ^{1}H- and ^{13}C-NMR and mass spectrometry.

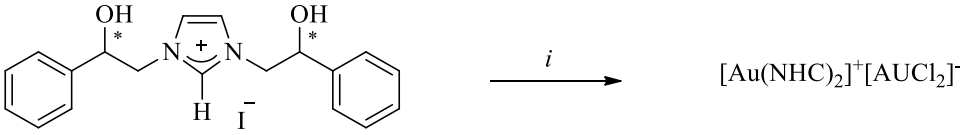

L7 **AuL7**

Schema 10: *Synthesis of bis-N,N'-[(2-hydroxy-2-phenyl)ethyl]-imidazole-[2-ylidine]-[gold(I)]$^{+}$[dichloride-gold(I)]$^{-}$ (**AuL7**). i) $(CH_3)_2AuSCl$, DMF, 56% yield.*

N-[4-(hydroxymethyl)phenyl]-*N'*-[(2-hydroxy-2-phenyl)ethyl]-imidazolium bromide (**L8**) was prepared in tetrahydrofuran by reaction of imidazole and 1,2-epoxyethylbenzene to obtain, after the opening of epoxy-ring, the monoalkylated product. Arylation of the second nitrogen atom was performed using 4-bromo-benzylalchol to produce the racemic mixture of the salts **L8** (Scheme 11) and characterized by ^{1}H- and ^{13}C-NMR spectroscopy, mass spectrometry and elemental analysis (38% yield).

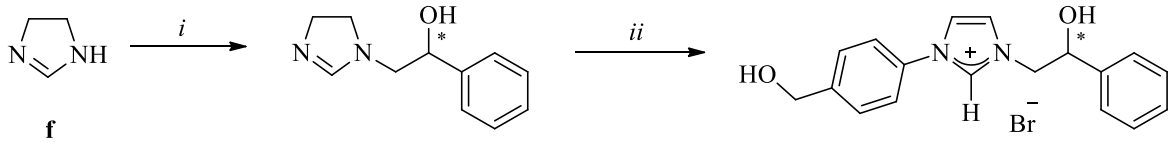

f **g** **L8**

Scheme 11: *Synthesis of N-[4-(hydroxymethyl)phenyl]-N'-[(2-hydroxy-2-phenyl)ethyl]-imidazolium bromide (**L8**). i) styrene oxide, THF, 60 °C; ii) 4-bromo-benzylalchol, THF, reflux 24h, 38% yield.*

As before, the salt **L8** was reacted in CH_2Cl_2 with silver oxide in nitrogen atmosphere and in the presence of molecular sieves. In these conditions [115], the silver oxide deprotonates carbon-2 giving the corresponding Ag–NHC complex (**AgL8**) (Scheme 12).

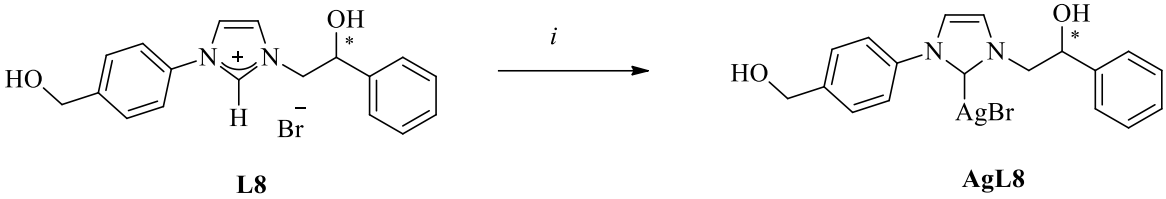

L8 **AgL8**

Schema 12: *Synthesis of N-[4-(hydroxymethyl)phenyl]-N'-[(2-hydroxy-2-phenyl)ethyl]-imidazole-[2-ylidene]silver(I)bromide (**AgL8**). i) Ag_2O, CH_2Cl_2, rt, 1h, 50% yield.*

The gold complex **AuL8** was obtained by *trans*-metallation from the corresponding silver complex (Scheme 13).

Thus, the silver complex **AgL8** was reacted with chloro-(dimethylsulfide)-gold(I) [$(CH_3)_2SAuCl$] in dichloromethane to give **AuL8** in 15% yield. The obtained solid was characterized by ^{1}H-NMR and ^{13}C-NMR, mass spectrometry and elemental analysis.

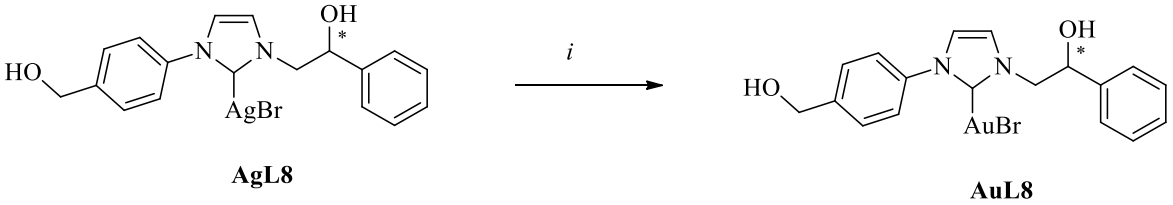

AgL8 **AuL8**

Scheme 13: *Synthesis of N-[4-(hydroxymethyl)phenyl]-N'-[(2-hydroxy-2-phenyl)ethyl]-imidazole-[2-ylidine]-gold(I)bromide* (***AuL8**). i) $(CH_3)_2AuSCl$, CH_2Cl_2, rt, 1h, 15% yield.*

2.2.2.2 Biology

The antitumor activity of these complexes was evaluated on two breast carcinoma lines, MCF-7 and MDA-MB-231, and on two uterine carcinoma lines (HeLa and Ishikawa). The obtained results (Table 7) established an interesting anti-tumor activity of the compound **AuL6** (IC_{50} = 2.10 ±0.7 μM), in particular on the highly aggressive and metastatic MDA-MB-231 cell line. The silver complex containing the **L6** ligand (**AgL6**) also exhibited a good anti-tumor activity, mostly toward the uterine cell lines (IC_{50} values= 9.76±0.6 and 6.55±0.9 μM on HeLa and ISHIKAWA, respectively). Silver and gold complexes containing the **L7** and **L8** ligands possessed no one or a lesser anti-tumor activity if compared with complexes

of **L6** series and also with *Cis*platin (**II**), used as reference molecule. Moreover, all the new synthesized complexes were found to be not cytotoxic on the proliferation of normal cell lines MCF-10A (see Table 7), if compared with *Cis*platin (**II**).

	IC_{50} (μM)				
	MCF-7	**MDA-MB-231**	**HeLa**	**ISHIKAWA**	**MCF-10A**
L6	>200	>200	>200	>200	>200
AgL6	10.5±0.8	3.2±1.2	9.8±0.6	6.6±0.9	>200
AuL6	5.2±0.4	2.1±0.7	31.9±0.5	29.9±0.9	>200
L7	>200	>200	>200	>200	>200
AgL7	29.7±0.3	57.9±0.5	47.7±0.4	26.7±0.5	143.4±0.8
AuL7	9.38±0.2	53.7±0.7	98.6±1.2	12.6±0.3	158.8±1.0
L8	>200	>200	>200	>200	>200
AgL8	>200	>200	>200	>200	>200
AuL8	18.2±0.5	31.7±0.8	44.5±0.9	54.9±1.0	>200
***Cis*platin (II)**	35.8±1.3	28.7±1.0	15.7±1.1	15.1±0.8	81.3±1.2

Table 7. *IC_{50} values of Au and Ag complexes and Cisplatin (**II**), expressed in micromolar (μM).*

Considering the promising effect of **AuL6** on the breast cancer proliferation, we have deepened its molecular mechanism. Nowadays, there is a general agreement that compounds able to interact simultaneously with different targets might be more active than single target agents. Because of the involvement of more signaling pathway in cancer development, a single targeted therapy might not be efficient to block tumor progression. Single target agents could also lead to the onset of frequent resistance phenomena and dramatic side effect. Thus, the discovering of new anticancer agents able to overcome these limitations is urgently needed. In this context, topoisomerases and microtubules represent important anticancer targets and the combination of inhibitors of both targets should enhance the final therapeutic outcome [134-136].

DNA topoisomerases are essential for DNA replication because of their ability to cause temporary DNA strand breakage in order to remove the supercoiled DNA. Anticancer agents targeting both isoform of Topoisomerases are widely used in cancer fighting [137]. Microtubules have also a crucial role in a large number of cellular functions and, for this

reason, their damage lead to perturbation of tubulin polymerization and of the function of the spindle apparatus, triggering apoptosis in cancer cells [138].

In order to assess the capability of **AuL6** to inhibit both forms of DNA topoisomerases, we performed an *in vitro* assay for topoisomerase I activity based on relaxation of supercoiled DNA and an assay for topoisomerase II based on the decatenation of double-stranded DNA. A principal function of topoisomerase I is the relaxation of supercoiled DNA. In this assay we exploited the different electrophoretic mobility on agarose gel of supercoiled and relaxed DNA in order to establish the ability of our compound to inhibit the activity of this enzyme. The total inhibition of the hTopo I supercoil relaxing activity in the presence of compound **AuL6** at the concentration of 1 μM was evidenced by a clear band of not-relaxed plasmid pHOT1 DNA in the bottom of the gel (Figure 40, lane 3). The only use of the vehicle DMSO did not exhibit any noticeable inhibition on the DNA topo I activity, under the identical experimental conditions (Figure 40, lane 2). It is possible to observe the presence of more band corresponding to the relaxed plasmid DNA. Figure 40, lane 1 shows the plasmid pHOT1 DNA, used as marker.

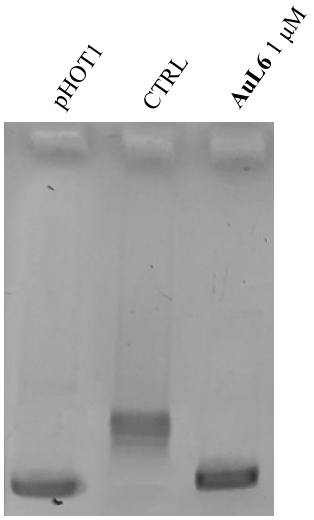

Figure 40. *hTopoI assay.* ***Supercoiled DNA was incubated without or with human topo I in the absence or presence of the test compounds at 1 μM: lane 1, plasmid pHOT1, lane 2, vehicle (DMSO), lane 3, AuL6 1 μM.***

Topoisomerase II possesses the ability to catalyze the decatenation of a double-stranded DNA. Thus, in this assay, interlocked kinetoplast DNA (kDNA) was used as

substrate and decatenated and linear kDNA (Figure 41, lane 1 and 2) were used as markers. Compound **AuL6**, already at the concentration of 1 μM, totally inhibited the hTopo II activity. It is possible to notice the presence of a remarkable band in the upper of the gel corresponding to the catenated circles of kDNA, which is unable to enter on agarose gel (Figure 41, lane 4). In the control reaction (with DMSO only) two band related to the decatenation products were detected (Figure 41, lane 3).

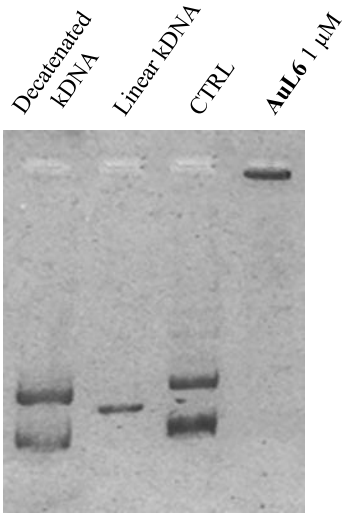

Figure 41. *hTopo II inhibition assay. kDNA was incubated with human Topoisomerase II in the absence (lane 3, vehicle DMSO) or in presence of compound **AuL6** at 1 μM (lane 4). Lane 1 and 2, decatenated and linear kinetoplast DNA (kDNA), respectively.*

At the end, we performed an *in vitro* tubulin-polymerization inhibition assay to assess whether the complex **AuL6** could be inhibitor of the tubulin polymerization.

In this assay, the tubulin polymerization through turbidity variation at 350 nm was measured, using a vehicle (DMSO) control, compound **AuL6** and two well-known microtubules targeting agents, Paclitaxel (**III**) and Vinblastine (**XIV**), as reference molecules, at the 10 μM concentration.

In the control experiment (vehicle, DMSO) tubulin heterodimers self-assemble, as indicated by the increase of the turbidity in a time-dependent manner (Figure 42). The microtubule-stabilizing agent Paclitaxel (**III**) caused a similar pattern but with a higher rate and amount of tubulin heterodimers assembly. Instead, the microtubule-destabilizing agent Vinblastine (**XIV**) was able to block strongly the tubulin polymerization, as indicated by the lower final turbidity value less than the half of the control reaction and by the reaching of the steady

state, only after a long time of about 40 minutes compared to 15 and 10 minutes, for control and Paclitaxel (**III**) respectively. Compound **AuL6** is also a valid tubulin polymerization inhibitor at 10 μM, influencing tubulin polymerization reaction as well, even if in a less rate compared to Vinblastine (**XIV**). However, when the curves reached the steady state the turbidity of tubulin is similar for Vinblastine (**XIV**) and **AuL6**.

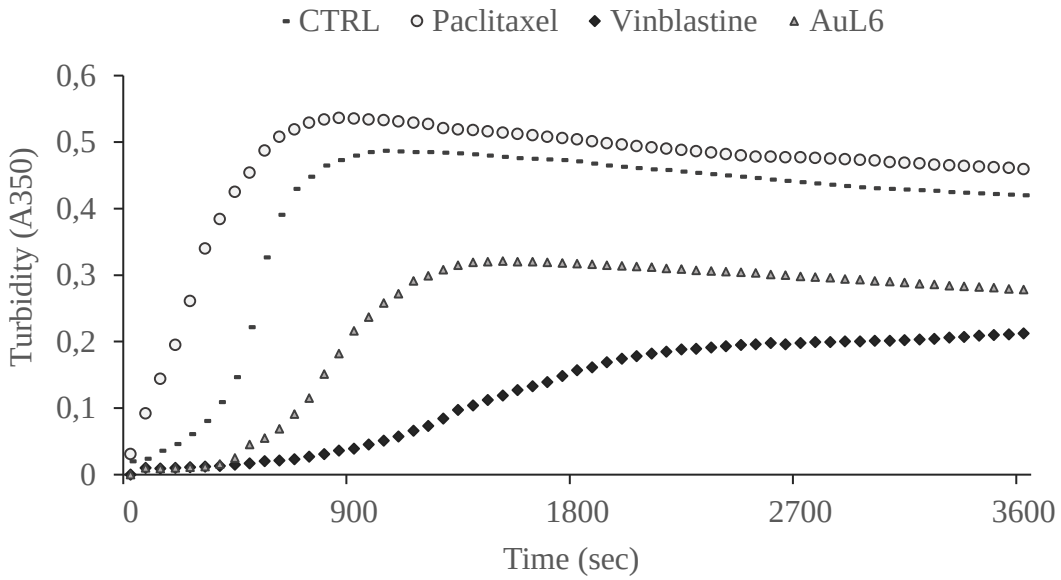

Figure 42. *Tubulin polymerization assay. The effect of compound **AuL6** on in vitro tubulin polymerization was evaluated. Two positive control molecules, Paclitaxel **(III)** and Vinblastine **(XIV)**, were used as tubulin-stabilizing and tubulin-destabilizing agents, respectively. DMSO was used as a negative control. Assembly of tubulin into microtubules was determined by measuring the turbidity at 350 nm for 3600 seconds at 37 °C. All the compounds were used at a concentration of 10 μM.*

In conclusion, the results obtained are very interesting considering that metal ions are exploited in many scientific fields thanks to their wide spectrum of reactivity. *Cis*platin (**II**) is one of the most-effective chemotherapeutic agents in clinical therapy, but its clinical use is limited because of severe dose-dependent side effects and the onset of inherent or acquired resistance [139]. In this context, the important results in terms of antiproliferative activity and of important targets involved, together with the absence of cytotoxic effects on different non-tumor cells, make our new complexes **AuL4** and **AuL6** very promising and valid candidates for the development of improved metal-based compounds and for further preclinical investigations.

2.3 NEW ALTERNATIVES TO TRADITIONAL CHEMOTHERAPY

2.3.1 Thalidomide (XV) analogues: old drug repurposing as new anticancer agent

Drug repurposing has become popular because discovering and bringing new drugs to the market takes too long and costs too much. An existing drug has already been approved by the Food and Drug Administration. Thus, repurposing and screening of new targets can reduce economic and practical research efforts.

In this context, Thalidomide (**XV**) was first used for alleviation of morning illness in pregnant women [140] and then withdrawn from the market because of its dramatic effects on fetal development [141]. Recently, interest in this old drug has been renovated, due to its effectiveness in several important pathologies, such as erythema nodosum leprosum [142], multiple myeloma [143], breast cancer [144], refractory Crohn's disease [145] and HIV-related diseases [146]. Its multiple mechanism of action interested many research groups to design new derivatives and to evaluate their biological properties, particularly in oncology.

Here, we studied the antitumor activity of several Thalidomide (**XV**) derivatives (Figure 43) in two breast cancer cell lines. These compounds possessed better activity than Thalidomide (**XV**), inducing TNFα-mediated apoptosis, without any cytotoxicity on non-tumoral cells. Some of these analogues interfere also with cancer cell migration, through the regulation of the expression of two important proteins involved in epithelial-mesenchymal transition (EMT), E-cadherin and vimentin.

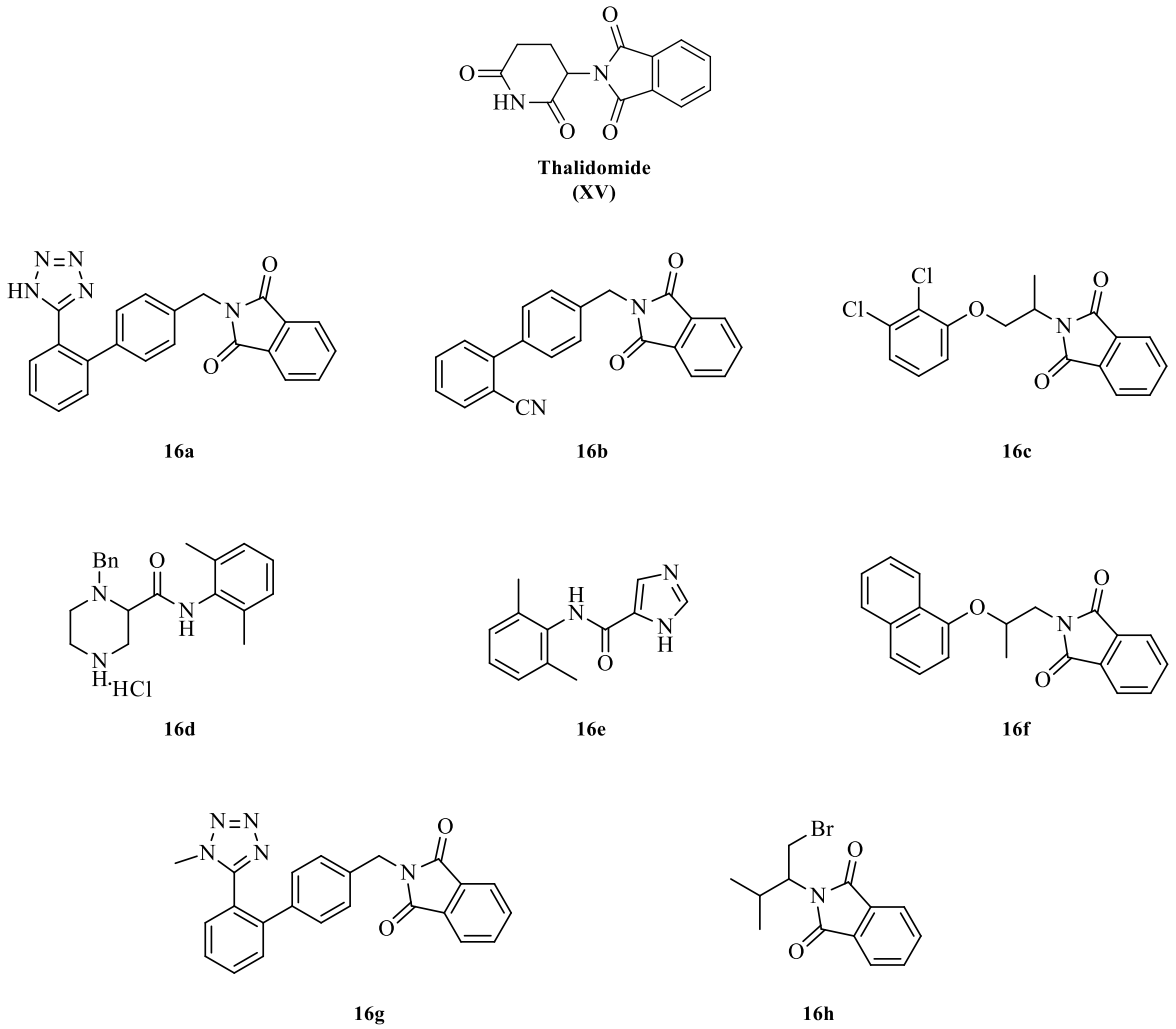

Figure 43. *Chemical structure of Thalidomide (**XV**) and its correlated compounds (**16a-h**)*

2.3.1.1 Chemistry

Compounds **16a** [147], **16b** [148], **16c** [149], **16f** [149] and **16g** [147] (Figure 43) were synthetized as reported. All the synthesis details were described in our work [150]. The chiral compounds (**16c**, **16d**, **16f**, **16h**) were prepared in their racemic forms.

Compound **16d** was obtained as shown in Scheme 14. The selective protection with Boc-group of piperazine-2-carboxylic acid (**i**) at the 4-position, and the further Cbz-group protection at the 1-position [151] permitted to obtain compound **l**. It was then treated with 2,6-dimethylaniline in the presence of 2-isobutoxy-1-isobutoxycarbonyl-1,2-diihydroquinoline (IIDQ) to give the corresponding carboxamide **m** [152]. Selective Cbz deprotection of **C** with triethylsilane and palladium chloride [153] produced **n**. It was reacted with benzyl bromide, obtaining the N-benzylderivative **o** [154]. Boc deprotection of **o** and

conversion of the resulting amine into the corresponding hydrochloride salt was performed with gaseous HCl as previously described [155].

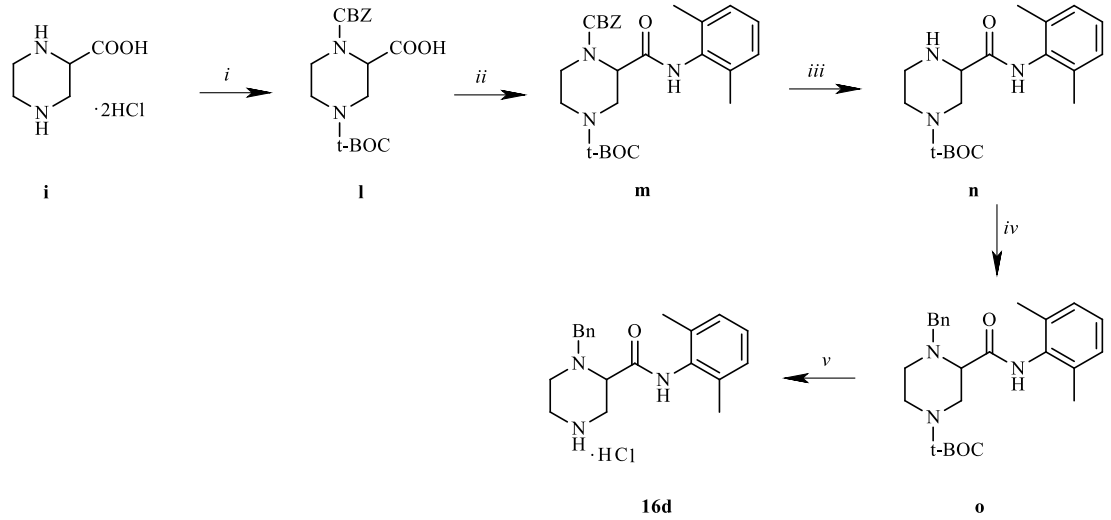

i **l** **m** **n** **16d** **o**

Scheme 14. *Synthesis of compound **16d**. Reagents and conditions: (i) Boc-ON, benzyl chloroformate, dioxane/water, rt, 24 h; (ii) 2,6-dimethylaniline, IIDQ, Et_3N, $CHCl_3$, reflux, 6 h, 25% yield; (iii) Et_3SiH, $PdCl_2$, Et_3N, CH_2Cl_2, reflux, 3 h, 79% yield; (iv) BnBr, K_2CO_3, dioxane/water, 70 °C, 45 min, 47% yield; (v) g. HCl, anhyd Et_2O, rt, 15 min, 67%.*

Compound **16e** was obtained through the reaction between methyl imidazole-4-carboxylate (**p**) and 2,6-dimethylaniline (Scheme 15), as already reported [156].

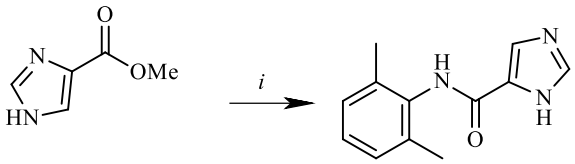

p **16e**

Scheme 15. *Synthesis of compound **16e**. Reagents and conditions: (i) 2,6-dimethylaniline, NaH, dry dioxane/dry DMF, reflux, 5 h, 53% yield.*

Compound **16h** was prepared as showed in Scheme 16. The protection of amino alcohol **q** with phthalic anhydride [157] gave the phthalimido alcohol **r**, which was converted into the corresponding bromo derivative **16h** by treatment with PBr_3.

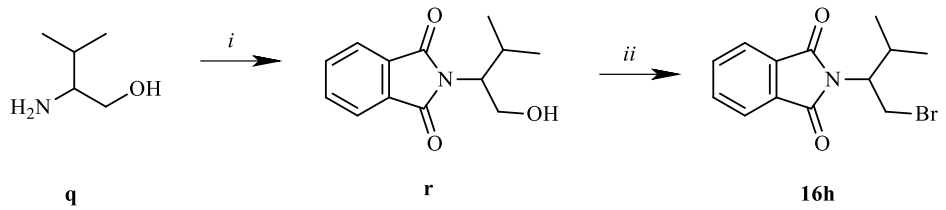

Scheme 16. *Synthesis of compound **16h**. Reagents and conditions: (i) phthalic anhydride, Et_3N, toluene, reflux, 3 h, 48% yield; (ii) PBr_3, 0°C, 2 h, then RT, 6 h, 66% yield.*

2.3.1.2 Biology

Thalidomide (**XV**) analogues were studied to test their antiproliferative effect towards two human breast cancer cell lines, namely estrogen receptor (ER)-positive (ER+) MCF-7 and triple-negative (ERα, PRα and HER-2/Neu unamplified) MDA-MB-231 cells [158], using MTT assay. Table 8, in which the IC_{50} values are reported, highlights a very interesting effect of all the synthetized compounds if compare with a low antitumor activity of Thalidomide (**XV**) (it exerted a weak activity only at a concentration higher than 300 μM). In particular, compound **16c** and **16h** possessed the best antitumor activity, with IC_{50} values of 47±1 and 40.3±0.8 μM toward MCF-7 cells and 56.5±1.3 and 37.2±1.0 μM toward MDA-MB-213 cells, respectively. The other derivatives also exhibited good antiproliferative effects, but they were a bit less powerful than **16c** and **16h** (Table 8). We also demonstrated that our compounds did not produce toxic effects on the viability of normal breast epithelial cells MCF-10A, at least at a concentration of 500 μM.

	IC_{50} (μM)		
	MCF-7	**MDA-MB-231**	**MCF-10A**
Thalidomide (XV)	360±2.2 μM	413±1.8 μM	>500 μM
16a	293,8±1.0 μM	>500	>500 μM
16b	99.59±1.2 μM	165.5±1.8 μM	>500 μM
16c	47.07±0.98 μM	56.48±1.3 μM	>500 μM
16d	204.8±0.68 μM	119.3±1.8 μM	>500 μM
16e	>500 μM	>500 μM	>500 μM
16f	302.6±2.1 μM	151.9±1.6 μM	>500 μM
16g	57.29±2.2 μM	80.89±2.2 μM	>500 μM
16h	40.28±0.8 μM	37.16±1.0 μM	>500 μM

Table 8. *IC_{50} values of Thalidomide (**XV**) and its analogues (**16a-h**), expressed in micromolar (μM).*

The promising antitumor effects of our compounds pushed us to explore the biological mechanism of the most active Thalidomide (**XV**) derivatives.

Literature data report that Thalidomide (**XV**) is able to interfere with the expression of TNFα mRNA [159], triggering the mitochondrial apoptotic pathway. Thus, the capability of compound **16c** and **16h** to modulate TNFα cell levels was evaluated by immunofluorescence analysis. MCF-7 cells were treated for 24 h with these Thalidomide (**XV**) analogues at concentrations corresponding to their respective IC_{50} values. Cells were then subjected to immunofluorescence assays with an anti-TNFα antibody. **16c** and **16h** were able to increase three- and two-fold TNFα expression, respectively, when compared to control cells (treated with the only vehicle) (Figure 44).

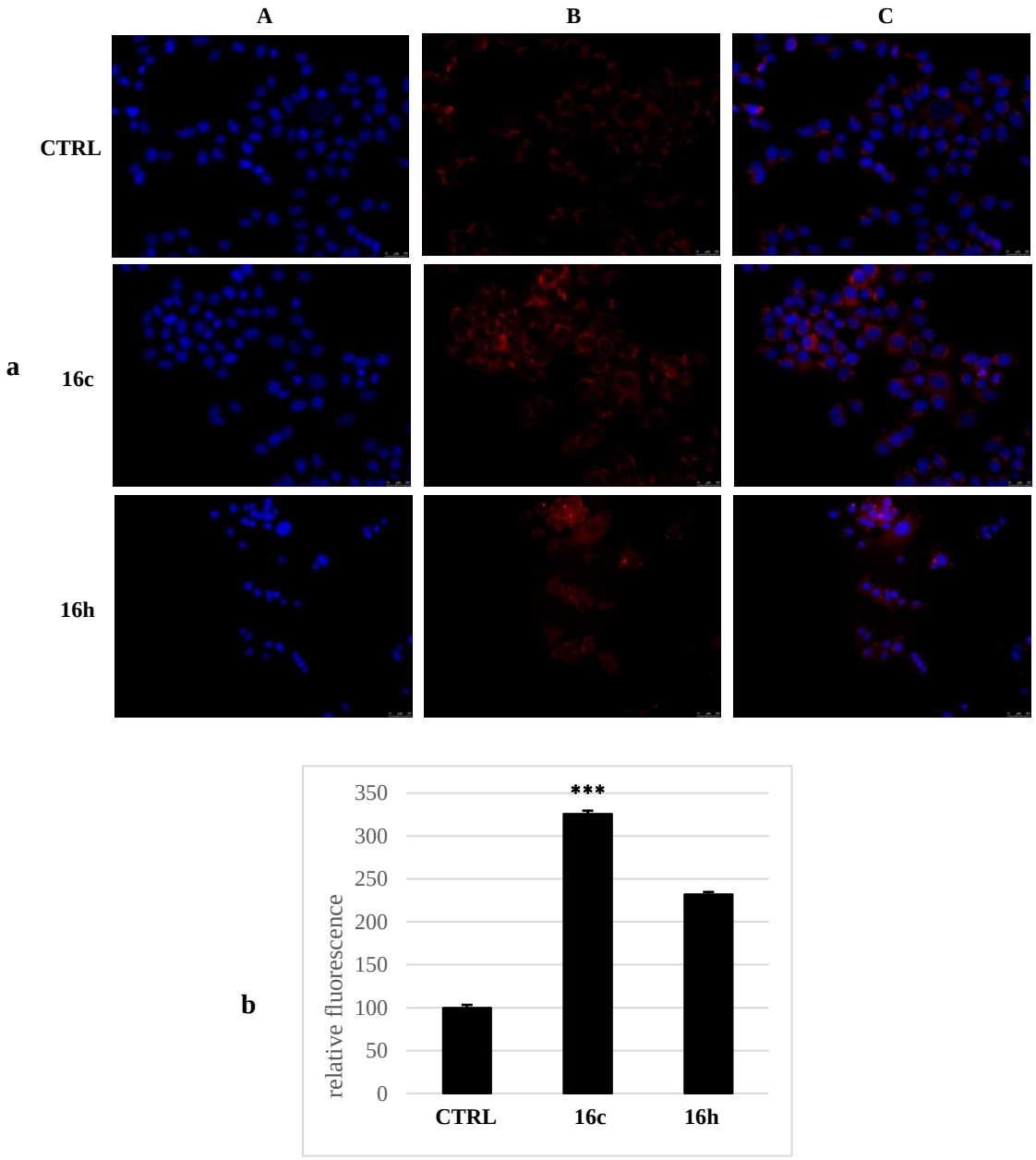

Figure 44. *Immunofluorescence analysis of TNFα levels in MCF-7 cells. Cells were treated for 24 h with compounds* ***16c*** *and* ***16h*** *or vehicle (CTRL), then processed as described in Experimental section. Images were acquired at 20X magnification. Panel A: DAPI; Panel B: Alexa Fluor 568; Panel C: Overlay. Images are representative of three separate experiments. Fluorescence quantification was shown. *** P<0.001*

The triggering of the mitochondrial apoptotic pathway leads to increased mitochondrial permeability with consequent release in the cytosol of cytochrome c, a small protein that may act as apoptogenic factor, located in the internal membrane of intact mitochondria [160]. Thus, in order to determinate the localization of cytochrome c in MCF-7 cells treated with compound **16c** or **16h**, we used an immunofluorescence assay with an anti-cytochrome c antibody (Figure 45). The obtained results clearly demonstrated the presence of an increased and diffused red fluorescence in cells treated with our compounds, indicating the release of cytochrome c in the cytosol (Figure 45). In the vehicle-treated cells the fluorescence associated with this protein is still placed in the mitochondrial network.

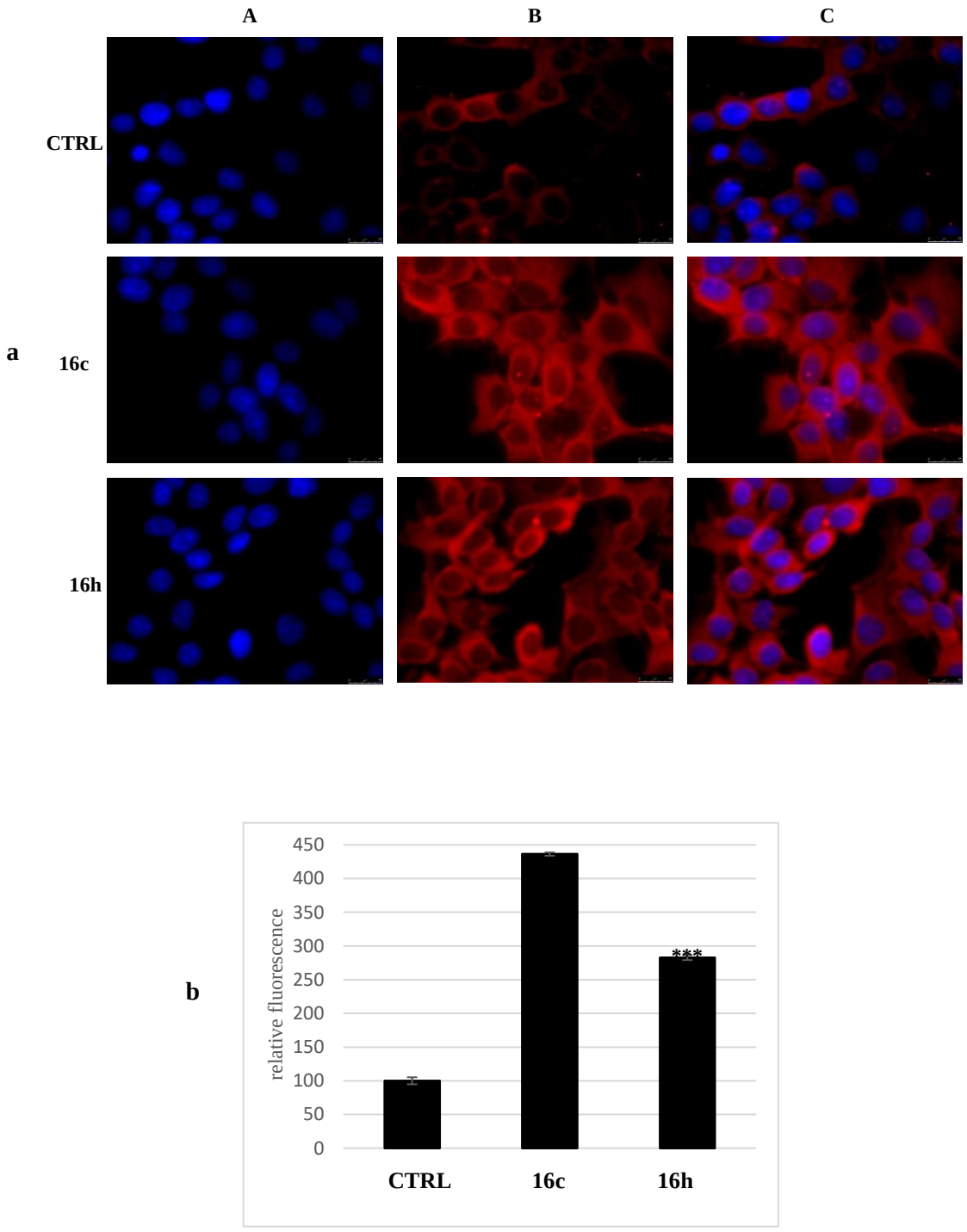

Figure 45. *Immunofluorescence analysis of cytochrome c. MCF-7 cells were treated for 24 h with compounds **16c** or **16h**, or with vehicle (CTRL). Images were acquired at 63X magnification. Panel A: DAPI; Panel B: Alexa Fluor 568; Panel C: Overlay. Images are representative of three separate experiments. Fluorescence quantification was shown. *** P<0.001*

With the aim to verify if compound **16c** and **16h** were able to induce programmed cell death, a TUNEL assay was carried out using MCF-7 cells. The green fluorescence in the cell nuclei, present in the cells treated with both compounds and absent in the veichle-treated cells, confirmed the DNA fragmentation correlated with the apoptotic process (Figure 46).

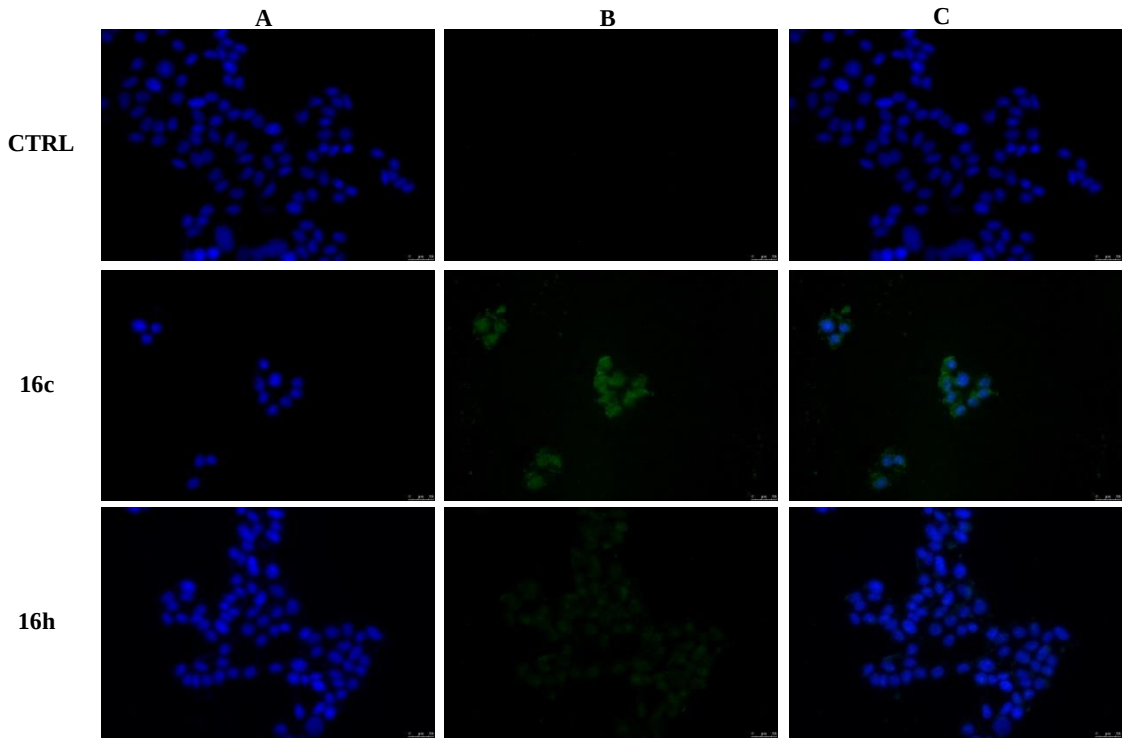

Figure 46. *Apoptosis detection by TUNEL assay on MCF-7 breast cancer cells. Cells were treated for 24 h with compounds **16c** and **16h**, then cold methanol fixed and subjected to TUNEL procedure. Then, cells have been washed, dyed with DAPI and observed and imaged under an inverted fluorescence microscope (20x magnification). Panels A: CF™488A; Panels B: DAPI; Panels C: Overlay. Representative fields were shown.*

Considering the importance of the metastatization in carcinogenesis, we evaluated the effect of our molecules on it, using a simple, low-cost and well-developed *in vitro* method: the wound-healing assay. The experiment was performed causing a scratch (wound) on a cells monolayer of breast cancer cells (both types). Then cells were treated with compounds **16a-16h** at concentrations corresponding to their respective IC_{50} values (Table 8) for 48 and 72 h, for MDA-MB-231 and MCF-7 cells, respectively. These different endpoint times are related to the higher growth rate and capability to give metastases of MDA-MB-231 compared to MCF-7 cells [52]. In both breast cancer cell lines, compound **16b** demonstrated the best ability in cell migration inhibition (Figures 47 and 48) with

respect to the other active compounds, even if it possesses a lower antiproliferative activity (see Table 8). Compounds **16c**, **16g** and **16h** resulted also capable to prevent the MCF-7 and MDA-MB-231 wound closure with good percentages (Figures 47 A and B, respectively). In addition, compound **16f** exerted an impressive effect in preventing wound closure only in MDA-MB-231 (Figure 47B). The other compounds had no significant effects in such experiments. Considering the promising results in terms of antiproliferative activity (see Table 8) and cell migration inhibition (see Figures 47 and 48), we have choose compounds **16c** and **16h** in order to deepen their biological properties.

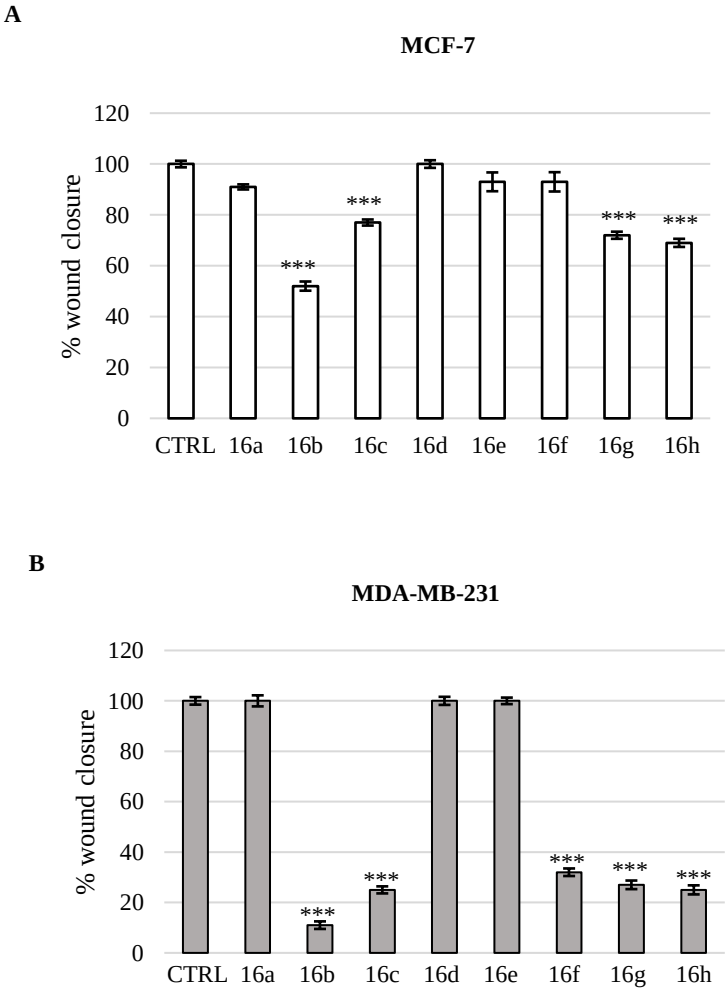

Figure 47. *Wound-healing assay conducted on A) MCF-7 and B) MDA-MB-231 cells treated with compounds **16a-h**. Wound closure was monitored by recording the area of the cell-free wound at 0 and 72 h for MCF-7 and at 0 and 48 h for MDA-MB-231, by the use of an inverted microscope. The wound-healing effect was estimated as the percentage of wound closure calculated as reported in the Experimental Section. Vehicle-treated (CTRL) cells were used as a control; ***p<0.001.*

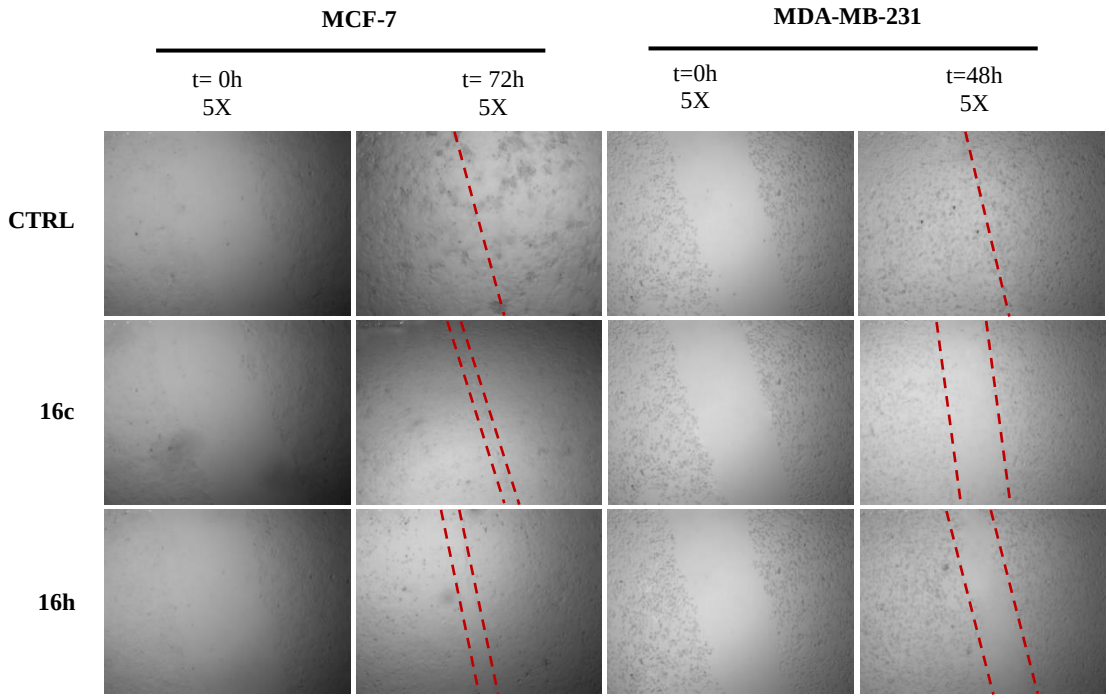

Figure 48. *Wound-healing assay conducted on A) MCF-7 and B) MDA-MB-231 cells plated on six-well plates and treated with compounds **16c** or **16h** and vehicle (CTRL). Wound closure was monitored at 0 and 72 h for MCF-7 and at 0 and 48 h for MDA-MB-231, by the use of an inverted microscope (5X magnification). Dotted red lines define the areas that lack cells.*

Several proteins are involved in the cell migration, including those that mediate cell adhesion and some cytoskeletal proteins, such as E-cadherin and vimentin. The first one is a transmembrane protein whose expression changes in the transition from epithelial to mesenchymal cells (ETM) and a decrease in its expression is implicated in the metastatic process. Vimentin is a mesenchymal marker that increases during ETM [161]. With this in mind, their expression levels after exposure of MCF-7 cells to compounds **16c** and **16h**, were evaluated using the immunofluorescence analysis. The obtained results showed a decrease in vimentin expression (Figure 49) and at the same time a significant increase of expression, together with a localization at the level of the cytoplasmic membrane and in the cell-cell contact regions, of E-cadherin (Figure 50). These outcomes indicate that the tumor cells remain more adherent to each other, decreasing the ability to give rise to micrometastases.

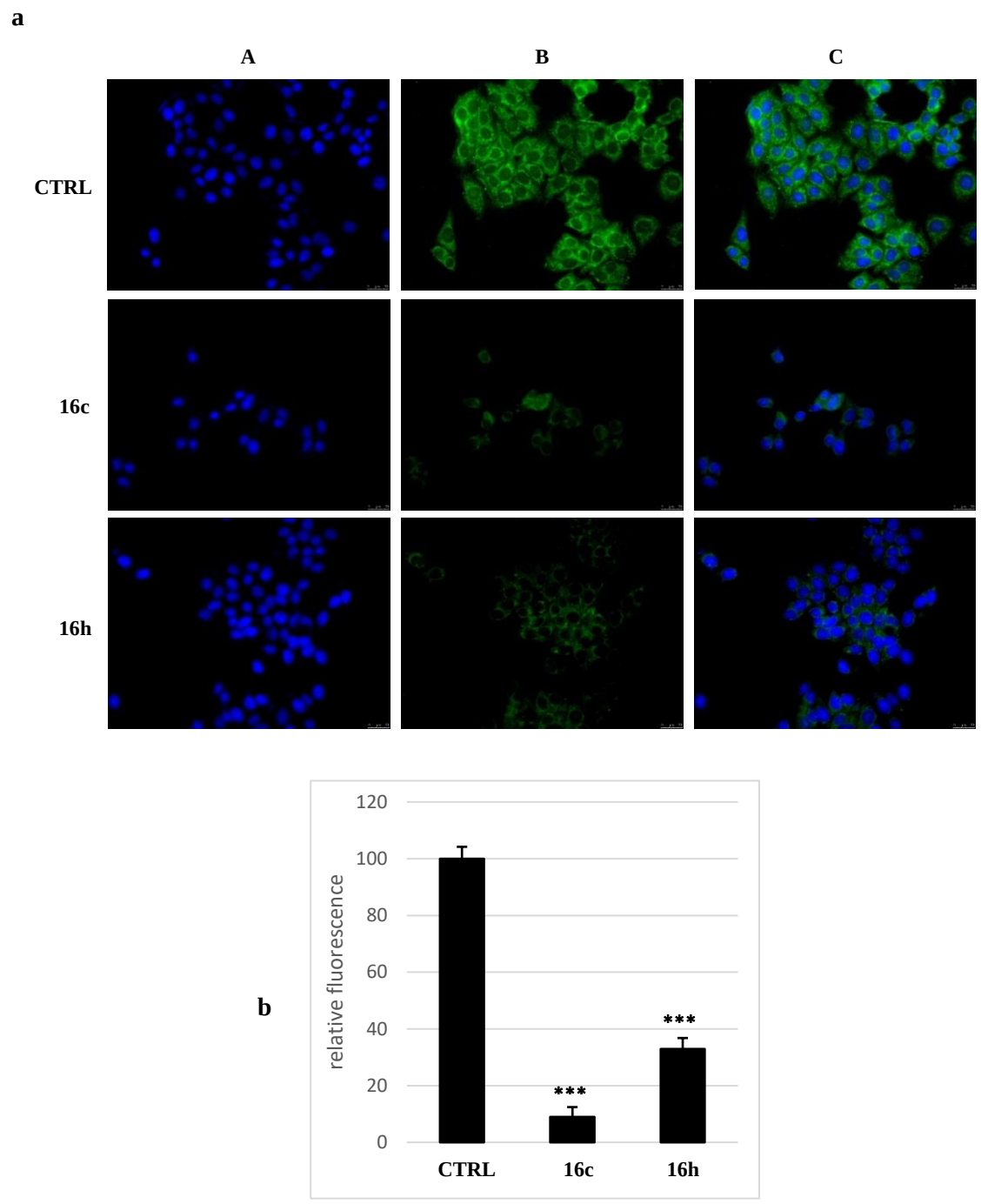

Figure 49. *Immunofluorescence analysis of vimentin. a) MCF-7 cells were treated for 24 h with compounds **16c**, **16h**, or vehicle (Ctrl). Images were acquired at 20x magnification. A) DAPI, B) Alexa Fluor® 488, C) overlay; images are representative of three separate experiments. b) Fluorescence quantification, ***p<0.001.*

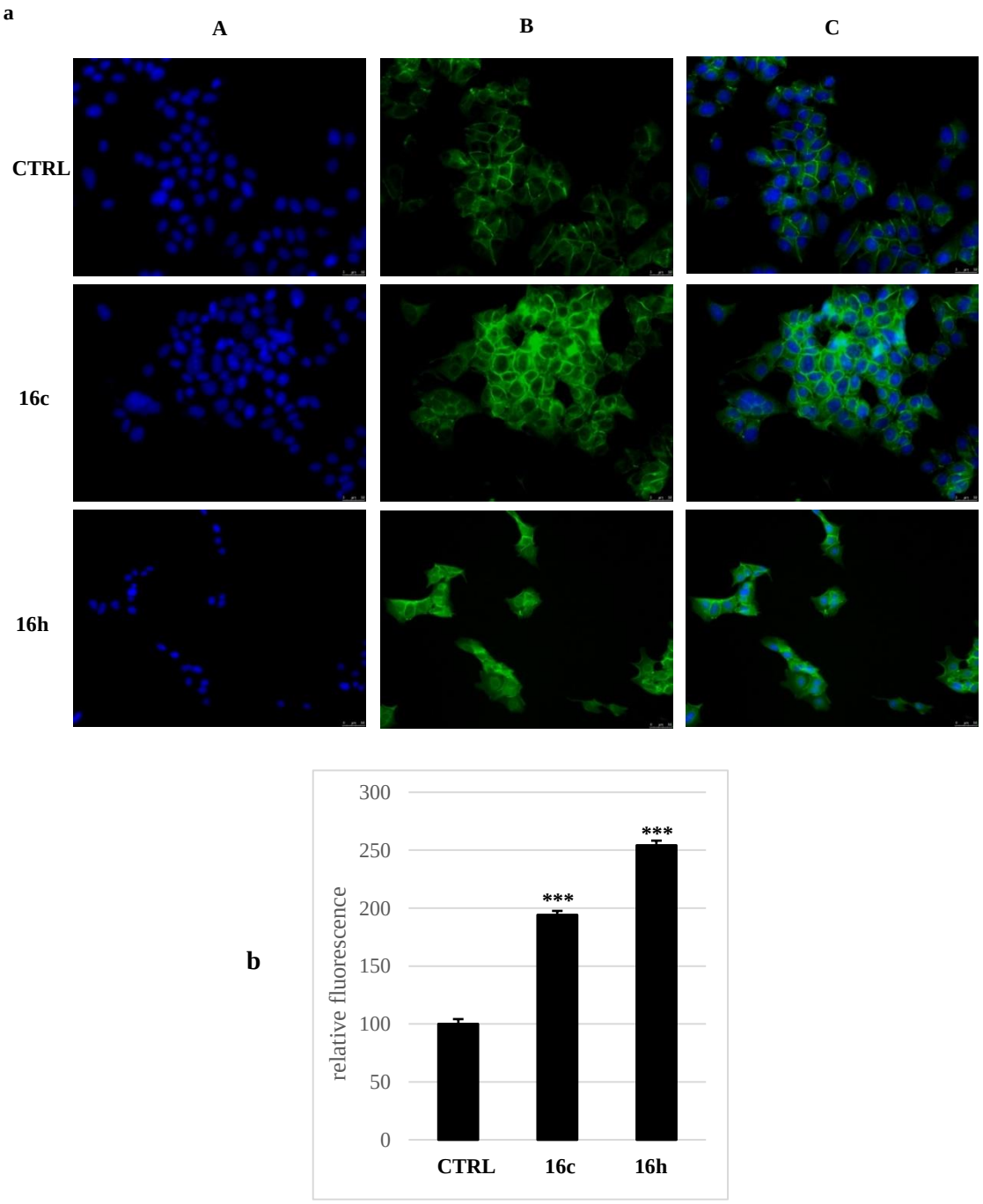

Figure 50. *Immunofluorescence analysis of E-cadherin. a) MCF-7 cells were treated for 24 h with compounds **16c**, **16h**, or vehicle (Ctrl). Images were acquired at 20X magnification. A) DAPI, B) Alexa Fluor® 488, C) overlay; images are representative of three separate experiments. b) Fluorescence quantification, ***p<0.001.*

Considering the important role played by the angiogenic process in the development of tumours, we evaluated the expression in MCF-7 cells of vascular endothelial growth factor (VEGF), a pro-angiogenic cytokine that mediates the formation of new blood vessels, thus promoting tumour growth [162]. The cells treated with compound **16c** and **16h** showed lower expression levels of VEGF than the cells treated with the vehicle (DMSO) (Figure 51), indicating interference with VEGF biosynthesis. The cells exposed to compound **16h** also exhibited an evident change in subcellular localization of VEGF, which is evidently no longer localized in the perinuclear area, as in the vehicle-treated cells, but was also diffused in the nuclei (Figure 51A, white arrows). This difference could indicate a decreased biosynthesis at the endoplasmic reticulum network and an interaction with nuclear receptors.

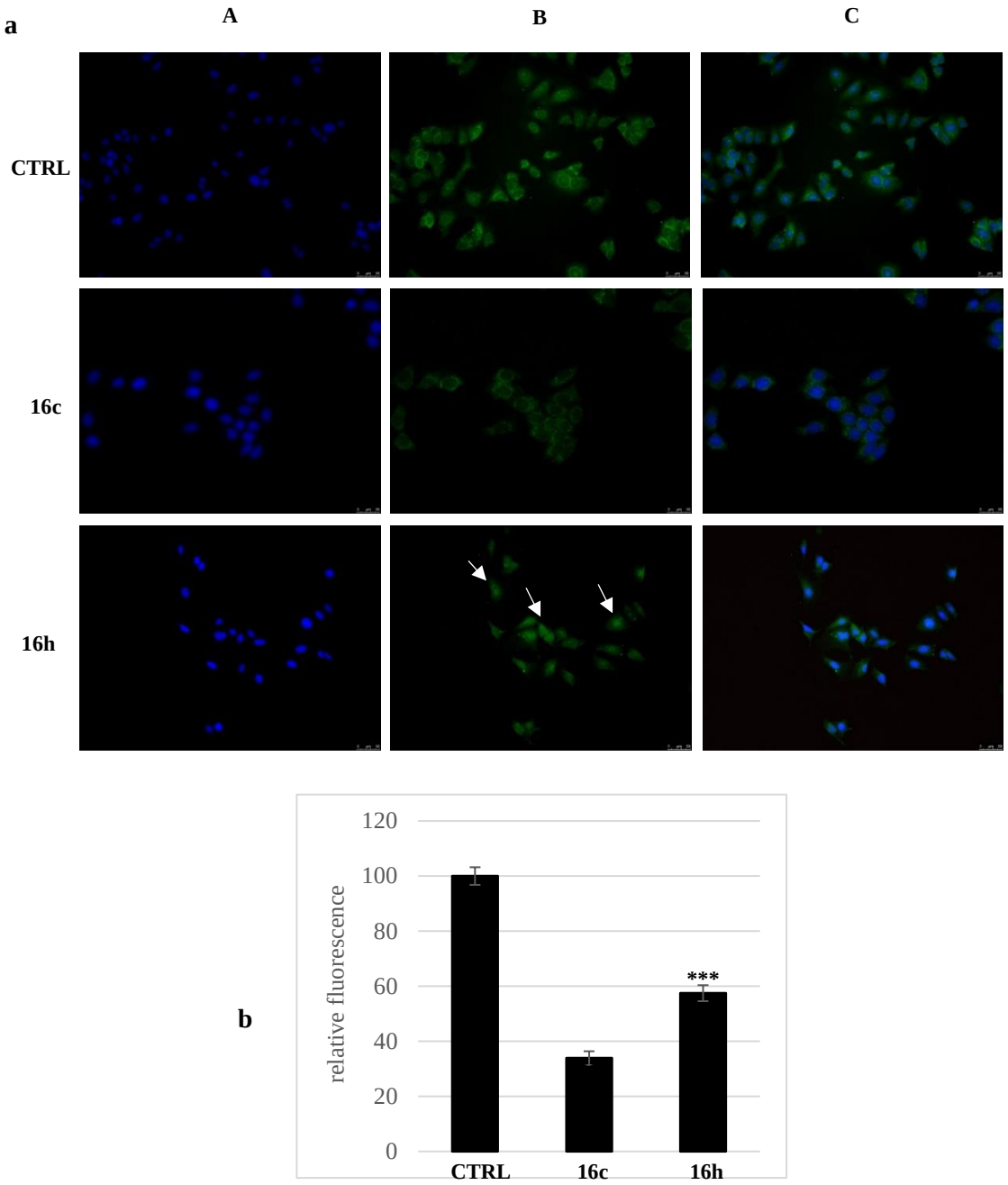

Figure 51. *Immunofluorescence analysis of VEGF.* ***a)*** *MCF-7 cells were treated for 24 h with compounds* ***16c***, ***16h***, *or vehicle (CTRL). White arrows indicate the different subcellular localization of VEGF in MCF-7 cells treated with compound* ***16h***, *with respect to the vehicle-treated cells. Images were acquired at 20X magnification. A) DAPI, B) Alexa Fluor® 488, C) overlay; images are representative of three separate experiments.* ***b)*** *Fluorescence quantification, ***p<0.001.*

2.3.2 Structural modifications of natural compounds: Quercetin (XVI) derivatives as new anticancer agents

Traditional chemotherapy is responsible of high systemic toxicity and for this reason its therapeutic use is often limited. Currently natural-based alternatives with less toxicity have become more important. Among the natural compounds, Quercetin (**XVI**) shows very limited toxicity on healthy cells; but despite this, its therapeutic use is limited due to its low water solubility, its instability in physiological systems and its reduced bioavailability (only 30-50% of ingested Quercetin (**XVI**) is absorbed and this amount is then reduced, metabolized by the intestine and liver) [163].

In order to overcome these limitations, we studied the anticancer profile of a small library of Quercetin (**XVI**) analogs in which the hydrophilic hydroxyl groups have been replaced, totally or partially, with different hydrophobic groups easily removable in *in vivo* conditions (acetyl, ethyl or benzyl ethers, or diphenyl ketal of the catechol system) (Figure 52).

These chemical structurally substitutions permitted to obtain compounds with improved anticancer activity, with respect to Quercetin (**XVI**). In addition, using *in silico* and *in vitro* assays, we demonstrated that our derivatives were able to inhibit human Topoisomerases I and II and the capability of lead compounds **17a** and **17d** to interfere with ROS productions.

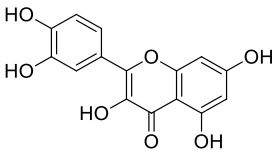

Quercetin (**XVI**)

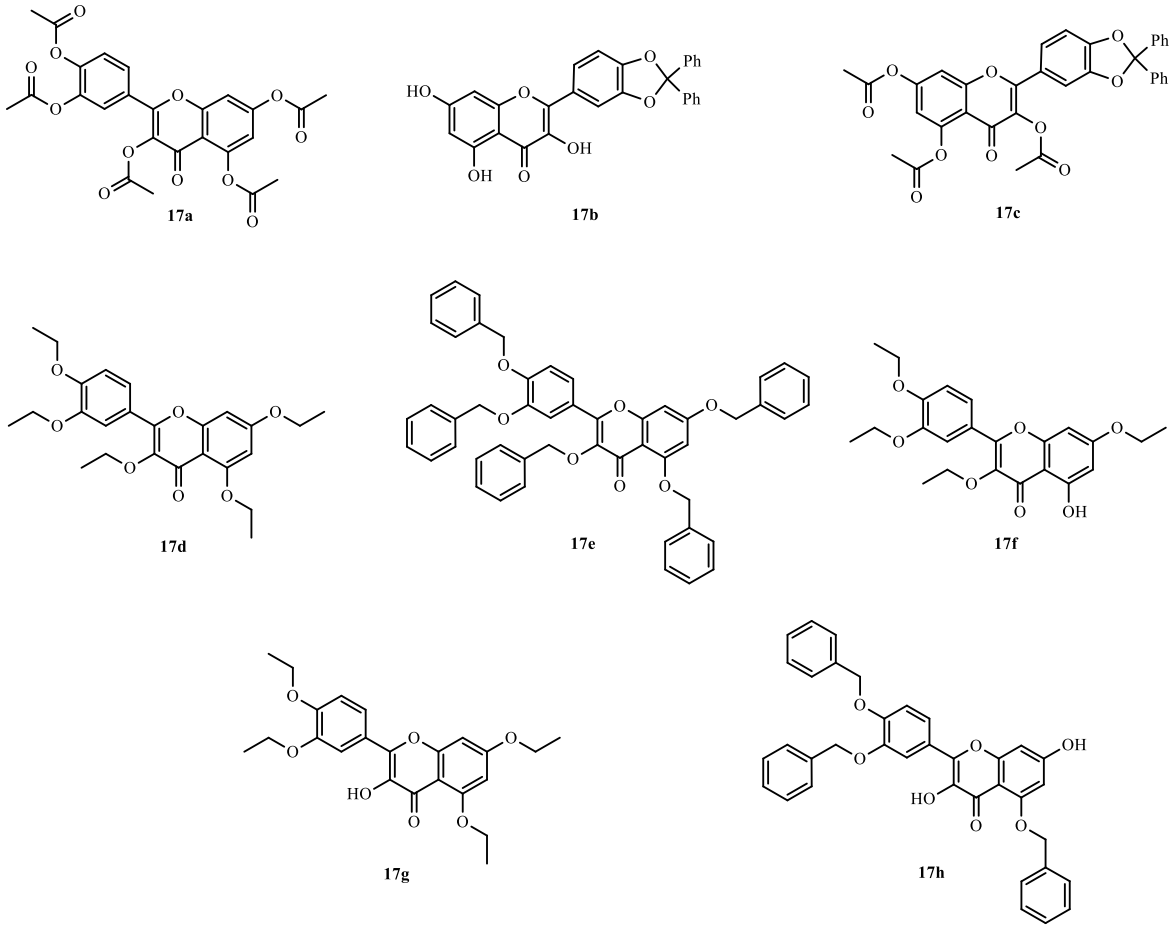

Figure 52. *Chemical structure of **Quercetin (XVI)** and its derivatives (**17a-h**).*

2.3.2.1 Chemistry

A small series of Quercetin (**XVI**) derivatives (**17a**–**h**) has been prepared with the aim to improve its pharmacokinetic profile, using chemical procedures already described. In particular, compounds **17a**–**e** have been obtained following the procedures previously reported [164-168], while **17f** and **17g** have been recovered during purification procedures of **17d** and, equally, **17h** has been isolated from **17e** purification [169].

2.3.2.2 Biology

The antiproliferative activity of all Quercetin (**XVI**) derivatives was evaluated towards two breast cancer cell lines (ER-α positive MCF-7 cells and triple negative MDA-MB-231 cells) by using MTT assay.

The resulting cell viability percentage enabled us to calculate the IC_{50} values for each derivative, showed in Table 9. Quercetin (**XVI**) and its analogs exhibited a remarkable anticancer activity, particularly in the highly metastatic and invasive triple negative MDA-MB-231 cells. The most active compounds on both breast cancer cell lines resulted **17b** and **17c**, maybe because of the presence of the bulky cyclic ketal, but they possessed also a high cytotoxicity toward non-tumoral cells used in this assay (MCF-10A and HEK-293). For this reason, they have not been used for additional examination.

Compound **17a** and **17d** also exerted a good antitumor activity toward both tumor cell lines without any toxic effect on healthy cells (MCF-10A and HEK-293).

The other derivatives, **17e-17h**, exhibited a minimal or neither effect on MCF-7 cells viability, although they conserved an evident antitumor activity in MDA-MB-231 cells, probably related to the higher metabolic and cell division rate possessed by MDA-MB-231 cells. Similarly, we evaluated the cytotoxic activity of these compounds toward the normal counterpart and they showed little (in the case of **17g**) or no effect, at least at concentrations amounting to 200 μM. In conclusion, compound **17a** and **17d** resulted the derivatives with the best anticancer effect against both the breast cancer cell lines without affecting the viability of the healthy cells.

	IC_{50}			
	MCF-7	**MDA-MB-231**	**MCF-10A**	**HEK-293**
Quercetin (XVI)	137±0.9	40.3±0.9	>200	>200
17a	14.6±0.6	10.9±0.9	>200	>200
17b	9.2±0.7	7.6±0.8	41.4±0.9	4.2±0.3
17c	10.3±0.3	0.8±0.2	27.6±0.4	0.6±0.7
17d	41.9±0.6	16.6±0.4	>200	>200
17e	>200	50.0±1.0	>200	>200
17f	>200	75.9±0.8	>200	>200
17g	157.8±0.3	19.6±0.4	174.7±0.5	164.5±0.3
17h	>200	>200	>200	>200

Table 9. *IC_{50} values of **Quercetin (XVI)** and its analogues (**17a-h**), expressed in micromolar (μM).*

Quercetin (**XVI**) is able to induce DNA damages through different pathways, such as DNA intercalation, DNA metabolizing enzymes inhibition and radical oxygen species regulation. Considering these literature data, we analyzed the ability of Quercetin (**XVI**) derivatives to regulate two important DNA metabolizing enzyme, human Topoisomerases I and II. These nuclear enzymes play a fundamental role in the supercoiling and in the replication of DNA, introducing some temporarily break in the single or double strand of DNA. Thus, their inhibitors are considered promising lead in antitumor therapy [170].

We carried out an *in vitro* inhibition assay using the human Topoisomerase I (hTopo I), Quercetin (**XVI**) and its derivatives at a concentration amounting to 25 μM.

Figure 53 shows that Quercetin (**XVI**) and its analogues **17a**-**17d** caused the inhibition of hTopo I activity, as evidenced by the band at the bottom of the gel, representing the uncleaved plasmid pHOT1 used as hTopo I substrate. It should be underlined that compounds **17d** and **17b** induced a partial inhibition of this enzyme: in fact, in addition to the uncleaved form, it is possible to appreciate the presence of some light bands related to the cleaved forms of the plasmid. Contrarily, derivatives **17e**-**h** did not exert any activity on hTopo I, as demonstrate by multiple bands due to plasmidic DNA cleavage at the bottom of the gel. The same profile was recovered in the control (CTRL) lane, where enzyme was exposed only to vehicle (DMSO).

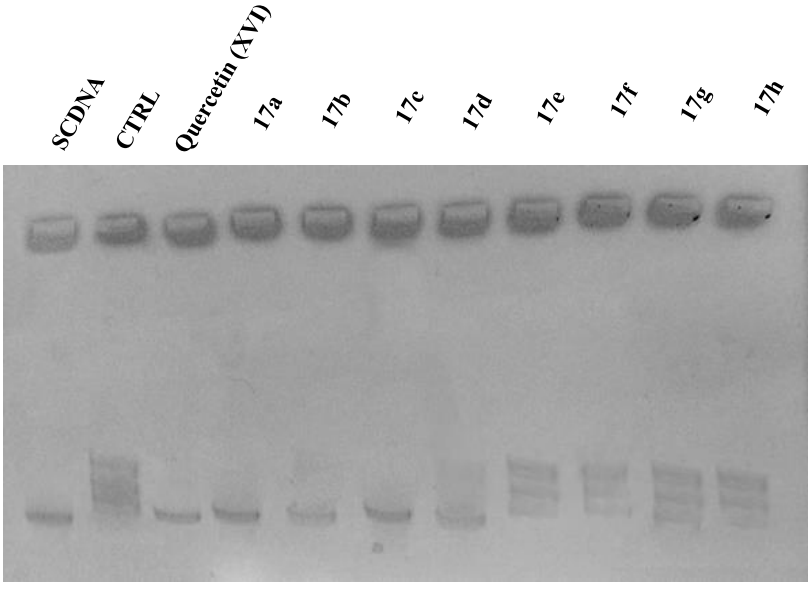

Figure 53. *hTopo I relaxation assay. hTopo I has been incubated in the absence (CTRL) or presence of the compounds to test (25 μm) for 1 h at 37◦C, then the activity of hTopo I has been estimated and visualized on agarose gel.* ***Quercetin*** (**XVI**) *and* ***17a-h****, assayed compounds. The image is representative of three separated experiments. CTRL: Control (DMSO); SCDNA: Supercoiled DNA.*

We also evaluated the inhibitory effect of Quercetin (**XVI**) and its derivatives (used at 25 μM) against human Topoisomerase II (hTopoII). The obtained results reported in Figure 54, suggested a total inhibition of hTopo II by compounds **17a** and **17d** due to the presence of a band in the top of the gel corresponding to the catenated DNA (kDNA). Instead, Quercetin (**XVI**) and compound **17b** and **17c** seem able to induce a partial inhibition of hTopo II. These compounds caused the formation of two bands at the bottom of the gel (decatenation products of kDNA) and also a single band at the top of the gel (catenated DNA). At the end, a decatenated DNA bands are visible at the bottom of the gel for compounds **17e-h** and for the control reaction, indicating a total absence of inhibitory activity toward hTopo II.

Table 10 reports a schematic summary related to the inhibitory activity of Quercetin (**XVI**) and its analogs on hTopo I and II.

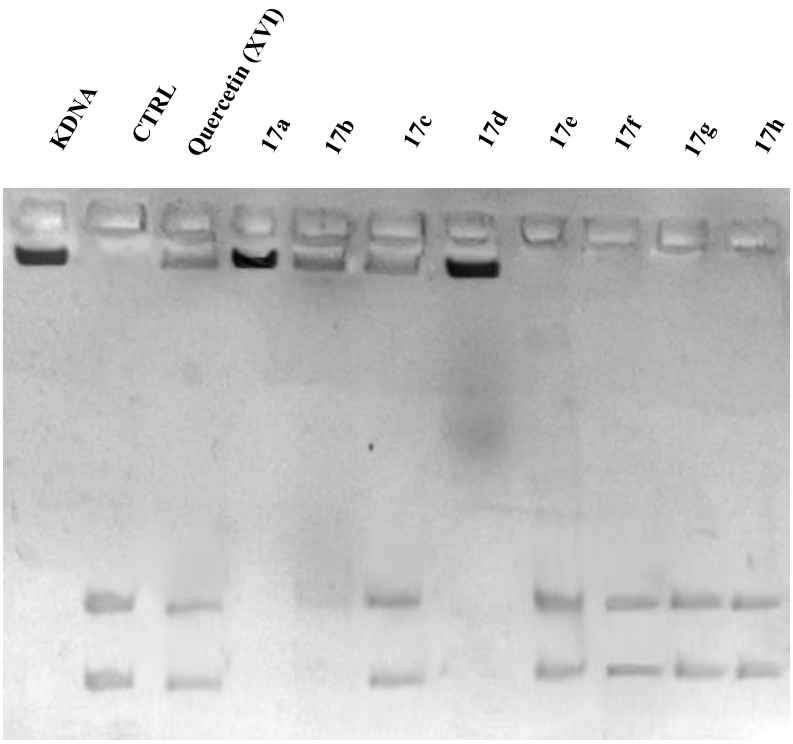

Figure 54. *hTopo II decatenation assay. hTopo II has been incubated in absence (control) or presence of the compounds to test (25 μm) for 1 h at 37◦C. The activity of hTopo II has been evaluated by loading the reaction products, after purification, on agarose gel.* ***Quercetin (XVI)*** *and* ***17a-h****, assayed compounds. The image is representative of three separated experiments. CTRL: Control (DMSO); KDNA: Kinetoplast DNA.*

	hTopo I	*hTopo II*
Quercetin (XVI)	+++	+
17a	+++	+++
17b	++	++
17c	+++	+
17d	+	+++
17e	-	-
17f	-	-
17g	-	-
17h	-	-

Table 10. *Inhibitory activity of **Quercetin (XVI)** and its analogs (**17a-h**) on hTopo I and II. The increasing number of + indicates an increased inhibition, determined by gel bands observation and quantification using Image J software.+: Indicates the inhibitory effect; −: The absence of inhibition.*

The inhibition of both isoform of the human Topoisomerases could cause DNA damage and cell death by apoptosis [171]. With this in mind, a TUNEL assay on MDA-MB-231 cells treated with the most active compounds **17a** and **17d** was carried out, in order to establish if they were able to induce apoptosis. Figure 55 shows a green nuclear fluorescence appreciable only in MDA-MB-231 cells exposed to our compounds (Figure 55, **17a** and **17d**, panel B) and not in the control cells (Figure 55, CTRL, panel B,). These outcomes indicate that our derivatives caused DNA fragmentation in MDA-MB-31 cells, leading to apoptosis.

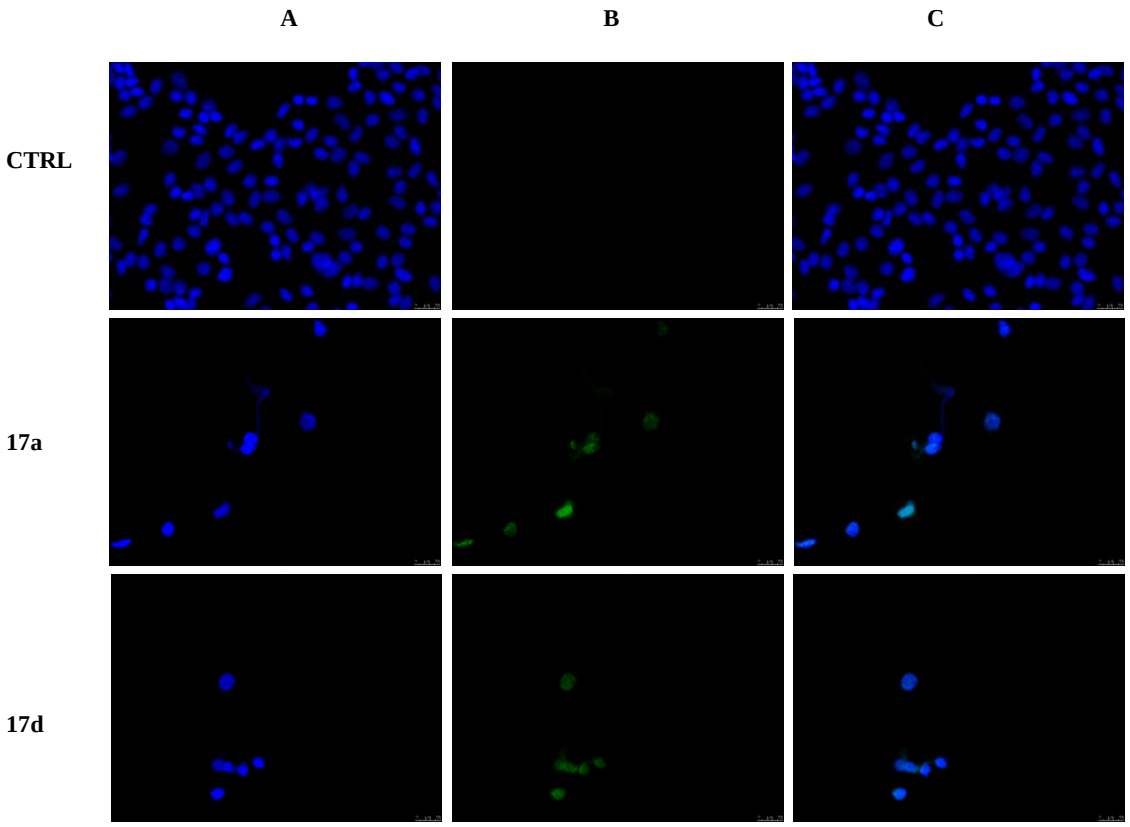

Figure 55. *TUNEL assay. MDA-MB-231 cells were treated with compounds **17a** and **17d** or with vehicle (CTRL) for 24 h. After treatment, cells were methanol fixed and subjected to TdT reaction. Then, cells were washed, dyed with DAPI and observed and imaged under an inverted fluorescence microscope (20× magnification). The green fluorescence indicate nuclei of cells undergoing apoptosis. Panel A: DAPI (CTRL, **17a** and **17d**) excitation/emission wavelength 350 nm/460 nm. Panel B: CF™488A (CTRL, **17a** and **17d**) excitation/emission wavelength 490 nm/515. Panel C (CTRL, **17a** and **17d**) show the overlay channel.*

New research fields highlight the double valence of the induction of oxidative stress in cancer cells, in association with the consequent increased metabolic activity and ROS production. In fact, ROS production seems to play an important role in maintaining cancer phenotype due to their stimulating effects on cell growth and proliferation [172]. At the same time, increased ROS levels in cancer cells are often considered as an adverse factor, because several studies reported that they cause cytotoxicity, oxidative mitochondrial damage and massive cell death [123]. Thus, we studied the ability of our Quercetin (**XVI**) analogues, **17a** and **17d**, to interfere with intracellular ROS production using a fluorescence assays, in a breast cancer model (MDA-MB-231 cell lines). We exposed these cells with each compound for 24 h; then cells were incubated with DCF-DA and examined under an inverted

fluorescence microscope. Figure 56 shows the presence of a green fluorescence produced by the intracellular oxidation of DCFH-DA in cells treated with compounds **17a** and **17d**. Quercetin (**XVI**) was also able to induce ROS production, even though in a lower manner. These effects, together with the ability of **17a** and **17d** to inhibit both isoform of human Topoisomerases, caused the triggering of the programmed cell death.

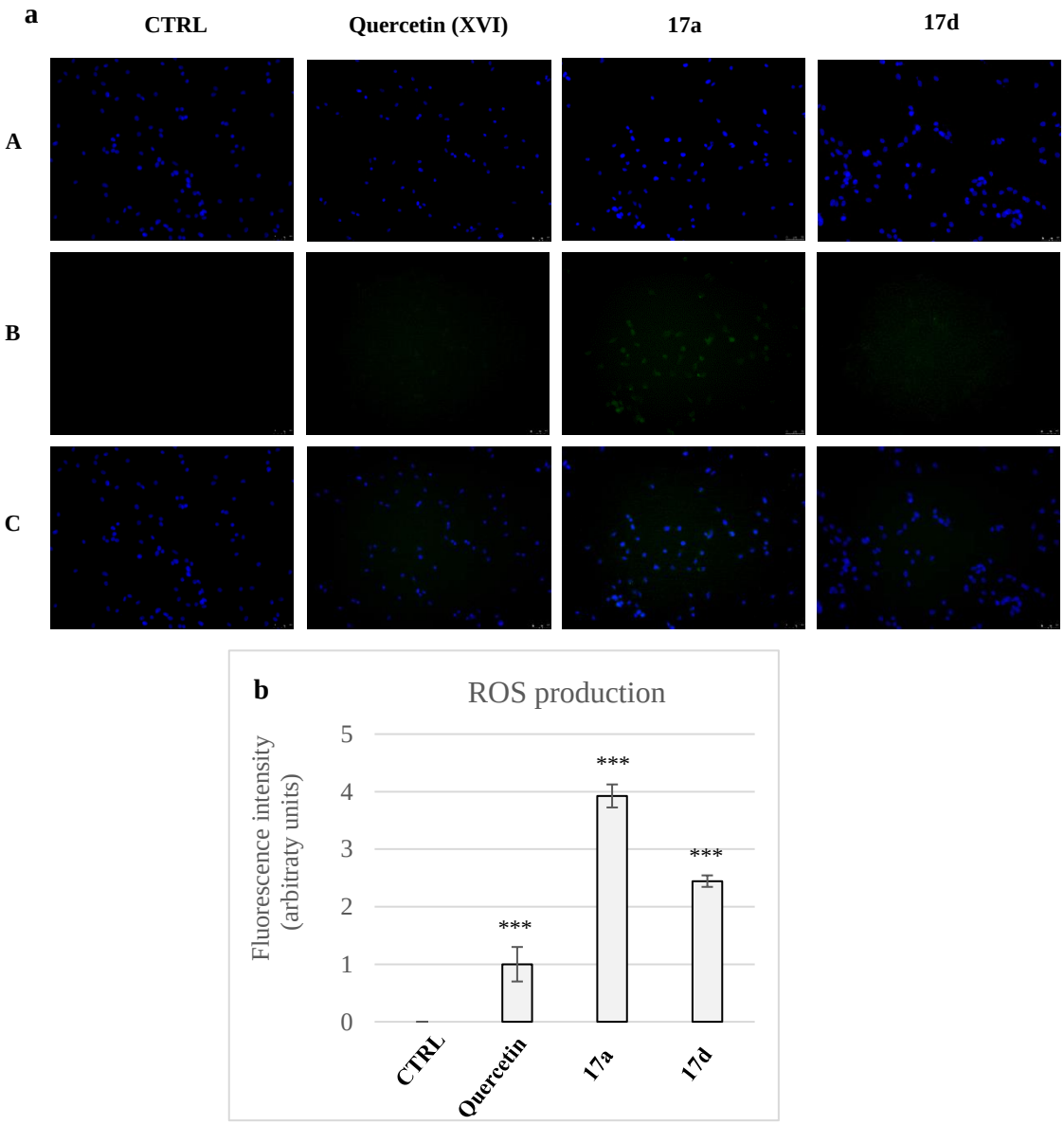

Figure 56. *ROS production evaluation.* ***(a)*** *Evaluation of ROS production, using DCF-DA (CF™488A), in MDA-MB-231 treated with* ***Quercetin (XVI)***, ***17a*** *and* ***17d*** *or vehicle. Images were acquired at 20x magnification. White arrows indicate examples of cells with increased ROS production (green fluorescence). Panel A: DAPI (CTRL,* ***Quercetin (XVI)***, ***17a*** *and* ***17d****) excitation/emission wavelength 350 nm/460 nm. Panel B: CF™488A (CTRL,* ***Quercetin (XVI)***, ***17a*** *and* ***17d****) 490 nm/515 nm. Panel C (CTRL,* ***Quercetin (XVI)***, ***17a*** *and* ***17d****) show the overlay channel.* ***(b)*** *Fluorescence quantification; ***p < 0.001,* ***17a*** *and* ***17d*** *versus* ***Quercetin (XVI)****.*

The interesting ability of Quercetin (**XVI**) to protect from oxidative stress is well-know. Considering this property and the lack of any cytotoxic effect toward non-tumoral cells of compound **17a** and **17d**, we evaluated their capability to interfere with ROS production in non-tumoral human embryonal kidney HEK-293 cells, carrying out ROS scavenging assays. After a pre-treatment of 24 h with our compounds (Quercetin (**XVI**), **17a** and **17d**), we exposed cells to menadione (Men), used as ROS inducer. Figure 57 shows that the pre-treatment with our compounds caused, in a different manner, a reduction of the green fluorescence, related to ROS intracellular levels with respect to HEK-293 cells treated only with Men. In particular, the data relative to the fluorescence quantification demonstrate that Quercetin (**XVI**) and compound **17a** exhibited a similar scavenger activity; compound **17d** showed a lesser, but still significant, effect (Figure 57b).

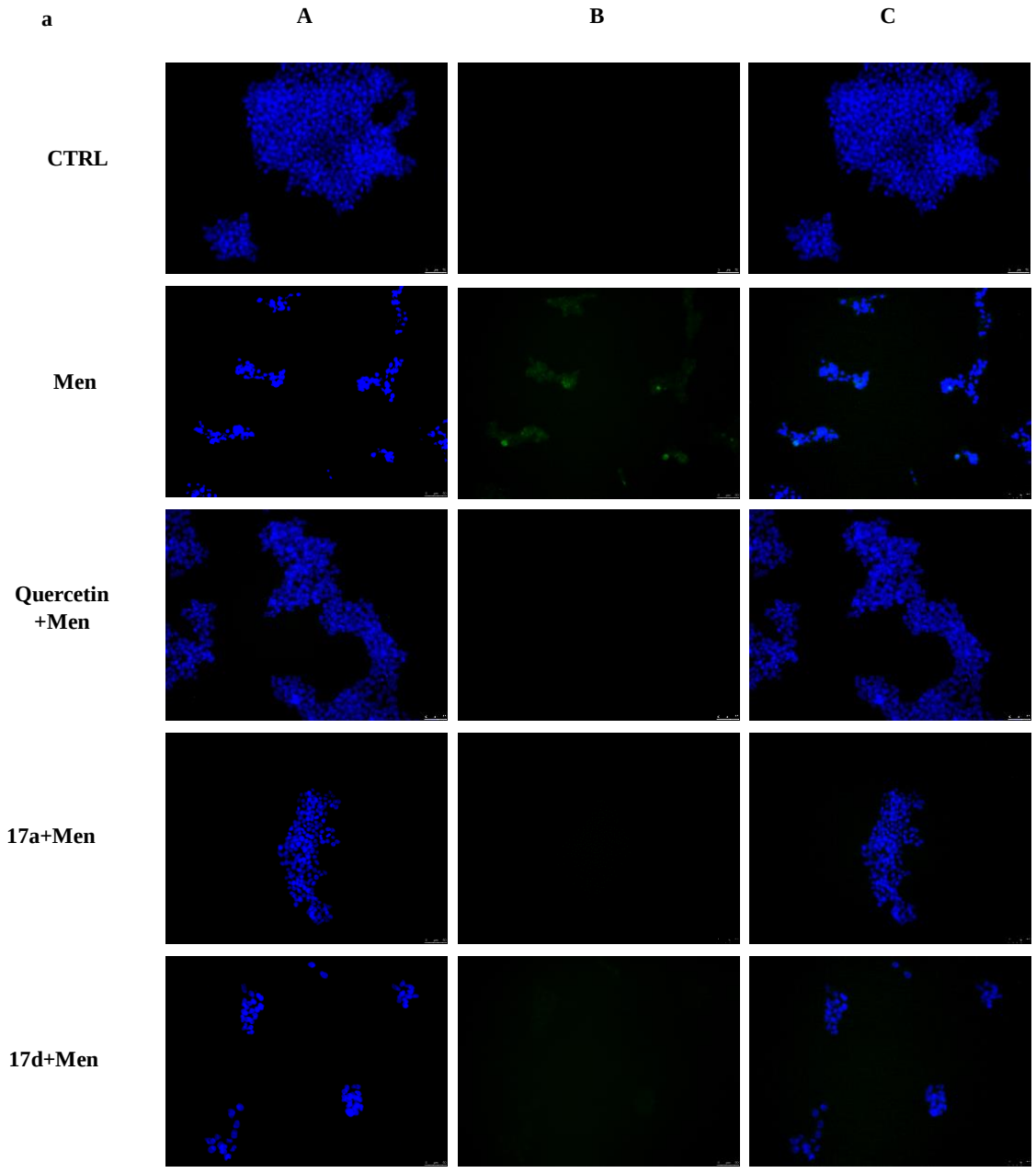
a
A
B
C
CTRL
Men
Quercetin
+Men
17a+Men
17d+Men

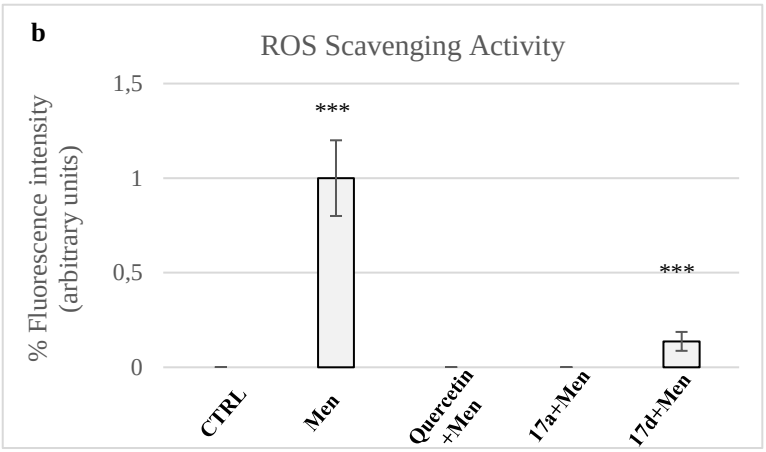
b
ROS Scavenging Activity
% Fluorescence intensity
(arbitrary units)
1,5
1
0,5
0
***
***
CTRL
Men
Quercetin
+Men
17a+Men
17d+Men

Figure 57. *ROS scavenging activity.* ***(a)*** *Evaluation of ROS scavenging activity using DCF-DA (CF^{TM}488A), in HEK-293 treated with* ***Quercetin (XVI)***, ***17a***, ***17d*** *and* ***Men*** *(used as positive control). Images were acquired at 20× magnification. White arrows indicate examples of cells producing ROS (green fluorescence). Panel A: DAPI (CTRL,* ***Men***, ***Quercetin (XVI)*** *+* ***Men***, ***17a*** *+* ***Men*** *and* ***17d*** *+* ***Men****) excitation/emission wavelength 350 nm/460 nm. Panel B: CF^{TM}488A (CTRL,* ***Men***, ***Quercetin (XVI)*** *+* ***Men***, ***17a*** *+* ***Men*** *and* ***17d*** *+* ***Men****) excitation/emission wavelength 490 nm/515 nm. Panel C (CTRL,* ***Men***, ***Quercetin (XVI)*** *+* ***Men***, ***17a*** *+* ***Men*** *and* ***17d*** *+* ***Men****) show the overlay channel.* ***(b)*** *Fluorescence quantification; *** $p < 0.001$,* ***Quercetin (XVI)*** *+* ***Men***, ***17a*** *+* ***Men*** *and* ***17d*** *+* ***Men*** *versus* ***Men****.* ***Men:*** *Menadione; ROS: Reactive oxygen species.*

2.3.2.3 Docking studies

With the aim to study the binding modes and the affinities between Quercetin (**XVI**) derivatives and both hTopo I and hTopo II, we carried out *in silico* molecular docking simulations. The fitness scores of compounds **17a**-**17d** were reported in Table 11.

Figure 58 (Panels A–F) explains the binding modes of selected ligands on the targets. Ligands binding with both hTopo I and II happens in a region in which normally DNA is located [173]. Therefore, all the ligands binding modes may interfere with the regular activity of both the proteins, even if with a different affinity.

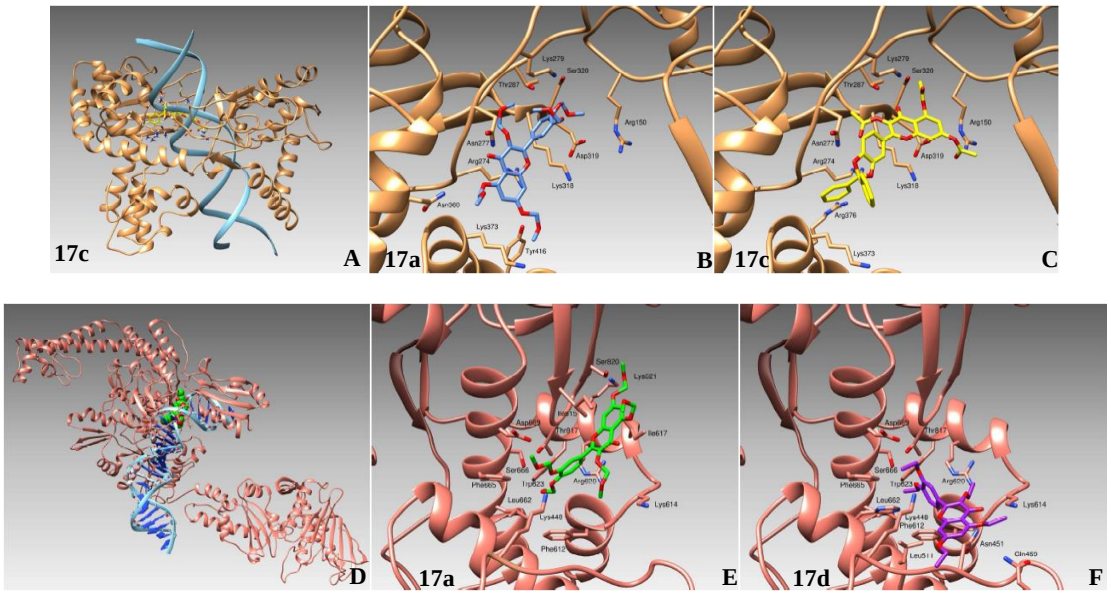

Figure 58. *Docking studies: binding mode of selected ligands to hTopo I (sandy ribbons, panel A) and hTopo II (pink ribbons, panel B).* ***(A)*** *Binding mode of* ***17c*** *(yellow) to hTopo I. The position of a DNA filament is reported in cyan.* ***(B)*** *Binding mode of* ***17a*** *(blue sticks).* ***(C)*** *Insight on the binding mode of* ***17c*** *to hTopo I.* ***(D)*** *Representation of the crystallographic structure of hTopo II (pink ribbons) bound to a DNA fragment (cyan ribbons). The position of* ***17a*** *binding mode is evidenced by green spheres.* ***(E)*** *Details of* ***17a*** *binding mode to hTopo II.* ***(F)*** *Binding mode of* ***17d*** *to hTopo II (cont.).*

Compound name	Fitness score on hTopo I	Fitness score on hTopo II
Quercetin (XVI)	66.63	47.14
17a	70.46	63.85
17b	62.18	57.08
17c	74.07	55.16
17d	60.14	60.23

Tabella 11. *Gold Fitness for the ligands tested.*

Chapter 3: Development of new formulations for anticancer drug delivery

Considering that the development of new drugs is expensive and takes long time and that too much old drugs show some limitations (low solubility, low bioavailability, instability, etc), the improvement of their safety and efficacy through the design of drug delivery systems has become a very attractive and smart alternative, mostly in oncology [174].

We focused the attention on the preparation and the biological evaluation of appropriate vehicles for the development of new formulations. For this purpose, innovative pharmaceutical matrices were used to obtain molecules with improved pharmaceutical profile, thanks to the adjustment of physical-chemical and pharmacokinetic/pharmacodynamics drugs properties, such as solubility, chemical and / or metabolic stability, bioavailability, release, etc. This strategy shows a significantly higher benefit/risk ratio when compared to the development of a new drug.

3.1 MOLECULARLY IMPRINTED HYDROGELS FOR THE CONTROLLED DELIVERY OF SUNITINIB (XVII)

In this scenario, Molecularly Imprinted Polymers (MIPs) are smart materials that can be applied as drug delivery hydrogel systems, endowed of the ability to selectively recognize a specific molecule [175]. Recognition is based on the interactions between functional chemical groups exposed on the internal surface of the polymer cavities and the drug substance. The creation of complementary cavities is possible thanks to the presence of the drug molecule that acts as template during polymerization process [175]. For these reasons, we studied a MIP based on methacrylic acid and ethylene glycol dimethacrylate for the administration of Sunitinib (XVII) (Figure 59) [176]. Sunitinib (XVII) is a tyrosine kinase inhibitor used to treat various forms of cancer. It suffers of low bioavailability and, at the same time, it is characterized by a slight therapeutic window [177].

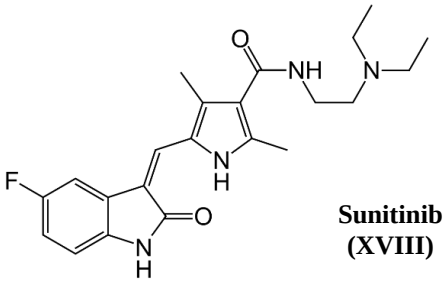

Sunitinib (XVIII)

Figure 59. *Chemical structure of Sunitinib **(XVII)***

MIP was obtained with irregular shape in the range of 20-63 μm by bulk polymerization according to the non-covalent approach and using:

• Sunitinib (**XVII**), as template;

• Methacrylic acid (MAA), as functional monomer;

• Ethylene glycol dimethacrylate (EGDMA), as cross-linker;

• Chloroform, as porogenic organic solvent;

• Azobisisobutyrronitrile (AIBN), as initiator.

Based on the obtained results, the optimal Sunitinib: MAA: EGDMA molar ratio for Sunitinib (**XVII**) imprinted polymer was 0.5: 16: 25.

In the aim to evaluate the success of the imprinting process and the selective binding between MIP and Sunitinib, rebinding assays were performed. The obtained data demonstrated that the Sunitinib (**XVII**) imprinted material and the corresponding Non-Imprinted Polymer (NIP) showed a percentage of rebinding of 70% and 46%, respectively. In these conditions, it was possible to obtain a valid value of molecular imprinting efficiency (α), which is defined as the ratio between the MIP and the NIP rebinding percentage (α = MIP rebinding % / NIP rebinding %), amounting to 1.52 [178].

Furthermore, the drug release profiles were studied for both MIP and NIP. MIP loaded with Sunitinib (**XVII**) exhibited a prolonged release during the 24 hours, reaching 58% after 6 hours and 76% at the final step. Instead, NIP released almost 90% of the loaded drug within 6 hours.

In order to test the controlled release of this drug, we exposed MCF-7 cells to MIP- Sunitinib and NIP-Sunitinib, using a concentration of Sunitinib able to induce a total inhibition of cell growth after 24 hours of treatment (70 μM). In fact, the obtained results (see Figure 60, panel A) demonstrated that MCF-7 cells treated with the Sunitinib (**XVII**) after 16 hours showed a 30% of residual cell viability compared to CTRL and it reached the 0% after 24 hours. In contrast, MIP-Sunitinib and NIP-Sunitinib did not influence cell proliferation after 16 hours,

but they caused a reduction in cell viability of about 38% and 27%, respectively after 24 hours.

NIP-Sunitinib produced the death of almost MCF-7 all the cells after 48 h, while a residual vitality of about 45% was recovered in the cells exposed to MIP-Sunitinib. Finally, after 72 hours the inhibitory effects on the cell viability of MIP-Sunitinib were total. The polymer alone did not affect cell growth in any way. Furthermore, the treatment of Sunitinib, MIP-Sunitinib and NIP-Sunitinib did not cause any cytotoxicity toward non-tumoral MCF-10A cells (Figure 60, panel B). These results clearly demonstrate that molecularly imprinted polymers are suitable systems for Sunitinib (**XVII**) release. The cytotoxic effect of Sunitinib (**XVII**) released from MIP, indeed, reached the maximum after 72 hours, while NIP completed its effect within 48 hours.

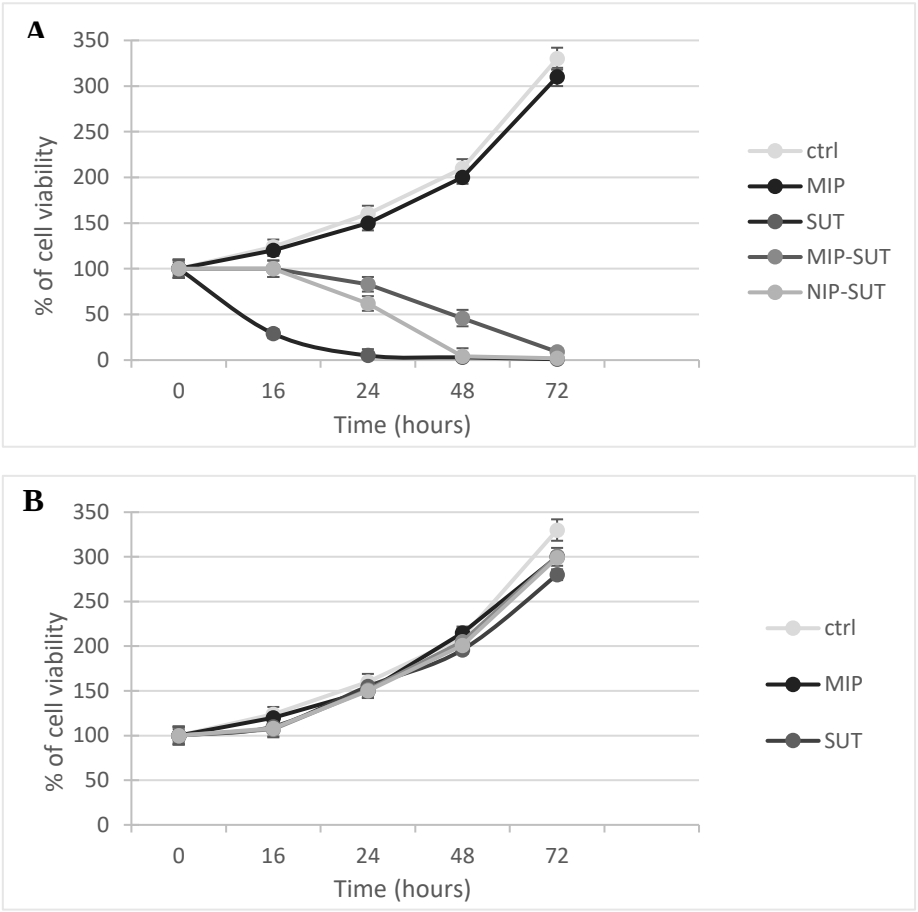

Figure 60. *Viability evaluation of MCF-7 (A) or MCF-10A (B) cells treated with Sunitinib (**XVII**) alone or loaded in MIP and NIP polymers. Figure shows also the vehicle-treated cells and the polymer by itself activity on cell proliferation.*

3.2 DEVELOPMENT OF NANOEMULSIONS FOR QUERCETIN (XVI) AND *CIS*PLATIN (II)

During my study and research period at the "Centre d'Études et de Recherche sur le Médicament de Normandie" (CERMN - Caen, France) I worked on the preparation of nanoemulsions for Quercetin (**XVI**) and *Cis*platin (**II**).

*Cis*platin (**II**) is a powerful antitumor agent, widely used in clinical, especially for the treatment of solid tumors (uterine, testicular, bladder, lung, head and neck tumors). It interacts with cellular proteins and lipids, forms DNA adducts that cause cell cycle arrest in the G2 / M phase [179-182] and can also interfere with cytoskeletal organization [183]. However, the development of resistance and its adverse effects, including nephrotoxicity, intestinal toxicity and myelosuppression, impair its effectiveness and use in clinical [184-187]. The mechanism underlying *Cis*platin (**II**)-induced nephrotoxicity is not yet known, but recent *in vitro* and *in vivo* studies indicate that this toxicity is closely associated with an increase in lipid peroxidation [185,188]. Thus, oxygen free radicals (ROS) play a central role in renal injury induced by such chemotherapy [185,189]. The oxidative stress responsible for *Cis*platin (**II**)-induced nephrotoxicity can be reduced by using different antioxidants, such as flavonoids. Among these, Quercetin (**XVI**) is one of the most abundant flavonoids in the human diet and it is commonly found in most edible fruits and vegetables [190]. Quercetin (**XVI**) is a powerful scavenger of oxygen free radicals, a metal chelator and it is capable of inhibiting lipid peroxidation, blocking the enzyme xanthine oxidase in *in vitro* and *in vivo* systems.

Among the flavonoids, Quercetin (**XVI**) shows a high radical scavenging activity already at low concentrations and it showed the highest antioxidant potential compared to the standard antioxidants (vitamin C and trolox) and to other powerful antioxidants (Resveratrol, Ferulic Acid, Gallic Acid, Kampferol, etc.) [191,192].

Several literature works report that a pre-treatment with Quercetin (**XVI**) has a protective role against *Cis*platin (**II**)-induced nephrotoxicity [182,185,193].

In addition to a powerful antioxidant effect, Quercetin (**XVI**) also exhibits excellent anti-proliferative activity, particularly on highly aggressive and metastatic breast cancer cells (MDA-MB-231) [169]. Thus, the pre-incubation of the cells with the flavonoid also possesses the ability to make tumor cells more vulnerable to apoptosis induced by treatment with *Cis*platin (**II**). The combination of Quercetin (**XVI**) and *Cis*platin (**II**) showed a synergistic

effect, resulting more effective in the induce growth suppression and apoptosis compared to treatment with a single agent [185,187].

However, such as *Cis*platin (**II**), also for this nutraceutical the clinical use is very limited due to its poor solubility in water and its poor bioavailability [194].

Recent studies have shown that the administration of drugs encapsulated in nanoparticles shows greater efficacy associated with a reduction in side effects [195].

For these reasons, we have decided to prepare different formulations (nanoemulsions) for these two drugs, in order to:

• increase the water solubility and the bioavailability of Quercetin (**XVI**), with consequent increase of its antioxidant and antitumor activity and in order to obtain an optimal and controlled drug release profile [196,197].

• improve the therapeutic profile and reduce the toxicity of *Cis*platin (**II**) [198,199].

3.2.1 Formulation of nanoemulsions

The formulation of the anhydrous mixture (2.42 g in total) was prepared mixing surfactants (Kolliphor HS15, 50% (w/w) and Transcutol, 10%, (w/w)) and oil (Labrafac, 20% (w/w)) (see Table 12). The drugs were added to the anhydrous mixture. The obtained mix was heated under gentle magnetic stirring (250 rpm) from room temperature to 85 °C, and then cooled down to 25 °C. The mixture was then subjected to sonication for 5 minutes and to a subsequent heating-cooling cycle. At 25 °C, the aqueous phase (10 mM phosphate buffer pH 7.4, 25 °C) was suddenly poured into the anhydrous mixture, leading to spontaneous emulsification. The sample was further magnetically stirred (750 rpm) for 10 min before characterization (Figure 61).

NE composition	Quantity
Kolliphor HS15	133.1 mg
Labrafac	84.7 mg
Transcutol-HP	24.2 mg
Drugs	% w/w
Buffer phosphate with NaCl	2 mL

Table 12. *Nanoemulsions composition.*

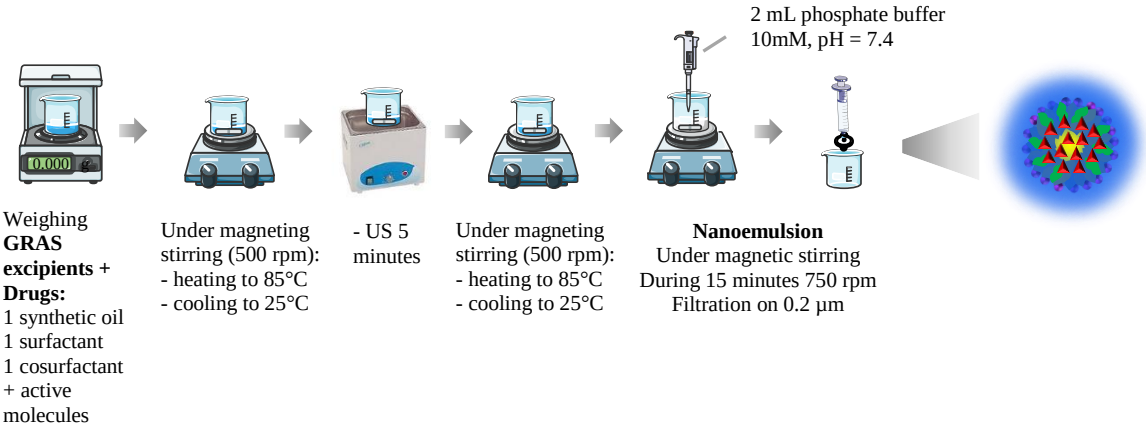

Figure 61: *Formulation of nanoemulsions*

In the adopted experimental conditions, whatever the heating temperature, nanoemulsions were obtained with comparable monodisperse droplet diameters.

Moreover, all nanoemulsions present physico-chemical properties compatible with parenteral administration. Furthermore, nanoemulsions can be extemporaneously reconstituted before use from drug-loaded anhydrous mixtures stored in ambient conditions, thanks to a very simple spontaneous emulsification process. In these conditions, any source of instability, even nearly negligible as Ostwald ripening, can be discarded. Thus, in drug discovery, nanoemulsion provides a valuable option as formulation strategy to improve properties of known drugs or those of promising leads.

*3.2.1.1 Quercetin (**XVI**) nanoemulsions*

Quercetin (**XVI**) nanoemulsions (NEs) at 2, 2.5 and 4 % w/w were formulated using the above-mentioned spontaneous process, without adding any organic solvent (Figure 61).

The best results in terms of size, polyspersity index (PDI), encapsulation efficiency (EE) and stability were obtained for Quercetin (**XVI**) NEs at 2 % w/w. In these conditions, the drug was well-encapsulated with a mean Z-average of 55.51 nm, PDI of 0.231 and a high encapsulation efficiency amounting to 85.95 %. In Table 13, the characteristics of nanoemulsions, determined directly at the end of the formulation process (after filtration), or after storage for 1 or 2 days at 4 °C, are reported. Quercetin (**XVI**) dosage was performed by using HPLC (see Experimental section for more details).

NE Q 2% (w/w)		Z-average (nm)	PDI	ζ-Potential (mV)	[Q] exp (mg/mL)	Encapsulation efficiency (%)
NE 1	**Day 0**	60.31 ± 0.6	0.246 ± 0.004	-9.67 ± 0.2	1.868 ± 0.06	86.5 ± 3.0
NE 2	**Day 0**	67.65 ± 1.6	0.365 ± 0.008	-11.8 ± 0.6	1.597 ± 0.04	73.1 ± 1.8
	Day 0+1	54.74 ± 0.5	0.193 ± 0.006	-11.9 ± 1.2	1.780 ± 0.06	81.5 ± 2.9
NE 3	**Day 0**	56.48 ± 0.8	0.244 ± 0.01	-20.5 ± 0.8	2.023 ± 0.0	91.4 ± 0.2
	Day 0+1	53.62 ± 0.7	0.214 ± 0.001	-18.3 ± 0.6	2.082 ± 0.06	94.0 ± 2.6
NE 4	**Day 0**	61.34 ± 0.4	0.317 ± 0.002	-17.2 ± 0.2	2.035 ± 0.03	92.8 ± 1.3
	Day 0+1	53.36 ± 1.1	0.206 ± 0.01	-15.3 ± 0.3	2.088 ± 0.06	95.2 ± 1.3
	Day 0+2	53.31 ± 0.6	0.192 ± 0.008	-13.7 ± 0.7	2.096 ± 0.02	95.5 ± 1.0
NE 5	**Day 0**	51.88 ± 0.2	0.193 ± 0.003	-11.6 ± 0.2	/	/
	Day 0+1	53.51 ± 0.4	0.213 ± 0.005	-14.4 ± 1.9	/	/
	Day 0+2	53.01 ± 0.4	0.211 ± 0.006	-16.0 ± 2.1	/	/
Mean Average Day 0		**55.51**	**0.231**	**-17.3**	**1.881**	**85.95**
Standard deviation		**2.7**	**0.01**	**6.2**	**0.2**	**9.0**

Table 13. *Characteristics of Quercetin (**XVI**) nanoemulsions (n = 3) determined directly at the end of the formulation process (after filtration), or after storage for 1 or 2 days at 4 °C.*

Moreover, the obtained NEs exhibited good values of pH and osmolarity, amounting to 7.34 and 281 mosm, respectively.

An *in vitro* stability study following hydrodynamic diameter, PDI, ζ-potential, drug concentrations and EE was performed after storage of the native nanoemulsions for 14 days at 4 °C (see Figure 62). In these conditions, NEs were stable.

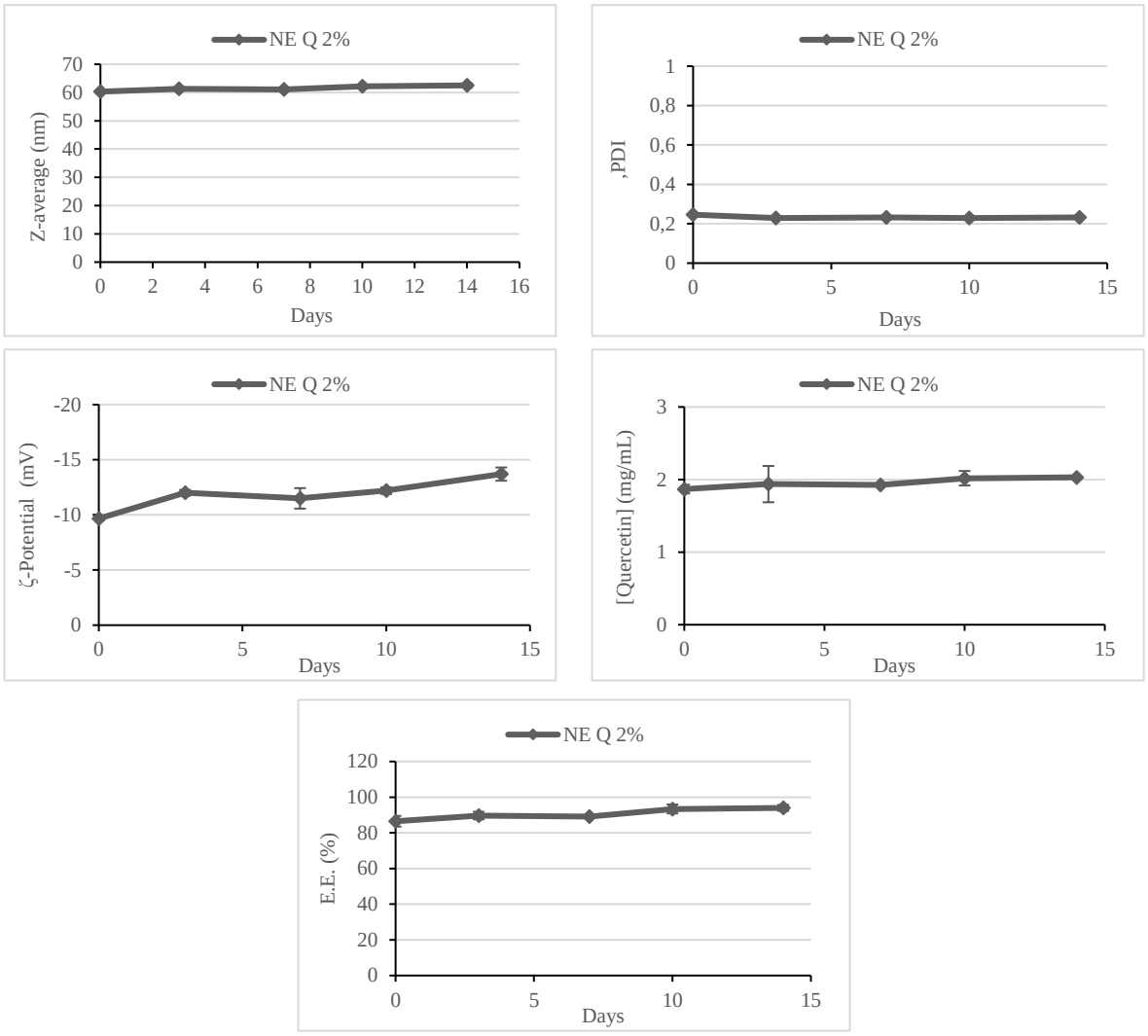

Figure 62. *Stability of Quercetin (**XVI**) nanoemulsions by measuring of their characteristics (Size, PDI, ζ-potential, Quercetin (**XVI**) concentration and EE) for 14 days at 4 °C.*

In addition, the stability of Quercetin (**XVI**) NEs at 2% w/w diluted in PBS at 37 °C (1/20 and 1/100) was tested, miming the condition used for cancer cells treatment. Surprising, size, PDI and ζ–potential of NEs resulted stable for at least 48 h (see Figure 63).

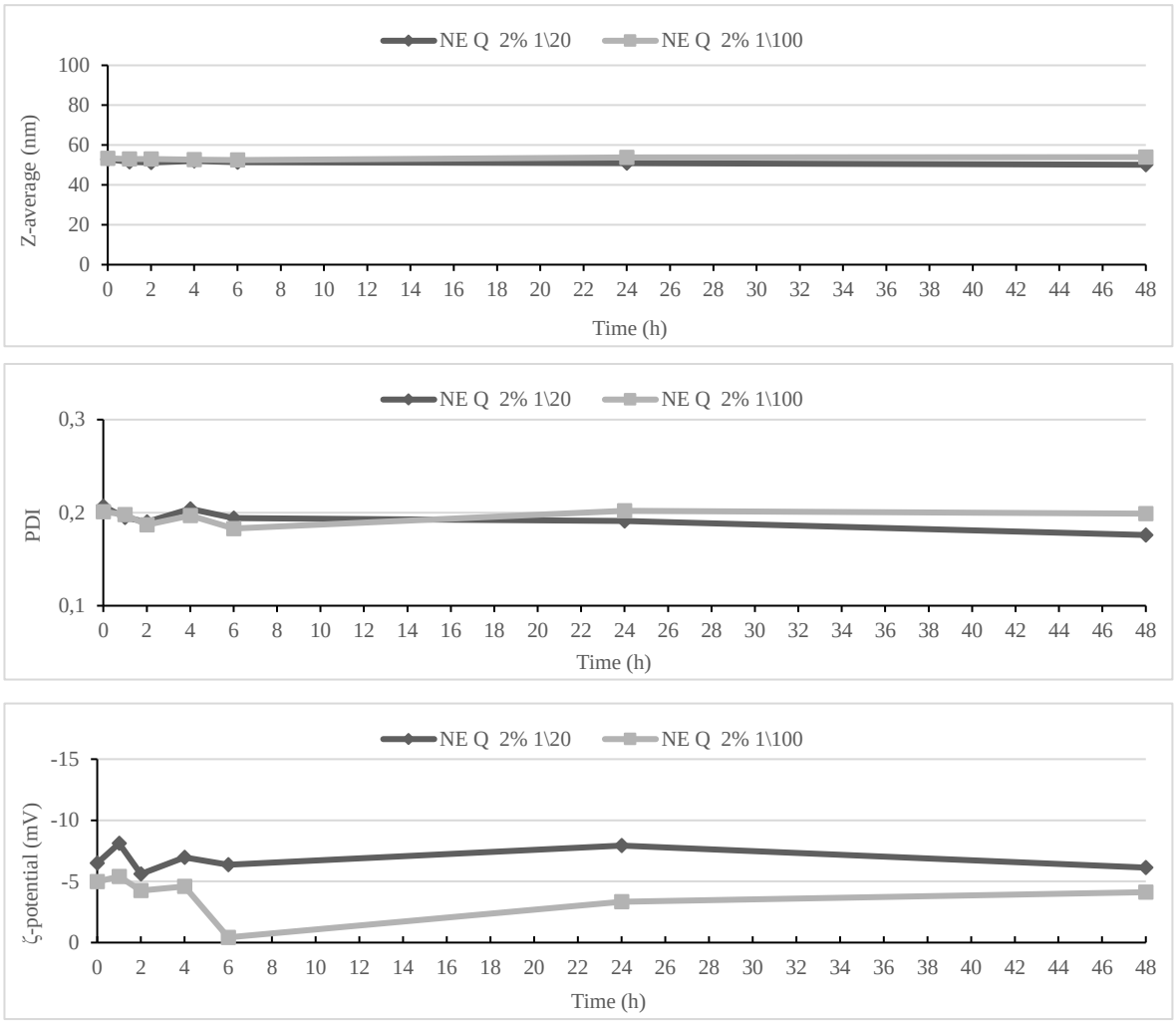

Figure 63. *Stability of Quercetin (**XVI**) nanoemulsions by measuring of their characteristics (Size, PDI, ζ-potential) for 48 h diluted in PBS at 37 °C (1/20 and 1/100).*

The stability of Quercetin (**XVI**) NEs 2%, in terms of drug concentration encapsulated in NE, diluted in PBS at 37°C (1/20 and 1/100) was evaluated, comparing it with the stability of Quercetin (**XVI**) in DMSO at the same conditions. Quercetin (**XVI**) nanoemulsions permitted to increase Quercetin (**XVI**) stability and solubility in PBS at 37 °C until 48 h at the above-mentioned dilutions, miming the conditions used for cancer cells treatment (see Figure 64).

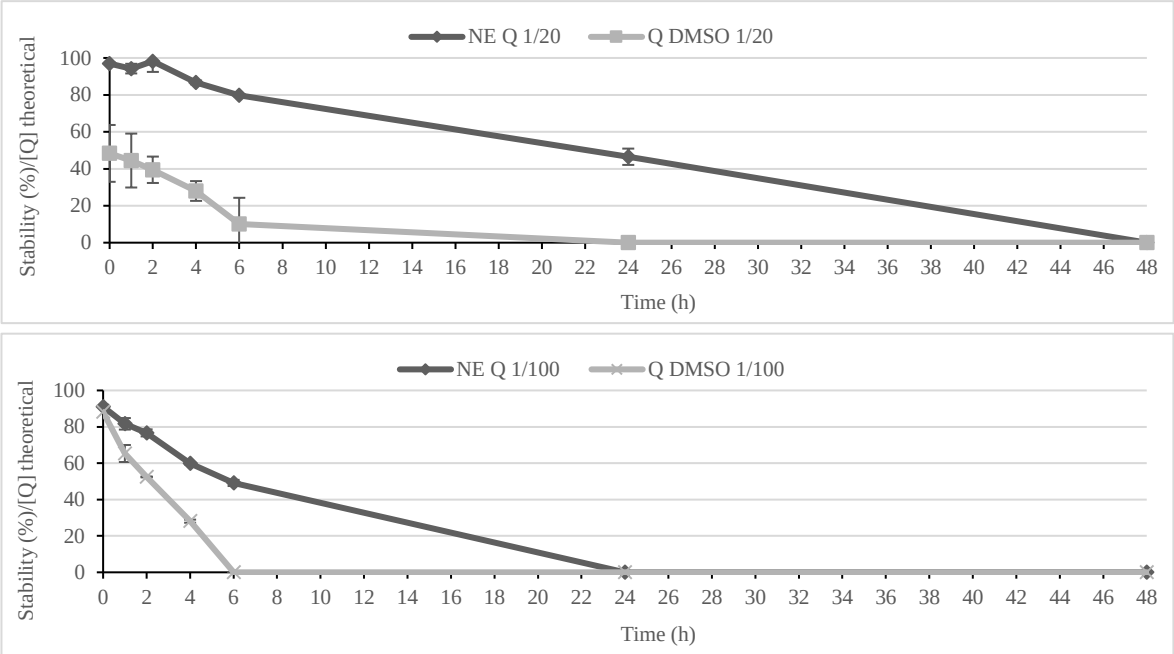

Figure 64. *Stability of Quercetin (**XVI**) nanoemulsions by measuring of drug concentration encapsulated in NE for 48 h diluted in PBS at 37 °C (1/20 and 1/100).*

The release of Quercetin (**XVI**) from nanoemulsions at 2% w/w was evaluated by the dialysis bag method (see experimental section for details). For this purpose, 250 µL of Quercetin (**XVI**)-loaded nanoemulsions were instilled into a cellulose ester dialysis bag and incubated in 100 mL of PBS pH 7.4. At appropriate times (from 0 minutes to 48 hours), 500 µL of PBS + 1% of Tween 80 were withdrawn and replaced with 500 µL of fresh PBS. Then, the samples were diluted in 500 µL of methanol and analyzed using UHPLC. Quercetin (**XVI**) was not detected neither in the bag dialysis solution neither in the PBS. Thus, the obtained results showed that Quercetin (**XVI**) was released from the membrane and probably it was degraded, because in the PBS solution some peaks, characterized by different retention times compared to Quercetin (**XVI**), have been detected.

Finally, in order to evaluate the oxygen radical antioxidant capacity of Quercetin (**XVI**) NE the ORAC assay was carried out and this activity was compared with those of Quercetin (**XVI**) itself (in a DMSO solution). The obtained data (see Table 14) showed a better antioxidant activity of Quercetin (**XVI**) NE than Quercetin (**XVI**) in DMSO (9.27 and 7.23 µM compound/µM Trolox, respectively). Thus, the use of nanoemulsions permitted also to improve the antioxidant activity of this drug.

Compound	ORAC (µM compound/µM Trolox)
Quercetin (XVI) DMSO	7.23 ± 0.03
NE Q 2%	9.70 ± 0.02
Trolox	1.00 ± 0.01

Table 14. *Oxygen radical antioxidant capacity of Quercetin (**XVI**) and Quercetin (**XVI**) nanoemulsion by using ORAC assay.*

In conclusion, the outcomes demonstrate that Quercetin (**XVI**) nanoemulsions (Q NEs) can be formulated using a simple and spontaneous process, with a high encapsulation efficiency. The obtained Q NEs 2% were stable for 14 days at 4 °C and for at least 48 h in PBS at 37 °C. These formulations permit to increase the Quercetin (**XVI**) stability and solubility in PBS at 37 °C up to 48 h in the conditions used for cancer cell treatment. Q NEs improved also the antioxidant effect of this drug. Thus, the use of nanoemulsions could increase the therapeutic efficiency of Quercetin (**XVI**) in cancer treatment by improving its physical-chemical properties (solubility and bioavailability).

*3.2.1.2 Cisplatin (**II**) nanoemulsions*

*Cis*platin (**II**) nanoemulsions (*Cis*Pt NE) 1% w/w were formulated using the same simple and spontaneous process, without adding any organic solvent (see Figure 61). Because of the high toxicity of *Cis*platin (**II**), we used a glove box to weight this drug and all manipulations were carried out under a laminar flow hood with a protective mask, taking all the necessary precautions.

*Cis*platin (**II**) was well-encapsulated in the obtained NEs, with an encapsulation efficiency of 56.1 %, Z-average of 49,81 nm and PDI of 0.180. Table 15 reports the characteristics of nanoemulsions determined directly at the end of the formulation process (after filtration), or after storage for 1 day at 4 °C. These NEs resulted stable for at least 1 day at 4°C, we could not follow the stability of *Cis*platin (**II**) NEs for a more long period because of the high toxicity of the drug. *Cis*platin (**II**) dosage was performed by using a mass spectrometer Element 2 (HR ICP-MS; Thermo) at "Plateau d'Isotopie de Normandie" (Caen, France) after mineralization of the samples.

NE CisPt 1%	Z-average (nm)	PDI	ζ-Potential (mV)	[CisPt] exp (mg/mL)	Encapsulation efficiency (%)
Day 0	49.81 ± 0.5	0.180 ± 0.02	-2.17 ± 0.3	0.499 ± 0.01	56.1 ± 1.3
Day 0+1	51.47 ± 0.3	0.170 ± 0.01	-3.52 ± 0.2	0.482 ± 0.001	55.9 ± 0.1

Table 15. *Characteristics of Cisplatin (**II**) nanoemulsion (n = 3) determined directly at the end of the formulation process (after filtration), or after storage for 1 day at 4 °C.*

An *in vitro* stability study following hydrodynamic diameter, PDI and ζ-potential, was performed after storage of the native nanoemulsions for 7 days at 4 °C (see Figure 65). In these conditions, NEs remained stable.

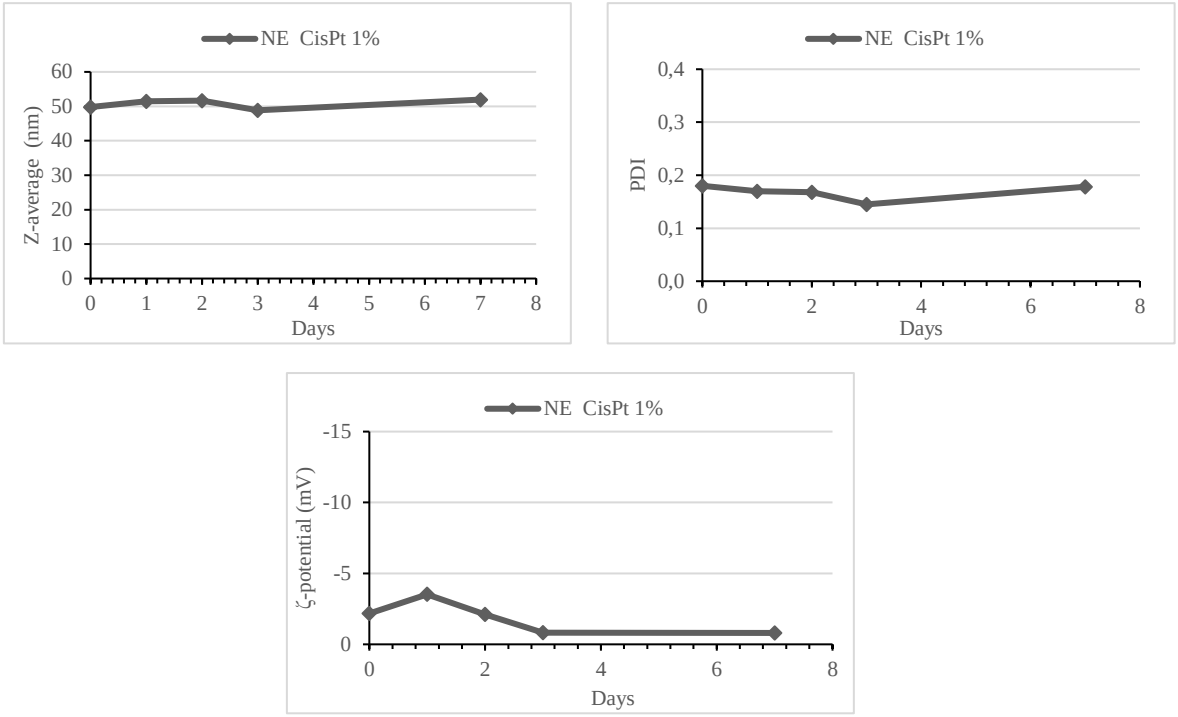

Figure 65. *Stability of Cisplatin (**II**) nanoemulsions by measuring of their characteristics (Size, PDI and ζ-potential) for 7 days at 4 °C.*

In conclusion, *Cis*platin (**II**) nanoemulsions can be formulated using a simple and spontaneous process, with a good encapsulation efficiency and a stability for at least of 7 day at 4 °C. This formulation could improve the therapeutic efficiency and reduce the toxicity of *Cis*platin (**II**) in cancer treatment by improving its bioavailability and solubility.

*3.2.1.3 Quercetin (**XVI**) and Cisplatin (**II**) nanoemulsions*

Formulation of nanoemulsions containing both Quercetin (**XVI**) 2% w/w and *Cis*platin (**II**) 1% w/w were obtained using the same simple and spontaneous process (see Figure 61). Because of the high toxicity of *Cis*platin (**II**), we took the same necessary precautions seen before.

Both drugs were well-encapsulated in the NE, with an encapsulation efficiency of 69.6 % and 100% for *Cis*platin (**II**) and Quercetin (**XVI**), respectively.

Table 16 reports the characteristics of nanoemulsions determined directly at the end of the formulation process (after filtration), or after storage for 1 day at 4 °C, with Z-average of 49,81 nm and PDI of 0.180. These NEs resulted stable for at least 1 day at 4°C, we could not follow the stability of NE for a more long period because of the high toxicity of the *Cis*platin (**II**). Quercetin (**XVI**) dosage was performed by using HPLC (see Experimental section for more details); *Cis*platin (**II**) dosage was performed by using a mass spectrometer Element 2 (HR ICP-MS; Thermo) at "Plateau d'Isotopie de Normandie" (Caen, France) after mineralization of the samples.

NE CisPt 1% + Q 2%	**Z-average (nm)**	**PDI**	**ζ-Potential (mV)**	**[CisPt] exp (mg/mL)**	**Encapsulation efficiency (%) CisPt**	**[Q] exp (mg/mL)**	**Encapsulation efficiency (%) Q**
Day 0	48.41± 0.4	0.189± 0.007	-4.03 ± 2.2	0.717 ± 0.01	69.6 ± 1.3	2.191 ± 0.0	100.5 ± 0.2
Day 0+1	49,74± 0,5	0,189 ± 0,01	-6.14 ± 0.5	0.625 ± 0.02	60.7 ± 1.5	2.058 ± 0.04	94.4 ± 2.6

Table 16. *Characteristics of Quercetin (**XVI**) + Cisplatin (**II**) nanoemulsion (n = 3) determined directly at the end of the formulation process (after filtration), or after storage for 1 day at 4 °C.*

An *in vitro* stability study following hydrodynamic diameter, PDI and ζ-potential, was performed after storage of the native nanoemulsion for 7 days at 4 °C (see Figure 66). In these conditions, NEs remained stable, even if a slight variation in ζ-potential was observed.

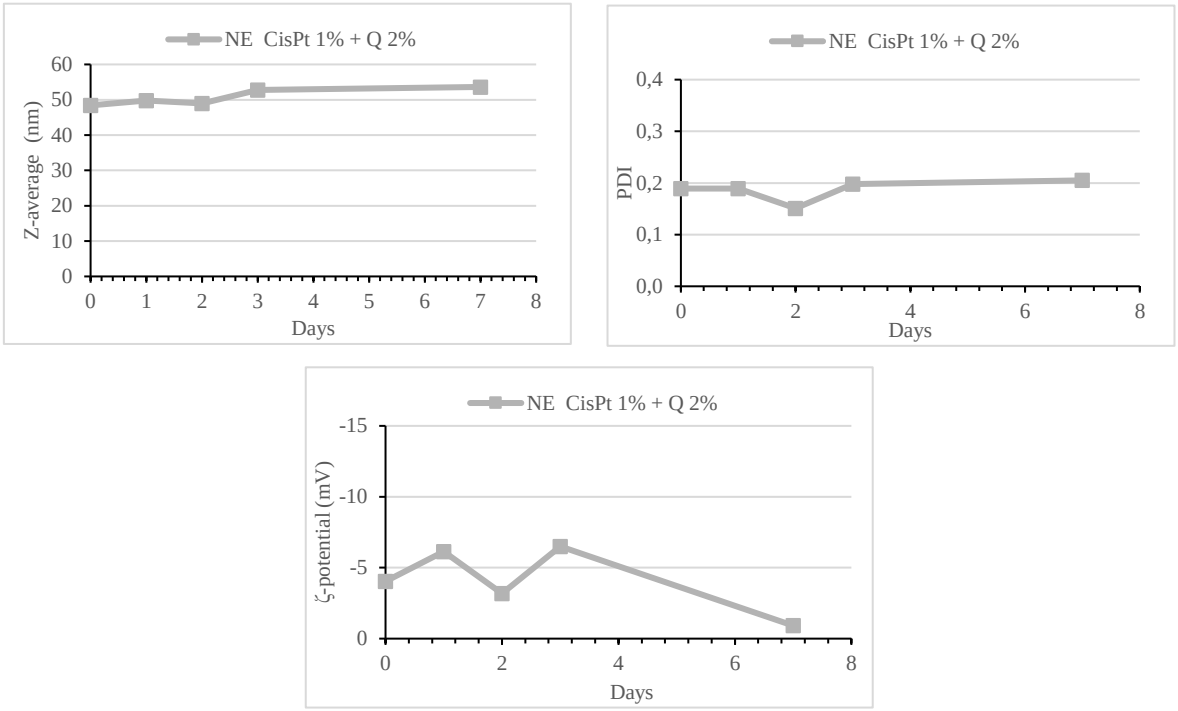

Figure 66. *Stability of Cisplatin (**II**) nanoemulsions by measuring of their characteristics (Size, PDI and ζ-potential) for 7 days at 4 °C.*

In conclusion, co-formulation of *Cis*platin (**II**) and Quercetin (**XVI**) in nanoemulsions can be obtained using the same simple process, with a good encapsulation efficiency and stability for at least 1 days at 4 °C. These NEs could be used as a promising formulation strategy for the improvement of some drug properties, such as bioavailability and solubility. Moreover, the developed NEs could be used to evaluate the possible synergistic action of these two drugs in different cancer cells and the protective effect of Quercetin (**XVI**) against *Cis*platin (**II**)-induced nephrotoxicity.

*3.2.1.4 Acetylated Quercetin (**17a**) nanoemulsions*

The preparation of suitable formulations also for Quercetin (**XVI**) derivatives, structurally modified in order to increase its lipophilicity, could be very interesting. In particular, the derivative in which all the hydroxyl groups were acetylated, was chosen in this study due to its better cytotoxic activity compared to Quercetin (**XVI**) itself (Figure 67) [169].

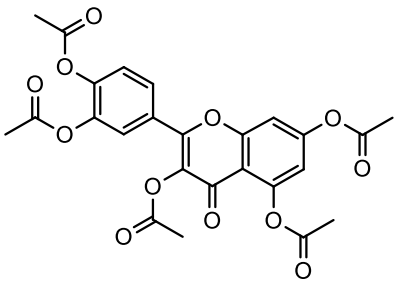

17a

Figure 67. *Chemical structure of Acetylated Quercetin (**17a**)*

This formulation could be used in co-treatment with *Cis*platin (**II**) in order to compare its activity with that obtained using Quercetin (**XVI**) itself.

Unfortunately, because of its low solubility in all the used excipients and solvents and the high instability and sensibility (at light and oxidation), it was not possible to obtain a nanoemulsions for compound **17a**. Table 17 reports the characteristics of nanoemulsions determined directly at the end of the formulation process (after filtration). Even though the size and PDI seems good, it was not possible to encapsulate the acetylated Quercetin at 2, 4 and 6% w/w in this kind of NE.

NE AcQ 2% (w/w)	Z-average (nm)	PDI	ζ-Potential (mV)	[Q] exp (mg/mL)	Encapsulation efficiency (%)
Day 0	51.41 ± 0.3	0.204 ± 0.005	-5.49 ± 0.3	0	0

NE AcQ 4% (w/w)	Z-average (nm)	PDI	ζ-Potential (mV)	[Q] exp (mg/mL)	Encapsulation efficiency (%)
Day 0	51.54 ± 0.5	0.199 ± 0.008	-9.72 ± 0.3	0	0

NE AcQ 6% (w/w)	Z-average (nm)	PDI	ζ-Potential (mV)	[Q] exp (mg/mL)	Encapsulation efficiency (%)
Day 0	52.55 ± 0.3	0.204 ± 0.005	-5.56 ± 0.3	0	0

Table 17. *Characteristics of Acetylated Quercetin nanoemulsion (n = 3) determined directly at the end of the formulation process (after filtration)..*

Other nanoemulsions obtained using different temperatures and excipients or adding antioxidant molecules (like vitamin E) were prepared, but the result did not change (data not showed).

Moreover, the solubility at 40 °C of acetylated Quercetin in the different excipients used to prepare nanoemulsions was tested. Effectively, the obtained results demonstrated that this compound possessed a very low solubility and stability in these excipients: **17a** was soluble only in transcutol for 3.4%; in the other two excipients (labrafac and kolliphor) it was insoluble and it was degraded (see Table 18). At the end, nanoemulsions containing acetylated Quercetin were prepared after its preventive dissolving in the minimum quantity of some solvents (acetone, DMSO and ethyl acetate). Unfortunately, the use of these solvents did not improve **17a** solubility and encapsulation (data not showed).

NE 17a 2% (w/w)	C_{theo} (mg/mL)	C_{exp} (mg/mL)	Solubility (%)
AcQ + Kolliphor	36.9	/	/
AcQ + Transcutol	205.5	6.955	3.4
AcQ + Labrafac	58.5	/	/

Table 18. *Solubility of Acetylated Quercetin (**17a**) in excipients used for nanoemulsions formulation.*

3.2.2 Biological evaluation of nanoemulsions

The possible Quercetin (**XVI**) protective action, due to its antioxidant activity, was evaluated against the *Cis*platin (**II**)-induced nephrotoxicity, which is one of the causes that limits the use of this chemotherapy in clinical, using the HEK-293 embryonic kidney cell line as model.

Particularly, an MTT assay using the nanoemulsion containing 1% *Cis*platin (**II**) (range of concentration from 3,5 to 52 μM) and the nanoemulsion with both drugs (*Cis*platin (**II**) at the same range of concentrations + Quercetin (**XVI**) from 10 to 100 μM) was performed. Even though we noticed a kind of cytotoxicity, that is under investigation, it was possible to note a clear improvement in the viability of HEK-293 co-treated with *Cis*platin (**II**)+Quercetin (**XVI**) compared to those treated with *Cis*platin (**II**) alone at all concentrations (see Figure 68).

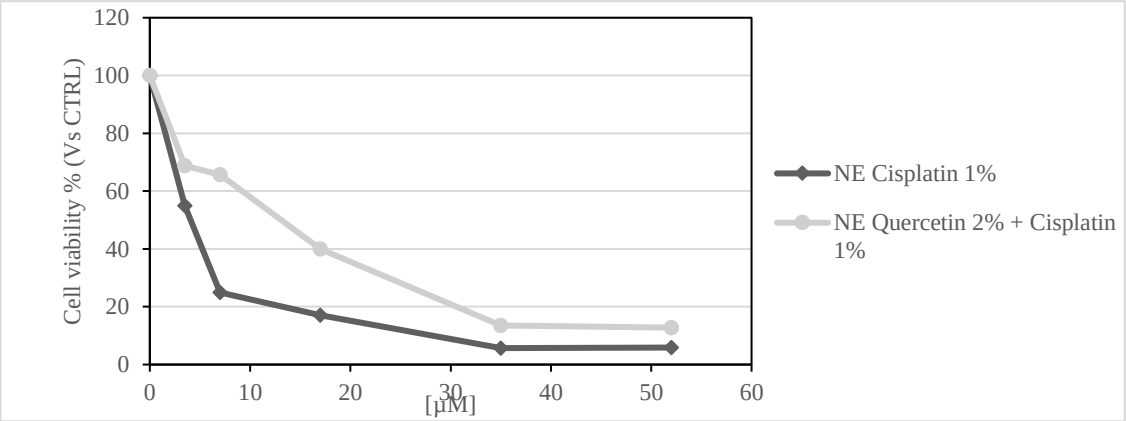

Figure 68. *HEK-293 cell viability after exposure at NE Cisplatin (**II**) and NE Quercetin (**XVI**) +Cisplatin (**II**) for 72h.*

The same experiment was performed on MDA-MB-231 breast cancer cell line, on which Quercetin (**XVI**) was found to be particularly active, in order to verify whether the co-treatment could have a synergistic effect, leading to greater cytotoxicity on tumor cells compared to single drugs.

Quercetin (**XVI**)-*Cis*platin (**II**) co-treatment led to a marked improvement in the antitumor activity when compared to that of *Cis*platin (**II**), even though the same high toxicity was observed (data not showed). Considering the high toxicity of *Cis*platin (**II**) at high doses, if it is associated with Quercetin (**XVI**) it can be used at lower doses showing a better cytotoxic profile, without the occurrence of side effects.

Because of the noticed toxicity on the used cell lines, we are currently working on investigating the reason of the NE toxicity, whether it is cell-specific or due to the NE formulation.

Future studies will be aimed at the design of different formulations that will lead to obtain better results, without any kind of toxicity.

Chapter 4: Experimental Section

4.1 CHEMISTRY

All of the reactions were carried out under nitrogen, using standard Schlenk or glovebox techniques. All of the reagents were purchased from TCI Europe N.V. All commercially available chemicals in the experiments were of reagent grade and used as received. The solvents were purified according to the standard procedures. Deuterated solvents (Euriso-Top products) were degassed under a nitrogen flow and stored in the dark over activated 4Å molecular sieves. NMR spectra were recorded on a Bruker AM300 or a Bruker AVANCE 400 operating at 300 and 400 MHz for ^{1}H and at 75 and 100 MHz for ^{13}C, respectively. The ^{1}H NMR and ^{13}C NMR chemical shifts are referred to $SiMe_4$ (δ=0 ppm) by using the residual proton impurities of the deuterated solvents as internal standards. Chemical shifts, δ, were reported in parts per million (ppm) for both ^{1}H and ^{13}C NMR. Multiplicities are abbreviated as follows: singlet (s), doublet (d), triplet (t), quartet (q), multiplet (m), and broad (br). Mass spectra (ESI) were obtained by a Waters Quattro Micro triple quadrupole mass spectrometer equipped with an electrospray ion source. Elemental analyses for C, H, and N were recorded with a Thermo-Finnigan Flash EA 1112 and were performed according to standard microanalytical procedures.

4.1.1 Synthesis of *N*-substitued bis-imidazolium salts (L7, L8)

*4.1.1.1 Synthesis of N,N'-bis-[(2-hydroxy-2-phenyl)ethyl]-imidazolium iodide (**L7**)*

Imidazole (1.0 g, 15 mmol) and styrene oxide (3.35 ml, 30 mmol, d = 1.054 g/l) in tetrahydrofuran (THF) (45 mL) were stirred for 24 h at 60 °C. The obtained dialkylated product was purified by dissolution in acetone and recovered at low temperature (-20 °C) by precipitation. The intermediate was dissolved in CH_2Cl_2 (70 ml) and HI (55%) (stoichiometric amounts) was added to obtain white solid (43 % yield).

^{1}H-NMR (300 MHz, DMSO): 9.03 (s, 1H), 7.67 (s, 1H), 7.63 (s, 1H), 7.37 (m, 10H, unsaturated protons), 5.93 (br, 2H), 4.96 (m, 2H), 4.44 (dd, 2H) 4.28 (dd, 2H). ^{13}C-NMR (75 MHz, DMSO): 141.21, 137.58, 127.94, 127.62, 127.20, 125.90, 119.89, 71.98, 53.43. Elemental analysis calcd (%) for $C_{19}H_{21}N_2O_2I$: C, 52.31, H, 4.85, N, 6.42%; found: C, 52.68, H, 4.82, N, 6.38%. ESI-MS (CH_3CN, m/z): 309.1 Dalton attributable to $[C_{19}H_{21}N_2O_2]^+$.

*4.1.1.2 Synthesis of N-[4-(hydroxymethyl)phenyl]-N'-[(2-hydroxy-2-phenyl)ethyl]-imidazolium bromide (**L8**)*

Imidazole (2.10 g, 29 mmol) and styrene oxide (3.35 ml, 29 mmol, d = 1.054 g/l) in tetrahydrofuran (90 mL) were stirred for 12 h at 60 °C. The monoalkylated product obtained was not isolated. Then, 4-bromo-benzylalcohol (5.44 g, 29 mmol) was added. The solution was warmed to reflux for 24 h. The reaction mixture was cooled to room temperature and the solvent was removed *in vacuo*. Diethyl ether (20 mL) was added to the crude product and filtered. The solution was washed with water (2x50 ml). The solvent was dried with Na_2SO_4 and then removed by evaporation *in vacuo*. The resulting residue was purified on a silica gel column chromatography in ethyl acetate/methanol (1/1) to give a yellow solid (38 % yield).

^{1}H-NMR (300 MHz, $CDCl_3$): 8.70 (s, 1H), 7.27 (m, 11H, unsaturated protons), 5.24 (m, 2H), 4.88 (dd, 1H), 4.14 (m, 1H), 4.07 (m, 1H). ^{13}C-NMR (75 MHz, $CDCl_3$): 141.62, 137.55, 136.71, 135.08, 128.86, 128.48, 127.98, 126.86, 125.95, 120.18, 118.84, 72.68, 63.78, 54.78. Elemental analysis calcd (%) for $C_{18}H_{19}N_2O_2Br$: C, 57.61, H, 5.10, N, 7.47; found: C, 57.29, H, 5.62, N, 7.59. ESI-MS (CH_3CN, m/z): 188.1 Dalton attributable to $[C_{11}H_{12}N_2O]^+$.

4.1.2 Synthesis of complexes AgL7, AuL7, AgL8, AuL8

Silver and gold complexes were prepared by using a slightly modified literature procedure [115,116].

*4.1.2.1 Synthesis of bis-N,N'-[(2-hydroxy-2-phenyl)ethyl]-imidazole-[2-ylidine]-[silver(I)]$^+$[diiodide-silver(I)]$^-$ (**AgL7**)*

L7 (0.20 g, 0.65 mmol) and Ag_2O (0.09 g, 0.37 mmol) in 41 mL acetonitrile were kept at reflux for 12 h. Then, the mixture was filtered over Celite® and the solvent was dried with Na_2SO_4 and removed *in vacuo.* The residue was washed with hexane, dried over Na_2SO_4 and evaporated under high vacuum to give compound **AgL7** as a yellow powder (50 %, yield).

^{1}H-NMR (300 MHz, DMSO): 7.40 (m, 5H, aromatic protons), 7.09 (s, 1H), 6.80 (s, 1H), 5.70 (br, 1H, O*H*), 4.80 (m, 1H), 4.10 (dd, 1H), 4.01 (dd, 1H). ^{13}C-NMR (75 MHz, DMSO): 143.1, 138.1, 128.5, 128.1, 127.9, 127.7, 126.5, 126.2, 120.4, 72.56, 54.0. Elemental analysis calcd (%) for $C_{19}H_{20}N_2O_2AgI$: C, 42.02, H, 3.71, N, 5.16; found: C, 42.05, H, 3.79, N, 5.07. ESI-MS (CH_3CN, m/z): 482.8 and 485.3 Dalton attributable to $[C_{22}H_{23}AgN_4O_2]^+$.

*4.1.2.2 Synthesis of bis-N,N'-[(2-hydroxy-2-phenyl)ethyl]-imidazole-[2-ylidene]-[gold(I)]$^{+}$[dichloride-gold(I)]$^{-}$ (**AuL7**)*

KHMDS [potassium-bis-(trimethylsilyl)-amide] (0.097 g, 0.48 mmol) was added to a solution of **L7** (0.15 g, 0.48 mmol) in DMF (7 mL). The resulting orange solution was stirred for 15 min. Then, a solution of $(CH_3)_2SAuCl$ (0.12 g, 0.38 mmol) in DMF (2 mL) was added dropwise. The mixture was stirred at room temperature for 3 h. The solvent was removed under vacuum. The resulting dark yellow solid was washed with CH_2Cl_2 (3 × 10 mL), essiccated with Na_2SO_4 and dried under vacuum to give compound **AuL7** (56 % yield).

^{1}H-NMR (300 MHz, DMSO): 7.48 (m, 7H, aromatic protons), 5.84 (br, 1H), 4.90 (m, 1H), 4.29 (dd, 1H), 4.16 (dd, 1H). ^{13}C-NMR (75 MHz, DMSO): 162.2, 142.1, 128.2, 127.53, 126.0, 71.5, 54.9. Elemental analysis calcd (%) for $C_{19}H_{20}N_2O_2AuCl$: C, 42.20, H, 3.73, N, 5.18; found: C, 42.01, H, 3.62, N, 5.28. ESI-MS (CH_3CN, m/z): 669.0 Dalton attributable to $[C_{32}H_{32}AuN_4]^{+}$.

*4.1.2.3 Synthesis of N-[4-benzylalcohol]-N'-[(2-hydroxy-2-phenyl)ethyl]-imidazole-[2-ylidene]-silver(I)bromide (**AgL8**)*

Ligand **L8** (0.250 g, 0.66 mmol) was added to a suspension of silver oxide (0.308 g, 1.33 mmol) in CH_2Cl_2 (15 mL) containing molecular sieves (4 Å). The reaction was carried out with the exclusion of light. The mixture was heated at reflux for 1.5 h. Then, the mixture was filtered on Celite® and solvent was removed under high vacuum, the residue washed with hexane and dried *in vacuo* to give compound **AgL8** as a light brown powder (50 % yield).

^{1}H-NMR (400 MHz, CD_2Cl_2): 7.22 (m, 11H, unsaturated carbons), 5.29 (m, 2H), 4.92 (dd, 1H), 4.20 (m, 1H), 4.10 (m, 1H). ^{13}C-NMR (100 MHz, $CDCl_3$): 137.96, 137.36, 137.01, 129.30, 127.09, 126.07, 120.05, 118.78, 73.71, 64.87, 63.73, 54.90. Elemental analysis calcd (%) for $C_{18}H_{18}N_2O_2AgBr$: C, 44.84, H, 3.76, N, 5.81; found: C, 44.28, H, 4.07, N, 5.89. ESI-MS (CH_3CN, m/z): 485.8 - 483.0 Dalton are attributable to $[C_{18}H_{19}AgBrN_2O_2]^{+}$.

*4.1.2.4 Synthesis of N-[4-benzylalcohol]-N'-[(2-hydroxy-2-phenyl)ethyl]-imidazole-[2-ylidene]-gold(I)bromide (**AuL8**)*

N-[4-benzylalcohol]-*N*'-[(2-hydroxy-2-phenyl)ethyl]-imidazole-[2-ylidene]-gold(I)bromide (**AuL8**) was prepared by *trans*-metalation from **AgL8**. The silver complex

(0.150 g, 0.031 mmol) and $(CH_3)_2SAuCl$ (0.091 g, 0.031 mmol) were suspended in 23 mL of dichloromethane and allowed to stir at room temperature for 12 h in the absence of light. The resulting suspension was then passed through a Celite pad. The solvent was concentrated and then treated with an excess of hexane to precipitate as a violet powder (15 % yield). ^{1}H-NMR (400 MHz, DMSO): 8.03 (s, 1H), 7.72 (s,1H), 7.24 (m, 9H, aromatic protons), 5.60 (br, 2H), 4.91 (br, 1H), 4.10 (br, 2H). ^{13}C-NMR (100 MHz, DMSO): 161.2 (N*C*N), 141.8, 141.7, 140.9, 140.4, 140.2, 139.6, 139.0, 137.1, 136.9 137.96, 137.36, 137.01, 128.8, 128.5, 128.4, 128.2, 127.6, 127.0, 128.9, 122.0, 121.7, 120.7, 120.4, 71.1, 64.0, 62.3, 54.7. Elemental analysis calcd (%) for $C_{18}H_{18}N_2O_2AuCl$: C, 41.04, H, 3.44, N, 5.32; found: C, 41.14, H, 3.65, N, 5.41. ESI-MS (CH3CN, m/z): 571.3 and 573.0 Dalton attributable to $[C_{18}H_{19}AuBrN_2O_2]^+$.

4.2 BIOLOGY

4.2.1 Cell culture

The seven cell lines used in this work were purchased from American Type Culture Collection (ATCC, Manassas, VA, USA). MCF-7 human breast cancer cells, estrogen receptor (ER)-positive, were maintained in Dulbecco's modified Eagle's medium/nutrient mixture Ham F-12 (DMEM/F12), supplemented with 10% fetal bovine serum (FBS) and 100 UmL^{-1} penicillin/streptomycin, as previously described [90]. MDA-MB-231 human breast cancer cells, known as triple-negative cells (i.e., not overexpressing human epidermal growth factor receptor 2 (HER2), estrogen and progesterone receptors), were cultured in DMEM/F12 supplemented with 5% FBS, 1% L-glutamine and 100 U mL^{-1} penicillin/streptomycin. HeLa human epithelial cervix carcinoma cells, estrogen receptor (ER)-negative, Ishikawa human endometrial adenocarcinoma cells, and estrogen receptor (ER)-positive were maintained in minimum essential Eagle's Medium (MEM), supplemented with 10% FBS, 1% l-glutamine, 100 UmL^{-1} penicillin/streptomycin, and 1% nonessential amino acids (NEAA). MCF-10A human mammary epithelial cells, were cultured in DMEM/F12 medium, supplemented with 5% horse serum (HS; Eurobio, Les Ullis, Cedex, France), 100 UmL^{-1} penicillin/streptomycin, 0.5 mg mL^{-1} hydrocortisone, 20 ng mL^{-1} human epidermal growth factor (hEGF), 10 mg mL^{-1} insulin, and 0.1 mg mL^{-1} cholera enterotoxin (Sigma–Aldrich, Milan, Italy). 3T3-L1 cells line of murine fibroblasts of embryonic type, were maintained in DMEM, supplemented with 10% NCS and 100 U/ml penicillin/ streptomycin. HEK-293 human embryo kidney cells were cultured in DMEM,

supplemented with 10% FBS, 1% l-glutamine, and 100 U mL^{-1} penicillin/streptomycin. Cells were maintained at 37 °C in a humidified atmosphere of 95% air and 5% CO_2 and periodically screened for contamination [89]. All compounds were dissolved in dimethyl sulfoxide (DMSO; Sigma, St. Louis, MO, USA) and opportunely diluted in cultured medium to obtain working concentrations.

4.2.2 Cell viability

Cells were grown in complete medium, and before being treated, they were starved in serum-free medium for 24 h, to allow cell-cycle synchronization. Cells were then grown in phenol-red-free medium supplemented with 1% dextran-coated charcoal (DCC)-treated FBS. Cells were treated with increasing concentrations of each compound for 72 h. Untreated cells were supplemented with DMSO (final concentration 0.1 %) and used as a control [200]. Cell viability was assessed using the 3-(4,5-dimethylthiazol- 2-yl)-2,5-diphenyltetrazolium bromide reagent (MTT), according to the manufacturer's protocol (Sigma–Aldrich, Milan, Italy), as previously described [115]. For each sample, mean absorbance, measured at 570 nm, was expressed as a percentage of the control and plotted versus drug concentration to determine the IC_{50} values (i.e., drug concentrations able to decrease cell viability by 50 % with respect to control) for each cell line, using GraphPad Prism 6 software (GraphPad Inc., San Diego, CA, USA). Mean values and standard deviations (SD) of three independent experiments carried out in triplicate and are shown.

4.2.3 Human topoisomerase I relaxation assay

hTopo I relaxation assays have been performed in a final volume of 20 μL as follows. 0.25 μg of supercoiled pHOT1 in TE buffer [TE: 10 mM Tris-HCl (pH 7.5), 1 mM EDTA] (TopoGEN, Port Orange, FL, USA) has been added to a solution containing water (variable volume) and 1× assay buffer (10 mM Tris-HCl (pH 7.9), 1 mM EDTA, 0.5 mM NaCl, 0.1% bovine serum albumin, 0.1mMspermidine and 5% glycerol). Compounds have been added and the reaction initiated by addition of recombinant hTopo I (2 U) (TopoGEN, Port Orange, FL, USA), incubated at 37 °C for 30 min and terminated by the addition of 5× stop buffer (5% sarkosyl, 25% glycerol, 0.125% bromophenol blue). After Proteinase K digestion (50 μg/mL) at 37 °C for 30 min, samples have been extracted with an equal volume of chloroform:isoamylic alcohol (24:1), vortexed and centrifuged for 30 s. The upper aqueous

phase has been loaded onto a 1% agarose gel containing 1× TAE buffer (diluted from50× buffer containing 242 g Tris base, 57.1 mL glacial acetic acid and 100 mL of 0.5 M EDTA) without ethidium bromide (EB). At the end, 1× TAE buffer containing EB (0.5 μg/mL) has been used to stain agarose gel for 30 min and after wash with distilled water for 15 min, it has been visualized using a UV transilluminator.

4.2.4 Human topoisomerase II decatenation assay

hTopo II decatenation assays have been performed in a final volume of 20 μL using 0.3 μg of kinetoplast DNA (kDNA) (topoGEN, Port Orange, FL, USA), 1× assay buffer [50 mM Tris-HCl, pH of 8, 150 mM NaCl, 10 mM MgCl2, 0.5 mM Dithiothreitol (DTT), 30 μg/mL bovine serum albumin (BSA)], and 1 mM ATP. The compounds have been added and the reaction started by adding 3 U of hTopo II (topoGEN, Port Orange, FL, USA) and incubating at 37 °C for 30 min. Then, 5x stop buffer has been added and the samples treated as described in the previous paragraph. The aqueous phase has been loaded on a 1% agarose gel containing 1× TAE buffer with EB (0.5 μg/mL) and visualized using an UV transilluminator.

4.2.5 TUNEL assay

Apoptosis was detected by the TUNEL assay, according to the guidelines of the manufacturer (CFQ488A TUNEL Assay Apoptosis Detection Kit, Biotium, Hayward, CA, USA), with some modifications [51]. In brief, cells were grown on glass coverslips. After treatment, they were washed three times with PBS, then methanol-fixed at -20 °C for 15 min. Fixed cells were washed three times with 0.01 %(v/v) Triton X-100 in PBS and incubated with 100 μL TUNEL equilibration buffer for 5min; this was then removed and 50 μL of TUNEL reaction mixture containing 1 μL terminal deoxynucleotidyl transferase (TdT) was added to each sample and incubated in a dark and humidified chamber for 2h at 37 °C. Samples were washed three times with ice-cold PBS containing 0.1 % Triton X-100 and 5 mg mL^{-1} bovine serum albumin (BSA). DAPI (0.2 μg mL^{-1}) counterstain was performed for 10 min at 37 °C under dark and humidified conditions. Cells were then washed three times with cold PBS, adding one drop of mounting solution, then they were observed and imaged under a fluorescence microscope (Leica DM 6000; 20x magnification) with excitation/emission wavelength maxima of 490 nm/515 nm (CF^{TM}488A) or 350 nm/460 nm (DAPI). Images are representative of three independent experiments.

4.2.6 Caspases assay

The activities of caspases 3/7, 8 and 9 were measured by using the Caspase-Glo Assay according to the manufacturer's guidelines (Caspase-Glo 3/7, 8, and 9 Assay Systems, Promega Corporation, Madison, WI, USA). Cells were grown in white walled 96-well plates. After treatment, the Caspase-Glo reagent and the 96-well plates containing cells were equilibrated to room temperature. Then, a different caspase (100 mL) was added to each well of a white-walled 96-well plate containing blank, negative control cells and treated cells in culture medium (100 mL) (ratio 1:1). Contents of wells were gently mixed using a plate shaker at 300–500 rpm for a few minutes and were then incubated at room temperature. The luminescence of each samples was measured in a plate-reading luminometer (Synergy H1 Hybrid Reader, BioTek) for 30 min to 3 h (λ_{ex}= 490 nm, λ_{em}= 510–570 nm), depending on the cell-culture system. Results were plotted as signal-to-noise ratios, and background readings were determined from wells containing culture medium without cells.

4.2.7 Detection of intracellular H_2O_2

Cells were grown in 48-well plates and then treated with the compound to test or menadione (Sigma-Aldrich), which causes ROS production, or co-treated for ROS scavenging assays. After treatment, cells were washed with PBS and 10 μM 2´-7´-dichlorofluorescein diacetate (Sigma-Aldrich) was added for 40 min, and then they were incubated at 37°C, 5% CO_2. In presence of intracellular H_2O_2, non-fluorescent 2´-7´-dichlorofluorescein diacetate (DCF-DA) is oxidized and converted to green fluorescent 2´,7´-dichlorofluorescein (DCF). Then, cells were washed with PBS and methanol-fixed at -20°C for 15 min. After three washes with ice-cold PBS, 2-(4-amidinophenyl)-6- indolecarbamidine dihydrochloride (DAPI; 0.2 μg mL^{-1}) counterstain was performed for 10 min at 37°C under dark conditions. Cells were then washed three-times with cold PBS, one drop of mounting solution was added, and then they were observed and imaged under a fluorescence microscope (Leica DM6000; 20× magnification) with excitation/emission wavelength maxima of 490 nm/515 nm (DCF) or 350 nm/460 nm (DAPI). Images are representative of three independent experiments. The increase or the decrease of ROS generation in treated cells, shown as green fluorescence, was quantified using ImageJ.

4.2.8 Protein lysate and immunoblot analysis

Cells were grown in 6-well plates in complete medium, and before being treated, they were starved in serum-free medium for 24 h. Then cells were treated for 24–48 h with different compounds.

Then cells were rinsed twice with ice cold phosphate-buffered saline (PBS) and were then lysed immediately with 200 µL of cell lysis buffer (20 mM Tris–HCl, pH 7.4, 15 mM NaCl, 1 mM bglycerophosphate, 1 mM sodium orthovanadate, and 10 % glycerol). Cell lysates were cleared by centrifugation at 10,000 rpm for 2 min at 4 °C. Protein concentrations were determined using Bradford BIO-RAD protein assay. Equal amounts of lysates were resolved on a 7.5% SDS-polyacrylamide gel, transferred to a nitrocellulose membrane, and probed with antibodies directed against PARP-1 and GAPDH (Santa Cruz Biotechnology, TX, USA). The antigen–antibody complex was detected by incubation of the membranes for 1 h at room temperature with peroxidase coupled goat anti-rabbit IgG and was revealed using the ECL western blotting detection system (Amersham Pharmacia Biotech, Piscataway, NJ). Immunoblots show one representative image of three separate experiments.

4.2.9 Mitochondrial staining

For mitochondrial staining, cells were grown on coverslips in full media and were then serum-starved for 24 h for the indicated time with examined compounds. Then, they were incubated with pre-warmed (37 °C) staining solution containing MitoTracker Deep Red FM probe (MitoTracker Mitochondrion-Selective Probes, Invitrogen European Headquarters, Paisley PA4 9RF, UK) for 20 min (fluorescence excitation= 644 nm, fluorescence emission= 665 nm). Then, the cells, after PBS washes, were fixed with cold methanol. Coverslips were then washed three times with PBS. Nuclei were stained using DAPI (Sigma) for 10 min at a concentration of 0.2 µg mL^{-1} then washed three times with PBS. Fluorescence was detected by fluorescence microscopy (Leica DM 6000). LAS-X software was used to acquire and process all images.

4.2.10 Immunofluorescence

For immunocytochemistry, cells were grown on coverslips in full media, then serum-starved for 24 h and treated for the indicated time with examined compounds. Then they were PBS-washed and fixed with cold methanol (15 min/-20 °C) and washed three times (10 min/room temperature) with cold PBS containing 0.01% Triton X-100. After incubation (30 min/room

temperature) with blocking solution (PBS, 2% BSA), they were incubated with primary antibodies diluted in blocking solution (4 °C/overnight).

The primary antibody were raised against the following proteins:

- Cytochrome c (556433) was purchased from BD Biosciences (Franklin Lakes, NJ) and used at 1:100 dilution.
- E-cadherin (4065) and vimentin (3932) were purchased from Cell Signaling (Cell Signaling technology, Milan, Italy) and both used at 1:100 dilution;
- TNF-α (52B83), VEGF (A-20) and β-tubulin (9104) were acquired from Santa Cruz Biotechnology Inc. (Santa Cruz, CA, USA), were used at 1:50 (TNF- α), 1:100 (VEGF) and 1:200 (β-actin and β-tubulin) dilutions.

Coverslips were then washed three times with PBS, then fixed cells were incubated with the secondary antibodies Alexa Fluor® 568 conjugate goat-anti-mouse or Alexa Fluor® 488 conjugate goat-anti-rabbit (both used at 1:500 dilution and acquired from Thermo Fisher Scientific, MA, USA). Nuclei were stained using DAPI (Sigma) for 10 min at a concentration of 0.2 μg mL^{-1} then washed three times with PBS. Fluorescence was detected by fluorescence microscopy (Leica DM 6000). LAS-X software was used to acquire and process all images.

4.2.11 In vitro tubulin polymerization assay

Tubulin polymerization inhibition was measured using an in vitro tubulin polymerization assay kit purchased from EMD Millipore Corporation using the manufacturer's instructions. The polymerization reaction occurs in a 70 μL final volume, with 60 μM tubulin in 1× PB-GTP and the assayed at a concentration of 10 μM. Both Paclitaxel (**III**) and Vinblastine (**XIV**) (used as a control) were dissolved in DMSO and used at a final concentration of 10 μM. The mixtures were combined in a 96-well plate and readings were obtained using a Tecan microplate reader (37 °C, 10 second shaking before each reading) and the turbidity variation was measured every 30 seconds at 350 nm for 90 minutes.

4.2.12 Wound-healing assay

Cells were plated on six-well plates and cultured in full medium to produce confluent monolayers. They were wounded in a line using a standard 200-μL sterile pipette tip, then washed with phosphate buffered saline (PBS) to remove cell debris before incubation with various concentrations of each compound at its IC_{50} value. Images at time zero (t =0 h) were

acquired to record the initial area of the wound, and the recovery of the wounded monolayer due to cell migration toward the scratched area was estimated at 48 and 72 h (t =Δh). Images were captured using an inverted microscope equipped with digital camera (Leica DM 6000). The migration of cells toward the wounds was expressed as percentage of wound closure [Eq. (1)]:

$$\text{wound closure [\%]} = [(At_0 - At_{\Delta h}) \times (At_0)^{-1}] \times 100 \qquad (1)$$

for which At_0 is the area of wound measured immediately after scratching, and $At_{\Delta h}$ is the area of wound measured 48 or 72 h after scratching. Vehicle-treated cells were used as a control. The collected images were analyzed with Leica Application Suite X (LAS X) software. Each experiment was performed three times, and each treatment was conducted in three replicates. Representative images are shown.

4.3 NANOEMULSIONS

4.3.1 Materials

Kolliphor® HS15 (macrogol 15 hydroxystearate: 70% PEG 660 hydroxystearate and 30% free PEG 660), was kindly provided by BASF (Ludwigshafen, Germany). Labrafac® WL 1349 (triglycerides medium chain) and Transcutol® HP (diethylene glycol monoethyl ehter) were gifts from Gattefossé S.A. (Saint-Priest, France). Due to the complex composition of the excipients, the brand names are used throughout the text. KH_2PO_4, $Na_2HPO_4 \cdot 12\ H_2O$, $NaH_2PO_4 \cdot H_2O$, Dulbecco's phosphate buffered saline (DPBS), Quercetin (**XVI**) and *Cis*platin (**II**) were obtained from Sigma-Aldrich (Steinheim, Germany). NaCl was provided by Acros Organics (Geel, Belgium). Water, methanol and acetonitrile of HPLC analytical grade were obtained from Fisher Scientific (Loughborough, United Kingdom). The used demineralized water was obtained using a mixed bed ion exchange resin Distiplus DS450 (Grosseron, Couëron, France).

4.3.2 Formulation of nanoemulsions

Nanoemulsion formulation was adapted from spontaneous nano-emulsification method previously described by Gué E. *et al.* in 2016 [201]. The organic phase, composed of oil (Labrafac® WL 1349), surfactant (Kolliphor® HS 15) and cosurfactant (Transcutol® HP), was heated at 85 °C under gentle magnetic stirring (250 rpm) and cooled down at 25°C.

When the anhydrous mixture reached this temperature, the magnetic stirring was increased from 250 rpm to 750 rpm and the aqueous phase (10 mM or 65 mM phosphate buffer, 25 °C) was suddenly poured in, leading to spontaneous emulsification. After the addition of water, the stirring was maintained for 15 minutes at room temperature. In case of drugs-loaded nanoemulsions, the drugs were weighed with the organic phase, heated at 85 °C under gentle magnetic stirring (250 rpm) and mixed for 5 minutes by ultrasonic treatment at room temperature. Then, NEs were prepared as previously described.

4.3.3 Physicochemical characterization of the nanoemulsions

Dynamic light scattering was used to determine the average hydrodynamic diameter in volume, the polydispersity index (PDI) and the diameter distribution by volume of the nanoemulsions using a NanoZS® apparatus (Malvern Instruments, Worcestershire, UK) equipped with a 633 nm laser at a fixed scattering angle of 173°. The temperature of the cell was kept constant at 25°C. The nanoemulsions were filtrated through 0.2 µm regenerated cellulose syringe filters (Minisart® Syringe Filter, Sartorius, Goettingen, Germany) and diluted 1/100 (v/v) in NaCl 1 mM in order to assure an appropriate scattered intensity on the detector before measurements. Measurements were taken in triplicate.

4.3.4 Zeta potential measurement

Zeta potential analyses were made, after filtration and 1/100 dilution in NaCl 1 mM, using a NanoZS® apparatus equipped with DTS 1070 cell. All measurements were performed in triplicate at 25°C, with a dielectric constant of 78.5, a refractive index of 1.33, a viscosity of 0.8872 cP and a cell voltage of 150 V. The zeta potential was calculated from the electrophoretic mobility using the Smoluchowski equation.

4.3.5 pH and osmolarity measurements

The pH of nanoemulsions was measured using a pH-meter (Eutech instrument, Landsmeer, Netherlands) equipped with a microprobe (Fisherbrand, Fisher Scientific, Illkirch, France). The osmolarity of nanoemulsions was measured using a micro-osmometer autocal type 15/15M (Löser Messtechnik, Berlin, Germany) via freezing-point method. Typically, 100µL of nanoemulsions were introduced in microtube and measurements were performed.

4.3.6 Determination of the encapsulation efficiency and the drug loading

The encapsulation efficiency (EE) for Quercetin (**XVI**) was determined after filtration through 0.2 µm syringe filters (Minisart® Syringe Filter, Sartorius, Goettingen, Germany) to remove unentrapped drugs. Then, these samples were diluted in methanol (1/500) and the concentration of Quercetin (**XVI**) was determined by ultra-high-performance liquid chromatography (UHPLC) as described in 5.3.9 paragraph. The EE was determined in triplicate and calculated as follows:

$$EE\ (\%) = 100\ \times \frac{Quantity\ of\ drug\ entrapped}{Total\ quantity\ of\ drug\ added}$$

The drug loading (DL) was defined as:

$$DL\ (\%) = 100\ \times \frac{Quantity\ of\ drug\ entrapped}{Total\ quantity\ of\ excipients}$$

4.3.7 Stability studies

The short-term stability of the native nanoemulsions was investigated over a storage period of 14 days (for Quercetin (**XVI**)) and 7 days for Cisplatin (**II**) and for co-formulation at 4°C. The stock formulations (without dilution to mimic storage conditions) were stored at 4°C and diluted at regular intervals with a 1/100 dilution in NaCl 1 mM for evaluating the size distribution and zeta potential. A stability study at 37°C for 48 hours was also accomplished for Quercetin (**XVI**) nanoemulsions to mimic operating conditions for future *in vitro* and *in vivo* studies. Nanoemulsions were diluted at 1/20 and 1/100 in phosphate buffered saline (PBS) pH 7.4 (European pharmacopeia, 9th ed.) and were then placed in tubes in a water bath WNB-22 (Memmert, Schwabach, Germany) at 37°C under gentle horizontal shaking. The size measurements and distribution, the drugs concentration and the EE (%) were performed just after dilution and incubation. All assays and measurements were performed in triplicate.

4.3.8 *In vitro* drug release kinetics studies

Quercetin (**XVI**) release from nanoemulsions was studied by the dialysis bag method. For this purpose, 250 µL of Quercetin-loaded nanoemulsions were instilled into a cellulose ester dialysis bag (Spectra/Por® Biotech membranes, molecular weight cut-off: 100kDa, Spectrum Laboratories, Rancho Dominguez, California, United States) and incubated in 100 mL of PBS pH 7.4 in a water bath WNB-22 at 37°C and under gentle horizontal shaking.

Samples of 500 µL of PBS were withdrawn at appropriate intervals and the same volume was replaced with fresh PBS. In the case of Quercetin (**XVI**), Tween 80 (1%, v/v) was added to the acceptor compartment to respect sink conditions. The percentage of released drug was measured by UHPLC taking into account the cumulative removed quantity. All measurements were performed in triplicate.

4.3.9 UHPLC methods

Quercetin (**XVI**) concentration was determined by UHPLC. The UHPLC methods were based on those previously described by Gué E. *et al*. in 2016 (30). The UHPLC system comprised an Agilent® 1290 Infinity binary pump, an Agilent 1290 Infinity autosampler and an Agilent 1260 Infinity diode-array detector (Agilent technologies, Santa Clara, CA, USA). A reversed phase column C18 (5 µm, 2.1 × 50 mm, Restek® Ultra, Lisses France) was used as analytical column. Mobile phase was composed of a mixture of acetonitrile (A) and water containing 0.1 % (v/v) formic acid (B). Detection wavelength (λ), flow rate, total run time (T), gradient, injection volume, concentration range and retention time (Rt) used to analyze Quercetin (**XVI**) are listed in Table 19. The column temperature was 35 °C. In presence of nanoemulsions, no interaction with the tested drugs was highlighted. Linearity was good within the concentration range studied with a correlation coefficient higher than 0.99.

Drugs	λ (nm)	Flow (mL/min)	T (min)	Gradient		V_{inj} (µL)	Concentration range (µg/mL)
				t (min)	A (%)		
Quercetin (**XVI**)	370	0.6	3.20	0	20	3.0	0.5 - 10
				2.70	60		
				2.71	90		
				3.20	90		

Table 19. *UHPLC methods used for the quantification of Quercetin (**XVI**) concentration.*

4.3.10 ORAC assay

The ORAC assay is based on the scavenging of peroxyl radicals generated by AAPH, which prevent the degradation of the fluorescein probe and, consequently, prevent the loss of fluorescence of the probe. The reaction was carried out in a final volume of 200 µL in

Costar® 96 well black opaque plate (Corning Costar). 25 μL of samples (Quercetin (**XVI**) in DMSO and Quercetin (**XVI**) in nanoemulsion at 2% w/w) at different concentrations (range of 1-250 μM) and 150 μL of fluorescein 8 nM were mixed in the wells and pre-incubated for 30 min at 37 °C. Then, 25 μL of AAPH solution 75 mM was then added in each well, and the fluorescence was recorded each minute for 60 min at excitation and emission wavelengths of 485 and 530 nm, respectively using Synergy™ 2 Multi-Detection Microplate Reader (BioTek Instruments, Inc.). A blank sample containing 200 μL of phosphate buffer in the reaction mix was prepared and used as control. Four calibration solutions of Trolox (6.25, 12.5, 25, 50 and 100 μM final concentration) was also tested to establish a standard curve. All samples were analyzed in triplicate. The area under the curve (AUC) was calculated for each sample by integrating the relative fluorescence curve. The net AUC of the sample was calculated by subtracting the AUC of the blank. The regression equation between net AUC and Trolox concentration was determined, and ORAC values were expressed as μM compounds/ μM Trolox using the standard curve established previously.

Future perspectives

Among the human cancers, breast and uterine types represent the death cause of almost the 26% and 7% of women, respectively. The availability of new and improved chemotherapies facing the resistance occurrence and the toxic side effects is still a major challenge.

In this context, the studies carried out during my PhD have brought to light the interesting anticancer activities of new synthetized molecules.

In particular, the reported results have demonstrated that carbazolic compounds **4f**, **9c**, **15a** and **15d**, structurally correlated to the most known anticancer agents Ellipticine (**XIII**) and Vinblastine (**XIV**), could represent new potential molecules useful as valid alternative to the classic therapies. These compounds are able to exert interesting antiproliferative effects on *in vitro* models of the most common cancer types in women.

I also reported interesting results about new gold complexes **AuL4** and **AuL6** that could represent very promising and valid candidates for the development of improved metal-based compounds and for further preclinical investigations. The use of these complexes, in fact, could overcome the limitations in the clinical use of *Cis*platin (**II**) (dramatic side effects and the onset of resistance phenomena).

Other interesting compounds studied are represented by Thalidomide (**XV**) analogues **16c** and **16h**. In fact, repurposing of old drugs and screening toward new targets can reduce economic and practical research efforts. In this context, these molecules possess a marked anti-tumor activity, mostly against the highly metastatic MDA-MB-231, inducing cell death by apoptosis and interfering with metastatic and angiogenic processes.

Moreover, considering that natural-based alternatives with less toxicity have become recently more important, also Quercetin (**XVI**) derivatives were studied. The most active compounds **17a** and **17d** demonstrated their double value in cancer fighting: they were capable to protect healthy cells from oxidative stress and to induce cancer cells death by apoptosis.

Ultimately, it is well known that the development of new drugs is expensive and takes long time and that old drugs show some limitations (low solubility, low bioavailability, instability, etc). For these reasons, the improvement of their safety and efficacy through the design of drugs delivery system have become a very attractive and smart alternative, mostly in oncology. In this context, new formulations for Sunitinib (**XVII**), Quercetin (**XVI**) and *Cis*platin (**II**) permitted to obtain molecules with improved pharmaceutical profile, thanks

to the adjustment of physical-chemical and pharmacokinetic/pharmacodynamics drugs properties (solubility, chemical and / or metabolic stability, bioavailability, release and so on). This strategy shows a significantly higher benefit/risk ratio when comparing to the development of a new drug.

Since the promising results obtained for the different active molecules studied in terms of simple synthetic routes, good anti-proliferative activity, absence of toxicity and important biological targets, future studies will focus on the formulation of suitable vehicles that will allow to improve their physical-chemical properties and further *in vivo* studies that will allow to deepen pharmacokinetic/pharmacodynamics properties. These studies will open new perspectives for the development and the employment of these new tools in oncology.

Carbazolic compounds: Ellipticine (XIII) and Vinblastine (XIV) analogues			
	Compounds	**IC_{50} (µM)**	**Targets**
***N*-Alkylcarbazoles**	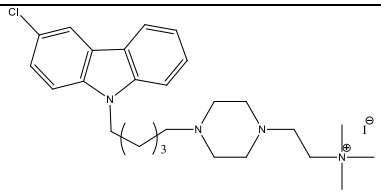 **4f**	4.4 ± 0.20 (MDA-MB-231)	hTopoII inhibition, ability to induce apoptosis (increase of caspases activity)
	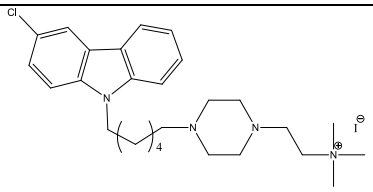 **4g**	5.8 ± 0.28 (MDA-MB-231)	
N-thioalkylcarbazoles	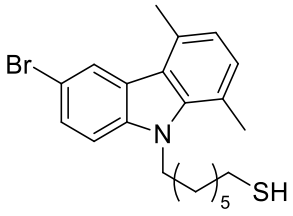 **9c**	11.3 ± 0.63 (HeLa)	hTopoII inhibition, ability to induce apoptosis (increase of caspases activity, release of cytocrom c and PARP-1 cleavage).
Benzothienoquinazolinones	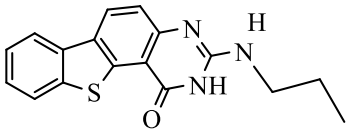 **15a**	3.88 ± 0.81 (MDA-MB-231)	Multi-target agents: hTopoI and Tubulin polimerization inhibition.
	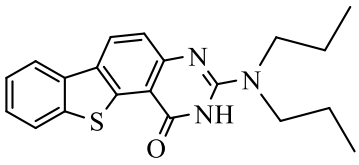 **15d**	4.69 ± 1.00 (MDA-MB-231)	

Table 20. *Summary of the biological properties of the most active carbazolic compounds studied*

New Au complexes: *Cis*platin (II) analogues		
Compounds	**IC_{50} (µM)**	**Targets**
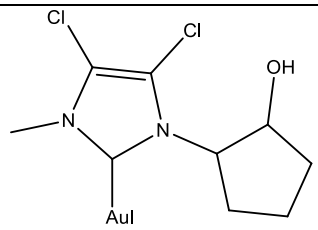 **AuL4**	1,63± 0.5 (MDA-MB-231)	Ability to induce apoptosis (increase of caspases activity, release of cytochrome c and PARP-1 cleavage and ROS production in cancer cells).
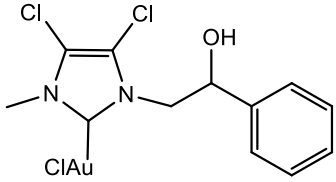 **AuL6**	2.10±0.7 (MDA-MB-231)	Multi-target tool: hTopoI, hTopo II and Tubulin polimerization inhibition.

Table 21. *Summary of the biological properties of the most active Au complexes studied*

Thalidomide (XV) analogues		
Compounds	**IC_{50} (µM)**	**Targets**
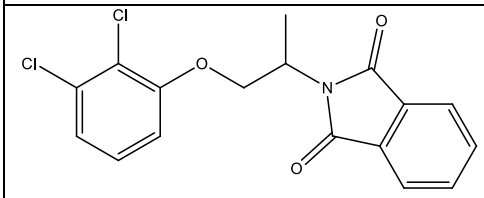 **16c**	56.48±1.3 (MDA-MB-231)	Ability to induce apoptosis, inhibition of cell migration and angiogenesis.
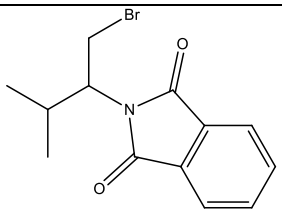 **16h**	37.16±1.0 (MDA-MB-231)	

Table 22. *Summary of the biological properties of the most active Thalidomide (**XV**) analogues studied*

Quercetin (XVI) analogues		
Compounds	**IC_{50} (µM)**	**Targets**
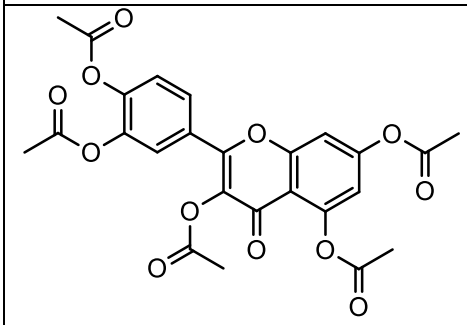 **17a**	10.9±0.9 (MDA-MB-231)	Ability to induce apoptosis, hTopoI and II inhibition, ROS production in cancer cells and ROS scavenging in non-tumoral cells.
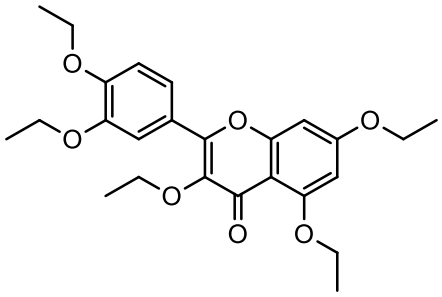 **17d**	16.6±0.4 (MDA-MB-231)	

Table 23. *Summary of the biological properties of the most active Quercetin (**XVI**) derivatives studied.*

Abbreviations

^{13}C-NMR = carbon-13 nuclear magnetic resonance
^{1}H-NMR = proton-1 nuclear magnetic resonance
A = adenine
ACTH = adenocorticotropic hormone
AIBN = azobisisobutyrronitrile
Ala = alanine
AMP-PNP = adenylyl-imidodiphosphate
APPH = 2,2'-azobis(2-amidinopropane) dihydrochloride
Asn = asparagine
Asp = aspartate
ATCC = American type culture collection
ATP = adenosine triphosphate
AUC = area under the curve
Boc = tert-butoxycarbonyl
BRCA-1 = breast cancer gene 1
BRCA-2 = breast cancer gene 2
BSA = bovine serum albumine
Cbz = carboxybenzyl
CDIS = carcinoma lobular in situ
CLIS = carcinoma ductal in situ
CTRL = control
DAPI = 4',6-diamidino-2-phenylindole
DCC = dextran-coated charcoal
DCF-DA = 2′,7′-dichlorofluorescin diacetate
DHFR = dihydrofolate reductase
DL = drug loading
DMEM = dulbecco's modified eagle's medium
DMEM-F12 = dulbecco's modified eagle's medium/nutrient mixture ham F-12
DMF = dimethylformamide
DMSO = dimethyl sulfoxide
DNA = deoxyribonucleic acid
DPBS = dulbecco's phosphate-buffered saline
DTT = dithiothreitol
E = earl
EB = ethidium bromide
EC = endometrial carcinoma
ECL = enhanced chemiluminescent
EDTA = ethylenediamine tetraacetic acid
EE = encapsulation efficiency
EGDMA = ethylene glycol dimethacrylate
EMT = epithelial-mesenchymal transition
ER = estrogenic
ESI = electrospray ionization
ESI-MS = electrospray ionization mass spectrometry
Et = ethyl
FBS = fetal bovine serum
FIGO = international federation of gynecology and obstetrics
FSH = folliculo-stimulating hormone

G = guanine
GADPH = gliceraldeide-3-fosfato deidrogenasi
GH = growth hormone
Gln = glutamine
Glu = glutamate
hEGF = human epidermal growth factor
HER2 = epidermal growth factor
HIV = human immunodeficiency virus
HPLC = high performance liquid chromatography
HPV = human papillomavirus
HS = horse serum
Hsp =heat shock protein
hTopo = human topoisomerase
IC_{50} = half maximal inhibitory concentration
Ile = isoleucine
k-DNA = kinetoplastic-deoxyribonucleic acid
L = late
LAS X = leica application suite X
LCR = long control region
Leu = leucine
LH = luteinized hormone
Lys = lysine
MAA = methacrylic acid
MEM = minimum essential eagle's medium
Men = menadione
MIP = molecularly imprinted polymer
MTT = 3-(4,5-dimethylthiazol- 2-yl)-2,5-diphenyltetrazolium bromide
NCS = newborn calf serum
NE = nanoemulsion
NEAA =non-essential amino acids
NHC = *N*-heteroclycic carbene
NIP = non-imprinted polymer
NMR = nuclear magnetic resonance
OD = optical density
ORAC = oxygen radical absorbance capacity
PARP-1 = poly(ADP-ribose) polymerase 1
PBS = phosphate-buffered saline
PDB = protein data bank
PDI =polydispersity index
PEG = polyethylene glycol
Phe = phenylalanine
pHOT1 = supercoiled plasmid
PI3K = phosphoinositide 3 kinase
PR = progesterone
Pr = propyl
PRL = prolactin
PTEN = phosphatase and tensin homologue
PTLC = preparative thin layer chromatography
PV = papillomavirus
RNA = ribonucleic acid

ROS = reactive oxygen species
Rt = retention time
SD = standard deviation
Ser = serine
T3 = triiodothyronine hormone
T4 = triiodothyroxine hormone
TAE = tris-acetate-EDTA buffer
TDLU = terminal ductal lobular unit
TdT = terminal deoxynucleotidyl transferase
TE = tris-EDTA buffer
THF = tetrahydrofuran
Thr = threonine
TNF-α = tumor necrosis factor alpha
TUNEL = terminal deoxynucleotidyl transferase dUTP nick end labeling
Tyr = tyrosine
UHPLC = ultra high performance liquid chromatography
UV = ultra-violet
Val = valine
VEGF = vascular endothelial growth factot
VLP = virus like particles

References

1. Siegel, R.L.; Miller, K.D.; Jemal, A. Cancer statistics, 2016. *CA Cancer J Clin* **2016**, *66*, 7-30, doi:10.3322/caac.21332.
2. Jesinger, R.A. Breast anatomy for the interventionalist. *Tech Vasc Interv Radiol* **2014**, *17*, 3-9, doi:10.1053/j.tvir.2013.12.002.
3. AIROM-AIRTUM. *I numeri del cancro in Italia, 2018*; 2018.
4. Miller, K. Estrogen and DNA damage: the silent source of breast cancer? *J Natl Cancer Inst* **2003**, *95*, 100-102, doi:10.1093/jnci/95.2.100.
5. AIOM. *Linee guida neoplasie della mammella*; 2018.
6. Wooster, R.; Bignell, G.; Lancaster, J.; Swift, S.; Seal, S.; Mangion, J.; Collins, N.; Gregory, S.; Gumbs, C.; Micklem, G. Identification of the breast cancer susceptibility gene BRCA2. *Nature* **1995**, *378*, 789-792, doi:10.1038/378789a0.
7. Malhotra, G.K.; Zhao, X.; Band, H.; Band, V. Histological, molecular and functional subtypes of breast cancers. *Cancer Biol Ther* **2010**, *10*, 955-960, doi:10.4161/cbt.10.10.13879.
8. Dai, X.; Li, T.; Bai, Z.; Yang, Y.; Liu, X.; Zhan, J.; Shi, B. Breast cancer intrinsic subtype classification, clinical use and future trends. *Am J Cancer Res* **2015**, *5*, 2929-2943.
9. Nounou, M.I.; ElAmrawy, F.; Ahmed, N.; Abdelraouf, K.; Goda, S.; Syed-Sha-Qhattal, H. Breast Cancer: Conventional Diagnosis and Treatment Modalities and Recent Patents and Technologies. *Breast Cancer (Auckl)* **2015**, *9*, 17-34, doi:10.4137/BCBCR.S29420.
10. Tong, C.W.S.; Wu, M.; Cho, W.C.S.; To, K.K.W. Recent Advances in the Treatment of Breast Cancer. *Front Oncol* **2018**, *8*, 227, doi:10.3389/fonc.2018.00227.
11. Gossman, W.; Fagan, S.E.; Sosa-Stanley, J.N.; Peterson, D.C. Anatomy, Abdomen and Pelvis, Uterus. In *StatPearls*, Treasure Island (FL), 2019.
12. AIOM. Linee guida "Neoplasie dell'utero: endometrio e cervice". **2018**.
13. de Villiers, E.M.; Fauquet, C.; Broker, T.R.; Bernard, H.U.; zur Hausen, H. Classification of papillomaviruses. *Virology* **2004**, *324*, 17-27, doi:10.1016/j.virol.2004.03.033.
14. Doorbar, J.; Ely, S.; Sterling, J.; McLean, C.; Crawford, L. Specific interaction between HPV-16 E1-E4 and cytokeratins results in collapse of the epithelial cell intermediate filament network. *Nature* **1991**, *352*, 824-827, doi:10.1038/352824a0.
15. Giroglou, T.; Florin, L.; Schafer, F.; Streeck, R.E.; Sapp, M. Human papillomavirus infection requires cell surface heparan sulfate. *J Virol* **2001**, *75*, 1565-1570, doi:10.1128/JVI.75.3.1565-1570.2001.
16. Pinidis, P.; Tsikouras, P.; Iatrakis, G.; Zervoudis, S.; Koukouli, Z.; Bothou, A.; Galazios, G.; Vladareanu, S. Human Papilloma Virus' Life Cycle and Carcinogenesis. *Maedica (Buchar)* **2016**, *11*, 48-54.
17. Sterling, J.; Stanley, M.; Gatward, G.; Minson, T. Production of human papillomavirus type 16 virions in a keratinocyte cell line. *J Virol* **1990**, *64*, 6305-6307.
18. Frazer, I.H. Prevention of cervical cancer through papillomavirus vaccination. *Nat Rev Immunol* **2004**, *4*, 46-54, doi:10.1038/nri1260.
19. Bulkmans, N.W.; Berkhof, J.; Bulk, S.; Bleeker, M.C.; van Kemenade, F.J.; Rozendaal, L.; Snijders, P.J.; Meijer, C.J.; Group, P.S. High-risk HPV type-specific clearance rates in cervical screening. *Br J Cancer* **2007**, *96*, 1419-1424, doi:10.1038/sj.bjc.6603653.

20. Peralta-Zaragoza, O.; Bermudez-Morales, V.H.; Perez-Plasencia, C.; Salazar-Leon, J.; Gomez-Ceron, C.; Madrid-Marina, V. Targeted treatments for cervical cancer: a review. *Onco Targets Ther* **2012**, *5*, 315-328, doi:10.2147/OTT.S25123.
21. Yee, G.P.; de Souza, P.; Khachigian, L.M. Current and potential treatments for cervical cancer. *Curr Cancer Drug Targets* **2013**, *13*, 205-220, doi:10.2174/1568009611313020009.
22. Charo, L.M.; Plaxe, S.C. Recent advances in endometrial cancer: a review of key clinical trials from 2015 to 2019. *F1000Res* **2019**, *8*, doi:10.12688/f1000research.17408.1.
23. Dahlgren, E.; Friberg, L.G.; Johansson, S.; Lindstrom, B.; Oden, A.; Samsioe, G.; Janson, P.O. Endometrial carcinoma; ovarian dysfunction--a risk factor in young women. *Eur J Obstet Gynecol Reprod Biol* **1991**, *41*, 143-150, doi:10.1016/0028-2243(91)90092-y.
24. Beretta, M.; Bauer, M.; Hirsch, E. PI3K signaling in the pathogenesis of obesity: The cause and the cure. *Adv Biol Regul* **2015**, *58*, 1-15.
25. Westin, S.N.; Ju, Z.; Broaddus, R.R.; Krakstad, C.; Li, J.; Pal, N.; Lu, K.H.; Coleman, R.L.; Hennessy, B.T.; Klempner, S.J., et al. PTEN loss is a context-dependent outcome determinant in obese and non-obese endometrioid endometrial cancer patients. *Mol Oncol* **2015**, *9*, 1694-1703, doi:10.1016/j.molonc.2015.04.014.
26. May, K.; Bryant, A.; Dickinson, H.O.; Kehoe, S.; Morrison, J. Lymphadenectomy for the management of endometrial cancer. *Cochrane Database Syst Rev* **2010**, 10.1002/14651858.CD007585.pub2, CD007585.
27. Dasari, S.; Tchounwou, P.B. Cisplatin in cancer therapy: molecular mechanisms of action. *Eur J Pharmacol* **2014**, *740*, 364-378, doi:10.1016/j.ejphar.2014.07.025.
28. Deane, F.M.; O'Sullivan, E.C.; Maguire, A.R.; Gilbert, J.; Sakoff, J.A.; McCluskey, A.; McCarthy, F.O. Synthesis and evaluation of novel ellipticines as potential anti-cancer agents. *Org Biomol Chem* **2013**, *11*, 1334-1344, doi:10.1039/c2ob27186a.
29. Akram, T.; Maseelall, P.; Fanning, J. Carboplatin and paclitaxel for the treatment of advanced or recurrent endometrial cancer. *Am J Obstet Gynecol* **2005**, *192*, 1365-1367, doi:10.1016/j.ajog.2004.12.032.
30. Waldau, D.; Mikolasch, A.; Lalk, M.; Schauer, F. Derivatization of bioactive carbazoles by the biphenyl-degrading bacterium Ralstonia sp. strain SBUG 290. *Appl Microbiol Biotechnol* **2009**, *83*, 67-75, doi:10.1007/s00253-008-1853-z.
31. Caruso, A.; Iacopetta, D.; Puoci, F.; Cappello, A.R.; Saturnino, C.; Sinicropi, M.S. Carbazole derivatives: a promising scenario for breast cancer treatment. *Mini Rev Med Chem* **2016**, *16*, 630-643, doi:10.2174/1389557515666150709111342.
32. Sinicropi, M.S.; Lappano, R.; Caruso, A.; Santolla, M.F.; Pisano, A.; Rosano, C.; Capasso, A.; Panno, A.; Lancelot, J.C.; Rault, S., et al. (6-bromo-1,4-dimethyl-9H-carbazol-3-yl-methylene)-hydrazine (carbhydraz) acts as a GPER agonist in breast cancer cells. *Curr Top Med Chem* **2015**, *15*, 1035-1042, doi:10.2174/1568026615666150317221549.
33. Stiborova, M.; Frei, E. Ellipticines as DNA-targeted chemotherapeutics. *Curr Med Chem* **2014**, *21*, 575-591, doi:10.2174/09298673113206660272.
34. Isah, T. Rethinking Ginkgo biloba L.: Medicinal uses and conservation. *Pharmacogn Rev* **2015**, *9*, 140-148, doi:10.4103/0973-7847.162137.
35. Miller, C.M.; O'Sullivan, E.C.; Devine, K.J.; McCarthy, F.O. Synthesis and biological evaluation of novel isoellipticine derivatives and salts. *Org Biomol Chem* **2012**, *10*, 7912-7921, doi:10.1039/c2ob26181b.
36. Bradley, W.G. Side-effects of Vinca alkaloids. *Br Med J* **1968**, *3*, 58, doi:10.1136/bmj.3.5609.58.

37. Caruso, A.; Chimento, A.; El-Kashef, H.; Lancelot, J.C.; Panno, A.; Pezzi, V.; Saturnino, C.; Sinicropi, M.S.; Sirianni, R.; Rault, S. Antiproliferative activity of some 1,4-dimethylcarbazoles on cells that express estrogen receptors: part I. *J Enzyme Inhib Med Chem* **2012**, *27*, 609-613, doi:10.3109/14756366.2011.603132.
38. Shaikh, M.S.; Karpoormath, R.; Thapliyal, N.; Rane, R.A.; Palkar, M.B.; Faya, A.M.; Patel, H.M.; Alwan, W.S.; Jain, K.; Hampannavar, G.A. Current perspective of natural alkaloid carbazole and its derivatives as antitumor agents. *Anticancer Agents Med Chem* **2015**, *15*, 1049-1065, doi:10.2174/1871520615666150113105405.
39. Liu, S.; Lin, P.; Niu, F.; Zeng, P.; Zhang, B. pi-Bridge Effect on Symmetric Carbazole-Based Small Molecules for Realizing Ultraviolet Fluorescent Emission. *Materials (Basel)* **2018**, *11*, doi:10.3390/ma11040617.
40. Zhu, D.; Chen, M.; Li, M.; Luo, B.; Zhao, Y.; Huang, P.; Xue, F.; Rapposelli, S.; Pi, R.; Wen, S. Discovery of novel N-substituted carbazoles as neuroprotective agents with potent anti-oxidative activity. *Eur J Med Chem* **2013**, *68*, 81-88, doi:10.1016/j.ejmech.2013.07.029.
41. Saturnino, C.; Iacopetta, D.; Sinicropi, M.S.; Rosano, C.; Caruso, A.; Caporale, A.; Marra, N.; Marengo, B.; Pronzato, M.A.; Parisi, O.I., et al. N-alkyl carbazole derivatives as new tools for Alzheimer's disease: preliminary studies. *Molecules* **2014**, *19*, 9307-9317, doi:10.3390/molecules19079307.
42. Nandy, B.C.; Gupta, A.K.; Mittal, A.; Vyas, V.; Academy, R. Carbazole: it's biological activity. *J Biomed and Pharm Res* **2014**, *3*, 42-48.
43. Rault, S.; Lancelot, J.C.; Caruso, A.; Lesnard, A.; Cresteil, N.; Aubert, G. Use Of Carbazole-phenone Derivatives For Treating Cancer. 2013.
44. Gluszynska, A. Biological potential of carbazole derivatives. *Eur J Med Chem* **2015**, *94*, 405-426, doi:10.1016/j.ejmech.2015.02.059.
45. Sinicropi, M.S.; Iacopetta, D.; Rosano, C.; Randino, R.; Caruso, A.; Saturnino, C.; Muia, N.; Ceramella, J.; Puoci, F.; Rodriquez, M., et al. N-thioalkylcarbazoles derivatives as new anti-proliferative agents: synthesis, characterisation and molecular mechanism evaluation. *J Enzyme Inhib Med Chem* **2018**, *33*, 434-444, doi:10.1080/14756366.2017.1419216.
46. Saturnino, C.; Palladino, C.; Napoli, M.; Sinicropi, M.S.; Botta, A.; Sala, M.; Carcereri de Prati, A.; Novellino, E.; Suzuki, H. Synthesis and biological evaluation of new N-alkylcarbazole derivatives as STAT3 inhibitors: preliminary study. *Eur J Med Chem* **2013**, *60*, 112-119, doi:10.1016/j.ejmech.2012.11.004.
47. Nakamura, K.; Sugumi, H.; Yamaguchi, A.; Uenaka, T.; Kotake, Y.; Okada, T.; Kamata, J.; Niijima, J.; Nagasu, T.; Koyanagi, N., et al. Antitumor activity of ER-37328, a novel carbazole topoisomerase II inhibitor. *Mol Cancer Ther* **2002**, *1*, 169-175.
48. Zhu, G.; Conner, S.E.; Zhou, X.; Chan, H.K.; Shih, C.; Engler, T.A.; Al-Awar, R.S.; Brooks, H.B.; Watkins, S.A.; Spencer, C.D., et al. Synthesis of 1,7-annulated indoles and their applications in the studies of cyclin dependent kinase inhibitors. *Bioorg Med Chem Lett* **2004**, *14*, 3057-3061, doi:10.1016/j.bmcl.2004.04.033.
49. Saturnino, C.; Caruso, A.; Iacopetta, D.; Rosano, C.; Ceramella, J.; Muia, N.; Mariconda, A.; Bonomo, M.G.; Ponassi, M.; Rosace, G., et al. Inhibition of Human Topoisomerase II by N,N,N-Trimethylethanammonium Iodide Alkylcarbazole Derivatives. *ChemMedChem* **2018**, *13*, 2635-2643, doi:10.1002/cmdc.201800546.
50. Vann, K.R.; Ergun, Y.; Zencir, S.; Oncuoglu, S.; Osheroff, N.; Topcu, Z. Inhibition of human DNA topoisomerase IIalpha by two novel ellipticine derivatives. *Bioorg Med Chem Lett* **2016**, *26*, 1809-1812, doi:10.1016/j.bmcl.2016.02.034.

51. Iacopetta, D.; Rosano, C.; Puoci, F.; Parisi, O.I.; Saturnino, C.; Caruso, A.; Longo, P.; Ceramella, J.; Malzert-Freon, A.; Dallemagne, P., et al. Multifaceted properties of 1,4-dimethylcarbazoles: Focus on trimethoxybenzamide and trimethoxyphenylurea derivatives as novel human topoisomerase II inhibitors. *Eur J Pharm Sci* **2017**, *96*, 263-272, doi:10.1016/j.ejps.2016.09.039.
52. Rizza, P.; Pellegrino, M.; Caruso, A.; Iacopetta, D.; Sinicropi, M.S.; Rault, S.; Lancelot, J.C.; El-Kashef, H.; Lesnard, A.; Rochais, C., et al. 3-(Dipropylamino)-5-hydroxybenzofuro[2,3-f]quinazolin-1(2H)-one (DPA-HBFQ-1) plays an inhibitory role on breast cancer cell growth and progression. *Eur J Med Chem* **2016**, *107*, 275-287, doi:10.1016/j.ejmech.2015.11.004.
53. Michetti, C.; Romano, E.; Altabella, L.; Caruso, A.; Castelluccio, P.; Bedse, G.; Gaetani, S.; Canese, R.; Laviola, G.; Scattoni, M.L. Mapping pathological phenotypes in reelin mutant mice. *Front Pediatr* **2014**, *2*, 95, doi:10.3389/fped.2014.00095.
54. Caruso, A.M.; Meyer, T.K.; Allen, C.T. Hoarseness after metastatic colon cancer treatment. *JAMA Otolaryngol Head Neck Surg* **2014**, *140*, 881-882, doi:10.1001/jamaoto.2014.1766.
55. Sanner, M.F.; Duncan, B.S.; Carrillo, C.J.; Olson, A.J. Integrating computation and visualization for biomolecular analysis: an example using python and AVS. *Pac Symp Biocomput* **1999**, 10.1142/9789814447300_0039, 401-412, doi:10.1142/9789814447300_0039.
56. Saturnino, C.; Caruso, A.; Longo, P.; Capasso, A.; Pingitore, A.; Caroleo, M.C.; Cione, E.; Perri, M.; Nicolo, F.; Nardo, V.M., et al. Crystallographic study and biological evaluation of 1,4-dimethyl-N-alkylcarbazoles. *Curr Top Med Chem* **2015**, *15*, 973-979, doi:10.2174/1568026615666150317222444.
57. Caruso, A.; Sinicropi, M.S.; Lancelot, J.C.; El-Kashef, H.; Saturnino, C.; Aubert, G.; Ballandonne, C.; Lesnard, A.; Cresteil, T.; Dallemagne, P., et al. Synthesis and evaluation of cytotoxic activities of new guanidines derived from carbazoles. *Bioorg Med Chem Lett* **2014**, *24*, 467-472, doi:10.1016/j.bmcl.2013.12.047.
58. D'Amours, D.; Desnoyers, S.; D'Silva, I.; Poirier, G.G. Poly(ADP-ribosyl)ation reactions in the regulation of nuclear functions. *Biochem J* **1999**, *342 (Pt 2)*, 249-268.
59. Kaufmann, S.H.; Desnoyers, S.; Ottaviano, Y.; Davidson, N.E.; Poirier, G.G. Specific proteolytic cleavage of poly(ADP-ribose) polymerase: an early marker of chemotherapy-induced apoptosis. *Cancer Res* **1993**, *53*, 3976-3985.
60. Soldani, C.; Scovassi, A.I. Poly(ADP-ribose) polymerase-1 cleavage during apoptosis: an update. *Apoptosis* **2002**, *7*, 321-328, doi:10.1023/a:1016119328968.
61. Elmore, S. Apoptosis: a review of programmed cell death. *Toxicol Pathol* **2007**, *35*, 495-516, doi:10.1080/01926230701320337.
62. Cullen, S.P.; Martin, S.J. Caspase activation pathways: some recent progress. *Cell Death Differ* **2009**, *16*, 935-938, doi:10.1038/cdd.2009.59.
63. Kadam, C.Y.; Abhang, S.A. Apoptosis Markers in Breast Cancer Therapy. *Adv Clin Chem* **2016**, *74*, 143-193, doi:10.1016/bs.acc.2015.12.003.
64. Suen, D.F.; Norris, K.L.; Youle, R.J. Mitochondrial dynamics and apoptosis. *Genes Dev* **2008**, *22*, 1577-1590, doi:10.1101/gad.1658508.
65. Khodarahmi, G.; Asadi, P.; Hassanzadeh, F.; Khodarahmi, E. Benzofuran as a promising scaffold for the synthesis of antimicrobial and antibreast cancer agents: A review. *J Res Med Sci* **2015**, *20*, 1094-1104.
66. Yu, B.L.; Dietz, B.M.; Dunlap, T.; Kastrati, I.; Lantvit, D.D.; Overk, C.R.; Yao, P.; Qin, Z.H.; Bolton, J.L.; Thatcher, G.R.J. Structural modulation of reactivity/activity

in design of improved benzothiophene selective estrogen receptor modulators: induction of chemopreventive mechanisms. *Mol Cancer Ther* **2007**, *6*, 2418-2428, doi:10.1158/1535-7163.MCT-07-0268.
67. Koruznjak, J.D.; Grdisa, M.; Slade, N.; Zamola, B.; Pavelic, K.; Karminski-Zamola, G. Novel derivatives of benzo[b]thieno[2,3-c]quinolones: Synthesis, photochemical synthesis, and antitumor evaluation. *J Med Chem* **2003**, *46*, 4516-4524, doi:10.1021/jm0210966.
68. Ceramella, J.; Caruso, A.; Occhiuzzi, M.A.; Iacopetta, D.; Barbarossa, A.; Rizzuti, B.; Dallemagne, P.; Rault, S.; El-Kashef, H.; Saturnino, C., et al. Benzothienoquinazolinones as new multi-target scaffolds: Dual inhibition of human Topoisomerase I and tubulin polymerization. *Eur J Med Chem* **2019**, *181*, 111583, doi:10.1016/j.ejmech.2019.111583.
69. Caruso, A.; Lancelot, J.C.; El-Kashef, H.; Sinicropi, M.S.; Legay, R.; Lesnard, A.; Rault, S. A rapid and versatile synthesis of novel pyrimido[5,4-b]carbazoles. *Tetrahedron* **2009**, *65*, 10400-10405, doi:10.1016/j.tet.2009.10.025.
70. Caruso, A.; Lancelot, J.C.; El-Kashef, H.; Panno, A.; Sinicropi, M.S.; Legay, R.; Lesnard, A.; Lepailleur, A.; Rault, S. Four Partners, Three-Step, One-Pot Reaction for a Library of New 2-Alkyl(dialkyl)aminoquinazolin-4(3H)-ones. *J Heterocycl Chem* **2014**, *51*, E282-E293, doi:10.1002/jhet.1942.
71. Wu, Y.C.; Li, J.C.; Wu, J.J.; Morgan, P.; Xu, X.; Rancati, F.; Vallese, S.; Raveglia, L.; Hotchandani, R.; Fuller, N., et al. Discovery of potent and selective matrix metalloprotease 12 inhibitors for the potential treatment of chronic obstructive pulmonary disease (COPD). *Bioorg Med Chem Lett* **2012**, *22*, 138-143, doi:DOI 10.1016/j.bmcl.2011.11.046.
72. Zabka, A.; Winnicki, K.; Polit, J.T.; Maszewski, J. The effects of anti-DNA topoisomerase II drugs, etoposide and ellipticine, are modified in root meristem cells of Allium cepa by MG132, an inhibitor of 26S proteasomes. *Plant Physiol Biochem* **2015**, *96*, 72-82, doi:10.1016/j.plaphy.2015.07.016.
73. Abal, M.; Andreu, J.M.; Barasoain, I. Taxanes: microtubule and centrosome targets, and cell cycle dependent mechanisms of action. *Curr Cancer Drug Targets* **2003**, *3*, 193-203.
74. Jordan, M.A.; Wilson, L. Microtubules as a target for anticancer drugs. *Nat Rev Cancer* **2004**, *4*, 253-265, doi:10.1038/nrc1317.
75. Gan, P.P.; McCarroll, J.A.; Po'uha, S.T.; Kamath, K.; Jordan, M.A.; Kavallaris, M. Microtubule dynamics, mitotic arrest, and apoptosis: drug-induced differential effects of betaIII-tubulin. *Mol Cancer Ther* **2010**, *9*, 1339-1348, doi:10.1158/1535-7163.MCT-09-0679.
76. Brouhard, G.J.; Rice, L.M. The contribution of alphabeta-tubulin curvature to microtubule dynamics. *J Cell Biol* **2014**, *207*, 323-334, doi:10.1083/jcb.201407095.
77. Banerjee, S.; Hwang, D.J.; Li, W.; Miller, D.D. Current Advances of Tubulin Inhibitors in Nanoparticle Drug Delivery and Vascular Disruption/Angiogenesis. *Molecules* **2016**, *21*, 1468-1504, doi:10.3390/molecules21111468.
78. Kaur, R.; Kaur, G.; Gill, R.K.; Soni, R.; Bariwal, J. Recent developments in tubulin polymerization inhibitors: An overview. *Eur J Med Chem* **2014**, *87*, 89-124, doi:10.1016/j.ejmech.2014.09.051.
79. McWhinney, S.R.; Goldberg, R.M.; McLeod, H.L. Platinum neurotoxicity pharmacogenetics. *Mol Cancer Ther* **2009**, *8*, 10-16, doi:10.1158/1535-7163.MCT-08-0840.

80. Ott, I.; Gust, R. Preclinical and clinical studies on the use of platinum complexes for breast cancer treatment. *Anticancer Agents Med Chem* **2007**, *7*, 95-110, doi:10.2174/187152007779314071.
81. van Rijt, S.H.; Sadler, P.J. Current applications and future potential for bioinorganic chemistry in the development of anticancer drugs. *Drug Discov Today* **2009**, *14*, 1089-1097, doi:10.1016/j.drudis.2009.09.003.
82. Abu-Surrah, A.S.; Kettunen, M. Platinum group antitumor chemistry: design and development of new anticancer drugs complementary to cisplatin. *Curr Med Chem* **2006**, *13*, 1337-1357, doi:10.2174/092986706776872970.
83. Ingawale, D.K.; Mandlik, S.K.; Naik, S.R. Models of hepatotoxicity and the underlying cellular, biochemical and immunological mechanism(s): a critical discussion. *Environ Toxicol Pharmacol* **2014**, *37*, 118-133, doi:10.1016/j.etap.2013.08.015.
84. Zanella, A.; Gandin, V.; Porchia, M.; Refosco, F.; Tisato, F.; Sorrentino, F.; Scutari, G.; Rigobello, M.P.; Marzano, C. Cytotoxicity in human cancer cells and mitochondrial dysfunction induced by a series of new copper(I) complexes containing tris(2-cyanoethyl)phosphines. *Invest New Drugs* **2011**, *29*, 1213-1223, doi:10.1007/s10637-010-9466-7.
85. Berners-Price, S.J. Activating platinum anticancer complexes with visible light. *Angew Chem Int Ed Engl* **2011**, *50*, 804-805, doi:10.1002/anie.201004552.
86. Gao, E.; Liu, C.; Zhu, M.; Lin, H.; Wu, Q.; Liu, L. Current development of Pd(II) complexes as potential antitumor agents. *Anticancer Agents Med Chem* **2009**, *9*, 356-368, doi:10.2174/1871520610909030356.
87. Bruijnincx, P.C.; Sadler, P.J. New trends for metal complexes with anticancer activity. *Curr Opin Chem Biol* **2008**, *12*, 197-206, doi:10.1016/j.cbpa.2007.11.013.
88. Napoli, M.; Saturnino, C.; Sirignano, E.; Popolo, A.; Pinto, A.; Longo, P. Synthesis, characterization and cytotoxicity studies of methoxy alkyl substituted metallocenes. *Eur J Med Chem* **2011**, *46*, 122-128, doi:10.1016/j.ejmech.2010.10.021.
89. Sirignano, E.; Saturnino, C.; Botta, A.; Sinicropi, M.S.; Caruso, A.; Pisano, A.; Lappano, R.; Maggiolini, M.; Longo, P. Synthesis, characterization and cytotoxic activity on breast cancer cells of new half-titanocene derivatives. *Bioorg Med Chem Lett* **2013**, *23*, 3458-3462, doi:10.1016/j.bmcl.2013.03.059.
90. Chimento, A.; Saturnino, C.; Iacopetta, D.; Mazzotta, R.; Caruso, A.; Plutino, M.R.; Mariconda, A.; Ramunno, A.; Sinicropi, M.S.; Pezzi, V., et al. Inhibition of human topoisomerase I and II and anti-proliferative effects on MCF-7 cells by new titanocene complexes. *Bioorg Med Chem* **2015**, *23*, 7302-7312, doi:10.1016/j.bmc.2015.10.030.
91. Sirignano, E.; Pisano, A.; Caruso, A.; Saturnino, C.; Sinicropi, M.S.; Lappano, R.; Botta, A.; Iacopetta, D.; Maggiolini, M.; Longo, P. Different 6-Aryl-Fulvenes Exert Anti-proliferative effects on Cancer Cells. *Anticancer Agents Med Chem* **2015**, *15*, 468-474, doi:10.2174/1871520614666141019190855.
92. Saturnino, C.; Sirignano, E.; Botta, A.; Sinicropi, M.S.; Caruso, A.; Pisano, A.; Lappano, R.; Maggiolini, M.; Longo, P. New titanocene derivatives with high antiproliferative activity against breast cancer cells. *Bioorg Med Chem Lett* **2014**, *24*, 136-140, doi:10.1016/j.bmcl.2013.11.058.
93. Gasser, G.; Ott, I.; Metzler-Nolte, N. Organometallic anticancer compounds. *J Med Chem* **2011**, *54*, 3-25, doi:10.1021/jm100020w.
94. Medvetz, D.A.; Hindi, K.M.; Panzner, M.J.; Ditto, A.J.; Yun, Y.H.; Youngs, W.J. Anticancer Activity of Ag(I) N-Heterocyclic Carbene Complexes Derived from 4,5-

Dichloro-1H-Imidazole. *Met Based Drugs* **2008**, *2008*, 384010, doi:10.1155/2008/384010.
95. Rubbiani, R.; Kitanovic, I.; Alborzinia, H.; Can, S.; Kitanovic, A.; Onambele, L.A.; Stefanopoulou, M.; Geldmacher, Y.; Sheldrick, W.S.; Wolber, G., et al. Benzimidazol-2-ylidene gold(I) complexes are thioredoxin reductase inhibitors with multiple antitumor properties. *J Med Chem* **2010**, *53*, 8608-8618, doi:10.1021/jm100801e.
96. Russell, A.D.; Hugo, W.B. Antimicrobial activity and action of silver. *Prog Med Chem* **1994**, *31*, 351-370, doi:10.1016/s0079-6468(08)70024-9.
97. Napoli, M.; Saturnino, C.; Cianciulli, E.I.; Varcamonti, M.; Zanfardino, A.; Tommonaro, G.; Longo, P. Silver(I) N-heterocyclic carbene complexes: Synthesis, characterization and antibacterial activity. *J Organomet Chem* **2013**, *725*, 46-53.
98. Thati, B.; Noble, A.; Creaven, B.S.; Walsh, M.; McCann, M.; Kavanagh, K.; Devereux, M.; Egan, D.A. In vitro anti-tumour and cyto-selective effects of coumarin-3-carboxylic acid and three of its hydroxylated derivatives, along with their silver-based complexes, using human epithelial carcinoma cell lines. *Cancer Lett* **2007**, *248*, 321-331, doi:10.1016/j.canlet.2006.08.009.
99. Liu, J.J.; Galettis, P.; Farr, A.; Maharaj, L.; Samarasinha, H.; McGechan, A.C.; Baguley, B.C.; Bowen, R.J.; Berners-Price, S.J.; McKeage, M.J. In vitro antitumour and hepatotoxicity profiles of Au(I) and Ag(I) bidentate pyridyl phosphine complexes and relationships to cellular uptake. *J Inorg Biochem* **2008**, *102*, 303-310, doi:10.1016/j.jinorgbio.2007.09.003.
100. Banti, C.N.; Kyros, L.; Geromichalos, G.D.; Kourkoumelis, N.; Kubicki, M.; Hadjikakou, S.K. A novel silver iodide metalo-drug: experimental and computational modelling assessment of its interaction with intracellular DNA, lipoxygenase and glutathione. *Eur J Med Chem* **2014**, *77*, 388-399, doi:10.1016/j.ejmech.2014.03.028.
101. Yilmaz, V.T.; Gocmen, E.; Icsel, C.; Cengiz, M.; Susluer, S.Y.; Buyukgungor, O. Di- and polynuclear silver(I) saccharinate complexes of tertiary diphosphane ligands: synthesis, structures, in vitro DNA binding, and antibacterial and anticancer properties. *J Biol Inorg Chem* **2014**, *19*, 29-44, doi:10.1007/s00775-013-1052-y.
102. Kasuga, N.C.; Sugie, A.; Nomiya, K. Syntheses, structures and antimicrobial activities of water-soluble silver(I)-oxygen bonding complexes with chiral and racemic camphanic acid (Hca) ligands. *Dalton Trans* **2004**, 10.1039/B411859F, 3732-3740, doi:10.1039/B411859F.
103. Mirabelli, C.K.; Johnson, R.K.; Sung, C.M.; Faucette, L.; Muirhead, K.; Crooke, S.T. Evaluation of the in vivo antitumor activity and in vitro cytotoxic properties of auranofin, a coordinated gold compound, in murine tumor models. *Cancer Res* **1985**, *45*, 32-39.
104. Simon, T.M.; Kunishima, D.H.; Vibert, G.J.; Lorber, A. Screening trial with the coordinated gold compound auranofin using mouse lymphocyte leukemia P388. *Cancer Res* **1981**, *41*, 94-97.
105. Sutton, B.M.; McGusty, E.; Walz, D.T.; DiMartino, M.J. Oral gold. Antiarthritic properties of alkylphosphinegold coordination complexes. *J Med Chem* **1972**, *15*, 1095-1098, doi:10.1021/jm00281a001.
106. Schuh, E.; Pfluger, C.; Citta, A.; Folda, A.; Rigobello, M.P.; Bindoli, A.; Casini, A.; Mohr, F. Gold(I) carbene complexes causing thioredoxin 1 and thioredoxin 2 oxidation as potential anticancer agents. *J Med Chem* **2012**, *55*, 5518-5528, doi:10.1021/jm300428v.
107. Krishnamurthy, D.; Karver, M.R.; Fiorillo, E.; Orru, V.; Stanford, S.M.; Bottini, N.; Barrios, A.M. Gold(I)-mediated inhibition of protein tyrosine phosphatases: a

detailed in vitro and cellular study. *J Med Chem* **2008**, *51*, 4790-4795, doi:10.1021/jm800101w.
108. Karver, M.R.; Krishnamurthy, D.; Kulkarni, R.A.; Bottini, N.; Barrios, A.M. Identifying potent, selective protein tyrosine phosphatase inhibitors from a library of Au(I) complexes. *J Med Chem* **2009**, *52*, 6912-6918, doi:10.1021/jm901220m.
109. Hopkinson, M.N.; Richter, C.; Schedler, M.; Glorius, F. An overview of N-heterocyclic carbenes. *Nature* **2014**, *510*, 485-496, doi:10.1038/nature13384.
110. Cavallo, L.; Correa, A.; Costabile, C.; Jacobsen, H. Steric and electronic effects in the bonding of N-heterocyclic ligands to transition metals. *J Organomet Chem* **2005**, *690*, 5407-5413.
111. Lin, J.C.; Huang, R.T.; Lee, C.S.; Bhattacharyya, A.; Hwang, W.S.; Lin, I.J. Coinage metal-N-heterocyclic carbene complexes. *Chem Rev* **2009**, *109*, 3561-3598, doi:10.1021/cr8005153.
112. Messori, L.; Marchetti, L.; Massai, L.; Scaletti, F.; Guerri, A.; Landini, I.; Nobili, S.; Perrone, G.; Mini, E.; Leoni, P., et al. Chemistry and biology of two novel gold(I) carbene complexes as prospective anticancer agents. *Inorg Chem* **2014**, *53*, 2396-2403, doi:10.1021/ic401731a.
113. Barnard, P.J.; Berners-Price, S.J. Targeting the mitochondrial cell death pathway with gold compounds. *Coord Chem Rev* **2007**, *251*, 1889 –1902.
114. Maftei, C.V.; Fodor, E.; Jones, P.G.; Freytag, M.; Franz, M.H.; Kelter, G.; Fiebig, H.H.; Tamm, M.; Neda, I. N-heterocyclic carbenes (NHC) with 1,2,4-oxadiazole-substituents related to natural products: synthesis, structure and potential antitumor activity of some corresponding gold(I) and silver(I) complexes. *Eur J Med Chem* **2015**, *101*, 431-441, doi:10.1016/j.ejmech.2015.06.053.
115. Saturnino, C.; Barone, I.; Iacopetta, D.; Mariconda, A.; Sinicropi, M.S.; Rosano, C.; Campana, A.; Catalano, S.; Longo, P.; Ando, S. N-heterocyclic carbene complexes of silver and gold as novel tools against breast cancer progression. *Future Med Chem* **2016**, *8*, 2213-2229, doi:10.4155/fmc-2016-0160.
116. Iacopetta, D.; Mariconda, A.; Saturnino, C.; Caruso, A.; Palma, G.; Ceramella, J.; Muia, N.; Perri, M.; Sinicropi, M.S.; Caroleo, M.C., et al. Novel Gold and Silver Carbene Complexes Exert Antitumor Effects Triggering the Reactive Oxygen Species Dependent Intrinsic Apoptotic Pathway. *ChemMedChem* **2017**, *12*, 2054-2065, doi:10.1002/cmdc.201700634.
117. Bocchino, C.; Napoli, M.; Costabile, C.; Longo, P. Synthesis of octahedral zirconium complex bearing [NHC□O] ligands, and its behavior as catalyst in the polymerization of olefins. *J. Polym. Sci. Part A* **2011**, *49*, 862–870.
118. Cooper, G.; Irwin, W.J. 1-Styrylimidazoles *J Chem Soc Perkin Trans 1* **1976**, 545-549
119. Mariconda, A.; Grisi, F.; Costabile, C.; Falcone, S.; Bertolasi, V.; Longo, P. Synthesis, characterization and catalytic behaviour of a palladium complex bearing a hydroxy-functionalized N-heterocyclic carbene ligand. *New J Chem* **2014**, *38*, 762–769.
120. Baker, M.V.; Barnard, P.J.; Berners-Price, S.J.; Brayshaw, S.K.; Hickey, J.L.; Skelton, B.W.; White, A.H. Synthesis and structural characterisation of linear Au(I) N-heterocyclic carbene complexes: New analogues of the Au(I) phosphine drug Auranofin. *J Organomet Chem* **2005**, *690*, 5625–5635.
121. Conchon, E.; Anizon, F.; Aboab, B.; Golsteyn, R.M.; Leonce, S.; Pfeiffer, B.; Prudhomme, M. Synthesis, checkpoint kinase 1 inhibitory properties and in vitro antiproliferative activities of new pyrrolocarbazoles. *Bioorg Med Chem* **2008**, *16*, 4419-4430, doi:10.1016/j.bmc.2008.02.061.

122. Jin, C.; Liu, J.; Chen, Y.; Li, G.; Guan, R.; Zhang, P.; Ji, L.; Chao, H. Cyclometalated iridium(iii) complexes with imidazo[4,5-*f*][1,10]phenanthroline derivatives for mitochondrial imaging in living cells. *Dalton Trans.* **2015**, *44*, 7538-7547
123. Sanpui, P.; Chattopadhyay, A.; Ghosh, S.S. Induction of apoptosis in cancer cells at low silver nanoparticle concentrations using chitosan nanocarrier. *ACS Appl Mater Interfaces* **2011**, *3*, 218-228, doi:10.1021/am100840c.
124. El Habbash, A.I.; Mohd Hashim, N.; Ibrahim, M.Y.; Yahayu, M.; Omer, F.A.E.; Abd Rahman, M.; Nordin, N.; Lian, G.E.C. In vitro assessment of anti-proliferative effect induced by alpha-mangostin from Cratoxylum arborescens on HeLa cells. *PeerJ* **2017**, *5*, e3460, doi:10.7717/peerj.3460.
125. Hwang, N.L.; Kang, Y.J.; Sung, B.; Hwang, S.Y.; Jang, J.Y.; Oh, H.J.; Ahn, Y.R.; Kim, D.H.; Kim, S.J.; Ullah, S., et al. MHY451 induces cell cycle arrest and apoptosis by ROS generation in HCT116 human colorectal cancer cells. *Oncol Rep* **2017**, *38*, 1783-1789.
126. Trachootham, D.; Alexandre, J.; Huang, P. Targeting cancer cells by ROS-mediated mechanisms: a radical therapeutic approach? *Nat Rev Drug Discov* **2009**, *8*, 579-591, doi:10.1038/nrd2803.
127. Hitomi, Y.; Iwamoto, Y.; Kashida, A.; Kodera, M. Mononuclear nonheme iron(III) complexes that show superoxide dismutase-like activity and antioxidant effects against menadione-mediated oxidative stress. *Chem Commun (Camb)* **2015**, *51*, 8702-8704, doi:10.1039/c5cc02019k.
128. Arnold, P.L.; Rodden, M.; Davis, K.M.; Scarisbrick, A.C.; Blake, A.J.; Wilson, C. Asymmetric lithium(I) and copper(II) alkoxy-N-heterocyclic carbene complexes; crystallographic characterisation and Lewis acid catalysis. *Chem Commun (Camb)* **2004**, 10.1039/b404614e, 1612-1613, doi:10.1039/b404614e.
129. Arnold, P.L.; Liddle, S.T. F-block N-heterocyclic carbene complexes. *Chem Commun (Camb)* **2006**, 10.1039/b606829d, 3959-3971, doi:10.1039/b606829d.
130. Pugh, D.; Danopoulos, A.A. Metal complexes with 'pincer'-type ligands incorporating N-heterocyclic carbene functionalities. *Coord Chem Rev* **2007**, *251*, 610-641, doi:10.1016/j.ccr.2006.08.001.
131. Zhou, Y.B.; Chen, W.Z. Synthesis and characterization of square-planar tetranuclear silver and gold clusters supported by a pyrazole-linked bis(N-heterocyclic carbene) ligand. *Organometallics* **2007**, *26*, 2742-2746, doi:10.1021/om070104j.
132. Bocchino, C.; Napoli, M.; Costabile, C.; Longo, P. Synthesis of Octahedral Zirconium Complex Bearing [NHC-O] Ligands, and Its Behavior as Catalyst in the Polymerization of Olefins. *J Polym Sci Part A-Polym Chem* **2011**, *49*, 862-870, doi:10.1002/pola.24495.
133. Mariconda, A.; Sirignano, M.; Costabile, C.; Longo, P. New NHC- silver and gold complexes active in A^3-coupling (aldehyde-alkyne-amine) reaction. *Mol Catal* **2020**, *480*, 110570.
134. Jackson, J.R.; Patrick, D.R.; Dar, M.M.; Huang, P.S. Targeted anti-mitotic therapies: can we improve on tubulin agents? *Nat Rev Cancer* **2007**, *7*, 107-117, doi:10.1038/nrc2049.
135. Nitiss, J.L. Targeting DNA topoisomerase II in cancer chemotherapy. *Nat Rev Cancer* **2009**, *9*, 338-350, doi:10.1038/nrc2607.
136. Rudolf, E.; Cervinka, M. Topoisomerases and tubulin inhibitors: a promising combination for cancer treatment. *Curr Med Chem Anticancer Agents* **2003**, *3*, 421-429, doi:10.2174/1568011033482242.

137. You, F.; Gao, C. Topoisomerase Inhibitors and Targeted Delivery in Cancer Therapy. *Curr Top Med Chem* **2019**, *19*, 713-729, doi:10.2174/1568026619666190401112948.
138. Xi, J.; Zhu, X.; Feng, Y.; Huang, N.; Luo, G.; Mao, Y.; Han, X.; Tian, W.; Wang, G.; Han, X., et al. Development of a novel class of tubulin inhibitors with promising anticancer activities. *Mol Cancer Res* **2013**, *11*, 856-864, doi:10.1158/1541-7786.MCR-12-0177.
139. Jung, Y.; Lippard, S.J. Direct cellular responses to platinum-induced DNA damage. *Chem Rev* **2007**, *107*, 1387-1407, doi:10.1021/cr068207j.
140. Vargesson, N. Thalidomide-induced teratogenesis: history and mechanisms. *Birth Defects Res C Embryo Today* **2015**, *105*, 140-156, doi:10.1002/bdrc.21096.
141. Kim, J.H.; Scialli, A.R. Thalidomide: The Tragedy of Birth Defects and the Effective Treatment of Disease. *Toxicological Sciences* **2011**, *122*, 1-6.
142. Wu, J.J.; Huang, D.B.; Pang , K.R.; Hsu, S.; Tyring, S.K. Thalidomide: dermatological indications, mechanisms of action and side-effects. *Br J Dermatol* **2005**, *153*, 254–273.
143. Wang, X.; Li, Y.; Yan, X. Efficacy and Safety of Novel Agent-Based Therapies for Multiple Myeloma: A Meta-Analysis. *Biomed Res Int* **2016**, *2016*, 6848902, doi:10.1155/2016/6848902.
144. El-Aarag, B.Y.A.; Kasai, T.; Zahran, M.A.H.; Zakhary, N.I.; Shigehiro, T.; Sekhar, S.C.; Agwa, H.S.; Mizutani, A.; Murakami, H.; Kakuta, H., et al. In vitro anti-proliferative and anti-angiogenic activities of thalidomide dithiocarbamate analogs. *Int Immunopharmacol* **2014**, *21*, 283–292.
145. Simon, M.; Pariente, B.; Lambert, J.; Cosnes, J.; Bouhnik, Y.; Marteau, P.; Allez, M.; Colombel, J.F.; Gornet, J.M. Long-term Outcomes of Thalidomide Therapy for Adults With Refractory Crohn's Disease. *Clin Gastroenterol Hepatol* **2016**, *14*, 966-972 e962, doi:10.1016/j.cgh.2015.10.034.
146. Charles, P.; Richaud, C.; Beley, S.; Bodard, L.; Simon, M. Pseudotumoral recto-sigmoid herpes simplex virus type 2 in an HIV-infected patient: Dramatic improvement with thalidomide. *J Clin Virol* **2016**, *78*, 12-13, doi:10.1016/j.jcv.2016.02.023.
147. Catalano, A.; Luciani, R.; Carocci, A.; Cortesi, D.; Pozzi, C.; Borsari, C.; Ferrari, S.; Mangani, S. X-ray crystal structures of Enterococcus faecalis thymidylate synthase with folate binding site inhibitors. *Eur J Med Chem* **2016**, *123*, 649-664, doi:10.1016/j.ejmech.2016.07.066.
148. Lamanna, C.; Catalano, A.; Carocci, A.; Di Mola, A.; Franchini, C.; Tortorella, V.; Vanderheyden, P.M.; Sinicropi, M.S.; Watson, K.A.; Sciabola, S. AT1 receptor ligands: virtual-screening-based design with TOPP descriptors, synthesis, and biological evaluation of pyrrolidine derivatives. *ChemMedChem* **2007**, *2*, 1298-1310, doi:10.1002/cmdc.200700082.
149. Carocci, A.; Lentini, G.; Catalano, A.; Cavalluzzi, M.M.; Bruno, C.; Muraglia, M.; Colabufo, N.A.; Galeotti, N.; Corbo, F.; Matucci, R., et al. Chiral aryloxyalkylamines: Selective 5-HT(1B/1D) activation and analgesic activity. *ChemMedChem* **2010**, *5*, 696-704, doi:10.1002/cmdc.200900530.
150. Iacopetta, D.; Carocci, A.; Sinicropi, M.S.; Catalano, A.; Lentini, G.; Ceramella, J.; Curcio, R.; Caroleo, M.C. Old Drug Scaffold, New Activity: Thalidomide-Correlated Compounds Exert Different Effects on Breast Cancer Cell Growth and Progression. *ChemMedChem* **2017**, *12*, 381-389, doi:10.1002/cmdc.201600629.
151. Bigge, C.F.; Hays, S.J.; Novak, P.M.; Drummond, J.T.; Johnson, G.; Bobovski, T.P. New preparations of the N-methyl-D-aspartate receptor antagonist, 4-(3-

phosphonopropyl)-2-piperazinecarboxylic acid (CPP). *Tetrahedron Lett* **1989**, *30*, 5193-5196.
152. Catalano, A.; Carocci, A.; Corbo, F.; Franchini, C.; Muraglia, M.; Scilimati, A.; De Bellis, M.; De Luca, A.; Camerino, D.C.; Sinicropi, M.S., et al. Constrained analogues of tocainide as potent skeletal muscle sodium channel blockers towards the development of antimyotonic agents. *Eur J Med Chem* **2008**, *43*, 2535-2540, doi:10.1016/j.ejmech.2008.01.023.
153. Catalano, A.; Carocci, A.; Lentini, G.; Di Mola, A.; Bruno, C.; Franchini, C. Facile routes for the preparation of 3,4-disubstituted 1,3-oxazolidines and 1,2,5-trisubstituted imidazolidin-4-ones. *J Heterocycl Chem* **2011**, *48*, 261–266.
154. Muraglia, M.; De Bellis, M.; Catalano, A.; Carocci, A.; Franchini, C.; Carrieri, A.; Fortugno, C.; Bertucci, C.; Desaphy, J.F.; De Luca, A., et al. N-aryl-2,6-dimethylbenzamides, a new generation of tocainide analogues as blockers of skeletal muscle voltage-gated sodium channels. *J Med Chem* **2014**, *57*, 2589-2600, doi:10.1021/jm401864b.
155. Catalano, A.; Carocci, A.; Cavalluzzi, M.M.; Di Mola, A.; Lentini, G.; Lovece, A.; Dipalma, A.; Costanza, T.; Desaphy, J.F.; Conte Camerino, D., et al. Hydroxylated analogs of mexiletine as tools for structural-requirements investigation of the sodium channel blocking activity. *Arch Pharm (Weinheim)* **2010**, *343*, 325-332, doi:10.1002/ardp.200900218.
156. Miyano, S.; Sumoto, K.; Satoh, F.; Shima, K.; Hayashimatsu, M.; Morita, M.; Aisaka, K.; Noguchi, T. New antiarrhythmic agents. N-aryl-8-pyrrolizidinealkanamides. *J Med Chem* **1985**, *28*, 714-717, doi:10.1021/jm00383a005.
157. Catalano, A.; Budriesi, R.; Bruno, C.; Di Mola, A.; Defrenza, I.; Cavalluzzi, M.M.; Micucci, M.; Carocci, A.; Franchini, C.; Lentini, G. Searching for new antiarrhythmic agents: evaluation of meta-hydroxymexiletine enantiomers. *Eur J Med Chem* **2013**, *65*, 511-516, doi:10.1016/j.ejmech.2013.05.008.
158. Palma, G.; Frasci, G.; Chirico, A.; Esposito, E.; Siani, C.; Saturnino, C.; Arra, C.; Ciliberto, G.; Giordano, A.; D'Aiuto, M. Triple negative breast cancer: looking for the missing link between biology and treatments. *Oncotarget* **2015**, *6*, 26560-26574, doi:10.18632/oncotarget.5306.
159. Moreira, A.L.; Sampaio, E.P.; Zmuidzinas, A.; Frindt, P.; Smith, K.A.; Kaplan, G. Thalidomide exerts its inhibitory action on tumor necrosis factor alpha by enhancing mRNA degradation. *J Exp Med* **1993**, *177*, 1675-1680, doi:10.1084/jem.177.6.1675.
160. Yang, J.C.; Cortopassi, G.A. Induction of the mitochondrial permeability transition causes release of the apoptogenic factor cytochrome c. *Free Radic Biol Med* **1998**, *24*, 624-631, doi:10.1016/s0891-5849(97)00367-5.
161. Singhai, R.; Patil, V.W.; Jaiswal, S.R.; Patil, S.D.; Tayade, M.B.; Patil, A.V. E-Cadherin as a diagnostic biomarker in breast cancer. *N Am J Med Sci* **2011**, *3*, 227-233, doi:10.4297/najms.2011.3227.
162. Komorowski, J.; Jerczynska, H.; Siejka, A.; Baranska, P.; Lawnicka, H.; Pawlowska, Z.; Stepien, H. Effect of thalidomide affecting VEGF secretion, cell migration, adhesion and capillary tube formation of human endothelial EA.hy 926 cells. *Life Sci* **2006**, *78*, 2558-2563, doi:10.1016/j.lfs.2005.10.016.
163. O'Leary, K.A.; Day, A.J.; Needs, P.W.; Mellon, F.A.; O'Brien, N.M.; Williamson, G. Metabolism of quercetin-7- and quercetin-3-glucuronides by an in vitro hepatic model: the role of human beta-glucuronidase, sulfotransferase, catechol-O-methyltransferase and multi-resistant protein 2 (MRP2) in flavonoid metabolism. *Biochem Pharmacol* **2003**, *65*, 479-491, doi:10.1016/s0006-2952(02)01510-1.

164. Kim, M.K.; Park, K.S.; Lee, C.; Park, H.R.; Choo, H.; Chong, Y. Enhanced stability and intracellular accumulation of quercetin by protection of the chemically or metabolically susceptible hydroxyl groups with a pivaloxymethyl (POM) promoiety. *J Med Chem* **2010**, *53*, 8597-8607, doi:10.1021/jm101252m.
165. Grande, F.; Parisi, O.I.; Mordocco, R.A.; Rocca, C.; Puoci, F.; Scrivano, L.; Quintieri, A.M.; Cantafio, P.; Ferla, S.; Brancale, A., et al. Quercetin derivatives as novel antihypertensive agents: Synthesis and physiological characterization. *Eur J Pharm Sci* **2016**, *82*, 161-170, doi:10.1016/j.ejps.2015.11.021.
166. Picq, M.; Prigent, A.F.; Nemoz, G.; Andre, A.C.; Pacheco, H. Pentasubstituted quercetin analogues as selective inhibitors of particulate 3':5'-cyclic-AMP phosphodiesterase from rat brain. *J Med Chem* **1982**, *25*, 1192-1198, doi:10.1021/jm00352a019.
167. Lu, C.; Huang, F.; Li, Z.; Ma, J.; Li, H.; Fang, L. Synthesis and Bioactivity of Quercetin Aspirinates. *Bull Korean Chem Soc* **2014**, *35*, 518–520.
168. Bouktaib, M.; Lebrun, S.; Atmani, A.; Rolando, C. Hemisynthesis of all the O-monomethylated analogues of quercetin including the major metabolites, through selective protection of phenolic functions. *Tetrahedron* **2002**, *58*, 10001–10009.
169. Iacopetta, D.; Grande, F.; Caruso, A.; Mordocco, R.A.; Plutino, M.R.; Scrivano, L.; Ceramella, J.; Muia, N.; Saturnino, C.; Puoci, F., et al. New insights for the use of quercetin analogs in cancer treatment. *Future Med Chem* **2017**, *9*, 2011-2028, doi:10.4155/fmc-2017-0118.
170. Sudan, S.; Rupasinghe, H.P. Quercetin-3-O-glucoside induces human DNA topoisomerase II inhibition, cell cycle arrest and apoptosis in hepatocellular carcinoma cells. *Anticancer Res* **2014**, *34*, 1691-1699.
171. Ferlin, M.G.; Marzano, C.; Gandin, V.; Dall'Acqua, S.; Dalla Via, L. DNA binding ellipticine analogues: synthesis, biological evaluation, and structure-activity relationships. *ChemMedChem* **2009**, *4*, 363-377, doi:10.1002/cmdc.200800368.
172. Trachootham, D.; Zhou, Y.; Zhang, H.; Demizu, Y.; Chen, Z.; Pelicano, H.; Chiao, P.J.; Achanta, G.; Arlinghaus, R.B.; Liu, J., et al. Selective killing of oncogenically transformed cells through a ROS-mediated mechanism by beta-phenylethyl isothiocyanate. *Cancer Cell* **2006**, *10*, 241-252, doi:10.1016/j.ccr.2006.08.009.
173. Madden, K.R.; Champoux, J.J. Overexpression of human topoisomerase I in baby hamster kidney cells: hypersensitivity of clonal isolates to camptothecin. *Cancer Res* **1992**, *52*, 525-532.
174. Tiwari, G.; Tiwari, R.; Sriwastawa, B.; Bhati, L.; Pandey, S.; Pandey, P.; Bannerjee, S.K. Drug delivery systems: An updated review. *Int J Pharm Investig* **2012**, *2*, 2-11, doi:10.4103/2230-973X.96920.
175. Cormack, P.A.; Elorza, A.Z. Molecularly imprinted polymers: synthesis and characterisation. *J Chromatogr B Analyt Technol Biomed Life Sci* **2004**, *804*, 173-182, doi:10.1016/j.jchromb.2004.02.013.
176. Scrivano, L.; Parisi, O.I.; Iacopetta, D.; Ruffo, M.; Ceramella, J.; Sinicropi, M.S.; Puoci, F. Molecularly imprinted hydrogels for sustained release of sunitinib in breast cancer therapy. *Polymers for Advanced Technologies* **2019**, *30*, 743-748, doi:10.1002/pat.4512.
177. Randrup Hansen, C.; Grimm, D.; Bauer, J.; Wehland, M.; Magnusson, N.E. Effects and Side Effects of Using Sorafenib and Sunitinib in the Treatment of Metastatic Renal Cell Carcinoma. *Int J Mol Sci* **2017**, *18*, doi:10.3390/ijms18020461.
178. Muhammad, P.; Tu, X.Y.; Liu, J.; Wang, Y.J.; Liu, Z. Molecularly Imprinted Plasmonic Substrates for Specific and Ultrasensitive Immunoassay of Trace

Glycoproteins in Biological Samples. *ACS Appl Mater Interfaces* **2017**, *9*, 12082-12091, doi:10.1021/acsami.7b00628.
179. Akiyama, S.; Chen, Z.S.; Sumizawa, T.; Furukawa, T. Resistance to cisplatin. *Anticancer Drug Des* **1999**, *14*, 143-151.
180. Melendez-Zajgla, J.; Garcia, C.; Maldonado, V. Subcellular redistribution of HSP72 protein during cisplatin-induced apoptosis in HeLa cells. *Biochem Mol Biol Int* **1996**, *40*, 253-261, doi:10.1080/15216549600201742.
181. Speelmans, G.; Staffhorst, R.W.; Versluis, K.; Reedijk, J.; de Kruijff, B. Cisplatin complexes with phosphatidylserine in membranes. *Biochemistry* **1997**, *36*, 10545-10550, doi:10.1021/bi9703047.
182. Jakubowicz-Gil, J.; Paduch, R.; Piersiak, T.; Glowniak, K.; Gawron, A.; Kandefer-Szerszen, M. The effect of quercetin on pro-apoptotic activity of cisplatin in HeLa cells. *Biochem Pharmacol* **2005**, *69*, 1343-1350, doi:10.1016/j.bcp.2005.01.022.
183. Hettinga, J.V.; Lemstra, W.; Meijer, C.; Los, G.; de Vries, E.G.; Konings, A.W.; Kampinga, H.H. Heat-shock protein expression in cisplatin-sensitive and -resistant human tumor cells. *Int J Cancer* **1996**, *67*, 800-807, doi:10.1002/(SICI)1097-0215(19960917)67:6<800::AID-IJC8>3.0.CO;2-V.
184. Meyer, K.B.; Madias, N.E. Cisplatin nephrotoxicity. *Miner Electrolyte Metab* **1994**, *20*, 201-213.
185. Aldemir, M.; Okulu, E.; Kosemehmetoglu, K.; Ener, K.; Topal, F.; Evirgen, O.; Gurleyik, E.; Avci, A. Evaluation of the protective effect of quercetin against cisplatin-induced renal and testis tissue damage and sperm parameters in rats. *Andrologia* **2014**, *46*, 1089-1097, doi:10.1111/and.12197.
186. Yang, J.X.; Luo, Y.; Qiu, H.M.; Tang, W.X. Characterization and resistance mechanisms of cisplatin-resistant human hepatocellular carcinoma cell line. *Saudi Med J* **2009**, *30*, 35-40.
187. Zhao, J.L.; Zhao, J.; Jiao, H.J. Synergistic growth-suppressive effects of quercetin and cisplatin on HepG2 human hepatocellular carcinoma cells. *Appl Biochem Biotechnol* **2014**, *172*, 784-791, doi:10.1007/s12010-013-0561-z.
188. Choie, D.D.; Longnecker, D.S.; del Campo, A.A. Acute and chronic cisplatin nephropathy in rats. *Lab Invest* **1981**, *44*, 397-402.
189. Matsushima, H.; Yonemura, K.; Ohishi, K.; Hishida, A. The role of oxygen free radicals in cisplatin-induced acute renal failure in rats. *J Lab Clin Med* **1998**, *131*, 518-526, doi:10.1016/s0022-2143(98)90060-9.
190. Heim, K.E.; Tagliaferro, A.R.; Bobilya, D.J. Flavonoid antioxidants: chemistry, metabolism and structure-activity relationships. *J Nutr Biochem* **2002**, *13*, 572-584, doi:10.1016/s0955-2863(02)00208-5.
191. Hatia, S.; Septembre-Malaterre, A.; Le Sage, F.; Badiou-Beneteau, A.; Baret, P.; Payet, B.; Lefebvre d'hellencourt, C.; Gonthier, M.P. Evaluation of antioxidant properties of major dietary polyphenols and their protective effect on 3T3-L1 preadipocytes and red blood cells exposed to oxidative stress. *Free Radic Res* **2014**, *48*, 387-401, doi:10.3109/10715762.2013.879985.
192. Majewska, M.; Skrzycki, M.; Podsiad, M.; Czeczot, H. Evaluation of antioxidant potential of flavonoids: an in vitro study. *Acta Pol Pharm* **2011**, *68*, 611-615.
193. Sanchez-Gonzalez, P.D.; Lopez-Hernandez, F.J.; Duenas, M.; Prieto, M.; Sanchez-Lopez, E.; Thomale, J.; Ruiz-Ortega, M.; Lopez-Novoa, J.M.; Morales, A.I. Differential effect of quercetin on cisplatin-induced toxicity in kidney and tumor tissues. *Food Chem Toxicol* **2017**, *107*, 226-236, doi:10.1016/j.fct.2017.06.047.
194. Geetha, T.; Malhotra, V.; Chopra, K.; Kaur, I.P. Antimutagenic and antioxidant/prooxidant activity of quercetin. *Indian J Exp Biol* **2005**, *43*, 61-67.

195. Gabizon, A.A. Stealth liposomes and tumor targeting: one step further in the quest for the magic bullet. *Clin Cancer Res* **2001**, *7*, 223-225.
196. Sharma, G.; Park, J.; Sharma, A.R.; Jung, J.S.; Kim, H.; Chakraborty, C.; Song, D.K.; Lee, S.S.; Nam, J.S. Methoxy poly(ethylene glycol)-poly(lactide) nanoparticles encapsulating quercetin act as an effective anticancer agent by inducing apoptosis in breast cancer. *Pharm Res* **2015**, *32*, 723-735, doi:10.1007/s11095-014-1504-2.
197. Ren, K.W.; Li, Y.H.; Wu, G.; Ren, J.Z.; Lu, H.B.; Li, Z.M.; Han, X.W. Quercetin nanoparticles display antitumor activity via proliferation inhibition and apoptosis induction in liver cancer cells. *Int J Oncol* **2017**, *50*, 1299-1311, doi:10.3892/ijo.2017.3886.
198. Liu, D.; He, C.; Wang, A.Z.; Lin, W. Application of liposomal technologies for delivery of platinum analogs in oncology. *Int J Nanomedicine* **2013**, *8*, 3309-3319, doi:10.2147/IJN.S38354.
199. Boulikas, T. Clinical overview on Lipoplatin: a successful liposomal formulation of cisplatin. *Expert Opin Investig Drugs* **2009**, *18*, 1197-1218, doi:10.1517/13543780903114168.
200. Sinicropi, M.S.; Caruso, A.; Conforti, F.; Marrelli, M.; El Kashef, H.; Lancelot, J.C.; Rault, S.; Statti, G.A.; Menichini, F. Synthesis, inhibition of NO production and antiproliferative activities of some indole derivatives. *J Enzyme Inhib Med Chem* **2009**, *24*, 1148-1153, doi:10.1080/14756360802693890.
201. Gue, E.; Since, M.; Ropars, S.; Herbinet, R.; Le Pluart, L.; Malzert-Freon, A. Evaluation of the versatile character of a nanoemulsion formulation. *Int J Pharm* **2016**, *498*, 49-65, doi:10.1016/j.ijpharm.2015.12.010.